

# Cyclic channel-shoal dynamics of ebb-tidal deltas

## Cyclische ontwikkeling van geulen en zandplaten op ebdelta's

(met een samenvatting in het Nederlands)

### PROFESSCHRIFFT

ter verkrijging van de graad van doctor aan de  
Universiteit Utrecht  
op gezag van de  
rector magnificus, prof.dr. H.R.B.M. Kummeling,  
ingevolge het besluit van het college voor promoties  
in het openbaar te verdedigen op

dinsdag 2 juni 2020 des middags te 12.45 uur

door

Klaas Johannes Hendrik Lenstra

geboren op 2 augustus 1988  
te Houten

**Promotor:**

Prof. dr. B.G. Ruessink

**Copromotor:**

Dr. M. van der Vegt

This research was funded by the Netherlands Organisation for Scientific Research (NWO)  
(project 869.15.009).

## **Cyclic channel-shoal dynamics of ebb-tidal deltas**

**Promotor:**

Prof. dr. B.G. Ruessink

**Copromotor:**

Dr. M. van der Vegt

**Examination Committee:**

Prof. dr. H.E. de Swart

*Utrecht University, the Netherlands*

Prof. dr. A. Kroon

*University of Copenhagen, Denmark*

Prof. dr. ir. J.A. Roelvink

*IHE Delft Institute for Water Education, the Netherlands*

Prof. dr. ir. Z.B. Wang

*Delft University of Technology, the Netherlands*

Dr. ir. R.C. de Winter

*Deltarès, the Netherlands*

**ISBN** 978-90-6266-577-8

**Published by** Faculty of Geosciences, Universiteit Utrecht, the Netherlands, in:  
*Utrecht Studies in Earth Sciences (USES) 213*, ISSN 221-4335

**Typeset using** X<sub>A</sub>T<sub>E</sub>X

**Printed by** IPSKAMPprinting || [www.proefschriften.net](http://www.proefschriften.net)

**Cover and illustrations by** Harryt Schimmel and Annelieke Warnar-van den Berg

Except where otherwise noted, this work is licensed under the Creative Commons Attribution 4.0 International License, <http://creativecommons.org/licenses/by/4.0/>

©2020 Klaas J.H. Lenstra

Utrecht Studies in Earth Sciences 213

## Cyclic channel-shoal dynamics of ebb-tidal deltas

Klaas J.H. Lenstra

Utrecht

Faculty of Geosciences, Utrecht University



*“The first principle is that you must not fool yourself - and you are the easiest person to fool.”*

**Richard Feynman**



# Overview

<b>Samenvatting</b>	xii
<b>Summary</b>	xv
<b>1 Introduction</b>	3
1.1 Barrier coasts and ebb-tidal deltas . . . . .	3
1.2 Natural cyclic channel-shoal dynamics . . . . .	5
1.3 Human activities . . . . .	8
1.4 Aims and outline of this thesis . . . . .	9
<b>2 Cyclic channel-shoal dynamics at the Ameland Inlet: the impact on waves, tides and sediment transport</b>	13
2.1 Introduction . . . . .	14
2.2 Material and methods . . . . .	15
2.2.1 Ameland Inlet . . . . .	15
2.2.2 Modeling system . . . . .	16
2.2.3 Model setup . . . . .	17
2.3 Results . . . . .	24
2.3.1 Wave energy patterns . . . . .	24
2.3.2 Sediment transport . . . . .	26
2.4 Discussion . . . . .	37
2.5 Conclusions . . . . .	39
<b>3 Unraveling the mechanisms that cause cyclic channel-shoal dynamics of ebb-tidal deltas</b>	43
3.1 Introduction . . . . .	44
3.2 Material and methods . . . . .	46
3.2.1 Modeling system . . . . .	46
3.2.2 Model domain . . . . .	47
3.2.3 Model setup . . . . .	47
3.2.4 Boundary conditions . . . . .	49
3.2.5 Model simulations and model analysis . . . . .	49
3.3 Results . . . . .	51
3.3.1 Modeled cyclic behavior . . . . .	51
3.3.2 Physical processes . . . . .	54
3.3.3 Time scale . . . . .	61
3.4 Discussion . . . . .	62
3.4.1 Comparison with real systems . . . . .	62
3.4.2 Mechanisms causing cyclic behavior . . . . .	64
3.4.3 Shortcomings . . . . .	65
3.5 Conclusions . . . . .	67
<b>4 The impact of sea-level rise and basin area reduction on the cyclic behavior of tidal inlet systems</b>	69
4.1 Introduction . . . . .	70

4.2	Material and methods . . . . .	71
4.2.1	Model domains and settings . . . . .	71
4.2.2	Model simulations . . . . .	72
4.2.3	Model analysis . . . . .	73
4.3	Results . . . . .	74
4.3.1	Undisturbed model runs . . . . .	74
4.3.2	Reduced basin area . . . . .	75
4.3.3	Relative sea-level rise . . . . .	82
4.4	Discussion . . . . .	85
4.4.1	Reduced basin area . . . . .	85
4.4.2	Relative sea-level rise . . . . .	86
4.5	Conclusions . . . . .	87
<b>5</b>	<b>The effect of mega-nourishments on long-term behavior of ebb-tidal deltas</b>	<b>89</b>
5.1	Introduction . . . . .	90
5.2	Material and methods . . . . .	92
5.2.1	Model domains and settings . . . . .	93
5.2.2	Model simulations . . . . .	93
5.2.3	Model analysis . . . . .	94
5.3	Results . . . . .	95
5.3.1	Nourishment on ebb-tidal delta platform . . . . .	95
5.3.2	Sensitivity to location . . . . .	100
5.3.3	Physical mechanisms . . . . .	101
5.4	Discussion . . . . .	104
5.4.1	Comparing model findings to nourishment objectives . . . . .	104
5.4.2	Shortcomings . . . . .	105
5.4.3	Applicability . . . . .	105
5.5	Conclusions . . . . .	106
<b>6</b>	<b>Synthesis</b>	<b>109</b>
6.1	Main Conclusions . . . . .	109
6.1.1	Effects . . . . .	109
6.1.2	Causes . . . . .	110
6.1.3	Problems . . . . .	112
6.1.4	Mitigation routes . . . . .	113
6.2	Discussion and perspectives . . . . .	114
6.2.1	Modeling system . . . . .	114
6.2.2	Implications of results for coastal safety and management strategies . . . . .	116
<b>Appendix A</b>	<b>Model description</b>	<b>119</b>
A.1	Hydrodynamics . . . . .	119
A.1.1	Currents . . . . .	119
A.1.2	Waves . . . . .	120
A.2	Sediment transport . . . . .	121
A.2.1	Bed load . . . . .	121
A.2.2	Suspended load . . . . .	122
<b>Bibliography</b>		<b>125</b>
<b>About the author</b>		<b>131</b>
<b>Dankwoord/Acknowledgements</b>		<b>135</b>

## Samenvatting

De Waddeneilanden scheiden de Waddenzee van de Noordzee. Tussen de Waddeneilanden liggen zeegaten met diepe geulen. Deze geulen monden uit in ondiepe ebdelta's (ook wel buitendelta's genoemd). De zandige ebdelta's zijn om twee redenen belangrijk voor kustveiligheid. Ten eerste versterkt hun ondiepte de golfsbreking en -demping, wat de eilanden beschermt tegen stormgolven. Ten tweede is er een continue uitwisseling van zand tussen de ebdelta, de eilanden en het bekken. Hierdoor kan zand van de ebdelta naar aanliggende kustgebieden worden getransporteerd zodat aldaar erosie kan worden tegengegaan. In dit soort omgevingen bestaat een continue interactie tussen getijstromingen, golven en het zand op de bodem. Als gevolg daarvan zijn ebdelta's dynamisch: ze veranderen voortdurend van vorm. Deze morfologische verandering is cyclisch: de diepe geulen zoeken steeds een nieuwe oriëntatie (geulrotatie) afgewisseld met de vorming van een nieuwe geul die door de ebdelta heen snijdt (geulvorming) waarna de oude geul opgevuld wordt met zand. In de tussentijd ontstaan ook zandplaten op de ebdelta die zich langzaam naar de benedendriftse kust verplaatsen en er uiteindelijk aan vastgroeien. Dit cyclisch gedrag heeft vier karakteristieke fasen: geulrotatie, zandplaatgroei, geulvorming en geulgroei. Veel ebdelta's kennen een eroderende trend en daarmee komt hun veiligheids- en bufferfunctie in het gedrang. Deze problemen spelen op verschillende plekken in de wereld, en ook in de Nederlandse Waddenzee. De erosie van de ebdelta's wordt mogelijk veroorzaakt door zeespiegelstijging en door grootschalige ingrepen in het systeem, zoals landaanwinningssprojecten en dammen. Om erosie tegen te gaan worden zandsuppleties op ebdelta's overwogen. Omdat de invloed van de mens in kustsystemen steeds verder toeneemt, is het nodig om te begrijpen hoe zowel natuurlijke als menselijke processen het cyclisch gedrag sturen. Het doel van dit proefschrift is om fundamentele kennis op te doen over het cyclische gedrag van ebdelta's. Hiertoe werden numerieke modelsimulaties uitgevoerd met Delft3D en SWAN. De twee onderwerpen die in dit proefschrift aan bod komen, zijn (1) de oorzaken van het natuurlijke cyclische gedrag en het effect hiervan op golven, getij en zandtransport, en (2) de impact van menselijk handelen op ebdelta's.

De eerste stap is het begrijpen van de natuurlijke (ongestoorde) dynamica van ebdelta's. Pas daarna kunnen de effecten van menselijke invloeden als zeespiegelstijging, dijkbouw of zandsuppleties op de dynamica van de ebdelta worden ingeschat. De natuurlijke dynamica gaat over (1) het effect van de morfologie van de ebdelta tijdens de verschillende fasen van het cyclisch gedrag op getijstroming, golven en zandtransport en (2) de mechanismes die het cyclisch gedrag verklaren. In Hoofdstuk 2 bestuderen we de invloed van natuurlijke bodemverandering op golven, getij en zandtransport op de ebdelta en in het gehele zeegatsysteem. Het Amelander zeegat dient als voorbeeld voor vergelijkbare natuurlijke cyclische ontwikkeling van geulen en zandplaten op ebdelta's. Zoals bij vele zeegatsystemen is een afwisseling tussen één en twee geulen in het zeegat onderdeel van het cyclisch gedrag bij het Amelander zeegat. Vier historische bodemliggingen van dit systeem zijn typerend voor de vier fasen in het cyclisch gedrag. De modelsimulaties laten zien dat het dempen van

de golven afhangt van de positie van de zandplaat en van de hoek die de hoofdgeul maakt ten opzichte van het zeegat. Als de hoofdgeul bovenstrooms ombuigt (in dit geval naar het westen), dan worden het bovenendriftse eiland (Terschelling) en het bekken relatief goed beschermd tegen inkomende golven, zowel tijdens goed weer als tijdens stormen. De positie van de zandplaat op de ebdelta bepaalt de hoeveelheid golfenergie bij het benedendriftse eiland (Ameland). Als de zandplaat vlak voor de kust ligt bereikt slechts ~ 7% van de inkomende golfenergie uit de dominante golfrichting de kustzone, terwijl dit ~ 18% is met de zandplaat verder zeewaarts en zelfs ~ 41 – 44% als de zandplaat is vastgegroeid aan de kust. De cyclische ontwikkeling van de geulen heeft de meeste impact op het zandtransport op en bij de ebdelta. Het zandtransport langs de zeerand neemt af als de hoofdgeul van bovenstrooms naar benedenstrooms roteert (west naar oost). Daarnaast is het zandtransport langs de kusten van beide eilanden gerelateerd aan de hoeveelheid golfenergie bij deze eilanden. De zandtransport langs de kust van het benedendriftse eiland naar het zeegat neemt toe terwijl de zandplaat ontstaat, migreert en vastgroeit aan de kust omdat de hoeveelheid golfenergie in de kustzone ook toeneemt. De uitwisseling van zand tussen de ebdelta en het bekken door het zeegat is cyclisch en volgt de periode van de alternerende één en twee geulen zeegatconfiguratie. De export is maximaal wanneer zich twee geulen in het zeegat bevinden en minimaal wanneer er slechts één geul in het zeegat is. Deze variabiliteit wordt veroorzaakt door veranderingen in het verschil tussen maximale vloed- en ebstroming en door verandering in de residuale (getijgemiddelde) stromingen.

In Hoofdstuk 2 is de terugkoppeling van bovenstaande processen naar veranderingen in de bodem niet meegenomen. De geïdealiseerde modelopzet in Hoofdstuk 3 voegt deze interactie wel toe. Hiermee kunnen we de mechanismen ontrafelen die het cyclisch gedrag verklaren. De resultaten laten zien dat de relatieve rol van golven en getijstroming varieert tijdens de vier karakteristieke fasen: geulrotatie, zandplaatgroei, geulvorming en geulgroei. Tijdens de eerste fase zijn de golven dominant: de geul roteert in de benedendriftse richting door golfgedreven stromingen en zandopwoeling door golven. De geul roteert de andere kant op door getijstroming als golven niet worden meegenomen in de modellering. Vervolgens veroorzaken golven en getij gezamenlijk de groei van de zandplaat: de residuale stroming die het essentiële zandtransport verzorgt, is sterk van beide afhankelijk. In deze tweede fase is het een gradiënt in sediment concentratie - deze is hoger boven de ebdelta dan in de geul - die resulteert in meer transport naar de plaat toe dan van de plaat af en dus in groei. Ook het proces van geulvorming kan alleen worden verklaard door de combinatie van getij en golven. De vorming van een nieuwe geul die de ebdelta in tweeën scheidt, schaalt met zowel de maximale ebstromingsnelheid en met golfopwoeling door golven. Er blijkt zelfs een optimale golfhoogte te zijn voor geulvorming, dat wil zeggen dat hogere golven voor verdere geulrotatie zorgen en daarmee de geulvorming uitstellen. Het verzanden van de oude geul is vooral een golfeffect, terwijl het uitdiepen van de nieuwe geul tijdens de laatste fase door de combinatie van golven en getij komt. Ook in deze modelsimulaties zijn cyclische variaties in residuale getijstroming en zandtransport door het zeegat een inherent onderdeel van het cyclisch gedrag. Bij dit cyclisch gedrag neemt de typische periode toe met afnemende kustdrift.

De dynamica van veel ebdelta's is niet meer natuurlijk. Op dit moment zijn de drie belangrijkste menselijke invloeden (1) zandsuppleties, (2) de stijging van de zeespiegel en (3) veranderingen in bekkengrootte (zoals de transitie van Zuiderzee en Lauwerszee naar IJsselmeer en Lauwersmeer). Hoofdstuk 4 bestudeert de langetermijngevolgen van

zeespiegelstijging en bekkenverkleining op de dynamica van ebdelta's, met de uitkomsten van Hoofdstuk 3 als referentie. De resultaten laten zien dat niet de zeespiegelstijging, maar de bekkenverkleining zorgt voor erosie van ebdelta's. Bij beide ingrepen verplaatst zich meer zand naar het bekken toe dan in de referentiesituatie, al is dit slechts tijdelijk bij een verkleining van het bekken. De typische periode van het cyclisch gedrag neemt uiteindelijk af na de bekkenverkleining. Dit treedt pas op na een aanpassingsperiode waarin er juist langere periodes zijn. Bij zeespiegelstijging hangt de verandering in tijdschalen af van hoe snel de zeespiegel stijgt. Voor een relatief langzame zeespiegelstijging ( $\leq 15$  mm/jaar) versnelt het cyclisch gedrag, maar een snellere stijging zorgt juist voor langere periodes. Ondanks de erosie neemt de golfhoogte in het zeegat af na bekkenverkleining, wat samengaat met een vernauwing van het zeegat. Daarentegen neemt de golfenergie in het bekken juist toe bij een stijgende zeespiegel, ondanks het gelijk blijvende volume van de ebdelta.

Om structurele erosie tegen te gaan zijn er in het Nederlandse kustbeschermingsprogramma plannen om grote hoeveelheden zand direct op de ebdelta's te storten. Het is vooralsnog onduidelijk hoe efficiënt zulke megasuppleties zijn en simpele vragen als "wanneer?", "waar?" en "hoeveel?" moeten nog worden beantwoord. In Hoofdstuk 5 wordt ingeschatt wat het langetermijn effect is van een suppletie op het gedrag van ebdelta's. We testen verschillende mogelijke suppleties op de ebdelta, variërend in (plaatsings)moment, locatie en grootte. Modelresultaten laten zien dat alleen wanneer het zand op de ondiepe platen wordt geplaatst, er een toename is in dissipatie van golfenergie op de ebdelta. Voor een significante golfhoogte van 2.0 m op zee neemt de maximale golfhoogte in het zeegat af van 0.8-0.9 m naar 0.6-0.7 m (0.5-0.6 m) voor een suppletievolume van 5% (10%) van het volume van de ebdelta. Dit is slechts een kortetermijn effect, omdat het extra zand snel wordt weggevoerd. De toename in volume van de ebdelta door een suppletie op de platen is slechts tijdelijk, maar als het zand voor de zeewaartse rand wordt gelegd, blijft het langer behouden voor de ebdelta. Veel van de geteste suppleties zorgen voor een kortere periode van de eerste cyclus. Deze kortere tijdschalen vallen samen met een verandering in de oriëntatie van de geul die tijdens de geulvormfase ontstaat. Vooral suppleties op de zandplaten voordat de fase van geulvorming start, zorgen voor een meer benedendrifts georiënteerde geul na de geulvorming. Dit zorgt vervolgens voor een kortere periode van de cyclus, vooral voor de grotere suppleties. De suppleties in dieper water hebben een veel minder duidelijk effect dan de suppleties op de zandplaat. Toch worden ook voor deze suppleties benedendrifts verschoven geulvormingen en kortere periodes gevonden. Een ongewenst mogelijke neveneffect van een suppletie is dat de geul verder naar het benedendriftse eiland kan draaien, wat daar problemen met erosie veroorzaakt.

Dit proefschrift heeft inzicht gegeven in de complexe interacties tussen golven, getij en sediment transport die het cyclische gedrag veroorzaken van natuurlijke en niet-natuurlijke ebdelta's. In de modelsimulaties in dit proefschrift werd slechts één sedimentgrootte beschouwd en ook werd de uitwisseling van water en zand met naastgelegen bekens verwaarloosd. De volgende stap is om niet-uniforme sedimentdistributie en uitwisseling tussen de bekens mee te nemen. Dit zal helpen om de resultaten te generaliseren naar een breder scale aan geometrieën, condities en externe invloeden. Daarnaast is het een logisch vervolg om Hoofdstukken 4 en 5 te combineren en de efficiëntie van suppleties te bepalen tijdens periodes met zeespiegelstijging of suppleties te combineren met een bekkenverkleining.



## Summary

Barrier coasts, such as the Wadden Sea, are separated from the open sea by barrier islands, deep channels and ebb-tidal deltas. Because these deltas are shallow, they enhance the off-shore wave breaking and other forms of wave energy dissipation, protecting the down-wave islands from the full force of storm waves. A second key role of ebb-tidal deltas in coastal safety is their ability to (temporarily) provide the neighboring coastal areas and tidal basins with sediment to compensate for local erosion. Tidal currents and energetic waves continuously interact with the sandy bed, and as a result, like most systems in nature, ebb-tidal deltas are not static. Instead, ebb-tidal deltas often behave in a cyclic manner, in which channels rotate and periodically breach the ebb-tidal delta. Meanwhile, shoals form, migrate and attach to the downdrift barrier islands (i.e., cyclic channel-shoal dynamics). This cyclic behavior has four characterizing phases: channel rotation, shoal growth, channel breaching and channel deepening. Not only in the Netherlands, but throughout the world ebb-tidal deltas are eroding, which decreases their natural safety functions. This erosion is probably the result of sea-level rise and of large-scale interventions such as land reclamation and dam/dike construction. As a mitigation route, nourishments on the ebb-tidal deltas are being considered. As anthropogenic influences in the coastal environment are expected to increase, there is an urgent need to understand how both natural and human-induced processes drive different aspects of the cyclic channel-shoal dynamics. The overall aim of this thesis is to provide fundamental insight into the cyclic behavior of ebb-tidal deltas. For this, numerical model simulations were conducted using Delft3D and SWAN. The two topics of this thesis are (1) the causes of natural cyclic behavior and its effects on tides, waves and sediment transport, and (2) the influence of human activities and possible ebb-tidal delta nourishments on ebb-tidal deltas.

Before the effects of any human activities such as sea-level rise, dike construction or nourishments on ebb-tidal delta behavior can be assessed, the natural (non-disturbed) dynamics must be understood. These natural dynamics include (1) the effect of changed bathymetries during the different phases of the cyclic behavior on nearby tidal currents, waves and sediment transport, and (2) the mechanisms leading to the observed cyclic behavior. Therefore, first the natural influence of cyclic morphology on waves, tides and sediment transport on the ebb-tidal delta and the entire tidal inlet system was explored (Chapter 2). The Ameland Inlet was used as a case study with four historic bathymetries, representative of the four phases of cyclic behavior. The outcomes are expected to be applicable to other systems with similar cyclic channel-shoal dynamics. Like many tidal inlet systems, the Ameland Inlet features periodic shifting between one and two channels in the inlet. Of special interest are the wave energy dissipation over the ebb-tidal delta and the exchange of sediment with the barrier islands and the basin, i.e. the two key safety functions of the ebb-tidal delta. The results show that the wave filtering role strongly depends on both the shoal position and the orientation of the main channel. When the main channel has an relatively updrift orientation (in this case to the west), the updrift island (Terschelling) and the basin are better protected from

incoming wave energy, both during fair weather and during storms. However, the shoal on the ebb-tidal delta determines the amount of wave energy reaching the downdrift island (Ameland). With a shoal close to the coast, only  $\sim 7\%$  of the offshore wave energy reaches the nearshore zone, whereas this is  $\sim 18\%$  with the shoal further seaward and  $\sim 41 - 44\%$  after shoal attachment. The cyclic changes in channel position impact the patterns of sediment transport on the ebb-tidal delta, along the coasts and through the inlet. The exchange of sediment between the ebb-tidal delta and the basin is cyclic and follows the periodicity of the one- and two-channel inlet configurations. Net export is largest when there are two channels in the inlet and smallest when the inlet features one deep channel. This is related to changes in tidal asymmetry and mean flows throughout the cyclic behavior. Furthermore, the sediment bypassing along the seaward edge decreases as the main channel rotates from updrift to downdrift. Moreover, the sediment transport along both barrier islands is closely linked to the amount of wave energy in the nearshore zone. Along the downdrift island, the magnitude of the sediment transport directed towards the tidal inlet increases when the shoal forms, migrates, attaches and spreads out over the coast because the wave energy in the nearshore zone also increases.

In Chapter 2, updates in bed level were ignored, but they were included in the idealized model setup in Chapter 3 to study the mechanism causing the observed cyclic behavior. The model forcing was such that different ratios between tidal prism and littoral drift were obtained. Furthermore, sensitivity simulations were performed to identify the relative importance of the different forcing mechanisms. The relative role of tides and waves differs throughout the four characterizing phases: channel rotation, shoal growth, channel breaching and channel deepening. During the first phase, wave-induced mean flows and sediment concentrations cause the downdrift channel rotation. Without waves, the tidal currents cause updrift channel rotation. Subsequently, mean flows are the main driver of the sediment transport that causes shoal growth during the second phase. Contrary to the channel rotation phase, this is combined wave- and tide-induced mean flow. The sediment concentration at the updrift shoal exceeds that in the channel, and, as a result, the magnitude of the sediment transport decreases in downdrift direction. This gradient causes the delta expansion that characterizes this phase. Similar to shoal growth, the breaching of ebb-tidal deltas can only be explained by tides and waves operating simultaneously. This formation of a new channel increases with the increasing ebb flow velocity and wave-induced sediment concentration. In fact, there is an optimum wave height for breaching of the ebb-tidal delta; that is, larger waves cause further channel rotation rather than channel breaching. The deepening of the new channel during the last phase is only reproduced if waves and tides are both included, whereas the infilling of the old channel is attributable to waves. Similar to Chapter 2, cyclic variations in mean flows and sediment transport through the inlet are an inherent feature of the cyclic behavior. Generally, the typical period of cyclic behavior increases with decreasing littoral drift.

The second topic of this thesis covers the cyclic behavior of ebb-tidal deltas in human-affected environments. The three most influential human-induced impacts are sediment nourishments on the ebb-tidal delta, relative sea-level rise and changes to the basin size by dam construction or land reclamation (for example, the construction of the Afsluitdijk and the closure of the Lauwerszee). The long-term effects of sea-level rise and basin area reduction on cyclic behavior of ebb-tidal deltas were assessed in Chapter 4, with the outcomes of Chapter 3 as reference. The results show that a reduction in basin size causes erosion of ebb-

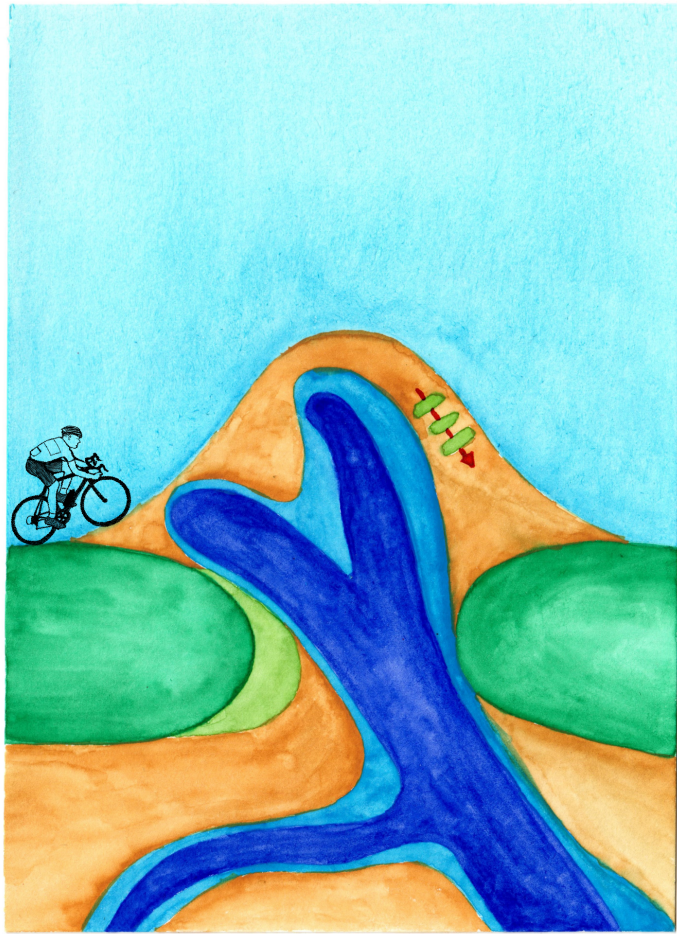
tidal deltas, which is not the case for relative sea-level rise. Despite this erosion, the wave height in the inlet decreases concurrently with a reduction in cross-sectional area after basin reduction. In contrast, more wave energy reaches the basin with sea-level rise, even though the volume of the ebb-tidal delta is unaffected. For both interventions, more sediment is imported to the basin than in the reference case, albeit only temporary for basin reductions. An instantaneous decrease in basin area size eventually leads to a shorter time scale of cyclic behavior. However, this is only after an initial adjustment period, during which the cyclic behavior severely slows down. The effect of relative sea-level rise on this time scale greatly depends on the rate of rise. For relatively low rates ( $\leq 15$  mm/year), the period of the cycles gradually shortens, but higher rates can cause longer periods.

To combat structural erosion, nourishments on ebb-tidal deltas are considered within the Dutch coastal defense program. However, basic questions such as “when?”, “where?” and “how much?” remain unanswered. Chapter 5 explored the interaction between the long-term behavior of ebb-tidal deltas and ebb-tidal delta nourishments that vary in location, size and implementation timing in the cycle. The nourishment only increases the wave energy dissipation over the ebb-tidal delta if it is implemented on the shallow area of the ebb-tidal delta (i.e., the platform). For an offshore significant wave height of 2.0 m, the maximum wave height in the inlet decreases from 0.8-0.9 m to 0.6-0.7 m and 0.5-0.6 m for a nourishment volume of 5% and 10% of the ebb-tidal delta volume, respectively. This is a short-term rather than a long-term effect as the nourishment rapidly disintegrates. The increase in volume for a platform nourishment is also only temporarily, whereas a nourishment at the ebb-shield does result in an long-terms increase in the ebb-tidal delta volume. Most tested nourishments initially lead to a shorter period of cyclic behavior, after which the ebb-tidal delta reverts back to its natural behavior and cycle period. This shorter time scale is linked to the orientation of the channel that is formed by the breach. Especially for a platform nourishment before the breach, the newly formed channel after the breach has a more downdrift orientation. This subsequently leads to a shorter period until the next breach, especially for the larger nourishments. The effects of nourishing the ebb-shield on the cyclic behavior is much less pronounced than if the platform is nourished. Nonetheless, these nourishment also yield downdrift shifted breaches and shorter time scales. An unwanted possible side-effect of a nourishment on the ebb-tidal delta is that it can force the channel to rotate further to the downdrift island, there causing erosional problems.

The four chapters have provided insights into the complex mutual interaction between cyclic behavior, tides, waves and sediment transport under natural and impacted conditions. The model simulations in this thesis did not include more than one sediment size and ignored the exchange of sediment and water between adjacent basins. The next step will be to incorporate nonuniform sediment distribution and basin connectivity. This will help to generalize the results for a wider range of geometries, conditions and external influences. Furthermore, a logical follow-up study is to combine Chapters 4 and 5 and to evaluate nourishment efficiency during periods of relative sea-level rise or to combine a nourishment with a change in basin geometry.







# Chapter 1 | Introduction

## 1.1 Barrier coasts and ebb-tidal deltas

Chains of barrier islands are found along approximately 10% of the world's coastlines, mainly in areas with an abundance of sediment (Stutz and Pilkey, 2011). This thesis considers barrier coasts in general, but places emphasis on the Wadden Sea. The Wadden Sea is, with its length of about 500 km along the coasts of the Netherlands, Germany and Denmark, one of the largest barrier island systems in the world. Figures 1.1 and 1.2 show the characterizing chain of narrow barrier islands and tidal inlets. The barrier islands and the mainland are separated by a complex network of tidal channels (blue) and large shallow areas (yellow) in the back-barrier basin. The latter are intertidal flats or 'wadden' (submerged during high water and exposed at low water). Each tidal inlet runs between two barrier islands and features one or more channels. Water, sediment, salt and nutrients are exchanged between the open sea and the back-barrier basin through these channels. On the seaward side of the inlet, the channels end in the ebb-tidal delta. This thesis focuses on the interaction between the channels, the ebb-tidal delta and the shoals or bars that are typically located on the ebb-tidal delta. Figures 1.1 also indicates that the Dutch Wadden Sea has been heavily influenced by human interventions. The construction of the Afsluitdijk in 1935 has resulted in consider-

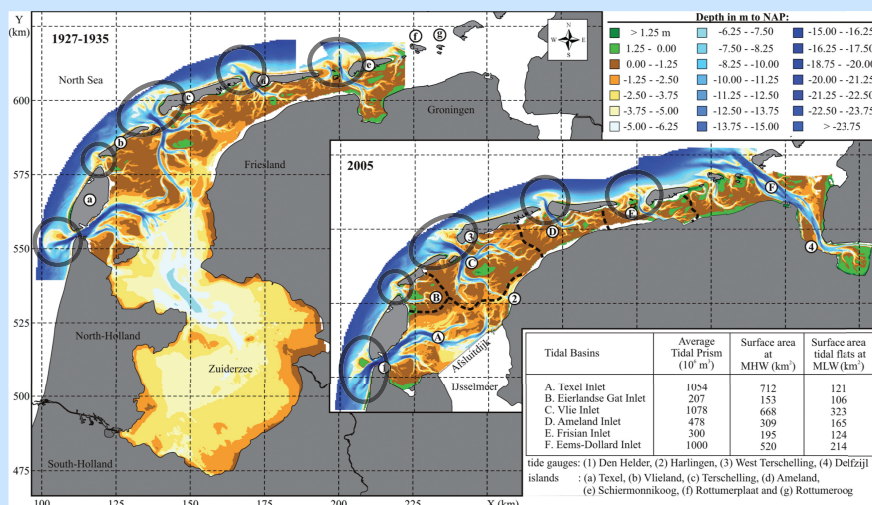


**Figure 1.1** Bathymetric maps of the Dutch (West Frisian) Wadden Sea illustrating the configuration of the inlets, basins, channels and shoals prior to the closure of the Zuiderzee and Lauwerszee (1927-1935) and after these interventions (2005, insert). The black ovals indicate the ebb-tidal deltas. Based on Elias et al. (2012).

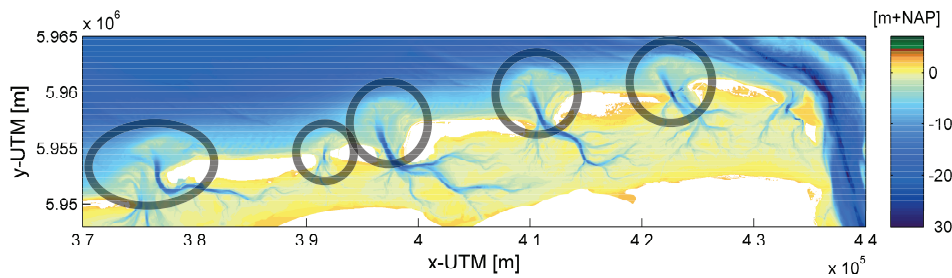


**Figure 1.2** German (East Frisian) Wadden Sea in the southern North Sea. The black ovals indicate the ebb-tidal deltas.

able changes in the shape and size of channels, ebb-tidal deltas and flats. Therefore, this thesis encompasses both natural dynamics and the influence of human activities.

The ebb-tidal deltas offer various functions for mankind, mostly related to the protection of the neighboring coastal areas. Firstly, the shallow water depth enforces wave breaking and other forms of energy dissipation. Thus, ebb-tidal deltas filter the offshore generated waves that approach the mainland (FitzGerald, 1988; Hansen et al., 2013). Secondly, the deltas can be a temporary source of sediment. Extra sediment can be provided to the islands and the basin in times of sea-level rise and after human interventions (Elias et al., 2012). Additionally, barrier coasts contribute to biological diversity (Vincent and Moore, 2015) by providing unique habitat for a wide range of birds, fish and plant species (e.g. Hamerlynck et al., 1992; Lotze et al., 2005). Finally, they have been developed for tourism (e.g. Yang et al., 2012), which adds to their economic value.

Many of these functions are now under threat because the sand volume of many ebb-deltas has reduced profoundly. This has been linked to land reclamation, dam/dike construction (Elias et al., 2012) and sea-level rise (Wang et al., 2018), but can also partly be explained by natural processes (Ridderinkhof et al., 2014b). Along the Dutch coast, large continuous sedimentation in the Wadden Sea basins (roughly 600 million m<sup>3</sup>) compensated for the sediment shortage caused by human activities during the last century. Most of this sediment has been supplied by the ebb-tidal deltas, which have thus reduced in volume. In the most pessimistic scenario of accelerated sea-level rise, the future sediment shortage in the Dutch Wadden Sea exceeds 1.5 billion m<sup>3</sup> by 2100. As a mitigation route, Dutch management authorities have proposed to nourish ebb-tidal deltas to make the Wadden Sea more resilient to climate change.

As human interventions in barrier systems are likely to become more common - not only in the Dutch Wadden Sea, but throughout the world - there is a need to understand and predict how natural and human-induced processes drive long-term ebb-tidal delta behavior. Therefore, this thesis covers two topics: (1) the natural dynamics of ebb-tidal deltas and (2) the human-induced disruptions of this behavior. These two topics are introduced in Sections 1.2 and 1.3, respectively. This chapter ends with the research questions in Section 1.4.

## 1.2 Natural cyclic channel-shoal dynamics

The shallow ebb-tidal delta and its environment are dynamic systems that are mainly shaped by tides and waves (Hayes, 1975). On the basis of mean tidal range and significant wave height, tidal inlets are often classified as wave-dominated, mixed-energy (wave-dominated), mixed-energy (tide-dominated), or tide-dominated (Hayes, 1979). In general, wave-dominated ebb-tidal deltas are relatively small (Hayes, 1980). In this thesis, the focus is on mixed-energy barrier island shorelines (such as the Wadden Sea), which typically have relatively large ebb-tidal deltas and short barrier islands between tidal inlets. The volume of the ebb-tidal delta does not correlate with the tidal range (i.e., the difference between high and low water), but is positively related to the tidal prism (i.e., volume of water that flows through the tidal inlet during one tidal cycle) (Walton and Adams, 1976). The mixed-energy (tide-dominated) Dutch Wadden Sea (Figure 1.1) has larger basins, tidal prisms and thus ebb-tidal deltas than the mixed-energy (wave-dominated) German Wadden Sea (Figure 1.2), even though the tidal range increases in the eastward direction (Sha and Van den Berg, 1993).

Not only the volume of the ebb-tidal delta depends on the relative importance of tidal currents and waves, but also its shape and orientation. For symmetric ebb-tidal deltas the main channel has a shore-normal orientation and the updrift half is a mirror image of the downdrift half. These are mainly found in regions with strong cross-shore and weak along-shore currents (Van der Vegt et al., 2006), such as the east coast of the USA. However, many ebb-tidal deltas are spatially asymmetric because they have a channel that is oriented either downdrift or updrift. For example, for the smaller German ebb-tidal deltas, the channels have a downdrift channel (to the east), whereas the channels of the larger Dutch deltas are oriented updrift (to the west). The observations of Sha (1989) indicate that the inlets with a large tidal prism are dominated by tidal currents. As a result of small phase differences between alongshore and cross-shore tidal currents, the currents leaving the inlet are deflected by the alongshore tidal currents in the updrift direction. For mixed-energy (tide-dominated) systems, this results in updrift-oriented channels (Van der Vegt et al., 2009; Ridderinkhof et al., 2014b). In contrast, the waves and the wave-induced littoral drift can push any ebb-tidal delta and its channel downdrift. This results in downdrift-oriented channels for mixed-energy (wave-dominated) systems (Sha, 1989).

Because the sediment of ebb-tidal deltas is continuously reworked by tidal currents and waves, the morphology of many ebb-tidal deltas is not static, but dynamic, resulting in cyclic behavior (e.g. Ridderinkhof et al., 2016a). This cyclic behavior is part of the sediment bypassing, i.e., the transport of sediment from the updrift to the downdrift coast. FitzGerald (1988) described three types of cyclic behavior, each with characteristic phases. In the conceptual model of *ebb-tidal delta breaching* (Figure 1.3a), shoal dynamics is related to changes in the ebb-tidal delta asymmetry, especially the channel orientation. First, during Phase 1, sediments supplied by the littoral drift accumulate on the updrift side of the ebb-tidal delta. Simultaneously, the main ebb-channel rotates in the downdrift direction. Subsequently, the shoal grows and migrates, causing further rotation of the main channel during Phase 2. Eventually, a breach creates a new channel that bisects the ebb-tidal delta. The old channel is abandoned and gradually fills with sediment during Phase 3, after which the shoal attaches to the downdrift island and the cycle starts over. On other ebb-tidal deltas, the breach takes place at the seaward end of the ebb-tidal delta (*outer delta breaching*, Figure 1.3b). A third option is when the channel is maintained in a more stable orientation while the shoals pe-

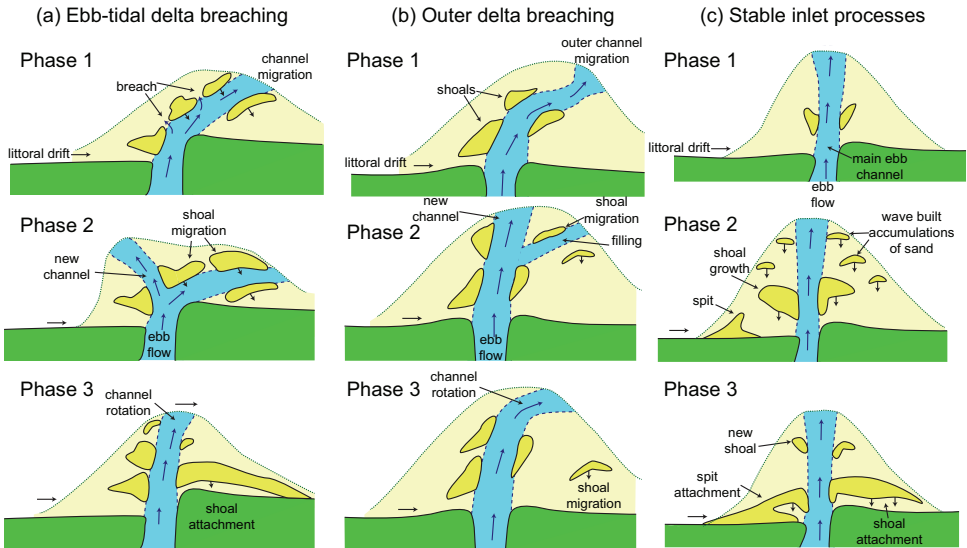


**Figure 1.3** Conceptual models of ebb-tidal delta cyclic behavior proposed by FitzGerald (1988).

riodically form on the both sides of the ebb-tidal delta and migrate landward (*stable inlet processes*, Figure 1.3c). According to FitzGerald (1982), these three types of cyclic behavior account for most of the sediment bypassing at mixed-energy tidal inlets.

Channel rotation and breaching are common to ebb-tidal deltas all over the world. For example, it has been observed at the coasts of Australia (Sedigh et al., 2014), China (Li and Sun, 2011), New Zealand (Ford and Dickson, 2018), Ireland (O'Connor et al., 2011), Portugal (Garel et al., 2014; Balouin et al., 2001), the United Kingdom (Burningham and French, 2006) and many inlets along the east coast of the USA (FitzGerald, 1988; Gaudiano and Kana, 2001). Furthermore, repeated shoal attachments have been observed for most inlets of the Wadden Sea (e.g. Ridderinkhof et al., 2016a). For some systems, the cyclic behavior differs from Figure 1.3 because the breach takes place further landward and thereby forces an alternation between one- and a two-channel inlet configurations. A well-known example of this is the Ameland Inlet (Israel and Dunsbergen, 1999). In this system, the cyclic behavior is characterized by not three, but four phases to incorporate this cyclic inlet configuration: (1) channel rotation and shoal formation; (2) development of secondary channel and continued main channel rotation; (3) fully-developed secondary channel in the inlet; and (4) secondary channel becomes main channel and old channel fills up such that the shoal can migrate and attach to the downdrift coast.

Gaudiano and Kana (2001) and Ridderinkhof et al. (2016a) identified a positive relationship between the tidal prism and the period between successive shoal attachments from observations. In particular, the shoal migration becomes slower leading to a larger period of shoal attachment with an increase in tidal prism. Moreover, modeling studies show that the shoal dynamics (formation and speed of migration) increase with wave height (Bertin et al., 2009; Ridderinkhof et al., 2016b), suggesting a relationship between the wave-induced littoral drift and the time scale of cyclic behavior. Bruun and Gerritsen (1960) related the

presence of stable or rotating channels to the ratio between tidal prism  $P$  (in  $\text{m}^3$ ) and littoral drift  $Q_{ld}$  (in  $\text{m}^3/\text{yr}$ ). Their observations indicate that for  $P/Q_{ld} < 100$  channel rotation and breaching (i.e., *ebb-tidal delta breaching* and *outer delta breaching*) are likely with a shoal return time of several years. In contrast, stable inlet channels are mainly located in tidal systems with  $P/Q_{ld} > 300$ . For these systems, channels often do not rotate and sediment bypasses the inlet via other pathways, for example via *stable inlet processes* or along the seaward end of the ebb-tidal delta (*ebb-tidal delta periphery bypassing*, Herrling and Winter, 2018). Cyclic channel-shoal dynamics including channel rotation has been observed for these high ratios, but only with substantially longer time scales. For example, the Ameland Inlet ( $P/Q_{ld} \approx 383$ ) has a 50-60 year return time of shoal attachment.

Several numerical model studies have tried to reproduce the conceptual models of FitzGerald (1988). Cayocca (2001) showed that littoral drift is essential for shoal formation and that new channels only breach when tidal currents are included. Additionally, Ridderinkhof et al. (2016b) showed that (1) storms can cause shoals to form and grow; (2) wave-driven residual flow over the shoal causes shoal migration (also see Bertin et al., 2009); and (3) shoal coherence during migration is attributable to skewed waves, i.e., waves with relatively strong orbital velocities in the wave crest compared to the trough. However, the model simulations of Ridderinkhof et al. (2016b) did not achieve the full cycle of shoal formation, migration and attachment. In addition, breaching of the ebb-tidal delta and shoal formation was imposed by a virtual extension of the main channel and transfer of the artificially removed sediment to the downdrift side of the ebb-tidal delta. Dastgheib (2012) was the first to successfully model channel rotation and subsequent breaching. *Ebb-tidal delta breaching* was modeled for highly wave-dominated boundary conditions, whereas *outer delta breaching* and *stable inlet processes* were found for wave-dominated mixed energy and tide-dominated forcing, respectively. Unfortunately, the underlying physical mechanisms and their dependence on tides and waves were not studied. Moreover, littoral drift values were not provided and the tidal prism varied throughout the model runs. One cycle of *ebb-tidal delta breaching* was also modeled by Nahon et al. (2012), again without a discussion of the underlying mechanisms.

Because the ebb-tidal delta is large source of sediment, the effect of cyclic behavior on exchange of sediment between basin and sea is of interest. This exchange largely depends on subtidal flows and the tidal asymmetry, i.e., the generation of higher harmonics of the principal symmetric tide. Most studies on tidal asymmetry have focused on the processes inside the basin (e.g. Speer and Aubrey, 1985; Friedrichs and Aubrey, 1988; Ridderinkhof et al., 2014a), which have lead to an adequate understanding of the effect of shallow areas and channels on tidal wave deformation. However, the effect of cyclic changes of the ebb-tidal delta on tidal asymmetry and mean flows has not been studied. Because both channels and shallow areas affect tidal characteristics, it is expected that changes in channel orientation and shoal position will influence the resulting patterns of tidal currents. It is likely that any changes in either tidal asymmetry or mean flows will also influence the patterns of sediment transport in the entire inlet system. The cyclic behavior will also affect wave propagation and the amount and the location of wave energy dissipation. For example, Hansen et al. (2013) showed that the large-scale contraction of the San Francisco bay ebb-tidal delta reduced the offshore wave energy dissipation.

FitzGerald (1988) suggested that the observed cyclic behavior can be attributed to the opposite effects that tides and waves have on the channel orientation. As discussed above, tidal currents with a small phase difference between alongshore and cross-shore currents result

in main channel that is asymmetric in the updrift direction. In contrast, incoming waves and the wave-induced littoral drift force the system in a downdrift asymmetric position. In this concept of counteracting waves and tides, channel rotation is thus a wave-effect and the eventual breaching a tide-induced event. However, this hypothesis has never been tested.

In short, the physical processes that drive the entire cycle of channel-shoal dynamics are not well understood. Also, a relationship between littoral drift and the time scale of cyclic behavior has yet to be identified. Furthermore, it is unclear how the cyclic behavior influences the patterns of tidal currents (mean flow and tidal asymmetry) and sediment transport. Similarly, it remains unknown how cyclic changes in ebb-tidal delta morphology affect the wave energy propagation into the basin and the nearshore zone of the barrier islands.

### 1.3 Human activities

Human interventions have disturbed the natural cyclic behavior of many ebb-tidal deltas. For example, before the closure of the Lauwerszee in 1969 (see Figure 1.1), the Frisian Inlet featured cyclic behavior including the switching between a one- and two-channel inlet system similar to the Ameland Inlet. Oost (1995) observed that the closure had two opposing effects on the cyclic behavior: (1) an unusually large shoal formed, migrated to and merged with Schiermonnikoog; and (2) channel rotation stopped. Subsequently, this significantly reduced the volume of the ebb-tidal delta, which in turn exposed the basin and barrier islands to more energetic waves. Elias et al. (2012) reported a recent formation of a shoal on the updrift side of the main channel, which eventually may very well initiate channel rotation. Because of the reduced tidal prism and ebb-tidal delta size, it is likely that shoals of smaller volume will attach more frequently.

A second example of human-affected cyclic behavior is the Vlie Inlet (Figure 1.1). Ridderinkhof et al. (2016a) suggested that some of the shoals attached to Terschelling were formed as a result of the continuing adjustment of the ebb-tidal delta to the Afsluitdijk in 1935. The closure of the Zuiderzee also forced sedimentation of the Texel and Vlie basins (Elias et al., 2012). The original channels in the basin were too deep for the smaller basin and sediment was imported from the ebb-tidal deltas to reduce channel size. Ebb-tidal delta erosion still continues, suggesting that a new equilibrium at the Texel and Vlie Inlets has not yet been achieved. Other inlets of the Wadden Sea have been forced as well out of their dynamic equilibrium by changes in back-barrier basin size. FitzGerald et al. (1984) showed that poldering behind the barrier islands and along the mainland reduced the basin areas of the East Frisian inlets between 1650 and 1960 by 149 km<sup>2</sup>, which is roughly 30% of their original drainage area.

Additional sediment import into the basins is needed to compensate for the rising mean sea levels. Up to now, sediment transported into the Dutch Wadden Sea through the tidal inlets has been sufficient to compensate for relative sea-level rise (Wang et al., 2018; Van der Spek, 2018). However, as the ebb-tidal deltas continue to lose volume and the sea-level rise during the 21st century is expected to be 2 to 5 times faster than during the 20th century (Vermeersen et al., 2018), it may be that sufficient sediment is no longer available to maintain system morphology (drowning of basins, see Wang et al., 2018). Because cyclic behavior of ebb-tidal delta is likely to depend on the sediment exchange with the basin, relative sea-level rise will affect the long-term behavior of ebb-tidal deltas as well. Moreover, when

the sediment import is insufficient, changes in tidal prism and tidal wave characteristics are expected (Ridderinkhof et al., 2014b), which in turn will influence the cyclic behavior.

Several mitigation routes have been proposed by Dutch authorities. They are considering to implement sediment nourishments in the order of 20 million m<sup>3</sup> in the vicinity of the tidal inlets (DeltaProgramma, 2014; Rijkswaterstaat, 2017). This innovative approach is part of the 'nature-based solutions' for coastal management and is inspired by the Sand Engine (Stive et al., 2013), a mega-nourishment implemented in 2011 at the wave-dominated western coast of the Netherlands. Many implementation locations have been suggested, such as the shallower ebb-tidal delta platform, the seaward front of the ebb-shield, between the ebb-tidal delta and the updrift island or in the main channel. The complex mutual interaction between morphology, waves, tides and sediment transport at an ebb-tidal delta makes it inherently difficult to predict nourishment efficiency for maintaining future sediment availability. Because of the involved uncertainties, a small pilot nourishment (roughly 5 million m<sup>3</sup>) was carried out in 2018 at the ebb-shield of the Ameland ebb-tidal delta and its effects are extensively monitored (Rijkswaterstaat, 2017; van Rhijn, 2019). The Ameland Inlet is the most undisturbed tidal inlet system of the Dutch Wadden Sea (Elias et al., 2012), which, like most Wadden Sea inlets, features clear cyclic channel-shoal dynamics (Israel and Dunsbergen, 1999). Because any nourishment instantaneously changes the ebb-tidal delta volume and forces changes in sediment import/export, wave energy dissipation, littoral drift and tidal flow characteristics (Bak, 2017; Fu, 2018), it is likely that a nourishment affects the natural cyclic behavior and associated time scales.

In short, the second topic of this thesis focuses on the dynamics of ebb-tidal deltas when they are forced out of dynamic equilibrium. It is unclear how the cyclic behavior of channels and shoals changes in response to man-made constructions in tidal inlet systems or to relative sea-level rise. Similarly, little is known about the effect of an ebb-tidal delta mega-nourishment on the morphological development and we are therefore lacking knowledge to design such a nourishment. Furthermore, it remains unknown how any disruption - basin reduction, sea-level rise or nourishment - affects the patterns of sediment fluxes, tidal currents and waves.

## 1.4 Aims and outline of this thesis

The overall aim of this thesis is to provide fundamental insight into the cyclic channel-shoal dynamics of ebb-tidal deltas by means of numerical modeling with a focus on (1) the causes of natural cyclic behavior and its effects on tides, waves and sediment transport, and (2) the influence of human activities on ebb-tidal deltas and possible mitigation routes. Emphasis is laid on cyclic behavior that features both periodic shoal dynamics and alternating phases of channel rotation and breaching (hence cyclic channel-shoal dynamics). The main conceptual models of interest are therefore *ebb-tidal delta breaching* and *outer delta breaching* (see Figure 1.3). Because this thesis offers tools for the qualitative and quantitatively evaluation of natural processes and human interventions, it will help with the design of these interventions. Furthermore, it contributes to the assessment of the future of barrier coasts in general. Motivated by the considerations above, the following four research questions are addressed in this thesis:

**1. How does the cyclic behavior of the ebb-tidal delta influence the tide and wave dynamics and the sediment transport patterns?**

The cyclic ebb-tidal delta morphology will most probably affect the spatial patterns of waves and tidal currents in the entire tidal inlet system. However, how the changing positions of the channels and shoals influence the wave patterns is unknown and so is the influence on the wave energy that is propagating into the tidal basin and towards the barrier coasts. Because the propagation of wave energy over complex morphology strongly depends on wave height, period and direction, different wave conditions should be taken into account. Similarly, it is likely that the changing morphology affects the magnitudes and asymmetry of tidal currents and the subtidal flows. Understanding the dependence of tides and waves on the cyclic behavior will be used to identify the change in sediment transport values, especially the exchange of sediment between basin and sea.

**2. What are the physical processes and feedbacks that drive the observed cyclic channel-shoal dynamics?**

It is unknown how the combination of tides and waves results in cyclic behavior. Are channel rotation and shoal growth indeed only caused by waves and the breaching of ebb-tidal deltas solely by tidal currents? Unraveling the mechanisms of cyclic behavior will show the relative role of tides and waves during the different phases. Moreover, understanding the feedbacks can be used to identify a relationship between the littoral drift and the period between successive shoal attachments.

**3. How do sea-level rise and basin area reduction affect the cyclic behavior of tidal inlet systems?**

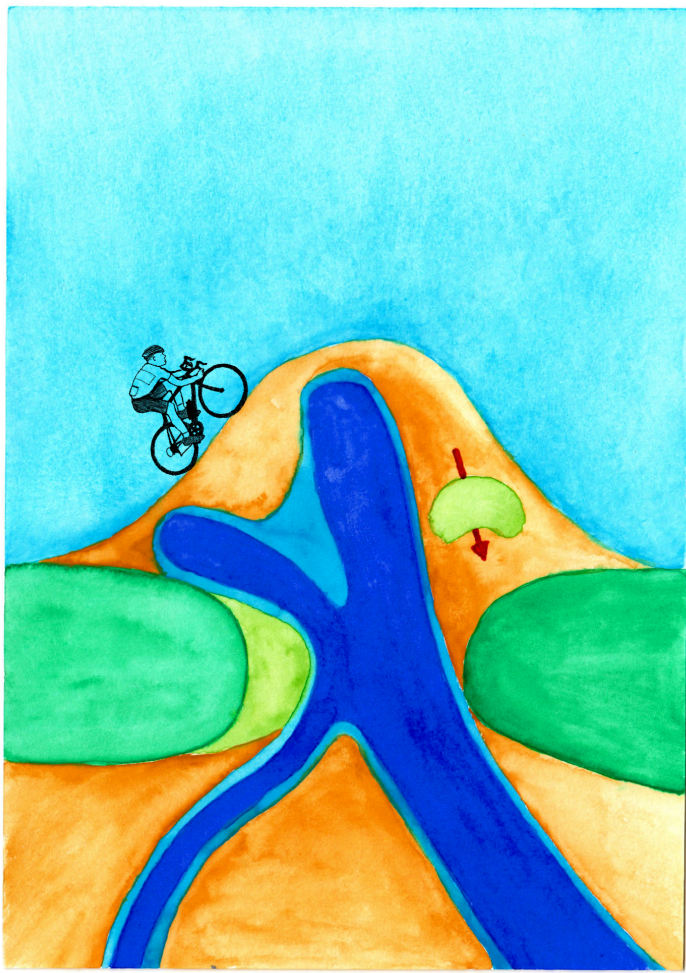
Most ebb-tidal deltas are subject to human activities, which are likely to change natural cyclic behavior. Here, two changes in the natural conditions are investigated: (1) basin reduction and (2) relative sea-level rise. The first disruption is motivated by historic interventions and several instances of an instantaneous reduction in basin area. Despite observed morphological changes, is it largely unknown how the long-term cyclic channel-shoal dynamics respond to different basin reductions and what the time scale of adaptation is. Secondly, rising mean water level will change the morphology of basin, inlet and ebb-tidal delta and enhance the import of sediment. It is unclear what the impact hereof is on the dynamics of ebb-tidal deltas and how this depends on the rate of accelerating sea-level rise.

**4. What is the effect of large-scale ebb-tidal delta nourishments on ebb-tidal delta dynamics?**

Currently, there are no frameworks to predict how the evolution of cyclic ebb-tidal deltas will be influenced by nourishments. It may be that the effect of the nourishment on ebb-tidal delta development will depend on the implementation timing in the cycle, its size or location. Predictive numerical modeling can give insight in these long-term effects on morphology. There is a need to explore the effect of nourishments with different sizes, locations and different timing within the cyclic evolution of the ebb-tidal delta on the long-term morphological evolution and wave propagation.

All four research questions are addressed with the numerical models Delft3D and SWAN. These models use and extend observations with limited spatiotemporal coverage, such that they can be used for studying long-term effects. Furthermore, a numerical model allows for isolated interventions and the adjustment of one variable while fixing the others. This is used here for quantitative analysis of ebb-tidal delta behavior for different forcing conditions and scenarios. The numerical model Delft3D has been successfully applied to simulate tides, sediment transport and bed level changes for tidal inlet systems, while coupling with SWAN incorporates the effects of waves. A brief description of both models is provided in Appendix A.

In Chapter 2, research question 1 is addressed by using the Ameland Inlet as a case study to examine tides, waves and sediment transport change during the different phases of the cyclic evolution of channels and shoals (*ebb-tidal delta breaching*). This chapter also includes effect of different wave conditions, varying in both direction and energy. The bathymetries, the representative tidal forcing and the different wave classes are based on historic measurements. Research question 2 is addressed in Chapter 3 by studying cyclic ebb-tidal deltas in an idealized model setup. It is examined how the modeled behavior (*ebb-tidal delta breaching* and *outer delta breaching*) depends on the ratio between tidal prism and littoral drift. Furthermore, the physical processes that result in the cyclic behavior and the relative roles of tides and waves during the different phases are unraveled. The idealized model setup and the outcomes of Chapter 3 for *ebb-tidal delta breaching* are used as reference in Chapter 4 and 5. A wide range of basin size reductions and different rates of relative sea-level rise are implemented to answer research question 3. In Chapter 5, research question 4 is addressed by implementing and studying the effects and evolution of several possible nourishments and comparing the outcome to non-nourished model simulations. Chapter 6 summarizes the main conclusions of this thesis, discusses their implications and provides an outlook for future research.



## **Chapter 2 | Cyclic channel-shoal dynamics at the Ameland Inlet: the impact on waves, tides and sediment transport**

### **Abstract**

Ebb-tidal deltas are shallow features seaward of tidal inlets, acting as a wave filter for the nearby barrier island and a source of sediment for the landward tidal basin. On many ebb-tidal deltas, channels rotate and shoals periodically attach to the downdrift island. This cyclic behavior can also include an alternation between one- and two-channel inlet configurations. The effect of the long-term ( $>$  years) cyclic behavior on the short-term patterns of waves, tidal currents and sediment transport is unknown. Here we use Delft3D/SWAN models to simulate the Dutch Ameland tidal inlet during four phases of the cycle to show that many of the physical processes on the ebb-tidal delta and in the entire tidal system are affected by the cyclic evolution of channels and shoals. In particular, the periodic variations in the channel positions appear to significantly influence the tidal asymmetry in the inlet and mean flow characteristics. As a result, the net sediment exchange between basin and sea is cyclic and follows the periodicity of the one- and two-channel inlet configuration. Moreover, we find that the wave energy dissipation on the ebb-tidal delta is enhanced by a shallow shoal or an updrift oriented ebb-channel, which shields the coast from the incoming waves. Our results demonstrate how the cyclic channel-shoal dynamics at natural tidal inlets is likely to affect the safety functions of the ebb-tidal deltas, varying the offshore wave energy dissipation as well as adjusting the sediment pathways on the ebb-tidal delta.

### **Published as:**

Klaas J.H. Lenstra, Stefan R.P.M. Pluis, Wim Ridderinkhof, Gerben Ruessink and Maarten van der Vegt (2019), Cyclic channel-shoal dynamics at the Ameland Inlet: the impact on waves, tides, and sediment transport. *Ocean Dynamics*, April 2019, Volume 69, Issue 4, pp 409–425.

## 2.1 Introduction

Tidal inlets connect back-barrier basins to the adjacent sea and facilitate the exchange of sediment. In periods of sea-level rise, the net import of sediment is important for the long-term stability of back-barrier basins to preserve the morphology of the basins. For example, insufficient sediment import may result in loss of salt marsh and tidal flat area (Dissanayake et al., 2012) and thus threaten local ecosystems. Data suggest that most tidal inlets of the Dutch Wadden Sea are importing sediment that is provided by ebb-tidal deltas (Elias et al., 2012). Ebb-tidal deltas are shallow features at the seaward side of tidal inlets and are formed by the joint action of waves and tides (Hayes, 1975). Many ebb-tidal deltas have a cyclic evolution, featuring a rotation of channels and formation of sandy shoals that migrate and attach to the downdrift coast (FitzGerald, 1984; FitzGerald et al., 2000; Ridderinkhof et al., 2016a).

de Swart and Zimmerman (2009) reviewed tidal inlet systems and the relevant processes and morphodynamics. Most studies on the exchange of sediment between basin and sea have focused on the basin geometry but not on the ebb-tidal delta (Speer and Aubrey, 1985; Friedrichs and Aubrey, 1988). Shallow areas are known to affect this exchange; basins with a large tidal range over depth ratio tend to be flood-dominant, while large intertidal areas cause ebb-dominant sediment transport. While we have a good understanding on how the basin geometry influences tidal asymmetry, the role of the cyclic changes of the shallow ebb-tidal delta on tidal wave deformation has not been studied. Tides also cause mean flows that can result in net import/export of sediment. For example, when tides have a (partly) progressive character in isolated basins, the Stokes return flow will result in export of sediment. Mean flows can also be generated by tide-topography interactions due to the presence of channels and shoals (Ridderinkhof, 1988). Therefore, it is expected that the cyclic evolution of ebb-tidal deltas influences both the mean flow patterns and tidal asymmetry at many locations.

Many studies on tidal inlet systems have neglected the effect of waves (Van Leeuwen et al., 2003; Van der Vegt et al., 2006; Van der Vegt et al., 2009; Dissanayake et al., 2012). However, ebb-tidal deltas are not only a source of sediment for the back-barrier basin, but also a filter for offshore incident wave energy. Waves propagate and dissipate their energy by means of bottom friction and wave breaking on the ebb-tidal delta, which thus protects the coasts and back-barrier basin (FitzGerald, 1988; van der Westhuysen, 2012; Elias and Hansen, 2013). Furthermore, waves can drive flows and are able to entrain sediment, which can be transported by currents. Therefore, waves are important for the sediment transport near tidal inlet systems (Nahon et al., 2012; Ridderinkhof et al., 2016b). Wave energy dissipation strongly depends on the relative wave height (wave height divided by water depth) and waves can refract over the shoals. It is therefore expected that the changes in location of channels and shoals influence the wave energy patterns, not only on the ebb-tidal delta but also in the inlet. For example, Hansen et al. (2013) have shown that the nearshore wave dynamics near a tidal inlet have changed as a response to the large-scale contraction of the nearby ebb-tidal delta. Herring and Winter (2014) have studied the hydrodynamics and sediment transport at an ebb-tidal delta in the German Wadden Sea and have shown that the sediment pathways during storm are significantly different from those during calm, tide-dominated conditions.

The aim of this chapter is to study how the cyclic behavior of the ebb-tidal delta influences the tide and wave dynamics and the sediment transport patterns. We addressed this aim by using the Ameland Inlet as a case study. This is a tidal inlet system that has a clear cyclic evolution with a typical period of 50-60 years (Israel and Dunsbergen, 1999); has good data

availability on bathymetry and wave conditions; has only minimally connectivity to adjacent tidal basins such that it can be considered an isolated system (Ridderinkhof, 1988; Cheung et al., 2007; Dissanayake et al., 2012); and it is the least disturbed system of the Dutch Wadden Sea (Elias et al., 2012). We used a modeling approach in which we calculated waves, flow and sediment transport for four different phases of the cyclic evolution. The wave climate was represented by 21 wave classes based on wave height and direction, and results were combined into yearly mean sediment transport patterns. The simulations allowed us to discriminate between effects of changes in tide-driven flows, waves and changes in position of the channels and shoals. We proceed by describing in more detail the dynamics of Ameland Inlet (Section 2.2.1), the model (Section 2.2.2) and the simulations performed (Section 2.2.3). The wave energy propagation and dissipation during the four phases are described in Section 2.3.1. Section 2.3.2 shows the patterns of yearly mean sediment transport, where a distinction between the effect of waves and tides is made. The results are discussed in Section 2.4 and the conclusions are in Section 2.5.

## 2.2 Material and methods

### 2.2.1 Ameland Inlet

Israel and Dunsbergen (1999) described four typical phases of the morphological cycle at the Ameland Inlet (Figure 2.1). During Phase 1, there is a one-channel system in the inlet; this ebb-channel (Westgat) is oriented to the northwest (for example, 1971). A shoal near the Ameland coast originates from the ebb-tidal delta. During Phase 2, the main ebb-channel (Akkepollegat) is more symmetric and in the inlet a second channel is present (1989). Furthermore, the shoal has completely merged with Ameland. During Phase 3, the second channel in the inlet became deeper, the channel rotation has continued while the sediment of the shoal that attached to Ameland has been redistributed (1999). During Phase 4, the main ebb-channel is building a new extension in northwestern direction. Also, the second channel in the inlet is decreasing in size and depth while the inlet has the tendency to become narrower (2011). Additionally, a new shoal is present at the northeastern side of the ebb-tidal delta. Although the patterns do not repeat exactly, the gross characteristic of channel rotation, switching between a one- and two-channel inlet system, development of a large sandy shoal and its subsequent migration towards Ameland, repeat on a typical time scale of about 50 years (Israel and Dunsbergen, 1999). In the conceptual model of FitzGerald et al. (2000) this is a typical example of ebb-tidal delta breaching. This type of cyclic behavior is common for tidal inlets systems along the Dutch and German Wadden Sea (Ridderinkhof et al., 2016a).

This cyclic morphodynamic evolution results from a combined forcing of tides and waves. Ameland Inlet is located in a region of mesotidal conditions with a typical semi-diurnal tidal range of 2.4 m at Nes near the Ameland Inlet. Diurnal inequality is relatively small. Peak water levels can be up to 3.5 m, caused by storm surges of up to 2 m. The Ameland Inlet has a typical width of 4 km and the depth of the main channel is up to 25 m; the typical tidal prism is 400 Mm<sup>3</sup> (Sha, 1989). The average offshore wave height is 1.3 m, but can be up to 7 m during severe storms. The waves have an oblique direction and typically come from the west and northwest. The waves drive longshore transport of sediment in the order  $10^6 \text{ m}^3/\text{yr}$  (Ridderinkhof et al., 2016a). The sediment is relatively fine in the basin ( $d_{50}$  of

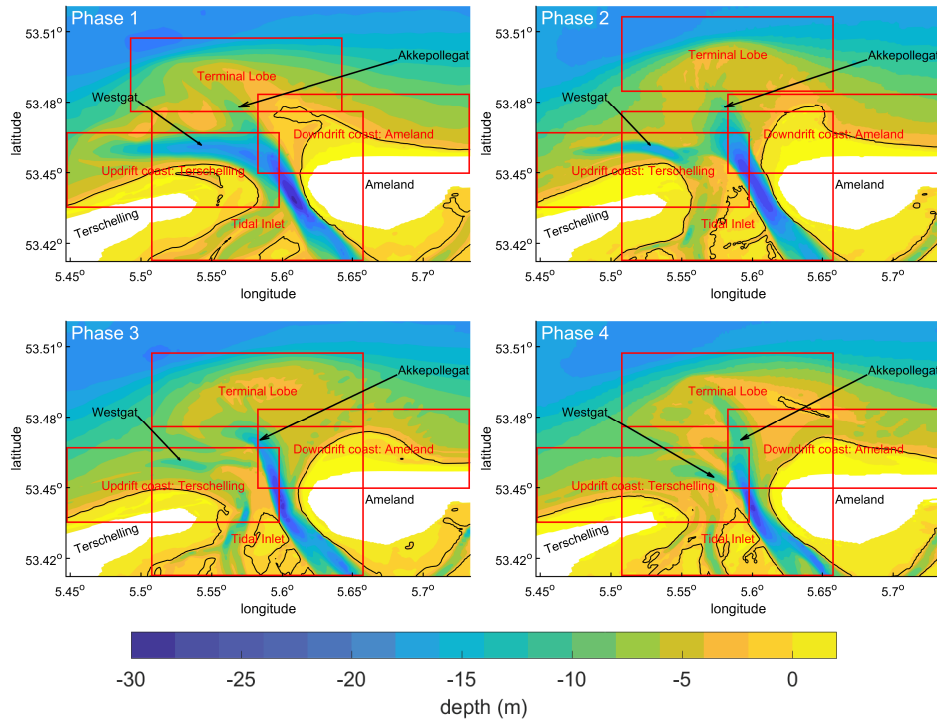


**Figure 2.1** Morphologic cycle of the Ameland Inlet, typical time scale is 50–60 years. Colors indicate local bathymetry in intervals of 2 m with black contour at 1 m isobath. Phase 1: One-channel system with shoal on ebb-tidal delta (1971-bathymetry). Phase 2: Transition to two-channel system with shoal attaching to the coast as coherent shoal (1989-bathymetry). Phase 3: Two-channel system with shoal distribution (1999-bathymetry). Phase 4: Transition to one-channel system with a new shoal on the ebb-tidal delta (2011-bathymetry). The areas indicated in red are the four key regions discussed in Section 2.3.2.

60 – 240  $\mu\text{m}$ ) and relatively coarse in the channel and on the ebb-tidal delta (240 – 350  $\mu\text{m}$ ) (Wang et al., 2016).

### 2.2.2 Modeling system

For simulations of the hydrodynamics and sediment transport in the Ameland Inlet, the coupled modeling system of Delft3D-FLOW and SWAN was used. The numerical model Delft3D-FLOW (Deltares, 2014) was applied in its 2DH mode, solving the depth-averaged shallow water equations on a staggered model grid. The phase-averaged wave model SWAN (Booij et al., 1999; Ris et al., 1999; Holthuijsen, 2010) was employed to compute the wave energy spectrum by solving the wave action balance equation in its stationary form. The SWAN and Delft3D model were coupled with a coupling time of 20 minutes. After SWAN is provided with the bed level, water level and flow velocity by Delft3D-FLOW, it computes the spectral wave energy and wave-induced forces. Subsequently, this information

is communicated to Delft3D-FLOW and used to calculate water levels, flow velocities and sediment transport.

In Delft3D-FLOW, several parameters values were set based on model calibration. The bed roughness was prescribed with a constant Chézy friction coefficient value of  $63 \text{ m}^{0.5}/\text{s}$ . The horizontal eddy viscosity and diffusivity were  $5 \text{ m}^2/\text{s}$  and  $1 \text{ m}^2/\text{s}$ , respectively. Furthermore, the bed consisted of homogeneous sediment ( $d_{50} = 250 \mu\text{m}$ ) and bed level updates were not considered. The SWAN model did not account for wind growth and non-linear triad-interactions were not included. The default settings were employed for white-capping, bottom friction and depth-induced breaking.

In the sediment transport module, we used the transport formulations of Van Rijn et al. (2004), which differentiate between bed and suspended load mechanisms. Unless mentioned otherwise, the default settings are used for sediment transport. In these formulations, the bed load transport predictor  $q_b$  is proportional to the instantaneous velocity of currents and waves  $u$  as  $q_b \propto u^{2.5}$ . As a result, skewed waves can transport sediment in the simulations, because of relatively strong orbital velocities in the crest of the wave compared to the trough. In the model this was achieved by the parametrization of Van Rijn et al. (2004), after the method of Isobe and Horikawa (1982). The effects of wave skewness on suspended transport were considered small and therefore neglected. However, waves do influence the suspended load transport in the model simulations in two ways. Firstly, the wave-induced forces drive currents that, combined with the tidal currents, determine the advection of entrained sediment. Secondly, there is non-linear interaction between the boundary layers at the bed associated with the waves and the current, which has the effect of enhancing both the mean and oscillatory bed shear stresses. Through the use of the parameterization of Soulsby et al. (1993), the wave-current interaction model of Van Rijn et al. (2004) is applied to account for the wave-induced increase in the bed shear stress. As a result, more sediment is entrained and made available for transport by currents. The complete expressions for sediment transport can be found in Van Rijn (2007a) and Van Rijn (2007b).

### 2.2.3 Model setup

#### 2.2.3.1 Model domain

The curvilinear computational grids (De Fockert, 2008; Wang et al., 2016) cover the Ameland Inlet system (Figure 2.2). To obtain more detailed results of patterns of net sediment transport, the flow grid has a factor 2 higher resolution than the wave grid. The flow grid consists of 324 and 348 cells in the east-west ( $x$ ) and north-south ( $y$ ) direction, respectively. The grid size ranges from 300 m by 350 m near the offshore boundary up to 30 m by 40 m near the Ameland Inlet. The wave grid is slightly larger than the flow grid to account for wave refraction and shadowing effects. In the east-west direction the wave grid was extended with 16 cells, making the number of grid cells 178 and 174 in  $x$ - and  $y$ -direction, respectively. To fulfill the Courant criterion the time step of Delft3D was set at 12 seconds.

Model bathymetries were assembled by interpolating measured data of sea bottom elevations onto curvilinear model grids. The measurements were conducted by the Dutch government (Rijkswaterstaat) and are publicly available via [opendap.deltares.nl](http://opendap.deltares.nl). To test the effect of changing ebb-tidal delta bathymetry, four different phases were based on the bathymetries of 1971, 1989, 1999 and 2011 (see Section 2.2.1).

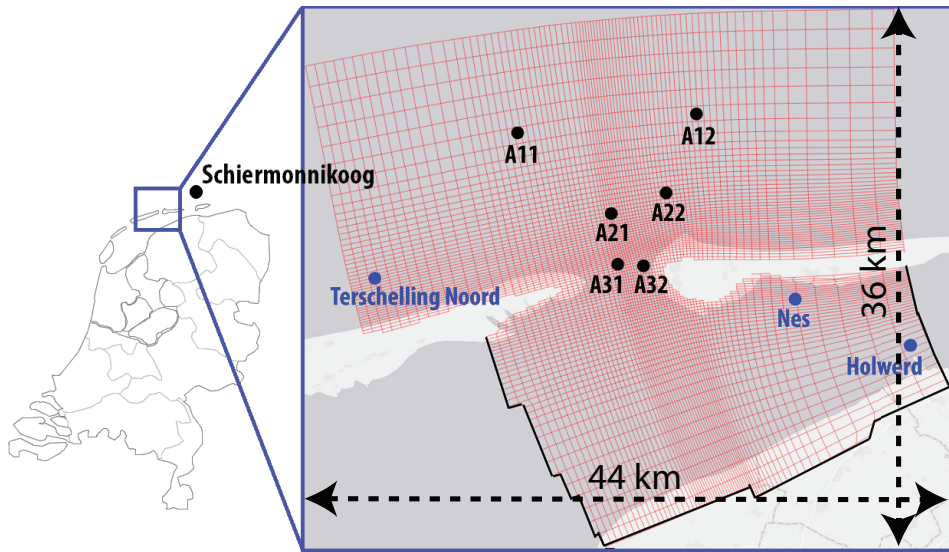


**Figure 2.2** High resolution curvilinear flow grid covering the Ameland Inlet system, located in the north of the Netherlands. Grid lines are shown with an interval of 4 lines. Dots indicate locations of water level measurement stations (blue) and wave buoys (black).

### 2.2.3.2 Boundary conditions

The Ameland Inlet has a relatively isolated basin, meaning that exchange of water over the watersheds is relatively small (Ridderinkhof, 1988; Cheung et al., 2007; Dissanayake et al., 2012; Elias et al., 2015). Therefore, the boundaries landward of the inlet (indicated by the black lines in Figure 2.2) were assumed to be closed and the normal component of flow and sediment transport were set to zero.

At the offshore boundaries, the model was forced by both tides and waves; representative tide and wave climates were used. At the open boundaries a so called morphological tide was described (Latteux, 1995). Instead of multiple species of the semi-diurnal and diurnal-tide, only one diurnal- ( $D_1$ ) and one semi-diurnal ( $D_2$ ) component were taken into account. Similarly, the higher harmonics are also represented by only one component per frequency class. The amplitudes were chosen such that the morphological tide gives the same mean sediment transport over a spring-neap tidal cycle as when taking all harmonic components into account. The morphological tide consisting of 7 constituents was derived by De Fockert (2008) by simulating two spring-neap cycles with the boundary conditions as extracted from the Extended Wadden Sea model (Deltares, 2009). At the northern open boundary the morphological tide was forced by prescribed water levels (Figure 2.3), while at the western and eastern open boundary Neumann conditions were prescribed (Roelvink and Walstra, 2004). The value of the mean water level was related to the wave conditions as will be explained below.

The wave climate was represented by wave classes (Table 2.1), which were based on data collected by Rijkswaterstaat at the measuring station of Schiermonnikoog (Figure 2.2). The analyzed dataset comprised 20 years (i.e., 1994 to 2014) of hourly measurements of the significant wave height  $H_s$ , mean wave direction  $\theta$  and mean wave period  $T_{mo2}$ . Subsequently,

**Table 2.1** Definition of wave classes, corresponding boundary conditions and relative yearly occurrence. The wave classes were based on data collected by Rijkswaterstaat at the measuring station of Schiermonnikoog (Figure 2.2). Bin refers to range in which the data was binned based on significant wave height  $H_s$ . Furthermore,  $T_{m02}$  and  $\theta$  are mean wave period and direction, respectively.

Wave Class		Bin	$H_s$	$T_{m02}$	$\theta$	Mean Water Level	Occurrence
Wo	West $247.5^\circ < \theta;$ $\theta < 292.5^\circ$	0 - 0.5 m	0.4 m	3.43 s	275.48°	0.06 m	2.19%
Wo.5		0.5 - 1 m	0.76 m	3.70 s	271.77°	0.10 m	7.87%
W1		1 - 2 m	1.39 m	4.37 s	273.55°	0.22 m	10.07%
W2		2 - 3 m	2.36 m	5.28 s	278.96°	0.47 m	1.77%
W3		3 - 6 m	3.42 m	6.15 s	284.16°	0.75 m	0.31%
NWo	Northwest $292.5^\circ < \theta;$ $\theta < 337.5^\circ$	0 - 0.5 m	0.35 m	4.10 s	317.84°	0.02 m	5%
NWo.5		0.5 - 1 m	0.75 m	4.51 s	316.42°	0.02 m	8.75%
NW1		1 - 2 m	1.45 m	5.04 s	316.14°	0.08 m	12.92%
NW2		2 - 3 m	2.41 m	5.76 s	316.82°	0.24 m	4.58%
NW3		3 - 4 m	3.43 m	6.63 s	317.3°	0.44 m	1.65%
NW4		4 - 5 m	4.40 m	7.37 s	319.56°	0.64 m	0.55%
NW5		5 - 8 m	5.67 m	8.35 s	322.33°	0.97 m	0.19%
No	North $337.5^\circ < \theta;$ $\theta < 22.5^\circ$	0 - 0.5 m	0.35 m	4.00 s	357.25°	-0.04 m	4.87%
No.5		0.5 - 1 m	0.74 m	4.52 s	356.12°	-0.07 m	7.77%
N1		1 - 2 m	1.40 m	5.02 s	353.51°	-0.09 m	7.63%
N2		2 - 3 m	2.39 m	5.66 s	351.25°	-0.05 m	1.71%
N3		3 - 6 m	3.60 m	6.69 s	349.69°	0.06 m	0.41%
NEo	Northeast $22.5^\circ < \theta;$ $\theta < 67.5^\circ$	0 - 0.5 m	0.38 m	3.35 s	42.66°	-0.06 m	2.72%
NEo.5		0.5 - 1 m	0.74 m	3.73 s	46.45°	-0.12 m	5.18%
NE1		1 - 2 m	1.37 m	4.38 s	47.17°	-0.25 m	3.92%
NE2		2 - 4 m	2.37 m	5.34 s	39.16°	-0.41 m	0.54%

the data were coupled to data of hourly measurements of water level at the measuring station Terschelling Noord (Figure 2.2). The storm surge height (tidal mean water level) was estimated by subtracting the astronomical tide from the measured water level. By this we had a data set of occurring wave conditions and related mean water level. The wave and mean

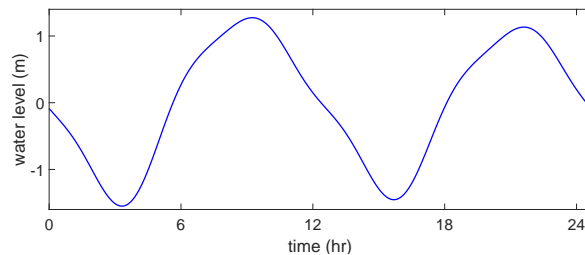


**Figure 2.3** Prescribed water levels at the Northern open boundary.

water level data were smoothed using a running mean with a 6-hour window in order to reduce impact of short-term fluctuations in wave height on the wave class determination. Subsequently, the data were binned based on wave direction ( $45^\circ$  increments) and sorted according to significant wave height. For each of the four offshore directions (west, northwest, north, northeast), the waves were binned in 0.5 m (1 m) increments for  $H_s < 1$  m ( $H_s > 1$  m). Wave classes accounting for less than 0.5% of that wave direction were combined with the previous wave class.

Together the 21 wave cases account for 91% of the total realizations, with the remaining 9% falling outside of the binned area because they come from directions that were not taken into account. The results show that mean water level is largest for waves coming from the northwest, and increases for increasing wave height. Waves that come from the north or northeast are concurrent with set down (negative mean water level).

For reasons of feasibility, wind forcing was not included in the simulations. The implications of excluding the wind effects will be discussed in Section 2.4.

### 2.2.3.3 Model simulations and model analysis

The duration of a model run was 12 D<sub>2</sub> tidal cycles (of 12h20m each), of which 10 D<sub>2</sub> tidal cycles were used as spin-up for the model and the last 2 were used for analysis. Since a morphological tide has been used, the 2 D<sub>2</sub> tidal cycles result in tidal mean sediment transport patterns that are representative for the spring-neap cycle. All combinations of wave class and bathymetry were simulated. Weighted mean values of tidally-averaged flow velocity and sediment transport were calculated as the sum of each individual value per wave class multiplied by the relative occurrence.

For each phase of the cyclic evolution, we analyzed the:

- tidally-averaged sediment transport;
- tidally-averaged flow (mean flow);
- tidally-averaged sediment transport through cross-sections

$$\text{SedTrans} = \int_{s_0}^{s_n} \langle \vec{q}_s \rangle \cdot \vec{n} ds, \quad (2.1)$$

where  $\langle \vec{q}_s \rangle$  is the tidally-averaged sediment transport vector, which can be either the value per wave class or the weighted mean of all wave classes. Furthermore,  $\vec{n}$  is the normal vector of the transect and  $s$  is the distance along the transect between  $s_0$  and  $s_n$ ;

- wave energy fluxes through cross-sections

$$\text{WaveFlux} = \int_{s_0}^{s_n} E \vec{C}_g \cdot \vec{n} ds \quad (2.2)$$

where  $E$  is the wave energy and  $\vec{C}_g$  is the group velocity vector;

- wave energy dissipation.

Details of the cross-section positions are given in Section 2.3.

Sensitivity simulations were performed to study the main driving processes:

- *default simulations*, with waves and surge;
- *simulations without waves*, only surge and tide forcing;

- *tide-only simulations*, neither surge nor waves;
- *symmetric tide-only simulations* with symmetric semi-diurnal  $D_2$ -tide, excluding diurnal tides and higher harmonics ( $D_4, D_6, \dots$ ) in the boundary conditions.

#### 2.2.3.4 Model validation

De Fockert (2008) verified the modeled water levels by conducting a harmonic analysis, in which the modeled tidal constituents were compared with the measured water level obtained from Terschelling Noord, Nes and Holwerd stations (Figure 2.2). For the offshore location (Terschelling North Sea), the maximum deviation in the modeled and measured amplitudes of the main constituents was less than 2%, with only a small differences in relative phases (less than  $9^\circ$ ). For the measurement location Nes, located inside the basin, the best results were obtained with the grid resolution used in this study. However, De Fockert (2008) found that the relative amplitudes of the higher harmonics were overestimated up to 30%. The third measurement location (Holwerd) is located far inside the tidal basin and the predictability regarding water levels was also accurate in this point far inside the basin. In total the modeled tidal water levels agreed well to the measurements. The robustness of the results was tested for different tidal boundary conditions and will be discussed in Section 2.4.

Wave propagation over the ebb-tidal delta was validated by comparing the tidally-averaged values of modeled and measured significant wave height based on data of the six wave buoys indicated in Figure 2.2. For this, we used the 2011-bathymetry because no wave data were available for other years. The measured data were averaged over a shifting 12.5-hour window. For all wave classes, comparable measured conditions for mean water level and wave direction were found for validation. As can be seen in Figure 2.4, the model compares well

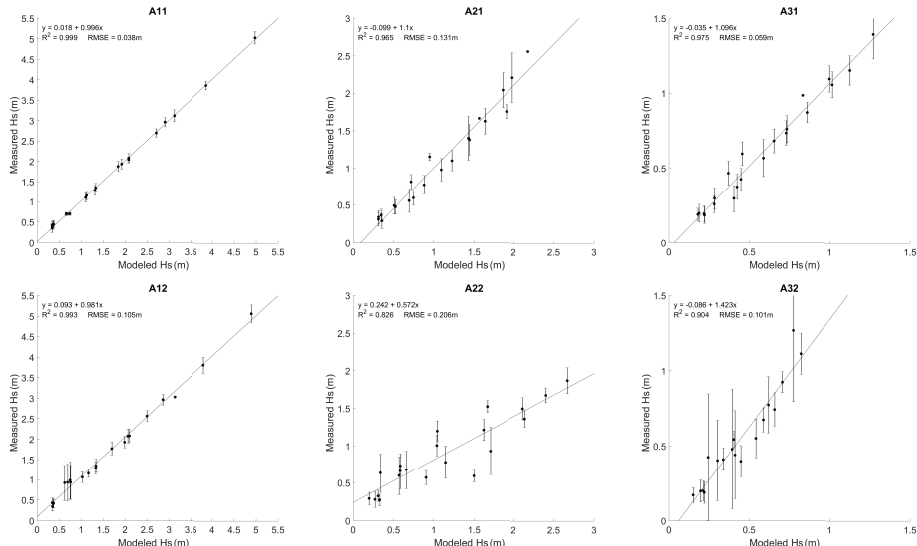


**Figure 2.4** Tidally-averaged values of modeled and measured significant wave height for the six wave buoys indicated by black circles in Figure 2.2. Every dot represents one wave class (Table 2.1) and the bars indicate the standard deviation of the measured data.

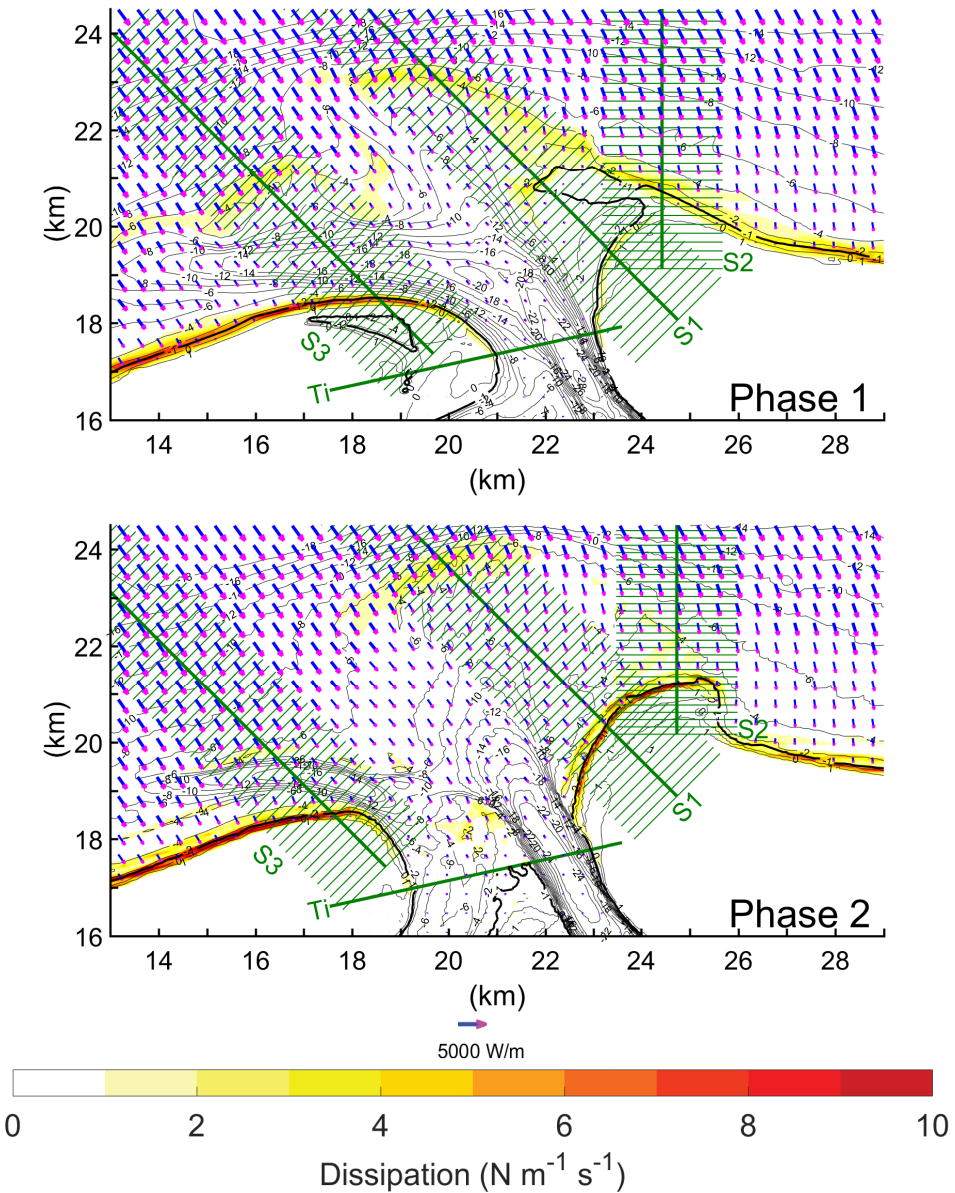


**Figure 2.5** Figure continues on next page.

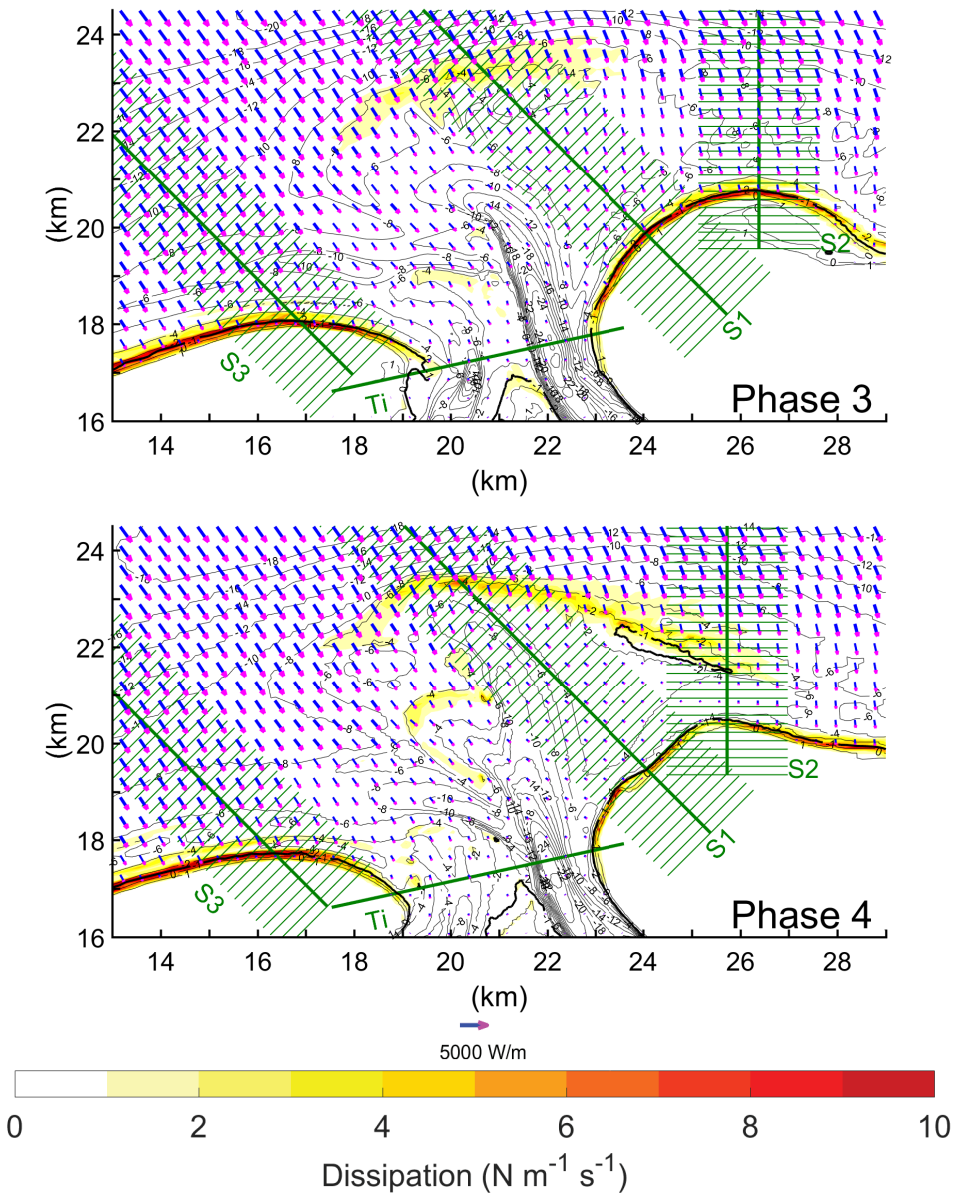


**Figure 2.5** Vector plot of the weighted mean wave energy flux during the four phases of the cyclic behavior. The arrows are interpolated to a rectilinear grid. Colors indicate wave energy dissipation. Cross-section Ti and the series of cross-sections S<sub>1</sub>, S<sub>2</sub> and S<sub>3</sub> are shown in green. Black lines represent the bathymetry in intervals of 2 m with thick line at 1 m isobath.

( $R^2 > 0.96$ , in which  $R$  is the correlation coefficient) with the measurements for the wave buoys offshore and on the west part of the inlet and ebb-tidal delta. The largest deviations were found for the eastern wave buoys A22 and A32, located near the terminal lobe of the ebb-tidal delta and in the main inlet channel. However, these are also the wave buoys that have the largest standard deviations in the measured data. This probably occurs because of the complex propagation of individual waves over the ebb-tidal delta situated between these wave buoys and the predominant wave direction. Additionally, van der Westhuysen (2012) also found good agreement between measured and modeled wave propagation inside the basin by comparing measured and model time series of wave data for the same system and model set-up. Overall, the wave model performs satisfactory.

## 2.3 Results

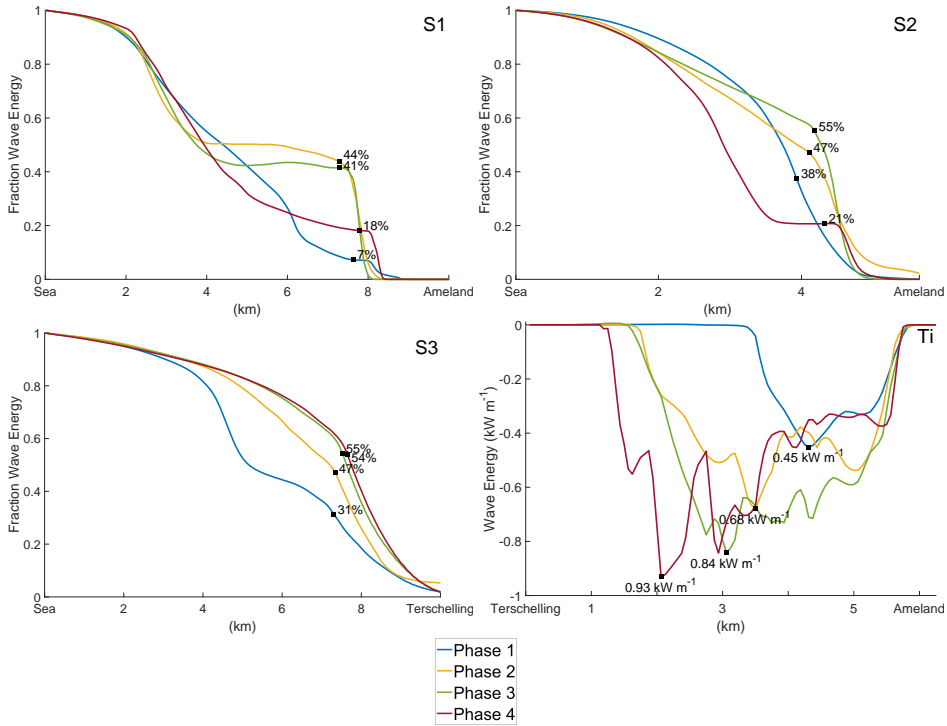
### 2.3.1 Wave energy patterns

Figure 2.5 shows the weighted mean wave energy flux and energy dissipation rate, indicating that waves dissipate their energy as they propagate over the shallow ebb-tidal delta, which in turn protects Ameland and Terschelling islands and the back-barrier basin from incoming wave energy. Particularly Ameland is well protected as the ebb-tidal delta is situated between the island and the predominant wave direction. Protection of the west part of Ameland is most evident during Phase 1, i.e., when the shoal is close to the island coast. After the shoal attachment, wave energy can propagate further landward and more energy is dissipated near the shore (Phases 2 and 3). The presence of a new shoal on the ebb-tidal delta causes the patterns during Phase 4 to resemble those of Phase 1, with energy dissipation over the shoal and less dissipation near the shore. However, as the shoal position differs, so does the area of increased wave energy dissipation.

Compared to Ameland, the east part of Terschelling is less well protected from the incoming wave energy flux as illustrated by the relatively high dissipation rates in the nearshore zone during all phases of the cyclic evolution. This exposure is mainly related to the mean wave direction and absence of protection against the northwestern waves by the ebb-tidal delta.

Wave energy dissipation by the various parts of the ebb-tidal delta was quantified using three series of 2500 m cross-sections perpendicular to the lines oriented to the northwest (S1) and to the north (S2) of Ameland and to the northwest of Terschelling (S3), respectively. The S1- and S2-line intersect with the northwesternmost and northernmost point of the Ameland coast. Similarly, the S3-line intersects with the northernmost grid cell of Terschelling. As the bathymetry varies per phase, so do the locations of S1, S2 and S3. In the sensitivity analysis, these locations were fixed; this did not cause qualitative differences in outcome.

The wave energy flux through the cross-sections relative to the most seaward cross-section is shown in Figure 2.6. The cross-sections S1 (facing the northwest of Ameland) show that the island is most effectively protected from offshore wave energy by the shoal on the ebb-tidal delta. During the phases with a shoal close to the coast (Phases 1 and 4), less than 18% of the incoming wave energy dissipates within 500 m of the coast, whereas during the other phases this is more than twice as much. Not surprisingly, the lowest values of remaining wave energy for S2 occur when the shoal is located more towards the north of Ameland. The cross-sections S3 indicate that the fraction of wave energy dissipation within 1000 m of the coast



**Figure 2.6** Fraction of remaining weighted mean wave energy flux through the series of cross-sections S<sub>1</sub>, S<sub>2</sub> and S<sub>3</sub> and weighted mean wave energy flux through cross-section Ti. The locations of the cross-sections are shown in Figure 2.5. The different line colors correspond to different phases. The percentages of remaining weighted mean wave energy flux for are taken 500 m (S<sub>1</sub> and S<sub>2</sub>) or 1000 m (S<sub>3</sub>) off the coast, respectively. The values shown for Ti are the maximum value per phase.

of Terschelling almost doubled during Phases 3 (54%) and 4 (55%) and that less energy is dissipated offshore compared to Phase 1. This trend seems to be related to the disappearance of the Westgat and its related ebb-shield north of Terschelling.

We also analyzed the weighted mean energy flux through a cross-section Ti in the inlet (Figure 2.6). The total amount of wave energy that enters the basin increases as the inlet transforms from a one-channel (Phase 1) to a two-channel system (maximum during Phase 3). This trend can only partially be explained by the increasing width of the inlet. As can be seen from the similar increase in maximum values (Figure 2.6), these variations are caused by the wave filtering on the ebb-tidal delta. It is worthwhile to note that the differences in wave energy through the inlet resemble those close to Terschelling; also, the increase in wave energy is mostly in the part of the inlet closest to Terschelling. This similarity suggests that most protection from incoming wave energy is provided by the west part of the ebb-tidal delta and the Westgat.

This analysis indicates that the cyclic evolution of the ebb-tidal delta has a significant impact on wave energy in the Ameland basin, and on the wave energy reaching the nearshore

zone of Ameland and Terschelling. It is expected that this also impacts the sediment transport patterns on the ebb-tidal delta and in the inlet.

### 2.3.2 Sediment transport

We focused on the four key regions indicated in Figure 2.1, namely: (1) the terminal lobe; (2) the downdrift coast; (3) the updrift coast; and (4) the tidal inlet. For these regions, we show the patterns and magnitudes of weighted mean, tidally-averaged, total (bed load + suspended load) sediment transport, hereafter referred to as weighted mean or net sediment transport.

#### 2.3.2.1 Terminal lobe

As shown in Figure 2.7, the direction of weighted mean sediment transport features a transition from seaward at the end of the ebb-dominant main channel/ebb-shield to downdrift further seaward. The latter transport represents the sediment bypassing of the ebb-tidal delta. Among the phases the patterns are roughly the same, following the rotation of the main ebb-channel; only sediment transport magnitudes differ. To quantify the sediment bypassing, a series of 1 km long cross-sections were defined ( $S_4$ ) perpendicular to the terminal lobe; the net sediment transports through these are presented in Figure 2.10a. The location of  $S_4$  was based on the 7 m isobath line and has a fixed east-west location (range of 4 km). Only for Phase 1,  $S_4$  was shifted slightly to the west because the Akkepollegat had a more updrift orientation.

As can be seen, the sediment bypassing decreases as the orientation of the Akkepollegat changes from northwest during Phase 1 to north during Phase 4. It was tested whether this reduction resulted from the variations in wave characteristics or from changes in tidal currents. The dashed lines in Figure 2.10a show the outcome of the *simulations without waves*. Excluding the waves diminishes the bypassing magnitude, but does not have significant influence on the fluctuations over the phases. Based on this, it was concluded that the decrease in sediment bypassing originates from tidal changes forced by rotation of the ebb-channel.

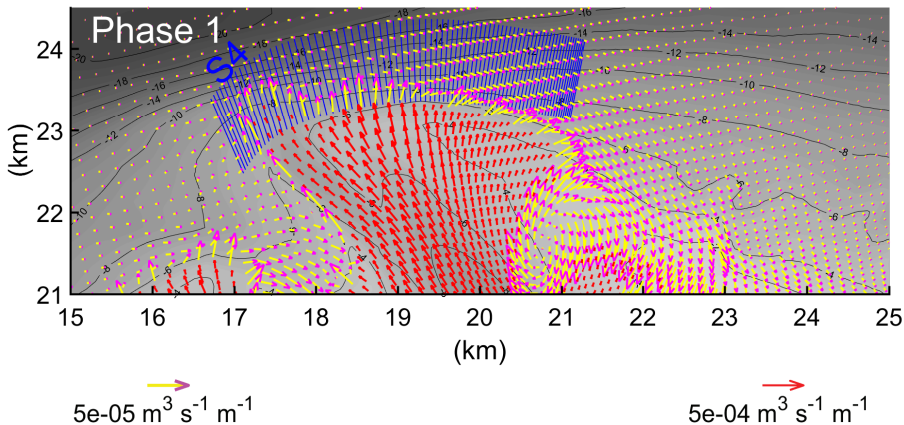


**Figure 2.7** Figure continues on next page.

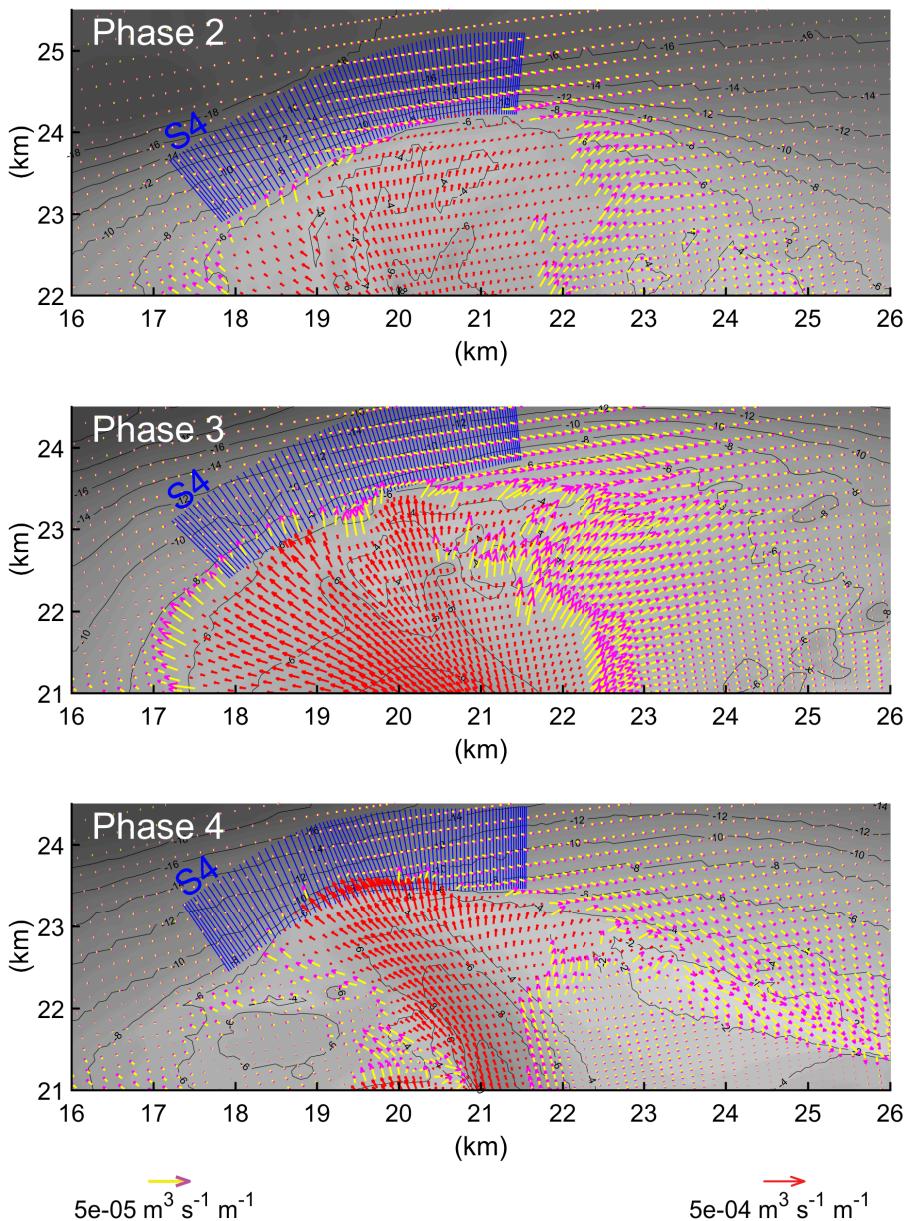


**Figure 2.7** Vector plot of the weighted mean sediment transport for the terminal lobe of the ebb-tidal delta. The arrows are shown in every second grid cell in both directions. The yellow/magenta vectors are a factor ten shorter than the red vectors for the same vector length. The blue lines indicate the series of cross-sections perpendicular to the terminal lobe (S4). Black lines represent the bathymetry in intervals of 2 m.

More specifically, the channel displacement changes mean flow along the terminal lobe with a maximum value during Phase 2 of 0.17 m/s and minimum value during Phase 4 of 0.11 m/s.

Another notable result of both *default simulations* and *simulations without waves* is that bypassing during Phase 1 was relatively strong in the west of the ebb-tidal delta and relatively weak in the east. This spatial variability also results from the tide-driven transport, possibly because during Phase 1 the Westgat was the dominant channel.

### 2.3.2.2 Downdrift coast: Ameland

The weighted mean sediment transport along the northwestern coast of Ameland shows a diverging pattern during all phases as its direction is towards the tidal inlet in the west and downdrift more in the east (Figure 2.8). Visual comparison of the four phases reveals differences in sediment transport towards the inlet; for example, transport of sediment was most intensive during Phase 3. Interestingly, the net sediment transport during Phase 4 south of the new shoal appears to be small with significant downdrift net transport on and directly seaward of the new shoal. The prominent role of the shoal (offshore blue line) in the pat-

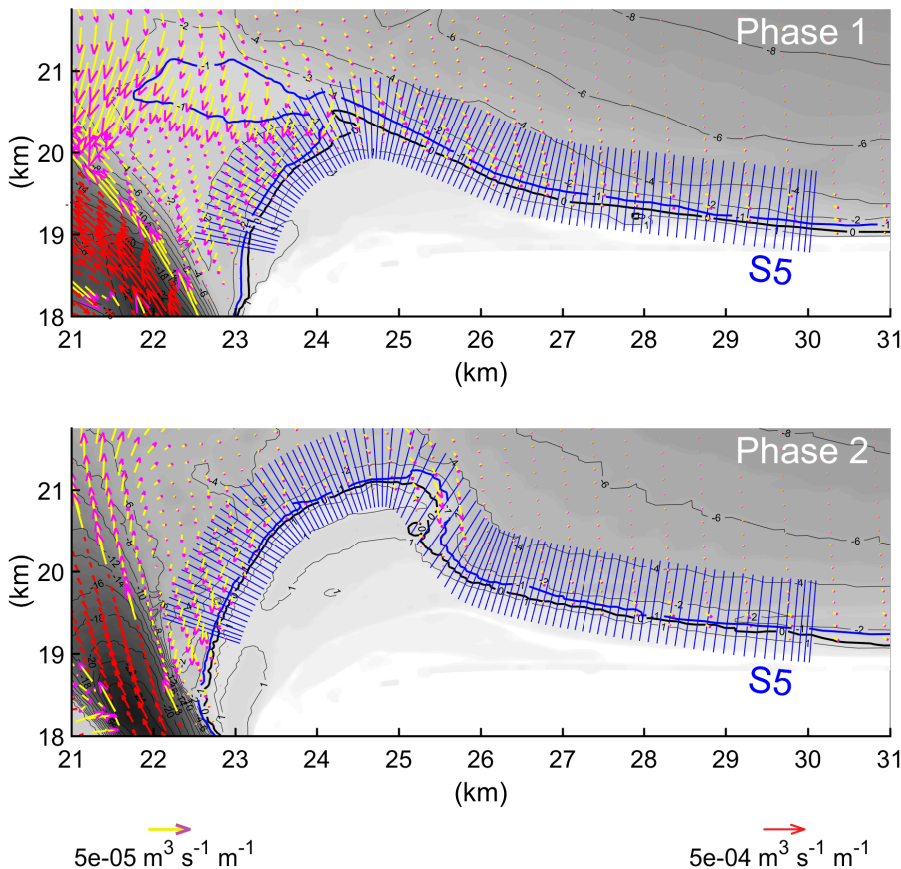


**Figure 2.8** Figure continues on next page.

terns of weighted mean sediment transport is also clear during Phase 1 as the convergence of the sediment transport vectors indicates that the ebb-tidal delta was in the phase of shoal migration.

Sediment transport along the coast was calculated for 1 km long cross-sections perpendicular to the coast (S5). Each cross-section of S5 intersects with the northernmost 0 m isobath at a predefined east-west location (range of 7 km). As shown in Figure 2.10b, the magnitude of the sediment transport through the westernmost cross-section is directed towards the tidal inlet (negative) and depends on the phase of the cyclic shoal dynamics with increasing sediment transport while the shoal forms (Phase 4), migrates (Phase 1), attaches (Phase 2) and spreads out over the coast (Phase 3). This dependency suggests a major role of changes in the wave filtering effect of the ebb-tidal delta. Therefore, *default simulations* (solid lines) and

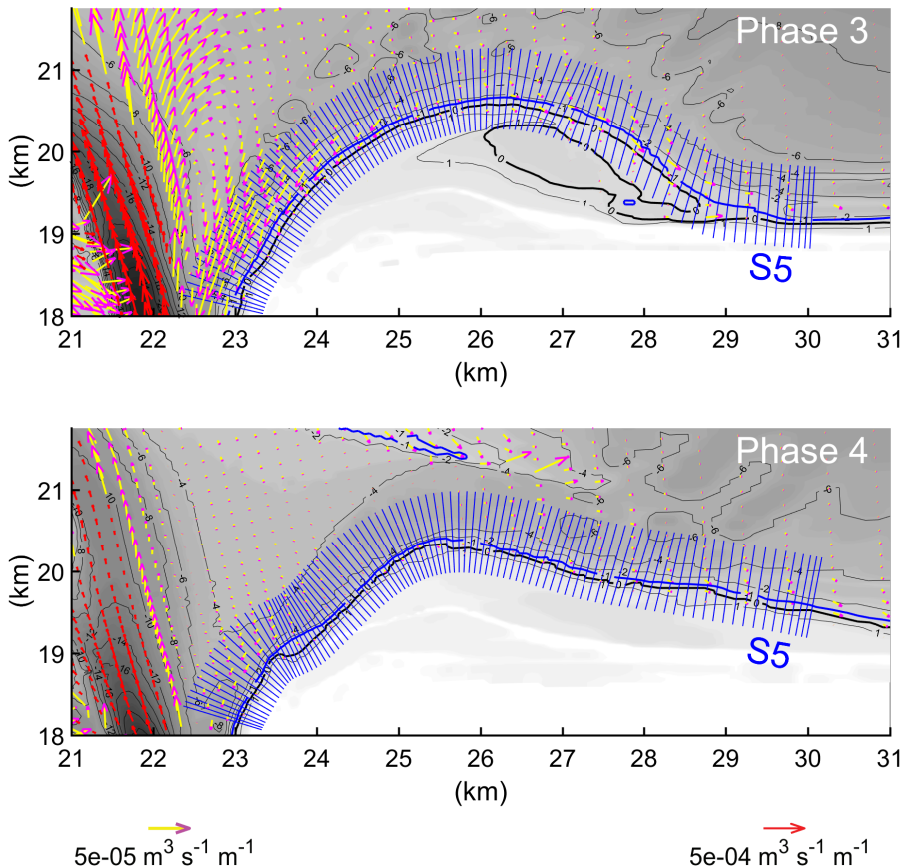


**Figure 2.8** Vector plot of the weighted mean sediment transport for the northwest part of Ameland. The arrows are shown in every fourth grid cell in both directions. The yellow/magenta vectors are a factor ten shorter than the red vectors for the same vector length. The thin blue lines indicate the series of cross-sections perpendicular to the coast (S5). Black lines represent the bathymetry in intervals of 2 m with blue contour at 1 m isobath.

*simulations without waves* (dashed) were compared. This indicates that the sediment transport is indeed strongly related to the amount of wave energy in the nearshore zone. However, it is the relatively strong tide driven transport during Phase 1 that explains why net sediment transport at certain cross-sections is relatively high.

### 2.3.2.3 Updrift coast: Terschelling

As shown in Figure 2.9, the weighted mean sediment transport near Terschelling is directed towards the inlet and represents the littoral drift. Variations in magnitude can be seen, both spatially and among the phases. During all phases the transport increases in the downdrift direction and reaches its maximum near the inlet. However, it can also be seen that the littoral drift during phases 3 and 4 is larger than during the first two phases. Further offshore in the Westgat, net sediment transport is in the opposite direction. This transport is largest during Phase 1 when this channel is deepest and directly connected to the deep channel in the inlet. During the other phases sediment transports through the Westgat is smaller as the channel is more filled up.

This spatial and temporal variability in alongshore sediment transport was quantified with 1 km long cross-sections perpendicular to the coast (S6, range of 5 km, defined using the same method as S5). As shown in Figure 2.10c, the alongshore sediment transport during Phases 3 and 4 exceed that during Phase 1 and 2. Comparison with the *simulations without waves* (dashed lines) reveals that this variability is wave-related. The ebb-shield related to the presence of the Westgat is smaller during Phases 3 and 4 (Section 2.3.1), thereby making the coast of Terschelling less protected. Closer to the inlet, however, it is the tide-driven transport that causes higher values during Phase 1 and 4.

The above analysis shows that the contraction of the Westgat has a significant impact on transport in sediment transport along Terschelling. As the formation of a new ebb-channel in northwestern direction is part of Phase 4, the outcome can be seen as part of a cycle rather than a trend.

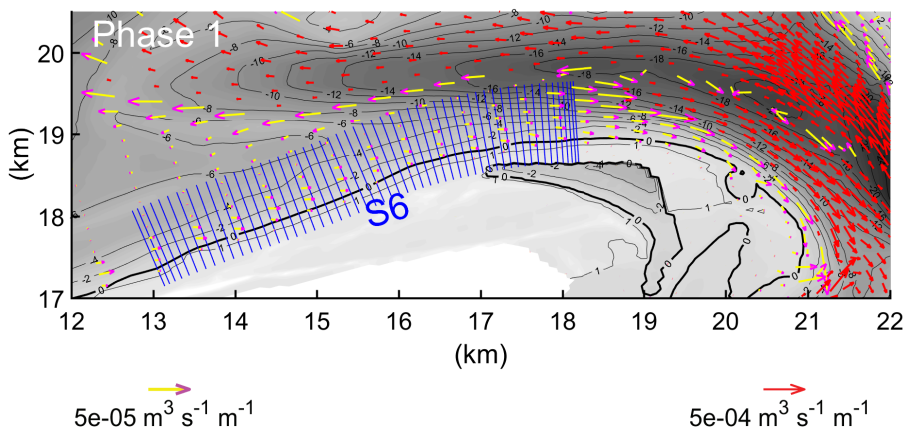
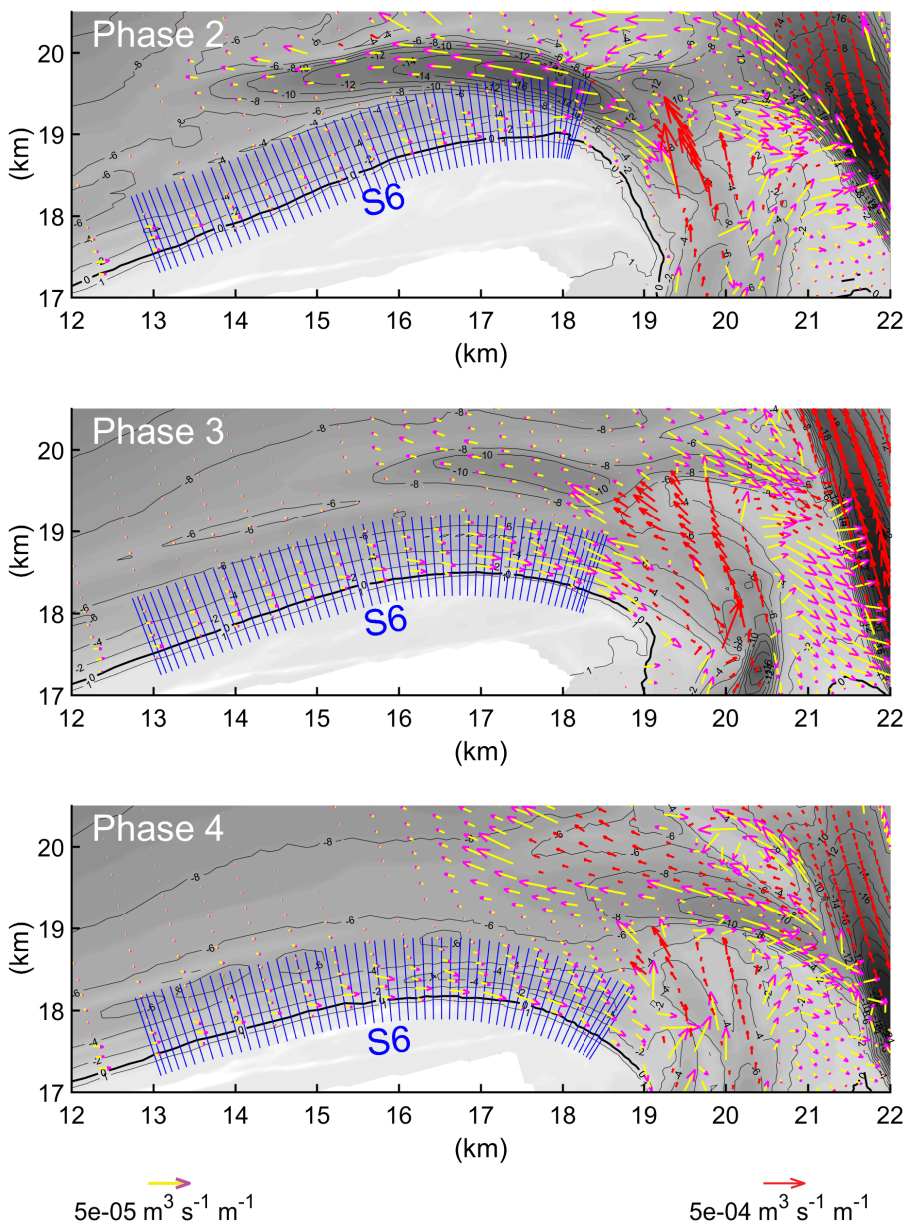
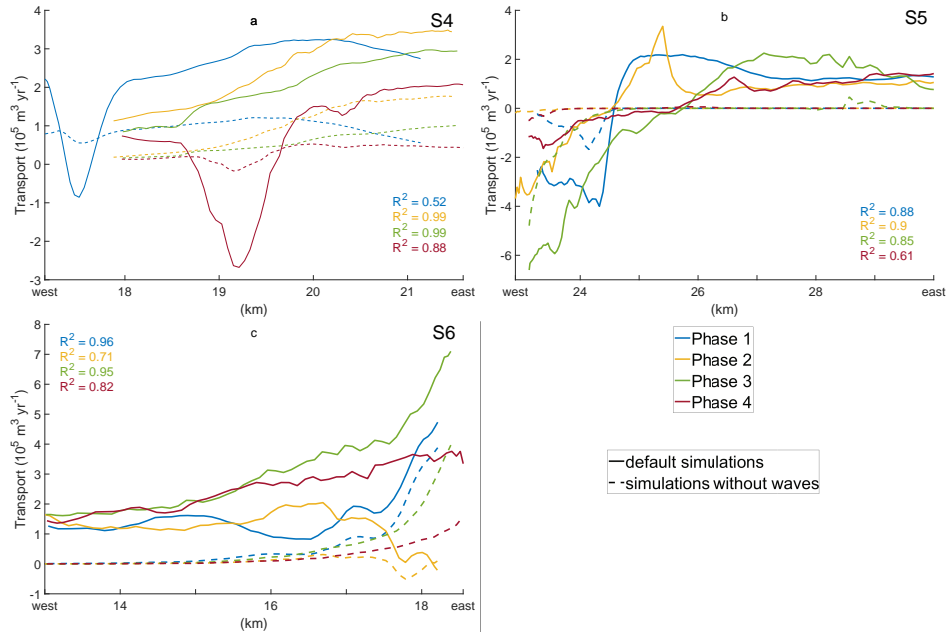


Figure 2.9 Figure continues on next page.



**Figure 2.9** Vector plot of the weighted mean sediment transport for the northeast part of Terschelling. The arrows are shown in every fourth grid cell in both directions. The yellow/magenta vectors are a factor ten shorter than the red vectors for the same vector length. The blue lines indicate the series of cross-sections perpendicular to coast (S6). Black lines represent the bathymetry in intervals of 2 m.



**Figure 2.10** Weighted mean sediment transport through the series of cross-sections S4 (a), S5 (b) and S6 (c) shown in Figures 2.7, 2.8 and 2.9, respectively. The average east-west location of each cross-section is used. Solid: default model simulations; dashed: model simulations without wave forcing. Positive values are in the downdrift (eastward) direction. The  $R^2$  between the solid and dashed lines is given per phase.

#### 2.3.2.4 Tidal inlet

As shown in Figure 2.11, the net sediment transport patterns in the inlet vary significantly among the phases. Net sediment transport is seaward in the eastern part when the inlet has a one-channel configuration during Phase 1. However, the relatively large tide-driven sediment transport along Terschelling cause a net transport into the basin in the western part of the channel. During Phases 2, 3, and 4 both channels transport sediment from basin to sea. This export via both channels appears to be largest when the western channel is deepest (Phase 3).

The net exchange between basin and sea was calculated for a cross-section across the Ameland Inlet. Cross-section Ti covers the entire inlet (as in Section 2.3.1); cross-section TiA and

**Table 2.2** Weighted mean net sediment transport in  $10^6 \text{ m}^3/\text{yr}$  through the cross-sections in the inlet. Positive values are in the seaward direction (export).

Cross-section	Phase 1	Phase 2	Phase 3	Phase 4
Ti	0.79	3.84	14.86	6.11
TiA	-5.93	0.82	5.90	2.31
TiB	6.81	2.97	7.71	2.84

TiB represent the western and eastern part of the inlet deeper than 2.5 m, respectively. The net sediment transport through the cross-sections is listed in Table 2.2. The results show that the net exchange is cyclic and follows the periodicity of the one- and two-channel inlet configurations. Net export is largest when the western channel reaches its maximum size (Phase 3) and smallest when the inlet features one channel (Phase 1). Cross-sections TiA and TiB show that a cyclic evolution of export is present for both channels. Interestingly, net export in the east (TiB) during Phase 1 exceeds total net export of Phase 2 and 4; however, this is compensated by import in the west (TiA).

Sensitivity experiments were analyzed to determine why the export through the tidal inlet is highly variable. First, it was tested whether waves in the inlet were the main factor by comparing *default simulations* and *simulations without waves*. During all four phases, excluding the waves had the same effect of an increase of the export of less than  $10^6 \text{ m}^3/\text{yr}$ . This indicates that the large variability in export is not related to the change in wave intensity and is thus caused by tidal dynamics.

Secondly, *tide-only simulations* (no waves and no surge) were analyzed to study the role of changes in the mean flow and changes in the tidal asymmetry. These mechanisms were quantified using harmonic analysis for the two locations in the inlet with the highest net transport in the two channels. As shown in Table 2.3,  $U_{ebb}$ ,  $U_{flood}$ ,  $C_{ebb}$  and  $C_{flood}$  are the maximum along-channel flow velocities  $U$  and sediment concentrations  $C$  during ebb and flood. Furthermore,  $A_0$ ,  $A_2$  and  $A_4$  are the amplitudes of mean, semi- and quarter-diurnal flow with phases  $\varphi_2$  and  $\varphi_4$ . Note that the effects of mean flow and tidal asymmetry on net

**Table 2.3** Maximum along-channel tidal flow and sediment concentration in the inlet at the locations of maximum net sediment transport in cross-section TiA and TiB. Positive flow velocity values are in the seaward (ebb) direction.

Western channel (cross-section TiA)	Phase 1	Phase 2	Phase 3	Phase 4
$U_{ebb}$ (m/s)	1.33	1.67	1.56	1.45
$C_{ebb}$ ( $10^{-5} \text{ m}^3/\text{m}^3$ )	7.88	16.4	37.53	11.58
$U_{flood}$ (m/s)	-1.69	-1.26	-1.37	-0.97
$C_{flood}$ ( $10^{-5} \text{ m}^3/\text{m}^3$ )	12.67	7.16	5.08	1.96
$A_0$ (m/s)	-0.36	0.16	0.04	0.18
$A_2$ (m/s)	1.23	1.45	1.47	1.23
$A_4$ (m/s)	0.28	0.07	0.07	0.05
$2\varphi_2 - \varphi_4$ (°)	123	78	92	2

Eastern channel (cross-section TiB)	Phase 1	Phase 2	Phase 3	Phase 4
$U_{ebb}$ (m/s)	1.94	1.74	1.92	1.68
$C_{ebb}$ ( $10^{-5} \text{ m}^3/\text{m}^3$ )	9.47	5.47	13.45	5.79
$U_{flood}$ (m/s)	-1.29	-1.22	-1.65	-1.25
$C_{flood}$ ( $10^{-5} \text{ m}^3/\text{m}^3$ )	1.60	1.06	3.07	1.11
$A_0$ (m/s)	0.23	0.06	0.10	0.08
$A_2$ (m/s)	1.66	1.46	1.82	1.48
$A_4$ (m/s)	0.07	0.18	0.05	0.14
$2\varphi_2 - \varphi_4$ (°)	26	32	26	20

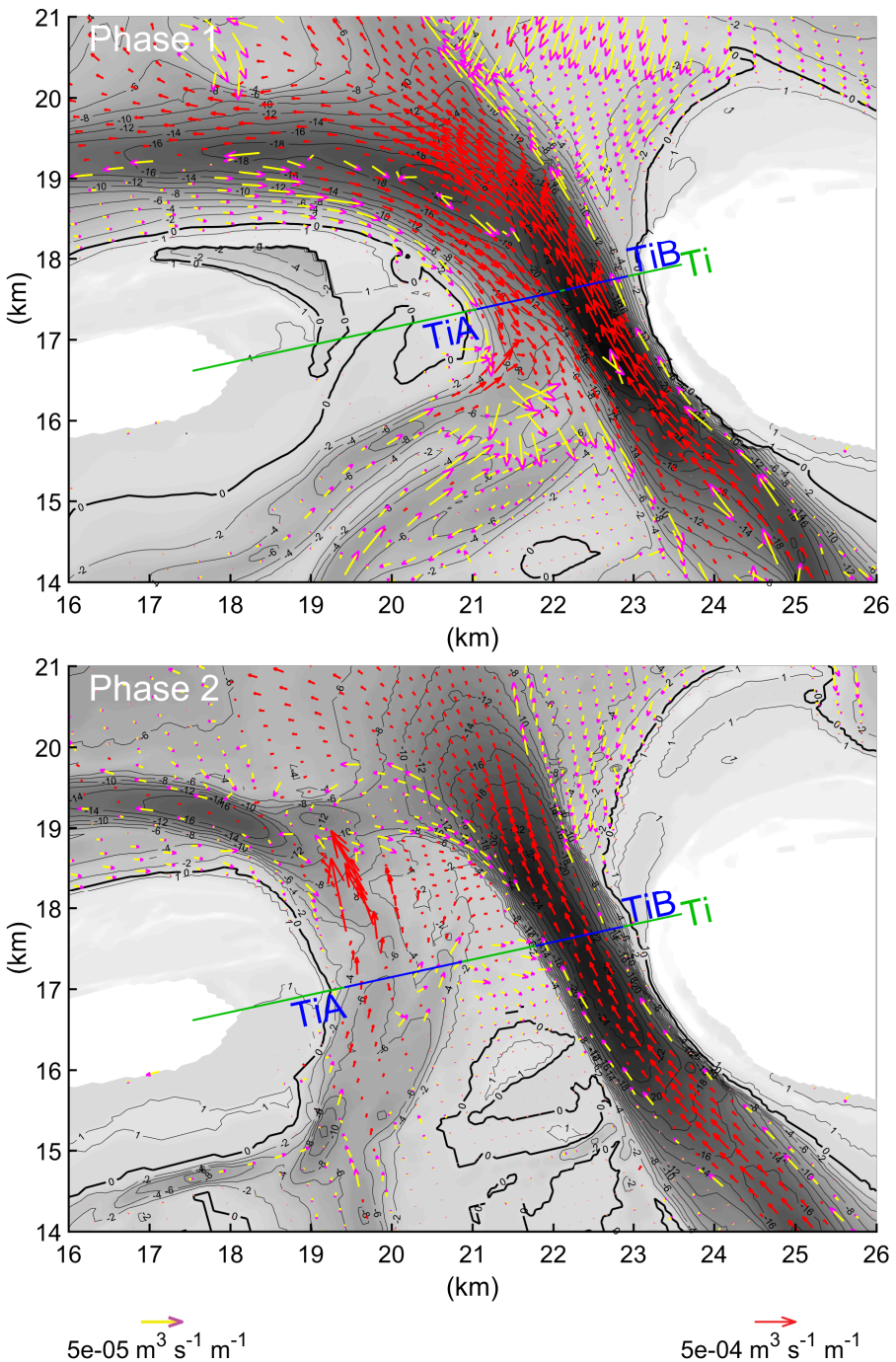
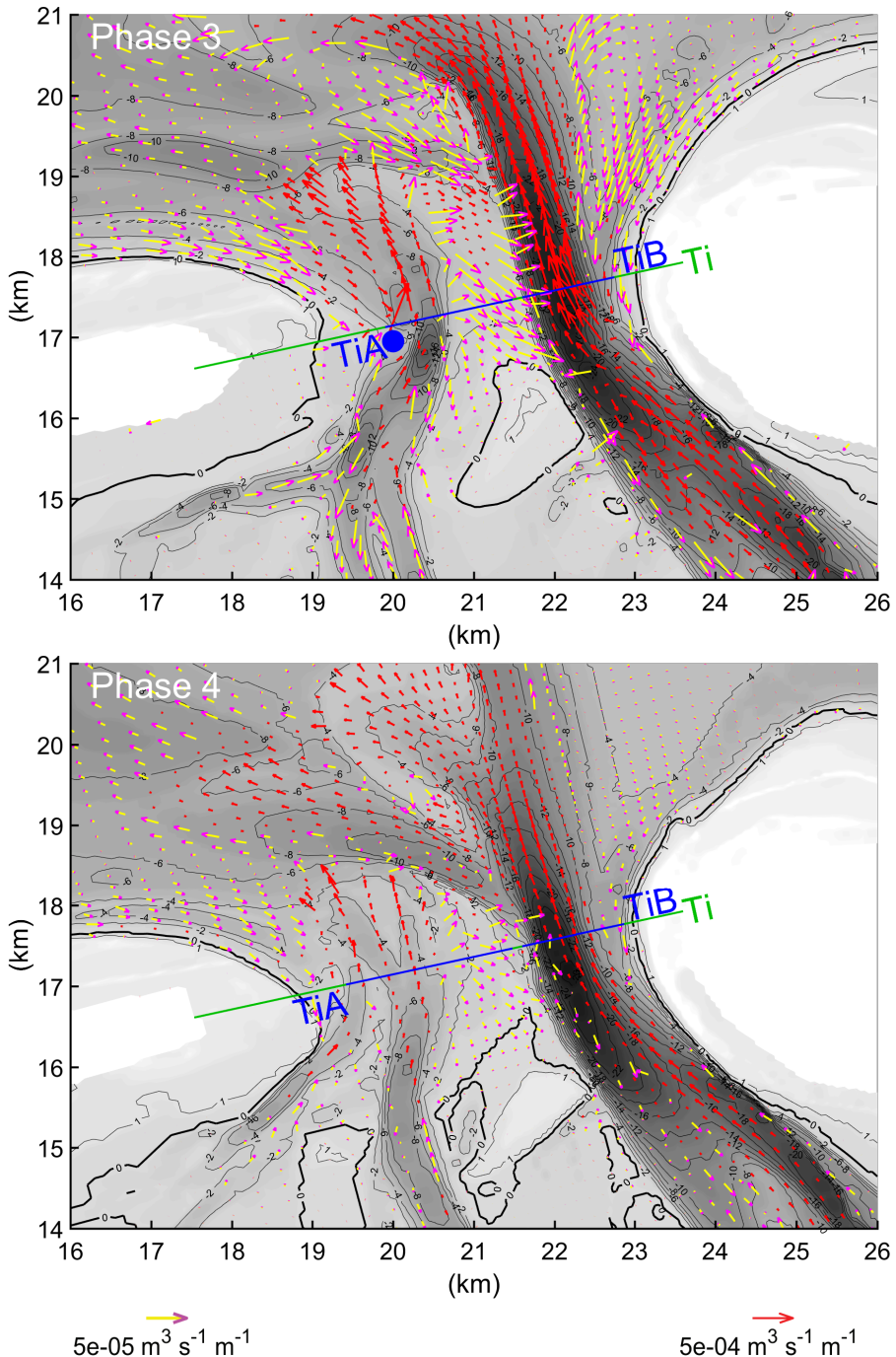


Figure 2.11 Figure continues on next page.



**Figure 2.11** Vector plot of the weighted mean sediment transport near the inlet. The arrows are shown in every fourth grid cell in both directions. The yellow/magenta vectors are a factor ten shorter than the red vectors for the same vector length. Cross-section Ti is shown in green and cross-sections TiA and TiB in blue. The blue dot in Phase 3 indicates the shallow part of the secondary channel. Black lines represent the bathymetry in intervals of 2 m.

sediment transport are in the direction of the sign of  $A_0$  and  $\cos(2\varphi_2 - \varphi_4)$ , respectively. In the latter,  $2\varphi_2 - \varphi_4$  is the relative phase difference between the semi- and quarter-diurnal flow. In the eastern channel, which is the main channel in all phases, the maximum ebb flow exceeds the maximum landward flood flow. In the western channel, the peak flow is in the flood direction during Phase 1 and in the ebb direction in the other phases. For the one-channel configuration (Phase 1), it is the relatively strong mean flow that causes larger flow velocities during ebb in the east and during flood in the west. When the bathymetry features a small secondary channel (Phases 2 and 4), larger  $A_4$  and smaller  $A_0$  values are found in the main eastern channel, with the relative phase difference indicating ebb-dominance; here, export appears to be a combined effect of mean flow and tidal asymmetry. In the western channel, export is limited because of limited water depth. With a fully developed second channel (Phase 3), the moderate  $A_0$  values and low  $A_4$  values minimizes the difference between maximum ebb and flood flow. However, export reaches maximum values because of strong semi-diurnal flow in the eastern channel and high sediment concentrations in the western channel. These are caused by ebb flow accelerating over the shallow part of this channel (indicated by the blue dot in Figure 2.11).

Subsequently, it was tested whether these differences result from internal or external asymmetry by analyzing *symmetric tide-only simulations* (no  $D_1, D_4, D_6, \dots$ ). Comparing the outcome for cross-section TiB in Table 2.4 with Table 2.3 reveals an increase in  $A_4$  and  $2\varphi_2 - \varphi_4$ . This indicates that the internally generated over-tides induce ebb-dominance. Since the externally forced tidal asymmetry is flood-dominant, the difference between maximum ebb and flood flow velocities is larger for symmetric forcing than in the *tide-only simulations* with external asymmetric tide. The values indicate that more tidal asymmetry is generated internally during the phases where tidal asymmetry was found to be an important exporting mechanism (Phases 2 and 4). As expected, the mean flow is not significantly affected.

Lastly, it was examined how the tides in the inlet are affected by the storm surge height (mean water level). Figure 2.12 shows the tidal characteristics for *simulations without waves*. Two main effects of increasing mean water level can be seen, namely: (1) the value of mean flow increases; and (2), ebb-dominance changes to flood-dominance, as indicated by the relative phase difference. This transition coincides with minimum values of the quarter-diurnal flow velocities and are caused by intertidal flats. For low mean water level values, the flats are flooded only at high water and cause ebb-dominance. However, at high mean water level, the flats are inundated during a larger part of the tidal cycle and since inundated flats enhance

**Table 2.4** Tidal flow characteristics at the location of maximum net sediment transport in cross-section TiB for tide-only simulations with symmetric tides (no external tidal asymmetry). Positive flow values are in the seaward/ebb direction.

Symmetric tidal forcing	Phase 1	Phase 2	Phase 3	Phase 4
$U_{ebb}$ (m/s)	2.01	1.76	2.07	1.73
$U_{flood}$ (m/s)	-1.25	-1.22	-1.57	-1.18
$A_0$ (m/s)	0.22	0.06	0.11	0.08
$A_2$ (m/s)	1.65	1.40	1.83	1.43
$A_4$ (m/s)	0.25	0.37	0.26	0.32
$2\varphi_2 - \varphi_4$ (°)	43	49	50	41

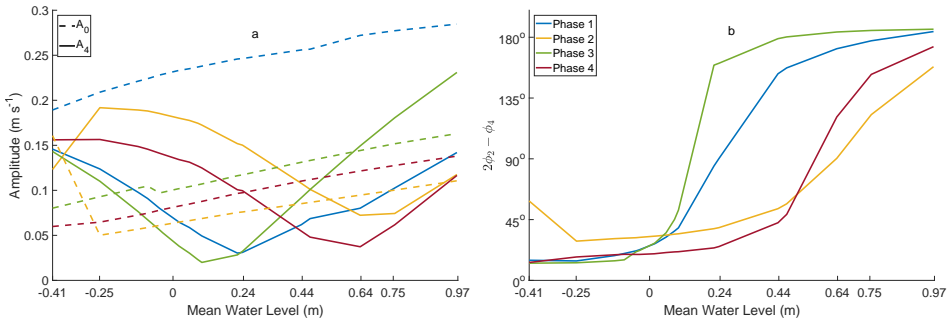


**Figure 2.12** Amplitude of mean flow (a, dashed line), quarter-diurnal flow (a, solid line) and the relative phase difference (b) in the inlet as a function of mean water level

the effect of friction, they cause flood-dominance. Additionally, non-linear effects become less important; thus, weaker overtones are generated internally and make the external asymmetry dominant. Since more ebb-asymmetry is generated internally during Phases 2 and 4, the transition to flood-dominance occurs for larger values of mean water level.

## 2.4 Discussion

The chapter first addressed the effect of changing ebb-tidal delta morphology on patterns of wave energy fluxes and wave energy dissipation rates. Figures 2.5 and 2.6 show that it is the position of the shoal that determines the wave energy fluxes towards the coast of the downdrift island and thus the nearshore wave energy dissipation. However, the wave energy entering the basin and the nearshore zone of the updrift island depends mostly on the size of the updrift channel. The modeled response of wave energy to morphodynamic changes is consistent with Hansen et al. (2013), who reported that the retreating ebb-tidal delta of San Francisco Bay increased the exposure of the adjacent beach to wave energy, particularly during energetic conditions.

Many studies on sediment transport near tidal inlet systems have neglected the effect of waves (Van Leeuwen et al., 2003; Van der Vegt et al., 2006; Van der Vegt et al., 2009; Dis-sanayake et al., 2012). However, as shown in Figure 2.10, the sediment transport patterns were directly influenced by the changes in wave propagation. Not surprisingly, transport along the coasts of the barrier islands is higher during the phases with more wave energy dissipation close to the coast. Consequently, these transports increased with increasing wave energy (not shown). This increase agrees with the findings of Herrling and Winter (2014) who found wave-induced alongshore currents that transport the entrained sand towards the inlet. Although every ebb-tidal delta is unique, many have similar cyclic behavior (FitzGerald et al., 2000; Ridderinkhof et al., 2016a). It is expected that these tidal inlets will share the periodic variations in wave energy near the barrier islands and into the basin. As shown, this causes cyclic changes in littoral drift along the updrift island and sediment transport along the downdrift island.

Herrling and Winter (2014) also showed that sediment bypassing along the terminal lobe is mostly wave-driven, which is confirmed in the present study. However, we show that the variations in wave patterns in this area did not significantly affect the fluctuations of the mod-

eled sediment bypassing along the terminal lobe. In fact, the magnitude of the downdrift-oriented tidal mean flow along the terminal lobe decreases when the ebb-channel rotates eastward. As many ebb-tidal deltas have migrating channels (FitzGerald et al., 2000), they are expected to have cyclic sediment bypassing.

In the inlet, the morphological changes have altered the tidal characteristics. The relative differences in tidal flow among the phases do not depend on the boundary conditions. For all tested sets of boundary conditions, the following three effects were found: (1) the mean flow in the inlet is especially strong for a one-channel configuration and weak for a two-channel configuration; (2) the tidal signal is deformed most by a shallow secondary channel; and (3) semi-diurnal flow in the inlet is strongest with a fully-developed secondary channel. The periodic shifting between one and two channels is observed at many tidal inlets (Cayocca, 2001; Kleinhans et al., 2015; Ridderinkhof et al., 2016a). These findings indicate that cyclic variations in tidal asymmetry, mean flow and flow magnitudes are an inherent feature of the cyclic inlet configuration.

These temporal variations in tidal characteristics result in distinct patterns of net sediment transport in the inlet. The exchange of sediment between basin and sea has only been studied as a function of basin geometry (Speer and Aubrey, 1985; Friedrichs and Aubrey, 1988; Ridderinkhof et al., 2014a; Ridderinkhof et al., 2014b) and the effects of ebb-tidal deltas has been ignored. However, the present study has shown that the cyclic behavior of ebb-tidal deltas affects the net sediment transport in the inlet. The largest value for export was found for a two-channel configuration in spite of a relatively weak tidal asymmetry and mean flows. In contrast, the strong mean flows that characterize the one-channel inlet result in a balance of import in the west and export in the east. Furthermore, the relatively distorted signal during the transitional phases in inlet configuration forces moderate export values. This suggests that the net exchange between basin and sea at this type of tidal inlets is cyclic and follows the periodicity of the one- and two-channel inlet configurations.

In this study, Ameland was used as a case study for the effect of cyclic ebb-tidal deltas on patterns of waves, tides and sediment transport. However, this study did not aim to accurately simulate or estimate the sediment budget of Ameland Inlet. Only the most relevant processes were modeled and the effects of wind, multiple grain sizes and connectivity with other basins were not taken into account. This simplified model setup had the effect of causing two noticeable discrepancies between measurements and model outcome.

Firstly, the model may have overestimated the export of sediment. As shown by Elias et al. (2012), both the ebb-tidal delta and the back-barrier basin were governed by volume gain (respectively 33.7 and 56 Mm<sup>3</sup>) between 1935 and 1995. They proposed that sediments in the basin were supplied by the adjacent Vlie Inlet, since accretion primarily occurred near this watershed. However, they also observed that subsequently (1995-2005) the ebb-tidal delta had lost 6.1 Mm<sup>3</sup>. Figure 2.11 shows that the model predicts transport of sand towards the ebb-tidal delta. This discrepancy can be attributed to (1) the use of a single grain size of 250 µm and (2) the tidal boundary conditions (De Fockert, 2008; Jiao, 2014).

The observed transition from export to import can partly be explained by relative sea-level rise. Dissanayake et al. (2012) modeled the long-term development of realistic analogue of Ameland Inlet system for various scenarios of relative sea-level rise, which were found to correlate with an increase of flood-dominance. This is in line with our finding that the tidal asymmetry depends on the mean water level for all the modeled phases. Rising the mean water level decreases the internally generated ebb-dominance. As a result, the tidal asym-

metry is largely determined by the externally generated asymmetry with the basin length the key factor in import and export (Ridderinkhof et al., 2014a; Ridderinkhof et al., 2014b).

Secondly, the model may have underestimated the littoral drift and sediment bypassing. It reproduces the littoral drift along the coasts of Terschelling and Ameland, but with magnitudes five times lower than previous estimates based on offshore wave climate (Cheung et al., 2007; Ridderinkhof et al., 2016a). A possible explanation is that the effects of wind are not accounted for in this study. Since the winds come predominantly from the west, wind-driven and wave-driven flows are mostly in the same direction. Therefore, excluding the wind effects may have led to an appreciable underestimation of the alongshore sediment transport. Similarly, the modeled bypassing magnitude would increase if the effects of wind were taken into account; however, no estimates of sediment bypassing along the terminal lobe of the Ameland ebb-tidal delta are available.

The question of what the effects of (1) wind, (2) multiple grain sizes, (3) morphological updates and (4) connectivity with other basins would be must be answered by future studies. Ongoing research aims to elucidate these physical processes.

## 2.5 Conclusions

This study identifies the impact of channel rotation, switching between a one- and two-channel inlet system and periodic development of a large sandy shoal on waves, tides and sediment transport. Using Delft3D/SWAN we have shown that many of the physical processes that characterize a tidal inlet system and an ebb-tidal delta are affected by the cyclic behavior of channels and shoals.

The alongshore sediment transport strongly relates to the amount of wave energy in the nearshore zone, whereas sediment transport through the inlet largely links with changes in tidal asymmetry and mean flow. The largest value for export was found for a two-channel inlet, the smallest for a one-channel inlet. Additionally, an updrift orientated main ebb-channel forces a mean flow that enhances the wave-driven sediment bypassing along the terminal lobe more than a symmetric channel.

A strong mean flow of up to 0.36 m/s was found in a one-channel inlet, which is more than two times higher than in a two-channel inlet. The overtidies that were generated internally counteract the flood-dominant tidal currents generated externally. The ratio of the amplitudes of the quarter- and semi-diurnal tides is largest when the inlet features a not-fully-developed second channel. In contrast, the tidal signal is least deformed when the inlet consists of one channel or when the second channel has reached its maximum size.

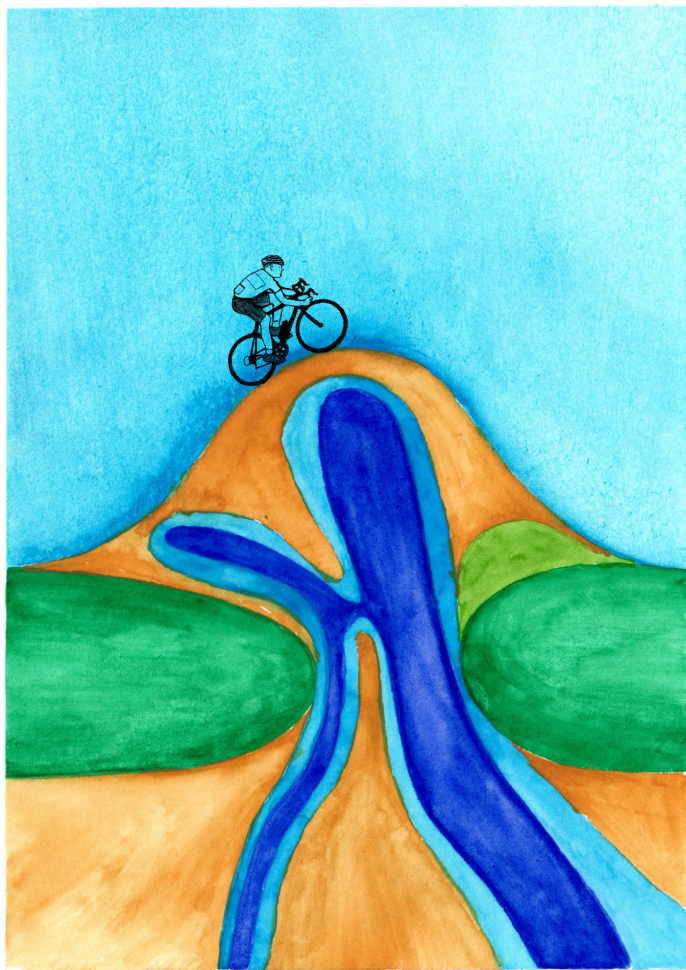
A shallow shoal on the ebb-tidal delta enhances the offshore wave energy dissipation, thereby protecting the downdrift coast from incoming wave energy. Similarly, the updrift island and the inlet are best protected by the banks of the updrift channel, which is deepest when the inlet features one channel.

Many ebb-tidal deltas have periodic shifting between one and two channels in the inlet, channel deflection and/or development of a large sandy shoal. This study reveals the patterns of wave energy, tidal currents and sediment transport during four phases of this cyclic behavior. Because it identifies and qualitatively evaluates the response of these physical processes to distinct bathymetries, the outcomes contribute to our understanding of the complex interaction between the hydrodynamics and sediment dynamics at natural tidal inlets.

## Acknowledgements

We thank Rijkswaterstaat for making their bathymetric and wave data available. We would like to thank J.A. Lenstra for critical reading. Also thanks to S.G. Pearson for helpful suggestions. We thank the anonymous reviewers for their valuable comments and suggestions. Funded by the Netherlands Organisation for Scientific Research (NWO) (project 869.15.009).





## Chapter 3 | Unraveling the mechanisms that cause cyclic channel-shoal dynamics of ebb-tidal deltas

### Abstract

The morphodynamics of many ebb-tidal deltas include cyclic patterns of channel deflection and breaching associated with sandy shoals migrating and attaching to the down-drift coast. These channel-shoal dynamics result from the complex combination of tides and waves; however, their precise role and the physical mechanisms forcing the cyclic patterns are unknown. Here, we use Delft3D/SWAN to simulate their periodic behavior and to study the underlying mechanisms during different phases of the cyclic behavior. The model forcing was such that different ratios between tidal prism and littoral drift were obtained. Two different types of cyclic behavior were modeled, namely ebb-tidal delta breaching and outer delta breaching. The typical time scale of modeled cyclic behavior generally increases with increasing tidal prism and decreasing littoral drift. No cyclic channel-shoal dynamics were found for high ratios tidal prism/littoral drift. Classically, channel deflection and shoal growth have been attributed to waves and the breaching solely to tidal currents. We confirm that shoal formation and channel deflection are forced by wave-induced currents and sediment concentrations. However, the subsequent shoal growth can only be explained by tides and waves operating simultaneously. Moreover, the breaching of ebb-tidal deltas is not a tide-only effect because waves entrain the sediment that is transported by the ebb flow. In fact, there exists an optimum wave height, i.e., larger waves cause further channel rotation rather than channel breaching. Furthermore, temporal variations in the sediment exchange between the back-barrier basin and the sea are found to be an inherent feature of the modeled ebb-tidal delta breaching.

### Published as:

Klaas J.H. Lenstra, Wim Ridderinkhof and Maarten van der Vegt (2019), Unraveling the mechanisms that cause cyclic channel-shoal dynamics of ebb-tidal deltas: a numerical modeling study. *Journal of Geophysical Research: Earth Surface*, December 2019, Volume 124, Issue 12, pp 2778-2797.

### 3.1 Introduction

Ebb-tidal deltas are shallow sandy features seaward of tidal inlet systems that are formed by the joint action of waves and tides (Hayes, 1975). Observations show that many ebb-tidal deltas have cyclic channel-shoal dynamics (FitzGerald, 1988; Ridderinkhof et al., 2016a). This cyclic behavior often features downdrift channel deflection and formation of sandy shoals that migrate and attach to the downdrift coast. The overarching problem addressed in this chapter is to understand how the mutual combination of waves, tides and morphology causes this cyclic behavior of ebb-tidal deltas.

A solid understanding of ebb-tidal delta cyclic behavior, its causing mechanisms and involved time scales has purpose beyond scientific interest, in particular for coastal safety and management. For example, the extent to which the shallow ebb-tidal delta causes offshore wave energy dissipation depends on the presence and position of the shoal (Chapter 2). This directly influences the nearshore dynamics of the updrift and downdrift barrier islands (Hansen et al., 2013). Furthermore, tidal flow can cause erosion of coastal areas when the channel impinges against a barrier island (FitzGerald, 1988). In contrast, the welding of a large sandy shoal can cause temporary growth of the barrier island. Ebb-tidal deltas can also be a temporary source of sediment for the back-barrier basin (Elias et al., 2012). Furthermore, the channel orientation influences tidal asymmetry and mean flows in the inlet, thereby influencing the sediment exchange (import/export) between basin and sea (Chapter 2). Knowledge of the natural long-term behavior of tidal inlet systems is essential before assessing the effects of coastal development, sand nourishments, land reclamation and relative sea-level rise.

Bruun and Gerritsen (1960) related the occurrence of channel deflection and cyclic behavior to tidal prism  $P$  and littoral drift  $Q_{ld}$ . Their observations indicated that stable inlet channels were mainly found for inlets with a ratio  $P/Q_{ld} > 300$ . Channel rotation and breaching was likely for tidal systems with  $P/Q_{ld} < 100$ . Here, the predominant sediment bypassing mechanism was via (shallow) shoals across the ebb-tidal delta. FitzGerald (1988) proposed three conceptual models for ebb-tidal deltas which include periodic shoal attachments (Figure 3.1). Changes in main channel position are strongly related to the shoal dynamics in the model for ebb-tidal delta breaching (Figure 3.1a). During the first phase, sediments supplied by the littoral drift (alongshore sediment transport) accumulate on the updrift side of the ebb-tidal delta while simultaneously, the main ebb-channel deflects in the downdrift direction. Phase 2 is characterized by shoal growth and further deflection of the main channel. According to FitzGerald (1988), the migration of the main channel continues in some cases until the channel bends around the downdrift barrier island coast. Eventually, the ebb-tidal delta is breached by a shorter channel. During the third phase, most of the water entering and leaving the basin flows through the new channel. The old channel is abandoned and gradually fills with sediment. Phase 3 ends with the shoal merging with the downdrift island. On other ebb-tidal deltas, the breach occurs at the seaward end of the ebb-tidal delta (Figure 3.1b) or the channel is maintained in a more stable orientation while shoals form, migrate and attach to the downdrift barrier island (Figure 3.1c). FitzGerald (1988) refers to these processes as outer delta breaching and stable inlet processes, respectively. These different types of cyclic behavior all occur in various tidal inlet systems along the Dutch and German Wadden Sea with time scales ranging from 4 to 130 years (Ridderinkhof et al., 2016a). Other examples of ebb-tidal deltas that feature channel deflection/breaching are Manukau Harbour, New Zealand (Ford and Dickson, 2018), Loughros Beg, Ireland (O'Connor et al.,

(a) Ebb-tidal delta breaching (b) Outer delta breaching (c) Stable inlet processes

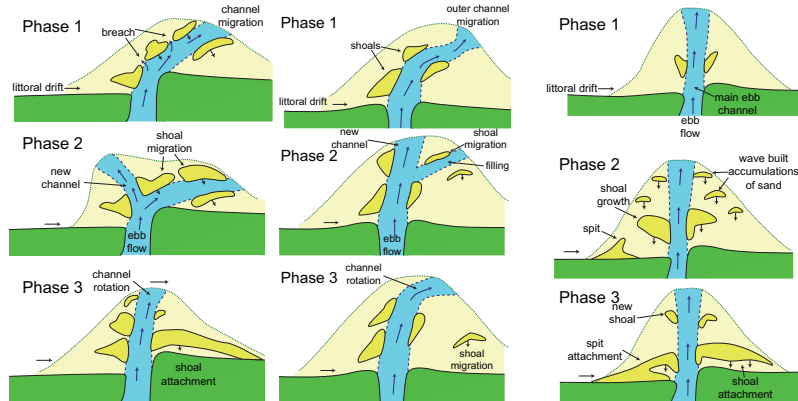


**Figure 3.1** Conceptual models of cyclic ebb-tidal deltas featuring shoal formation, migration and attachment to the downdrift coast as proposed by FitzGerald (1988).

2011), Barra Nova inlet and Guadiana estuary, Portugal (Garel et al., 2014; Balouin et al., 2001), Deben estuary, UK (Birmingham and French, 2006) and many inlets along the east coast of the USA (FitzGerald, 1988; Gaudiano and Kana, 2001).

Observations indicate that tidal inlet systems with a relatively high tidal prism have a larger period between successive shoal attachments (Gaudiano and Kana, 2001; Ridderinkhof et al., 2016a). Further, it has been suggested that the period decreases with increasing littoral drift; however, a clear relationship has not been identified. Ridderinkhof et al. (2016a) attributed this to the variety in geometry, tidal prism, and other parameters that affect the period.

Classically, the cyclic behavior has been attributed to the competition between waves and tides. The former tends to force the ebb-tidal delta and the channel in the downdrift direction (FitzGerald, 1988); therefore, the first two phases of the cyclic behavior (channel deflection and shoal growth) are thought to be wave-effects. In contrast, a small phase difference between alongshore and cross-shore tidal currents forces an updrift channel orientation (Sha, 1989). The formation of a new (more updrift) channel has thus been attributed to the tidal currents. However, this hypothesis has never been tested. Furthermore, how waves and tides interact in different phases and how these determine the morphological processes has not been studied before.

Several numerical model studies have tried to reproduce the conceptual models of FitzGerald (1988). The simulations of Dastgheib (2012) showed that ebb-tidal delta breaching is found in highly wave-dominated systems (see the classification of Davis and Hayes, 1984), whereas outer delta breaching and stable inlet processes occur in wave-dominated mixed energy and tide-dominated systems, respectively. Nahon et al. (2012) reproduced with his model one cycle similar to the ebb-tidal delta breaching model of FitzGerald (1988). However, these modeling studies did not discuss the underlying physical mechanisms and how these depend on the tides and waves. Moreover, the simulations of Cayocca (2001) show that wave-induced littoral drift is essential for shoal formation and that tidal currents force the opening of new channels (breaches). Ridderinkhof et al. (2016b) found that existing shoals can form and grow during storms as the ebb-tidal delta bathymetry is not in balance with the

incoming energetic waves. However, in the model simulation of Ridderinkhof et al. (2016b), neither the full cycle of shoal formation, migration and attachment nor the breaching of the ebb-tidal delta was modeled. Breaching of the ebb-tidal delta was imposed by a virtual extension of the main channel and transfer of the thereby removed sediment to the downdrift side of the ebb-tidal delta; therefore, the results can be categorized as part of the stable inlet processes model. The modeled landward shoal migration has successfully been attributed to waves, where a distinction can be made between the effects of wave skewness (Ridderinkhof et al., 2016b) and wave-driven residual flow over the shoal (Bertin et al., 2009).

To date, observations, conceptual models and numerical studies have qualitatively described the cyclic behavior of ebb-tidal deltas and identified relevant physical mechanisms for some of the processes. However, they do not allow a proper understanding of the processes that drive the cyclic bed changes or of the time scales involved. For example, it has not been tested whether it are indeed only the waves that cause channel deflection and shoal growth (as suggested by FitzGerald, 1988). Moreover, although it is known that tidal currents are essential for the opening of new channels (Cayocca, 2001), it is unknown if tides are solely responsible for this breach. Furthermore, the above mentioned studies focused on sediment supplied to the ebb-tidal delta by the littoral drift, but ignored the exchange of sediment with the basin and the temporal variations herein. In addition, we know from observations that the typical time scale of cyclic behavior increases with the tidal prism, but not how it is related to wave-induced littoral drift.

The main aim of this chapter is twofold. Firstly, the physical processes and feedbacks that drive cyclic channel-shoal dynamics are studied. We also aim to clarify the relative roles of tides and waves in the different phases of the cyclic behavior. Secondly, we study the relationship between the littoral drift and the period between successive shoal attachments. The goals of this chapter are approached by means of an idealized model setup in Delft3D/SWAN, the details of which are discussed in Section 3.2. The modeled cyclic behavior is shown in Section 3.3.1. Section 3.3.2 shows the mechanisms and the relative roles of tides and waves for the different phases. The relationship between littoral drift and the time scales is discussed in Section 3.3.3. A comparison between our model setup and real systems can be found in Section 3.4.1. The discussion of the main findings and shortcomings of this study are discussed in Sections 3.4.2 and 3.4.3, respectively, followed by the main conclusions in Section 3.5.

## 3.2 Material and methods

A simplified modeling approach was implemented in Delft3D/SWAN with an idealized geometry similar to that of Ridderinkhof et al. (2016b) and is briefly discussed below. The model Delft3D (Deltares, 2014) was employed in its 2DH mode together with the spectral wave model SWAN (Booij et al., 1999; Ris et al., 1999; Holthuijsen, 2010) to simulate currents, waves, sediment transport, and bed evolution.

### 3.2.1 Modeling system

The SWAN and Delft3D models were run with a coupling time of 60 minutes. SWAN computed the spectral wave energy and wave-induced forces by solving the wave action balance in its stationary form (Holthuijsen, 2010), after it was provided with the bed level, water level and flow velocity by Delft3D. Subsequently, the SWAN outputs were communicated to

Delft3D and used to calculate water levels and flow velocities by solving the depth-averaged shallow water equations and the continuity equation. Below, we discuss the relevant settings and parameter values as applied in the model setup; for a full description the reader is referred to Lesser et al. (2004) and Deltaires (2014).

### 3.2.2 Model domain

In the framework of Bruun and Gerritsen (1960), cyclic behavior relates to tidal prism  $P$  and littoral drift  $Q_{ld}$ . Since cyclic behavior and stable inlets are likely for  $P/Q_{ld} < 100$  and  $P/Q_{ld} > 300$ , respectively, the model domain was chosen such that it could represent a wide range of ratio  $P/Q_{ld}$ . In this study, we opted for a small inlet system because this is most suitable for numerical modeling. The model domain (Figure 3.2) consists of a rectangular domain with one inlet and doesn't represent any particular tidal inlet system in detail. The basin has an initial uniform water depth of 1.5 m and its size is 9 km by 3.5 km in the along-shore and cross-shore direction, respectively. The initial width of the tidal inlet is 1.8 km and its length 1.3 km. Depending on the model forcing (see Section 3.2.4), the modeled ratio  $P/Q_{ld}$  ranges from 50 to 500.

To allow for faster computations, the flow grid in Delft3D was divided into eight different subdomains using the domain decomposition option (white lines in Figure 3.2a). The grid cell size of the grids that cover the outer sea and the back-barrier basin is 450 m and 150 m, respectively. The area of interest is the tidal inlet and the adjacent part of the sea; here, the grid cell size is 50 m. This high resolution allows for detailed calculation of waves and currents and prevents unrealistic shoreface steepening (Brière and Walstra, 2006). It was extended in the western direction to ensure the updrift supply of sediment to the tidal inlet system throughout the modeled period. The wave grid (Figure 3.2b) consists of three nested grids with decreasing grid cell sizes of 1350 m (outer grid), 450 m (dashed red lines) and 50 m (solid red lines).

### 3.2.3 Model setup

In Delft3D, the time step was set at 12 s. The bed roughness was prescribed with a uniform Chézy friction coefficient value of  $65 \text{ m}^{0.5}/\text{s}$ . The horizontal eddy diffusivity and viscosity were calibrated to prevent unrealistic gradients in flow velocities and sediment transport and set at  $1 \text{ m}^2/\text{s}$  and  $10 \text{ m}^2/\text{s}$ , respectively. Furthermore, the bed consisted of homogeneous sediment ( $d_{50} = 250 \mu\text{m}$ ). Finally, the SWAN model considered wave breaking (formulation of Battjes and Janssen (1978),  $\gamma = 0.73$ ), white-capping (Komen et al., 1984) and bottom friction (JONSWAP). However, it did not account for wind growth, wave diffraction or non-linear triad-interactions.

In the sediment transport module, the transport formulations of Van Rijn et al. (2004) were used. Unless mentioned otherwise, the default settings were used for sediment transport. These differentiate between bed and suspended load transport. The latter was calculated with a depth-averaged advection-diffusion equation, where currents carry the sediment entrained by the combined bed shear stress of waves and currents, which was computed using the parameterization of Fredsøe (1984). Skewed waves have relatively strong orbital velocities in the crest of the wave compared to the trough. However, the effects of wave skewness on suspended transport were neglected. Its effect on bed load sediment transport ( $q_b$ ) was taken into account in the model, as  $q_b$  is proportional to the instantaneous velocity of cur-

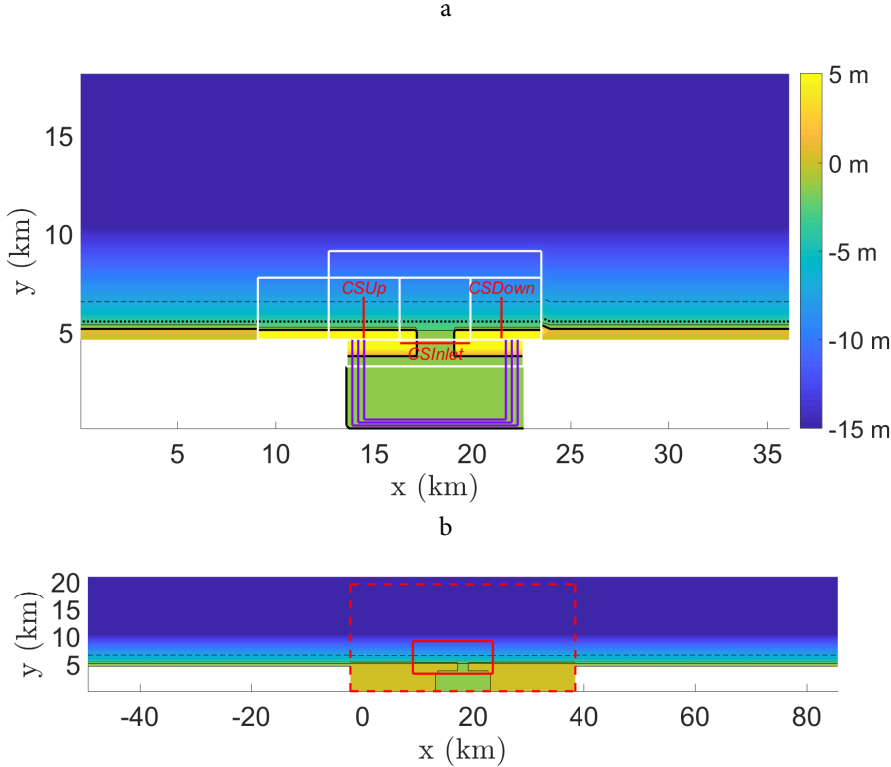


**Figure 3.2** Domains that are considered in Delft3D (a) and SWAN (b) with colors indicating initial bathymetry. The white lines in the flow domain enclose subdomains for domain decomposition, the red lines indicate cross-sections used for analysis and the purple lines indicate the basin area for the model runs with 90%, 80% and 70% of the default basin surface area. The red lines in the wave domain indicate the nested grids.

rents and waves  $u$  as  $q_b \propto u^{2.5}$ . This was achieved by the parametrization of Van Rijn et al. (2004) after the method of Isobe and Horikawa (1982).

Numerous test runs showed unrealistic shoreface steepening, coastal expansion and a littoral drift that decreased in time because of this. As a result, no dynamic equilibrium was obtained in these runs and the modeled behavior of the ebb-tidal delta varied on time scales shorter than that of natural cyclic behavior. Therefore, in order to reduce this shoreface steepening, the wave-related bed load transport factor  $BedW$  was calibrated (similar to e.g. Nienhuis et al., 2016). A major constraint in this calibration was the stable (steady) littoral drift, which was needed (1) to mimic the dynamic equilibrium of cyclic behavior and (2) to identify the relationship between littoral drift and typical period of cyclic behavior. Based on these test runs,  $BedW$  was set to a constant value of 0.3 and bed load transport due to the undertow was omitted. This parameter setting kept the littoral drift and the position of the coastline relatively steady at the time scales of interest, while also limiting the shoreface steepening.

Bed level changes in the morphological module of Delft3D are calculated as a result of sediment settling/entrainment and spatial gradients in sediment transport. The computed bed level changes were multiplied with a morphological acceleration factor  $M$  to reduce computation time. The simulated period of each model run was 625 days, which with  $M = 20$  is the equivalent of 12,500 modeled morphodynamic days (hereafter referred to as days).

### 3.2.4 Boundary conditions

Incoming waves (spatially and temporally constant) were prescribed at the north boundary of the wave domain. From the prescribed significant wave height  $H_s$ , peak period  $T_p$  and direction  $\theta_p$  a JONSWAP wave spectrum was calculated with a directional spreading with a cosine power of 4 and a peak enhancement factor of 3.3 (default). The chosen wave direction directs the littoral drift eastward:  $\theta_p = 335^\circ$  with respect to the north (positive in clockwise direction). Several model runs were conducted each with a different prescribed wave height and period. The following relationship based on the JONSWAP and Pierson-Moskowitz spectra was used:  $T_p = 5.3\sqrt{H_s}$ . The corresponding littoral drift magnitudes ranged from 0.1 to 1.1 Mm<sup>3</sup>/year.

The tides were represented by a single semi-diurnal tidal wave with amplitude  $A = 1$  m and period  $T_2 = 12$  hours. This roughly corresponds to an initial tidal prism of 63 Mm<sup>3</sup>. Here, the S<sub>2</sub> period was preferred over the M<sub>2</sub> period because this period is convenient for the interval between output files and the coupling between Delft3D and SWAN. The open boundaries were forced by sea surface elevations at the northern boundary and Neumann boundary conditions at the western and eastern open boundaries. As is common in the North Sea and many other barrier-island coasts in the northern hemisphere, the tidal wave propagates with the coast on its right-hand-side.

The sediment concentration at all boundaries did not affect the outcome in the area of interest and was set at 0. Furthermore, wind forcing was not included in the boundary conditions.

### 3.2.5 Model simulations and model analysis

An overview of the model runs and wave forcing is presented in Table 3.1. Even though modeled littoral drift magnitude  $Q_{ld}$ , tidal prism  $P$  and type of cyclic behavior are model output, they are included in Table 3.1. This is because we have adopted the framework of Bruun and Gerritsen (1960): the wave and tidal conditions were thus chosen such that a wide range of  $P/Q_{ld}$ -ratios were modeled. Three sets of model runs were conducted, namely:

- model runs 1 to 10. Here, only the wave forcing was varied to identify the relationship between the littoral drift and period between shoal attachments;
- model runs 2<sub>90%</sub>, 2<sub>80%</sub> and 2<sub>70%</sub>, which have 90%, 80% and 70% of the default basin surface area (see purple lines in Figure 3.2). To test the hypothesis that tidal prism, rather than range, impacts the time scale of cyclic behavior, the tidal range and wave forcing were not varied, and the tidal prism was varied by repeating model run 2 with smaller basins;
- model runs 5<sub>80%</sub>, 6<sub>80%</sub> and 7<sub>80%</sub>, i.e., the model run with 80% of the default basin surface area repeated with varying wave forcing (and thus littoral drift). These runs were conducted to test the robustness of the results.

Additionally, in model run 2N, the effect of a shore-normal waves on the modeled cyclic behavior was tested.

For each model run, we analyzed the:

- tidally-averaged sediment transport (bed load + suspended load);
- tidally-averaged sediment concentration ( $\langle C \rangle$ );
- tidally-averaged flow velocities ( $\langle \vec{u} \rangle$ , hereafter referred to as mean flow);
- amplitudes of semi-diurnal flow velocity and higher harmonics. For this, harmonic analysis was used;
- tidally-averaged magnitude of the combined bed-shears stress ( $|\langle \tau_b \rangle|$ , combined waves and current using the parameterization of Fredsøe (1984));
- tidal prism ( $P$ ), i.e., the volume of water entering and leaving the basin each tidal cycle;
- net sediment transport values through the inlet and along the coasts on both sides of the tidal inlet. This was done by placing cross-sections across the inlet ( $CS_{Inlet}$ ) and perpendicular to the coasts ( $CS_{Up}$  and  $CS_{Down}$ ), see Figure 3.2a;
- period between successive shoal attachments. The shoal was timed to attach by the merging of the closed 2 m isobaths;
- the total erosion/deposition in a certain area ( $\Delta h$ ). This parameter was used either as shoal growth rate (Section 3.3.2.2) or as breaching rate (Section 3.3.2.3);
- the orientation of the main channel ( $\theta$ ). For this, the path of the main channel was followed starting from the deepest grid cell in the inlet. The next point of the main channel was the deepest grid cell which was within 100 m of the previous point and

**Table 3.1** Overview of conducted model runs with wave forcing at the alongshore boundary. Here,  $H_s$  and  $T_p$  are significant wave height and peak wave period, respectively. For clarity, the modeled littoral drift magnitude  $Q_{ld}$  (positive eastward), tidal prism  $P$  and type of modeled cyclic behavior are shown here, even though they are part of the model output. The different types of modeled behavior are ETDB (ebb-tidal delta breaching), ODB (outer delta breaching) or SC (stable channel, i.e., no cyclic behavior).

Run	$H_s$ (m)	$T_p$ (s)	$Q_{ld}$ ( $Mm^3/year$ )	$P$ ( $Mm^3$ )	$P/Q_{ld}$	Modeled behavior
1	2.1	7.70	1.10	53	48	ETDB
2	2.0	7.50	0.90	55	61	ETDB
3	1.9	7.30	0.75	56	75	ETDB
4	1.8	7.10	0.60	56	93	ETDB
5	1.7	6.90	0.50	57	114	ETDB
6	1.6	6.70	0.40	58	145	ODB
7	1.5	6.50	0.30	59	197	ODB
8	1.4	6.27	0.25	63	252	SC
9	1.3	6.04	0.18	66	367	SC
10	1.2	5.80	0.14	66	471	SC
$2_{90\%}$	2.0	7.50	0.90	50	56	ETDB
$2_{80\%}$	2.0	7.50	0.90	45	50	ETDB
$2_{70\%}$	2.0	7.50	0.90	38	42	ETDB
$5_{80\%}$	1.7	6.90	0.50	47	94	ETDB
$6_{80\%}$	1.6	6.70	0.40	49	123	ODB
$7_{80\%}$	1.5	6.50	0.30	50	167	ODB
$2N$	2.0	7.50	0.10	60	600	SC

further seaward from the inlet than the previous point. The procedure was stopped either when the deepest point was above the 3.5 m isobaths or when this point was more than 2000 m from the first point. The orientation of the main channel was defined as the angle between the last and first grid point of its path with respect to the north (positive in clockwise direction);

- the range over which the main channel rotates ( $\Delta\theta$ ), i.e., the difference between the typical maximum and minimum  $\theta$  throughout the model run;
- the volume of the ebb-tidal delta ( $V_{ETD}$ ). This volume was calculated using the method introduced by Dean and Walton (1975). In this procedure, first an idealized no-inlet bathymetry was constructed based on the cross-shore profile at the locations of the cross-sections *CSUp* and *CSDown*, see Figure 3.2a. Secondly, the barrier islands were removed from the analysis by neglecting values above mean sea level. Finally, the volume was obtained by summation of the difference between the modeled and the no-inlet bathymetry multiplied by the grid cell area. Here, only the positive values were taken into account, i.e., channels were not considered to be negative volume.

The volume of the ebb-tidal delta greatly depends on the no-inlet bathymetry. We reconstructed this no-inlet bathymetry after each tidal cycle as the barrier islands (and thus the cross-shore profiles) evolved throughout the model run. Alternatively, this evolution could be ignored and a constant reference cross-shore profile was chosen, yielding a no-inlet bathymetry that is fixed in time. This alternative option will be discussed in Section 3.4, together with the implications of taking negative volumes into account.

Notably, the ebb-tidal delta volume cannot be interpreted as a closed box bounded by the cross-sections *CSIlet*, *CSUp* and *CSDown*. This volume will not only be affected by changes in no-inlet bathymetry (as mentioned above), but also by changes in channel dimensions (negative volumes) and sediment exchange with the barrier islands (shoal attachment). Since both negative volumes and barrier islands are not part of the ebb-tidal delta volume, not all changes herein will correspond to transport values through the cross-sections bounding the ebb-tidal delta.

### 3.3 Results

#### 3.3.1 Modeled cyclic behavior

As can be seen from Table 3.1, stable channels were modeled for higher ratios (model runs 8 to 10,  $P/Q_{ld} > 250$ ). Moreover, for lower ratios, periodic channel-shoal behavior was modeled with ebb-tidal delta breaching for  $P/Q_{ld} < 120$  and outer delta breaching for intermediate values. Between model runs 5 and 6 and between 5<sub>80%</sub> and 6<sub>80%</sub> a similar transition from ebb-tidal delta breaching to outer delta breaching was found. Our hypothesis that the type of cyclic behavior relates to littoral drift rather than wave height is supported by model runs 2 and 2N. For the same wave height, model run 2 shows clear cyclic behavior, whereas for shore-normal energetic waves the littoral drift almost vanished and no cyclic behavior is modeled.

Figure 3.3 shows the evolution of bathymetries obtained in the model run 2. This model run is a typical example of ebb-tidal delta breaching (FitzGerald, 1988). During the spin-up of around 2000 modeled days, the ebb-tidal delta forms and two channels develop in the inlet. The end of the spin-up is defined as when the tidal prism, littoral drift and cross-sectional

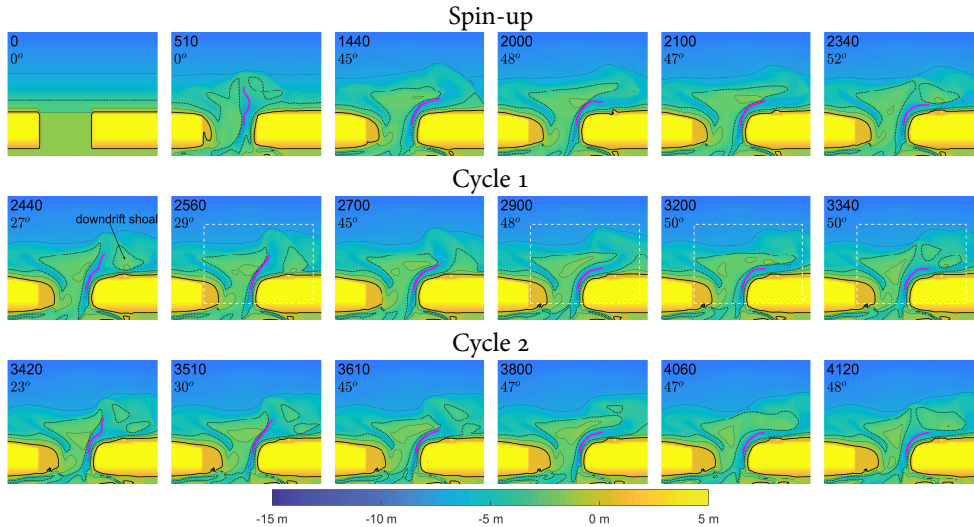
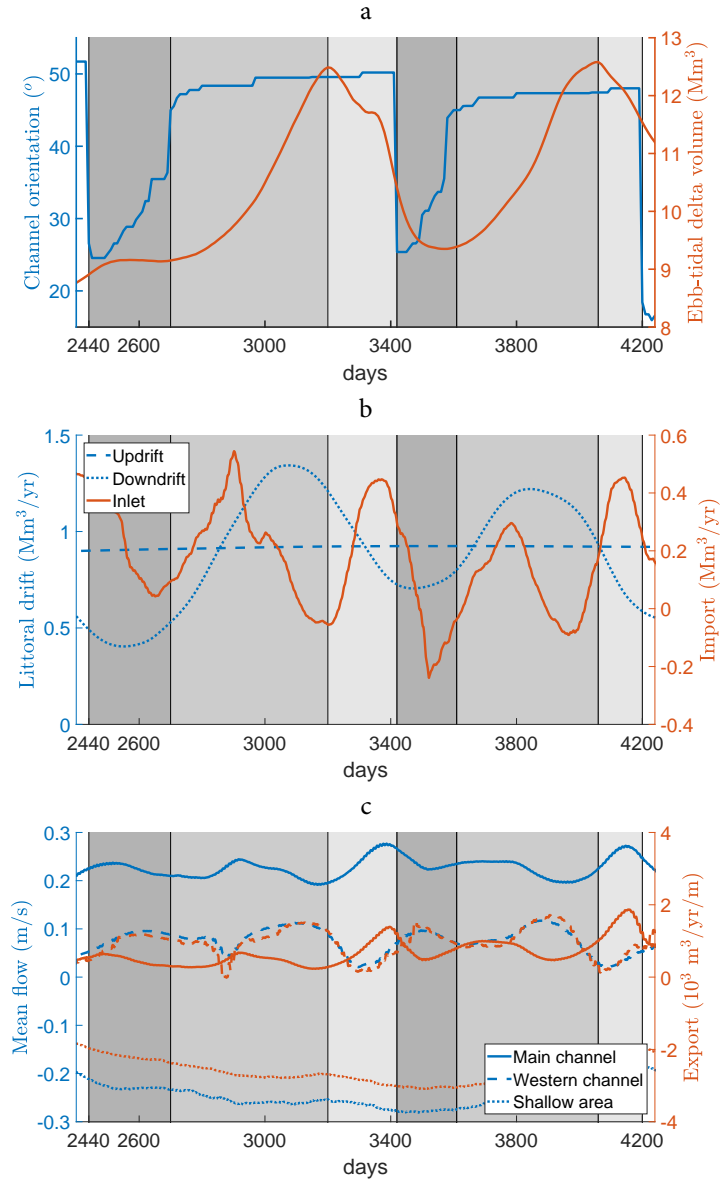


**Figure 3.3** Obtained bathymetries from the model run 2. In the upper left corner of each panel, the number of modeled days and the main channel orientation is shown. The magenta line indicates the pathway of the main channel. The white box in the first cycle indicates the area shown in Figures 3.6, 3.7, 3.8 and 3.9. The shown area is 5.5 km (east-west direction) by 4.5 km (north-south).

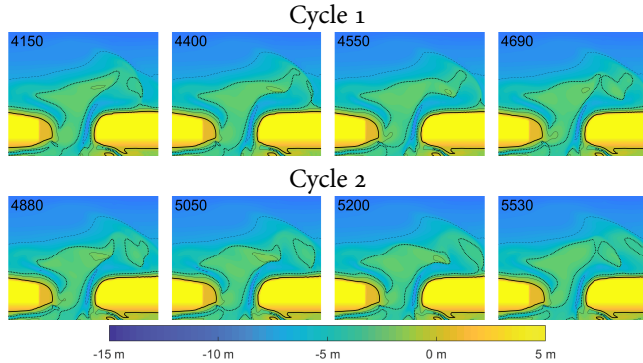
area of the inlet have adopted to the boundary conditions and are in dynamic equilibrium. Here, the main channel has a clear downdrift orientation, whereas the shallower secondary channel is oriented updrift. Several similar cycles were modeled after spin-up; although the patterns do not repeat exactly, the gross characteristic of channel rotation and breaching, development of a large sandy shoal and its subsequent migration towards the downdrift island, repeat on a typical time scale of about 1000 modeled days. The outcomes of model runs 1 to 5, 2<sub>90%</sub> to 2<sub>70%</sub> and 5<sub>80%</sub> are similar in behavior (ebb-tidal delta breaching), albeit with variations in ebb-tidal delta volume and period of cyclic behavior.

Figure 3.4a shows the orientation of the main channel (blue) and the volume of the ebb-tidal delta (orange) for two consecutive cycles of ebb-tidal delta breaching in model run 2. These parameters show the three phases of ebb-tidal delta breaching (see Section 3.1), visualized by the background color. Initially, the channel rotates rapidly (Phase 1), after which the channel deflection continues, albeit slower, and the volume of the ebb-tidal delta increases (Phase 2). During Phase 3, a breach through the large ebb-tidal delta platform does provide the main channel a new pathway. When the old channel fills up, an abrupt change in channel orientation occurs, which concludes the cycle.

Figure 3.4b shows for model run 2 the sediment transport through cross-sections *CSInlet*, *CSUp* and *CSDown*. Here, the cyclic variations in sediment transport along the downdrift coast demonstrate the effects of periodic attachments and distribution of sandy shoals. Notably, there is a time lag between the shoal attaching to the downdrift coast shortly after the breach (Phase 1, darkest gray) and the maximum downdrift littoral drift due to sediment redistribution.



**Figure 3.4** Modeled time series of (a) orientation of main channel and volume of ebb-tidal delta; (b) sediment transport values along the barrier islands (cross-sections *CSUp* and *CS-Down*) and through the inlet (*CSI*nlet, positive import); and (c) mean flow and net sediment transport (positive seaward) in the main channel in the east of the inlet (solid lines), in the secondary channel in the west of the inlet (dashed), and at the shallow area between the two channels (dotted) for model run 2. The different gray background colors roughly represent the different phases of cyclic behavior.



**Figure 3.5** Obtained bathymetries from the model run 6. In the upper left corner of each panel, the number of modeled days is shown. The shown area is 5.5 km (east-west direction) by 4.5 km (north-south).

Interestingly, the exchange of sediment between basin and sea is not steady and depends on the cyclic behavior of the channels and shoals. These variations can be explained by the cross-shore mean flow in the inlet, which is shown in Figure 3.4c for three locations in the inlet, namely the deepest locations of both channels and the shallowest location in between. The cross-shore mean flow in the inlet (blue lines) is landward over the shallow areas and seaward in both channels. Superimposed on this pattern, a time-varying circulation of mean flow was found with landward flow in the western channel and seaward flow in the main (eastern) channel. As can be seen, the net cross-shore sediment transport (orange lines) follows this pattern of mean flow in time. Because sediment concentrations in the west of the inlet are relatively high (sediment is provided to this part of the inlet by the littoral drift), a stronger circulation enhances the net import of sediment. An example of stronger circulation is between 2800 and 2900 days. Furthermore, the amplitudes and phases of the quarter- and semi-diurnal flow velocity (not shown) indicate that transport by tidal asymmetry in the inlet is relatively steady.

Figure 3.5 shows evolution of bathymetries obtained in the model run 6. This type of modeled cyclic behavior is a typical example of the outer delta breaching model of FitzGerald (1988). Note that the duration of the spin-up (here roughly 4000 days) increases with increasing  $P/Q_{ld}$ . When compared to the modeled ebb-tidal delta breaching, several differences can be observed. First, the breach occurs further from the inlet. Furthermore, the changes in bed level are smaller and limited to a smaller area, i.e., the eastern side of the up-drift shoal. As the part of the channel near the inlet does not migrate and retains a downdrift orientation; as a result, the exchange of sediment between basin and sea is relatively steady. For this system, the  $P/Q_{ld}$  threshold ratio for transition in type of cyclic behavior is between 114 and 145.

### 3.3.2 Physical processes

The following subsections present the physical mechanisms driving the morphological changes during each of the phases in the deflection-breaching cycle. Model run 2 is used here as case study; this model run is representative for ebb-tidal delta breaching. The mechanisms that cause ebb-tidal delta breaching and outer delta breaching differ slightly;

these differences will be discussed in section 3.3.2.4. Figures 3.6, 3.7, 3.8 and 3.9 show the patterns of erosion/deposition, sediment transport and semi-diurnal and mean flow velocities for four characterizing bathymetries. To identify the relative role of tides and waves, sensitivity runs were conducted where bathymetries obtained in the reference model run (tides+waves) were forced with changes in either the wave height (0-2.5 m with 0.5 m increments) or the tidal amplitude (0-1.2 m with 0.2 m increments). Thereby the littoral drift and tidal prism were also changed. These sensitivity runs were short-term runs without morphological updates and used to analyze patterns of erosion/deposition, sediment transport and amplitudes of semi-diurnal and mean flow. The outcomes of the sensitivity runs with only tides and that with only waves are shown in Figures 3.6-3.9. Note that the combination of waves and tides operating simultaneously produces morphologic outcomes that are not attributable to each process in an additive manner.

### 3.3.2.1 Phase 1: Channel rotation

During Phase 1, the main channel rotates in the downdrift direction. Meanwhile, the downdrift shoal migrates to and merges with the downdrift barrier island coast, after which its sediment distributes along the coast. Figure 3.3 shows that during the first phase the updrift part of the ebb-tidal delta expands in the eastward direction. Since the volume of the ebb-tidal delta does not significantly increase in this phase (Figure 3.4a), this expansion must be part of sediment redistribution.

The vectors in Figure 3.6a indicate that the sediment transport in the vicinity of the shoals largely follows the mean flow. Also, the effect of tidal asymmetry on sediment transport near the shoals was found to be negligible and the bed load transport due to wave skewness is at least one order of magnitude smaller than the total transport. Therefore, we conclude that the mean flows are the main driver of the sediment transport over the shoals, and thus of the channel-shoal migration.

Visual comparison of the mean flows found in the reference run and in the tide-only and wave-only sensitivity runs (Figure 3.6cd) reveals several wave-effects. At the downdrift shoal, waves induce an eastward mean flow which was not found in the tide-only runs. The second effect concerns the direction of mean flows at the updrift shoal. These are towards the channel when waves were included (similar to the reference run), whereas they are parallel to the channel for the tide-only run. For all runs, the sediment transport direction is largely determined by the mean flows. However, it must be noted that the sediment concentration near the shoals and thus also the sediment transport are significantly reduced in the tide-only run. As a result of these patterns of mean flow and sediment transport, the main channel rotates in the downdrift direction in the runs with waves, whereas without waves the channel deflection is in the opposite (updrift) direction.

The patterns of erosion/deposition in the channel were correlated to the gradients in bed level. In fact, the reference run yields correlation coefficient  $R < -0.7$  for the three thick black lines in Figure 3.6a. This negative correlation indicates eastward channel rotation, i.e., channel rotation arises from deposition at the western side of the channel and erosion at the eastern side. All sensitivity runs were used to test how  $R$  depends on the relative importance of tides and waves. Figure 3.6b shows that eastward migration scales with wave height for all three locations. Moreover, for small wave height, positive  $R$ -values even suggest channel deflection in the opposite (westward) direction. Furthermore, channel deflection is relatively unaffected by the tidal amplitudes.

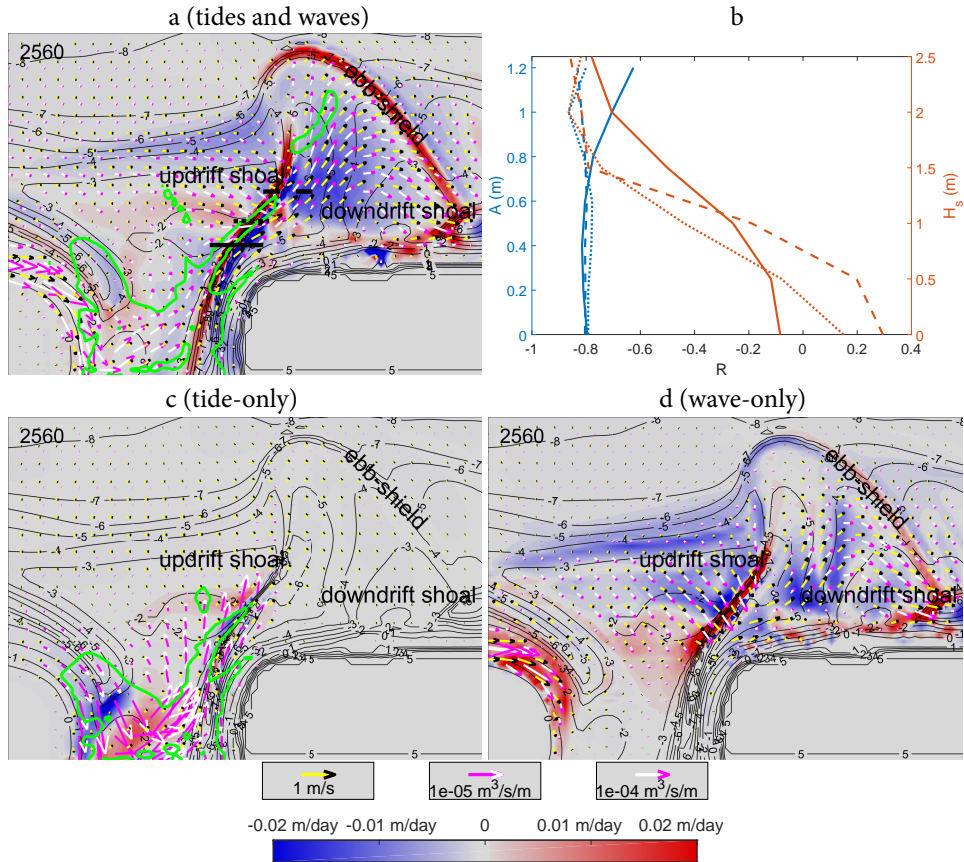


**Figure 3.6** (a) Erosion (blue) and deposition (red) after 2560 modeled days (during Phase 1) in the reference run (tides+waves). The vectors represent tidally-averaged total sediment transport (white/magenta) and flow velocities (yellow/black). The arrows are shown in every third grid cell in both directions. The green line encloses the area with semi-diurnal flow magnitude exceeding 0.23 m/s. The white box in Figure 3.3 is the area shown here. (b) Correlation coefficient between east-west gradient of the channel and erosion/deposition for the three thick black lines in (a) for varying tidal and wave forcing. Negative values indicate eastward channel deflection. (cd) As (a), but for tide- and wave-only. Note that the white/magenta vectors in (d) are a factor ten smaller than those in (a) and (c) for the same vector length. The shown area is 4 km (east-west direction) by 2.9 km (north-south).

Additionally, Figure 3.6c shows that the downdrift shoal does not migrate without waves. Besides, the reference and the wave-only runs have similar patterns of erosion/deposition. It is therefore concluded that the channel rotation and the migration of both shoals that characterize the first phase can be contributed to the wave-induced mean flows and increased bed shear stress. Furthermore, the tidal currents would deflect the channel in the opposite direction in the absence of waves.

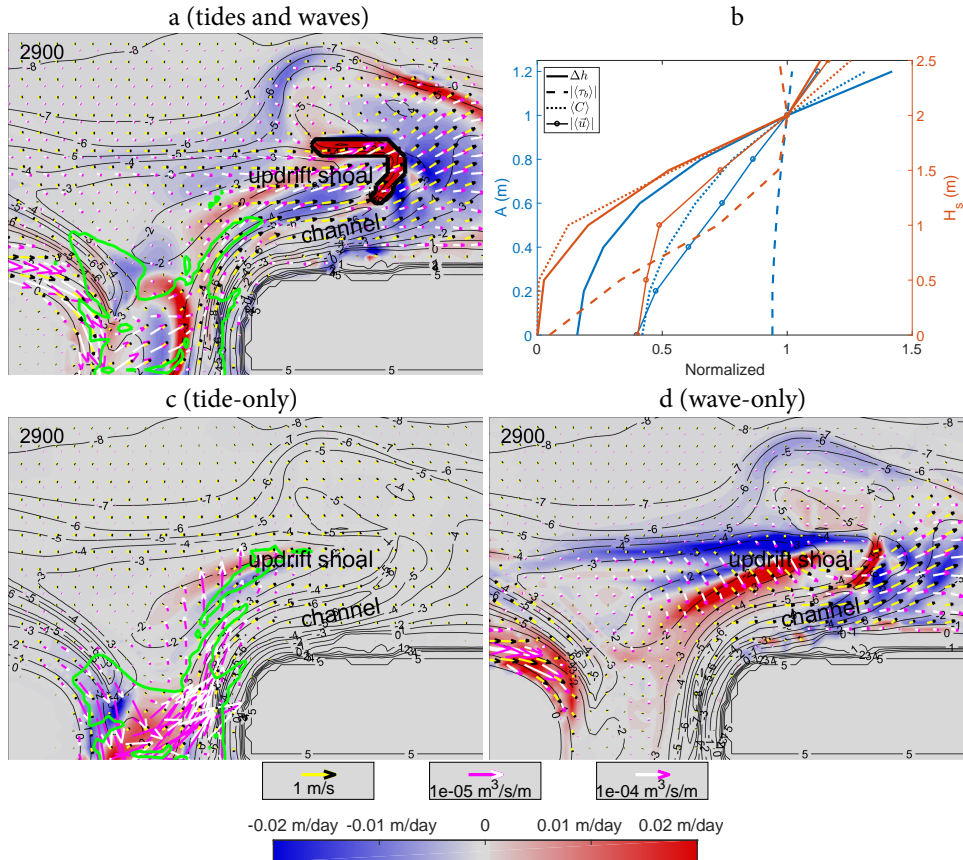


**Figure 3.7** (acd) As Figure 3.6acd, but after 2900 modeled days (during Phase 2) in the reference run. (b) For the area encircled by the thick black line in (a) the total erosion/deposition  $\Delta h$  (solid lines), tidally-averaged maximum bed shear stress  $|\langle \tau_b \rangle|$  (dashed lines), tidally-averaged sediment concentration  $\langle C \rangle$  (dotted lines) and mean flow magnitude  $|\langle \bar{u} \rangle|$  (solid lines with circles) as a function of tidal amplitude (blue) and wave height (orange). All values in (b) are divided by the value in the reference run. The shown area is 4 km (east-west direction) by 2.9 km (north-south).

### 3.3.2.2 Phase 2: Shoal growth

Relative to the other two phases, the changes in bed level during Phase 2 are less pronounced and occur on a longer time scale, i.e., Phase 2 takes almost half the period of the cycle. During this phase, the updrift shoal of the ebb-tidal delta continues its expansion in the eastward direction and the channel lengthens and continues its deflection.

Figure 3.7a shows sediment deposition on the eastern side of the updrift shoal (thick black contour). It can be seen that this sediment originates from both the inlet and the northern end of the updrift shoal. As during Phase 1, the mean flows are the main driver of the sediment transport in this area. However, in contrast to Phase 1, the mean flows over the updrift shoal during Phase 2 are parallel to the channel and increase in the eastward direction. How-

ever, the sediment concentration in the channel is lower than at the updrift shoal and, as a result, the magnitude of the sediment transport decreases in eastward direction. This gradient causes the delta expansion that characterizes this phase.

The wave-only erosion/deposition patterns (Figure 3.7d) are more quite similar to those of the reference run (tides+waves). However, the similarity is less pronounced than during Phase 1. Besides, in the wave-only run the direction of the mean flow over the updrift shoal is southeast rather than east, whereas in the tide-only run, the eastward increase in this flow was not found. Similar to the first phase, the main ebb channel deflects in the eastward direction in the wave-only run and in the westward direction in the tide-only run.

The relative importance of tides and waves during the eastward expansion of the shoal is quantified by further analysis of the sensitivity runs; the outcome is shown in Figure 3.7b. The analysis covers the shoal expansion area, defined as the eastern part of the updrift shoal in the reference run that has deposition rates exceeding 0.015 m/day (thick black contour in Figure 3.7a). For all sensitivity runs, total erosion/deposition (shoal growth rate)  $\Delta h$  was computed together with the tidally-averaged values of sediment concentration  $\langle C \rangle$ , mean flow magnitude  $|\langle \vec{u} \rangle|$  and combined bed shear stress  $|\langle \tau_b \rangle|$ . These values were normalized by dividing by the value in the reference run. Note that the magnitude of the combined bed shear stress includes the bed shear stress due to waves and is used a proxy for local sediment entrainment.

Four trends in Figure 3.7b are of interest. Firstly, the shoal growth rate (solid lines) increases with both larger tidal amplitudes and wave height. Secondly, when the tidal amplitude is reduced, the sediment concentration drops (blue dotted line), although the bed shear stress (blue dashed line) in this area is relatively unaffected. This suggests that the sediment concentrations in the reference run result from mean flows transporting sediment entrained at the updrift shoal eastward (sediment advection). Thirdly, reducing the tidal amplitude also weakens the mean flow magnitude (blue solid line with circles). As sediment concentrations peak at the updrift shoal, it is this change that decreases the sediment advection and concentrations. Fourthly, and last, the wave height directly affects the combined bed shear stress (orange dashed line) and the mean flow magnitude (orange solid line with circles). Therefore, both the local sediment entrainment and the sediment advection decreases for decreasing wave height and as a result, the sediment concentrations drop (orange dotted line). The combination of sediment entrainment and eastward mean flow that causes the shoal growth can therefore be explained by tides and waves operating simultaneously.

### **3.3.2.3 Phase 3: Channel breaching**

During Phase 3 a new channel is cut through the shoal updrift of the old rotated channel; subsequently, this new channel deepens as the old channel gradually fills up. This process is visible in the patterns of erosion/deposition: Figure 3.8a shows the breaching and Figure 3.9a the deepening. The new channel becomes the main channel at the end of the phase, bisecting the former updrift shoal.

In Figure 3.8a, it can be seen that the semi-diurnal flow velocities no longer peak in the channel when the breach occurs, but have maximum values at the updrift shoal. In fact, the erosion at this area occurs during the ebb phase of the tidal cycle. The currents transport the entrained sediment seaward creating a new ebb-shield. Here, a strong alongshore mean current causes eastward sediment transport. When the breached channel further deepens

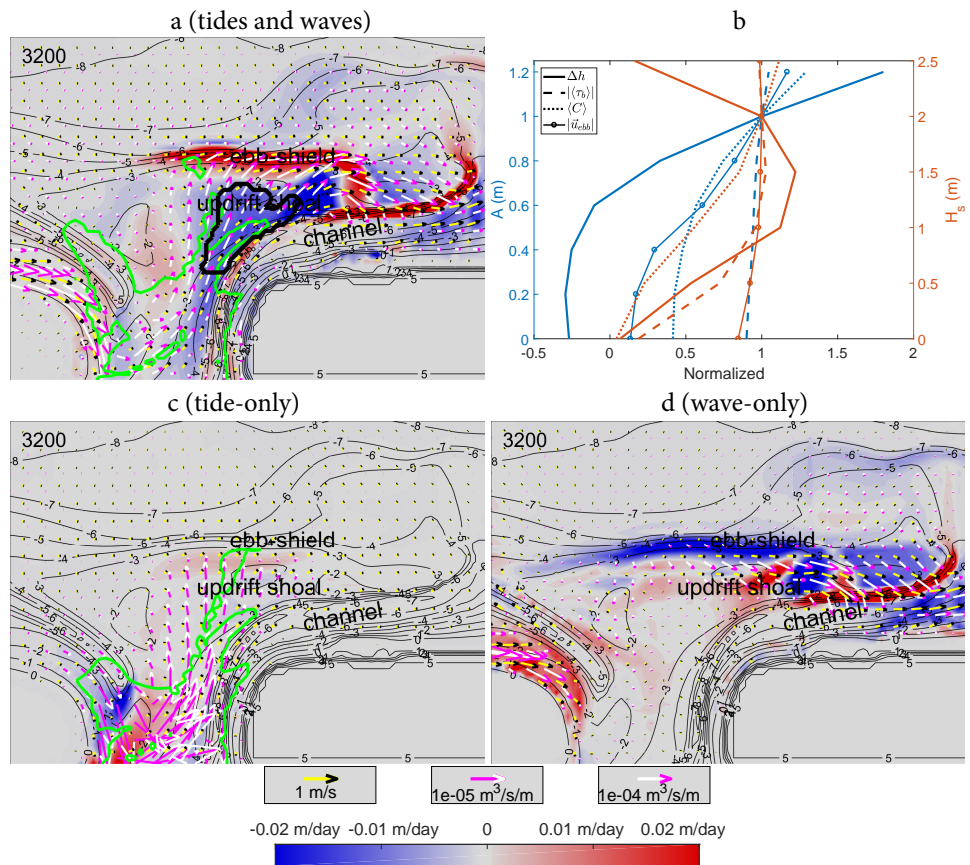


**Figure 3.8** (acd) As Figure 3.6acd, but after 3200 modeled days (transition Phase 2 to Phase 3) in the reference run. (b) For the area encircled by the thick black line in (a) the total erosion/deposition  $\Delta h$  (solid lines), tidally-averaged combined bed shear stress  $|\langle \tau_b \rangle|$  (dashed lines), tidally-averaged sediment concentration  $\langle C \rangle$  (dotted lines) and peak ebb flow velocity magnitude  $|\bar{u}_{ebb}|$  (solid lines with circles) as a function of tidal amplitude (blue) and wave height (orange). All values in (b) are divided by the value in the reference run. The shown area is 4 km (east-west direction) by 2.9 km (north-south).

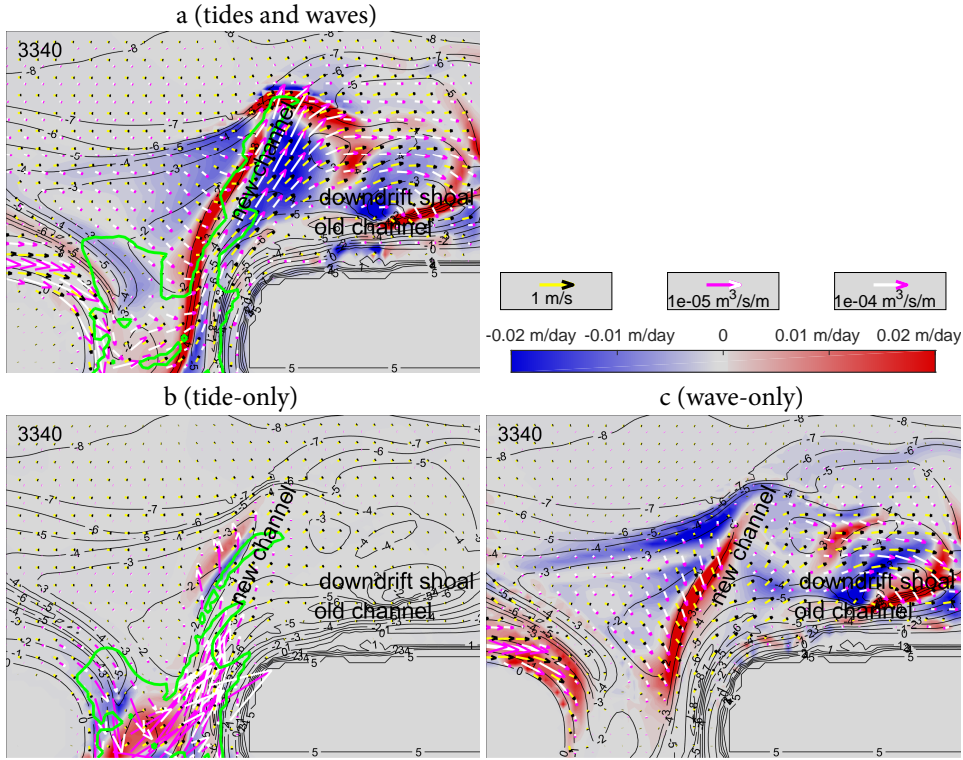


**Figure 3.9** As Figure 3.6acd, but after 3340 modeled days (during Phase 3). The shown area is 4 km (east-west direction) by 2.9 km (north-south).

(Figure 3.9a), the patterns of erosion-deposition, mean flows and sediment transport near the breach are similar to that of Phase 1 (compare Figure 3.9a and Figure 3.6a).

During the breach, the wave-only sensitivity run (Figure 3.8d) shows deposition instead of erosion at the part of the ebb-tidal delta that breaches in the reference run. Additionally, the location of the breach coincides with the area with largest semi-diurnal flow velocities both in the reference run and in the tide-only sensitivity run (Figures 3.8a&c). These two runs also have similar patterns of erosion/deposition and sediment transport, albeit with significantly lower magnitudes in the absence of waves.

The relative importance of tides and waves during the breach is quantified by an erosion rate in the breach area in the sensitivity runs. The breach area (thick black contour in Figure 3.8a) is defined as the part of the updrift shoal in the reference run that is both shallower than 3 m after 3200 days and deeper than 3.5 m after 3250 days. Figure 3.8b shows the erosion rate ( $\Delta h$ ) together with the tidally-averaged values of combined bed shear stress  $|\langle \tau_b \rangle|$  and sediment concentration  $\langle C \rangle$  and the magnitude of the peak ebb flow velocity  $|\bar{u}_{ebb}|$  divided by the values in the reference run.

Three trends arise from Figure 3.8b. Firstly, the erosion rate at the breach area (solid lines) increases with increasing tidal amplitude and is maximum for moderate wave heights. This erosion rate scales with both sediment concentration (dotted lines) and peak ebb flow ve-

locity (solid lines with circles). Secondly, it can be seen that higher waves increase the total bed shear stress in the breach area (orange dashed line) and thereby the sediment concentration (orange dotted line). Even for small waves ( $H_s = 0.5$  m), the erosion rate and the sediment concentration are more than five times larger than in the tide-only run. Therefore, even for similar  $|\vec{u}_{ebb}|$ -values, breaches are accelerated significantly by the wave-induced bed shear stress. However, the maximum erosion rate is found for moderate wave height because for  $H_s = 2.5$  m, the tidal flow is deflected in southeastern direction by relatively strong wave-induced forces. In this case, channel deflection continues and the breach is postponed. Thirdly, a small reduction in tidal amplitude ( $A = 0.8$  m) significantly reduced the erosion rate in the breach area (blue solid line), even for similar sediment concentrations (blue dotted line). Greater reduction in tidal range yields deposition instead of erosion because wave action transports more sediment towards this area than is being eroded by the weaker tidal flow (blue solid line with circles). Furthermore, for  $A = 1.2$  m, the erosion rate is almost twice the erosion rate in the reference run. We conclude (1) that the breaching of the ebb-tidal delta scales with the ebb flow velocity and (2) that the breach is significantly accelerated by the wave-induced sediment concentration. However, for too energetic wave conditions, the channel rotation continues, which shows the existence of and an optimum wave height for the opening of new channels.

Surprisingly, the tide-only sensitivity run (Figure 3.9b) does not show any subsequent deepening of the new channel or infilling of the old channel. However, the wave-only sensitivity run (Figure 3.9c) has infilling of the old channel with patterns of erosion/deposition, mean flows and sediment transport that are similar to the reference run (Figure 3.9a). Here, in both runs the downdrift shoal migrates to the downdrift island and deposits sediment in the old channel. These findings indicate that the infilling of the old channel is a wave-effect. However, deepening the new channel is not reproduced if waves or tides are not included and can thus only be explained by waves and tides operating simultaneously. In fact, it is the tidal flow that transports the sediment entrained by waves.

#### **3.3.2.4 Outer delta breaching**

The mechanisms that cause outer delta breaching are similar to that of ebb-tidal delta breaching. Here we will discuss the main differences.

During Phase 1, the channel deflection occurs further seaward and is negligible near the inlet. This shift can be explained by the larger ebb-tidal delta and smaller waves, which lose most of their energy before they reach the inlet area. Here, the sediment transported by the tidal currents in the channel is significantly reduced because waves do not stir sediment.

The growth of the updrift shoal during Phase 2 is more in the southeastern than in the eastward direction. The sediment transport from the inlet to the ebb-tidal delta is negligible. It is this difference that causes the relative growth of the southern side of the updrift shoal. In model run 2, the tides partly counteract this deposition (Figures 3.7c), whereas this was not found in model run 6.

The breaching (Phase 3) differs only in location and in lower sediment concentration. The latter can in turn be attributed to the difference in wave forcing.

#### **3.3.3 Time scale**

Table 3.2 shows that the period  $\overline{T_{shoal}}$  for ebb-tidal delta breaching increases with decreasing littoral drift. However, the variations in period within each model run ( $T_{shoal}$ ) and

**Table 3.2** Per model run the modeled littoral drift magnitude  $Q_{ld}$  (positive eastward), tidal prism  $P$ , type of modeled cyclic behavior, the periods between successive shoal attachments  $T_{shoal}$ , its average value  $\bar{T}_{shoal}$ , and the range over which the main channel rotates  $\Delta\theta$ . Only the model runs that feature cyclic channel-shoal dynamics (ETDB or ODB, see Table 3.1) are included here.

Run	$Q_{ld}$ ( $\text{Mm}^3/\text{year}$ )	$P$ ( $\text{Mm}^3$ )	$P/Q_{ld}$	Modeled behavior	$T_{shoal}$ (days)	$\bar{T}_{shoal}$ (days)	$\Delta\theta$ ( $^\circ$ )
1	1.10	53	48	ETDB	960 1100 860	973	37
2	0.90	55	61	ETDB	1020 780 1140	980	26
3	0.75	56	75	ETDB	1120 1040	1080	28
4	0.60	56	93	ETDB	1180 1300	1240	31
5	0.50	57	114	ETDB	1360 1100	1230	24
6	0.40	58	145	ODB	730 820 800	783	18
7	0.30	59	197	ODB	2520 2880	2700	19
$2_{90\%}$	0.90	50	56	ETDB	930 860 1050	947	27
$2_{80\%}$	0.90	45	50	ETDB	820 940 780 500	760	28
$2_{70\%}$	0.90	38	42	ETDB	870 520 920 810 470	718	38
$5_{80\%}$	0.50	47	94	ETDB	970 990	980	30
$6_{80\%}$	0.40	49	123	ODB	1680 1690	1685	22
$7_{80\%}$	0.30	50	167	ODB	2590	2590	19

amongst the runs are of the same magnitude. Surprisingly,  $\bar{T}_{shoal}$  drops between model runs 5 and 6 when the modeled cyclic behavior changes from ebb-tidal delta breaching to outer delta breaching. However, this drop did not occur for the transition between model runs  $5_{80\%}$  and  $6_{80\%}$ . Further reduction in littoral drift dramatically slows down the cyclic behavior, as can be seen by the large  $\bar{T}_{shoal}$  values for model runs 7 and  $7_{80\%}$ .

The values of  $\bar{T}_{shoal}$  for model runs 2,  $2_{90\%}$ ,  $2_{80\%}$  and  $2_{70\%}$  show a clear positive relationship with tidal prism. These model runs are equal in modeled behavior, tidal range, littoral drift and wave forcing and thus only vary in tidal prism. Therefore, our model abides by the known relationship between cycle period and tidal prism.

In Table 3.2,  $\Delta\theta$  is the range over which the channel rotates and breaches throughout the cycle (averaged over all cycles). It can be seen that  $\Delta\theta$  illustrates another difference between the two types of cyclic behavior:  $\Delta\theta \leq 22^\circ$  for outer delta breaching and  $\Delta\theta \geq 24^\circ$  for ebb-tidal delta breaching. Table 3.2 suggests that this value increases with littoral drift values, which could be because increased wave forcing causes more channel deflection before breaching. Furthermore,  $\Delta\theta$  tends to decrease with increasing tidal prism, illustrating that tides force the opening of the new channels.

## 3.4 Discussion

### 3.4.1 Comparison with real systems

Many ebb-tidal deltas have cyclic behavior very similar to that modeled in this study. For example, the conceptual model of FitzGerald (1988) was based on six barrier-coasts around the world including the coasts of: central South Carolina, Virginia, southern New Jersey, New

England, the East Frisian Islands (see also FitzGerald, 1984), and the Copper River Delta in Alaska. Our model setup does not represent any of these systems in particular. With that, our modeled behavior resembles the model depicted in Figure 3.1. Other examples of ebb-tidal deltas that feature channel deflection/breaching can be found along the coast of the Netherlands (Israel and Dunsbergen, 1999; Oost, 1995; Elias and van der Spek, 2006), New Zealand (Ford and Dickson, 2018), Ireland (O'Connor et al., 2011), South Portugal (Garel et al., 2014; Balouin et al., 2001) and the United Kingdom (Burningham and French, 2006).

The occurrence of channel deflection and cyclic behavior was first linked to tidal prism  $P$  and littoral drift  $Q_{ld}$  by Bruun and Gerritsen (1960). Based on observations, it was found that tidal systems with a ratio  $P/Q_{ld} > 300$  have a higher degree of channel stability. Inlets with  $P/Q_{ld} < 100$  were categorized as rather unstable and are usually characterized by one or more narrow, frequently shifting channels. In this study, we modeled ebb-tidal delta breaching for  $P/Q_{ld} < 120$ , stable channels for  $P/Q_{ld} > 250$  and outer delta breaching for intermediate values. Both ratios are indicated in Figure 3.10. This figure further shows the values obtained from model runs (blue markers) and those of Bruun and Gerritsen (1960) and Ridderinkhof et al. (2016a) (red). Furthermore, the red box indicates the tidal prisms of the cyclic ebb-tidal delta considered by Gaudiano and Kana (2001); for these systems, littoral drift values are unknown. Unfortunately, for most real systems there are no data regarding its type of cyclic behavior (ebb-tidal delta breaching, outer delta breaching or stable inlet processes, see

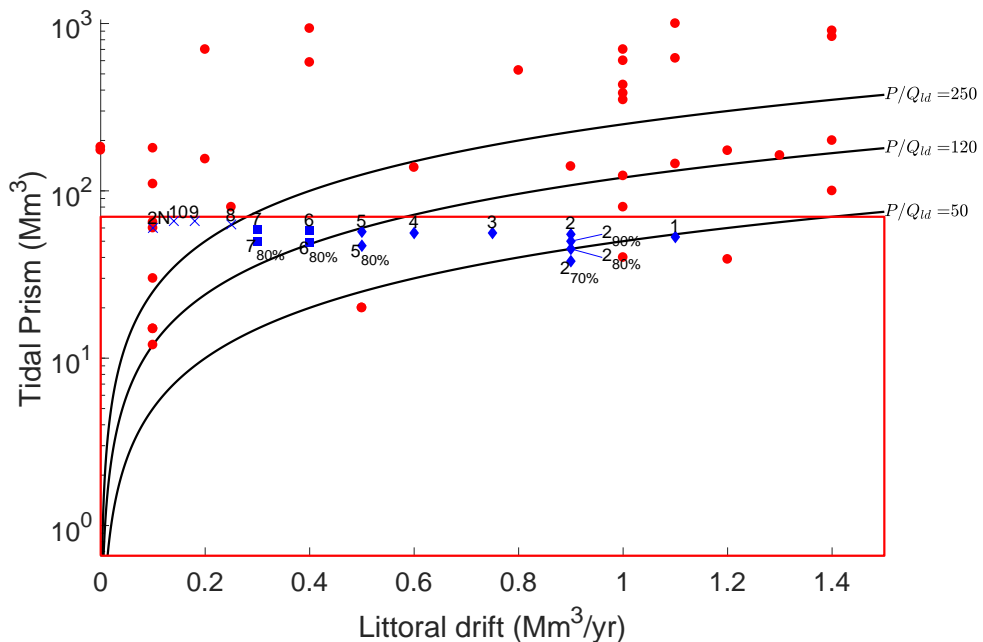


**Figure 3.10** Littoral drift  $Q_{ld}$  vs. tidal prism  $P$  for modeled and real tidal tidal systems. Blue: model runs with ebb-tidal delta breaching (diamond), outer delta breaching (square) and no cyclic behavior (cross). Red dots: data collected by Bruun and Gerritsen (1960) and Ridderinkhof et al. (2016a), see references herein; red box: ebb-tidal deltas considered by Gaudiano and Kana (2001) (littoral drift unknown).

Figure 3.1). However, they are all known to have periodic shoal attachment. Possibly, those with high ratios  $P/Q_{ld}$  feature stable inlet processes, i.e., shoal dynamics without channel deflection.

As can be seen, the modeled tidal prisms are in the lower range of real values and the model domain is therefore representative for relatively small tidal systems. In nature, these smaller systems have a shore-normal to downdrift channel orientation, and have periods between successive shoal attachments between 3 and 7 years (Ridderinkhof et al., 2016a; Gaudiano and Kana, 2001). The littoral drift values in our model simulations ranged from 0.1 to 1.1 Mm<sup>3</sup>/yr. Therefore, the ratio  $P/Q_{ld}$  in the model runs covered most of the observed range of the Wadden Sea and other barrier-coasts.

### 3.4.2 Mechanisms causing cyclic behavior

Both ebb-tidal delta breaching and outer delta breaching were reproduced successfully with the Delft3D/SWAN numerical model. Ebb-tidal delta breaching was found for the greatest littoral drift, outer delta breaching for moderate littoral drift values and no cyclic behavior occurred for small littoral drift. The channel rotation and shoal growth have been attributed to wave action and the subsequent formation of a new channel to tidal flow preferring a more updrift channel orientation (Sha, 1989). That is partly confirmed by this study. Sensitivity simulations showed that waves are necessary for shoals to form and migrate. However, we have shown that it is the combination of tides and waves (rather than waves alone) that cause the shoals to grow. Similarly, the breach is not only due tidal currents finding a new pathway over the shallow ebb-tidal delta. Although it is the strong peak ebb flow that transports the sediment seaward, most sediment is actually entrained by wave-induced bed shear stress. Sensitivity simulations showed that there exists an optimum wave height for the breach to occur.

Previous studies determined relevant physical mechanisms for only one of the phases (Cayocca, 2001; Bertin et al., 2009; Dastgheib, 2012; Nahon et al., 2012; Ridderinkhof et al., 2016b), but did not explain the full cycle of updrift shoal formation, channel deflection, delta breaching and shoal attachment. In accordance with Dastgheib (2012), ebb-tidal delta breaching was found here for wave-dominated boundary conditions and outer delta breaching for reduced wave forcing. Stable inlet processes including shoal formation were not reproduced in the present model runs with the lowest significant wave height, possibly because shoals in these conditions only form during storms (Ridderinkhof et al., 2016b).

In this chapter, shoal formation and migration were attributed to the wave-induced mean flows and sediment concentrations; the channel deflection was found to be a result of the shoal migration. This confirms the findings of Bertin et al. (2009), who also found shoal migration due to wave-induced mean flows. Furthermore, existing shoals in the model runs could grow because the tide- and wave-induced mean flows combined over the ebb-tidal delta. Continued channel deflection caused the semi-diurnal tidal flow to find a new pathway over the ebb-tidal delta. FitzGerald (1988) and Cayocca (2001) attributed the breaching of the ebb-tidal delta and the formation of a new channel solely to this change in tidal flow. However, we argue that waves also play an important role during this phase of the cyclic behavior. Incoming waves entrain the sediment that is transported from the ebb-tidal delta shoal by the ebb flow.

Cyclic import/export of sediment is an inherent feature of the modeled ebb-tidal delta breaching. These variations were explained by the effect of inlet bathymetry on the cross-

shore mean flow in the inlet (Ridderinkhof, 1988), similar to the findings of Chapter 2. However, significant cyclic changes in velocity asymmetry in the inlet were not modeled. In Chapter 2, cyclic velocity asymmetry was the result of the appearance and disappearance of a shallow secondary channel; however, in this study the position and depth of the secondary channel did not vary. The import/export was relatively steady for the modeled outer delta breaching because of the relatively stable inlet configuration.

It was unknown if there is a relationship between littoral drift and the period between successive shoal attachments. Our results (Table 3.2, runs 1 to 10) were obtained with no variations in tidal forcing and geometry amongst the model runs and therefore allowed for identification of such a relationship. It can be seen that the typical time scale increased with decreasing littoral drift. The period dropped when the modeled behavior changed between model runs 5 and 6. However, this drop was not reproduced for model runs with smaller basins. Eventually, the cyclic channel-shoal dynamics slowed down drastically with decreasing littoral drift and eventually came to a stop.

As stated in Section 3.4.1, the model geometry is representable for a small tidal inlet system. However, many ebb-tidal deltas with periodic channel deflection and breaching are seaward of tidal basins with a tidal prism one order of magnitude larger. Sometimes, this includes the alternation between a one- and two-channel inlet configuration (Israel and Dunsbergen, 1999; Oost, 1995). Furthermore, ebb-tidal deltas and their natural cyclic behavior are influenced by dam construction in the basin and relative sea-level rise; ebb-tidal delta nourishments as a mitigation route have been proposed (Elias et al., 2012). The question of what the effects of larger basins, basin size reduction, relative sea-level rise and ebb-tidal delta nourishments on the cyclic behavior are must be answered by future studies. Ongoing research aims to elucidate these unknowns.

### 3.4.3 Shortcomings

Ridderinkhof et al. (2016b) reported that wave skewness was essential for coherent shoal migration; however, in this study shoals do migrate coherently with a reduced wave-related bed load transport factor ( $BedW = 0.3$ ), whereas Ridderinkhof et al. (2016b) used  $BedW = 1$ . As a result of the reduced  $BedW$ , the migration speed of the downdrift shoal to the downdrift coast due to wave skewness might have been underestimated. Test runs with higher values for  $BedW$  showed unrealistic shoreface steepening and coastal expansion which also had the effect of reducing the littoral drift. Both the steepening of the coastal profile and the decline in sediment provided to the ebb-tidal delta caused substantial differences between two consecutive cycles of modeled channel-shoal dynamics. Enabling bed load transport due to the undertow (as in Ridderinkhof et al., 2016b) mitigated the unwanted coastal profile development, but did not yield a stable littoral drift in time. Furthermore, in this undertow formulation the Stokes drift is compensated locally rather than allowing for a circulation over and around the shoal as described by Bertin et al. (2009); this had the effect of counteracting the shoal migration by mean flows. There is a clear need for improved parametrization of the intra-wave near-bed horizontal velocities and associated sediment transport in numerical area models (2DH) in general (Boechat Albernaz et al., 2019).

The volume of the ebb-tidal delta has been calculated by taking the volume above the no-inlet bathymetry (see Section 3.2.5). Here, this volume did not include the negative volumes of the channels. Also, this reference bathymetry was updated throughout the model runs. Because shoal attachment on the downdrift coast changed its profile, this directly affected

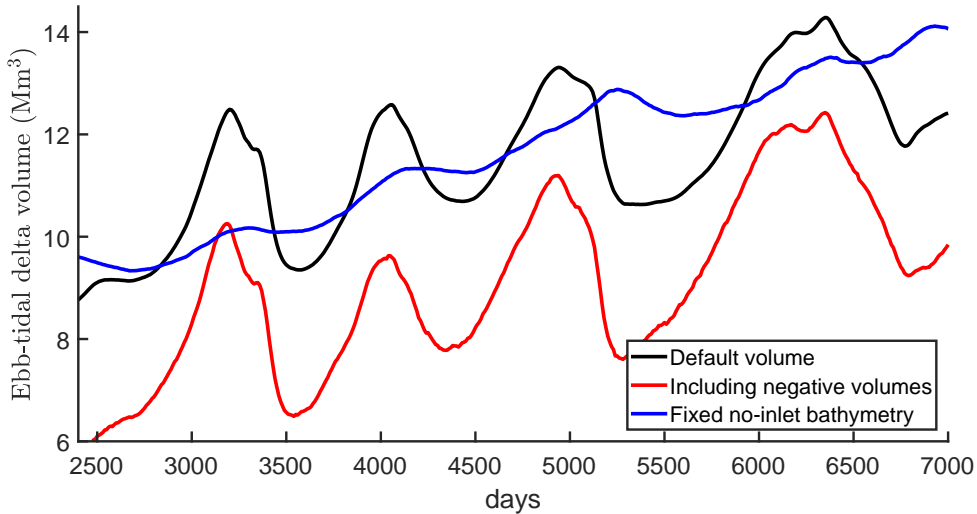


**Figure 3.11** The volume of the ebb-tidal delta for model run 2 computed as described in Section 3.2.5 (black, as Figure 3.4), when the negative volumes are included (red) and when the no-inlet bathymetry was fixed (blue).

the computed volume. Sensitivity analysis was performed to test how (1) a fixed reference bathymetry and (2) negative volumes would affect the computed volume. The outcome for model run 2 can be seen in Figure 3.11 and shows that including the negative volume has little effect on the temporal variations. However, these variations are reduced for a fixed no-inlet bathymetry. This is because the fixed no-inlet bathymetry does not adapt to the coastal expansion when a shoal merges with the downdrift island. As a result, the part of each attached shoal below mean sea level is still part of the ebb-tidal delta volume. Nevertheless, the volume eventually decreases as the sediment is distributed over the downdrift island, yielding similar (albeit reduced) periodic behavior. Since updating the no-inlet bathymetry better represents the attachment of the shoal, this method was preferred in this study.

In this study, a simplified idealized model setup was chosen and several processes were ignored. Firstly, time-varying wave forcing was not considered. As shown by Ridderinkhof et al. (2016b), waves associated with storm conditions can also induce shoal formation and growth of existing shoals. Therefore, including storms in time-varying wave boundary conditions could be crucial to represent stable inlet processes. However, the focus of this study was the development of shoals on the updrift side of the ebb-tidal delta. Secondly, the use of a single grain size of 250  $\mu\text{m}$  limited the sediment pathways on the ebb-tidal delta. Herring and Winter (2018) showed that shoal formation and migration is the preferred pathway for this sediment size at a mixed-energy tidal inlet. However, finer sediment (125  $\mu\text{m}$ ) mainly bypasses the inlet at the seaward limit of the ebb-tidal delta whereas coarser sediment (375  $\mu\text{m}$ ) is mostly circulated between inlet throat, main channel and downdrift shoal. The effect of multiple grain sizes on the modeled cyclic behavior is unknown, but was beyond the scope of this study.

### 3.5 Conclusions

This study has identified the mechanisms of cyclic ebb-tidal delta behavior and associated time scales of channel deflection, the formation of a new channel via breaching and the periodic development of a large sandy shoals that attach to downdrift barrier islands. Using Delft3D/SWAN, ebb-tidal delta breaching was successfully modeled for relatively low ratio tidal prism/littoral drift (<120), outer delta breaching for intermediate ratios (roughly between 120 and 200) and no periodic behavior for tidal prism/littoral drift above 250.

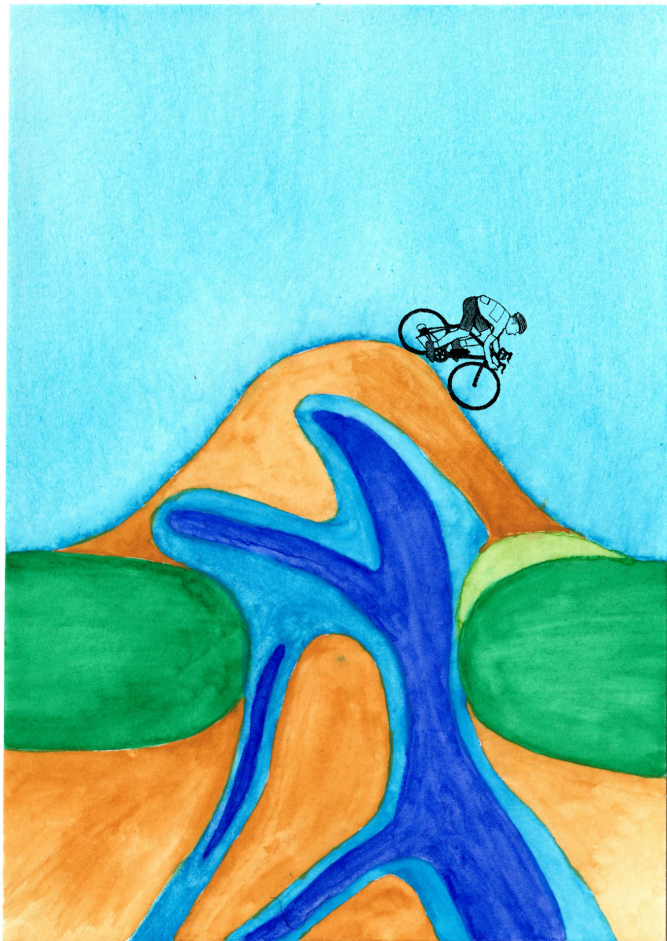
We show that the relative roles of tides and waves change throughout the phases of the cyclic channel-shoal dynamics. Our results conform that channel deflection is a wave-driven process. Although shoal formation and migration is a wave effect, it is the combined effect of tides and waves that causes shoal growth. Interestingly, even though tidal currents cause the ebb-tidal delta channel to breach, we have identified a optimum wave height for accelerating this process by making the sediment available for transport. For smaller waves, not enough sediment is entrained, whereas for larger waves channel deflection continues and the breaching process is postponed.

Our results also showed that the typical time scale generally increases with decreasing littoral drift and increasing tidal prism. Furthermore, we show that cyclic variations in mean flows and sediment transport through the inlet and in ebb-tidal delta volume are linked to the cyclic behavior.

Many ebb-tidal deltas have channel-shoal migration and periodic breaching of the ebb-tidal delta. Because this study identifies and quantitatively evaluates the physical processes, the outcomes contribute to our understanding of the long-term morphodynamics of natural tidal inlets.

### Acknowledgements

We would like to thank B.G. Ruessink and J.A. Lenstra for critical reading. The authors thank the three anonymous reviewers and the journal editors for their helpful suggestions and valuable criticism. Funded by the Netherlands Organisation for Scientific Research (NWO) (project 869.15.009). The modeled data are available from Lenstra et al. (2019) and can be found at <https://doi.org/10.5281/zenodo.2613407>.



## **Chapter 4 | The impact of sea-level rise and basin area reduction on the cyclic behavior of tidal inlet systems**

### **Abstract**

Ebb-tidal deltas filter incoming wave energy and mitigate erosion of basins and coasts by temporarily providing sediment. In many systems, these coastal safety functions are under threat from human activities. The effects of, for example, relative sea-level rise and changes in basin area on the long-term dynamics of ebb-tidal deltas are unknown. Here we use Delft3D/SWAN with an idealized model setup to assess these effects. The results show that the time scales of the cyclic channel-shoal dynamics of ebb-tidal deltas are affected. An instantaneous decrease in basin area slows down the cyclic behavior during the initial adjustment period. The duration of the adjustment period increases with basin area reduction. Especially the growth of the shoal reduces as a result of smaller tidal flow velocities. After the adjustment, smaller basins have shorter time scales. This is linked to a relative decrease in ebb-tidal delta volume and tidal prism. Despite this erosion, the wave height in the inlet decreases. Moreover, we find that the effects of relative sea-level rise depend on the rate of rising water levels. For relatively low rates, the period of the cycles eventually shortens, whereas higher rates can cause longer periods. The volume of ebb-tidal deltas appears to be unaffected by relative sea-level rise; but because the average water depth increases, more energetic waves reach the basin.

### **In preparation for submission:**

Klaas J.H. Lenstra and Maarten van der Vegt, The impact of sea-level rise and basin area reduction on the cyclic behavior of tidal inlet systems.

## 4.1 Introduction

During the last century, anthropogenic activities have disrupted the natural dynamics at many barrier island systems (Stutz and Pilkey, 2005). Human-induced disruptions can be direct (e.g. nourishments, channel dredging, jetty/dike construction) or indirect (climate change, relative sea-level rise). As a result, in the Dutch Wadden Sea, roughly 600 million m<sup>3</sup> of sediment has been deposited in the basin area since 1935, which is linked to erosion of the ebb-tidal deltas (~450 million m<sup>3</sup>, Elias et al., 2012). This poses problems for coastal safety for two reasons. Firstly, eroding ebb-tidal deltas lose their ability to absorb wave energy propagating to the coasts and basins (Hansen et al., 2013). Secondly, less sediment is available to balance local erosion of the islands and intertidal areas. Part of the deposition in the Dutch Wadden Sea is believed to be caused by relative sea-level rise (Van der Spek, 2018; Wang et al., 2018). Moreover, the closure of the Zuiderzee and the Lauwerszee resulted in additional sediment import to these basins (Ridderinkhof et al., 2014b).

Observations show that, at many tidal inlets, also the alongshore sediment bypassing changed significantly due to changes in basin area (Biegel and Hoekstra, 1995; Van de Kreeke, 2006; Ridderinkhof et al., 2016a). For the Dutch Wadden Sea, most of the sediment is bypassed through periodic shoal formation, migration and shore attachment accompanied by channel deflection and breaching (e.g. FitzGerald, 1982). Oost (1995) observed that initially the cyclic behavior had stopped at the Frisian Inlet system after the closure of the Lauwerszee. Because approximately 30% of the surface area of the basin area was closed off, the surplus in ebb-tidal delta sediment formed a substantial shoal, which eventually attached to the downdrift Schiermonnikoog island (Elias et al., 2012). In contrast, channel deflection and breaching were no longer observed on the ebb-tidal delta. Ridderinkhof et al. (2016a) observed the formation and migration of a second shoal from 2005 onwards. Elias et al. (2012) subsequently suggested that eventually a cyclic development as observed prior to the closure will reappear. However, the time scale of adjustment remains unknown. Furthermore, it is unclear how this cyclic behavior will differ and how the period between successive shoals will change. Because this period positively correlates with tidal prism (Gaudiano and Kana, 2001; Ridderinkhof et al., 2016a), the smaller ebb-tidal delta and reduced tidal prism render it likely that shoals of smaller volume will attach more frequently and merge closer to the inlet. Also for the nearby Texel and Vlie inlets it remains unclear how the time scale of the cyclic channel-shoal dynamics changed by the closure of the Zuiderzee in 1931. The natural variability in this period and the effects of relative sea-level rise makes it difficult to isolate the effect of the basin reduction in these observations or to quantify the adjustment time scale.

Furthermore, the dynamics of tidal inlet systems are also affected by relative sea-level rise (e.g. Dissanayake et al., 2009; Becherer et al., 2018; Vermeersen et al., 2018). Rising mean levels increased the volume of sediment accommodation space and generated additional sediment import through the inlets in the Wadden Sea (Elias et al., 2012; Van der Spek, 2018). Because especially the shoal formation and growth depends on this sediment exchange between basin and ebb-tidal delta (Chapter 3), relative sea-level rise is likely to result in longer time scales for the cyclic behavior of ebb-tidal deltas. Moreover, if the sediment import is insufficient to let the intertidal flats accrete (drowning of basins, see Wang et al., 2018), changes in tidal prism and tidal wave characteristics are expected (Ridderinkhof et al., 2014b). It is unknown how the dynamics of ebb-tidal deltas respond to the sea-level-rise-induced changes in sediment import and basin morphology.

Although this study is motivated by the observations and studies covering the Dutch Wadden Sea, its outcomes are not anticipated to be limited to this area. Not only is relative sea-level rise a worldwide phenomenon, but also are there many examples of basin reduction. For example, there has been land reclamation or dike construction in tidal basins in the USA (Hansen et al., 2013; Beck and Kraus, 2011), China (Wang et al., 2014), Australia (Sennes et al., 2007) and Italy (Rizzetto et al., 2009). FitzGerald et al. (1984) showed that poldering behind the barrier islands and along the mainland have reduced the basin areas of the East Frisian inlets (Germany) between 1650 and 1960 by 149 km<sup>2</sup>, which is roughly 30% of their original drainage area.

Here, we aim to elucidate how the natural volume and cyclic behavior of an ebb-tidal delta are affected by (1) an instantaneous reduction in basin size and tidal prism and (2) different rates of relative sea-level rise. These questions are addressed using an idealized geometry and simplified forcing in Delft3D/SWAN (Section 4.2), where we studied the morphodynamics of ebb-tidal deltas for a wide range of basin size reductions and rates of relative sea-level rise. The outcome will be compared in Section 4.3 with undisturbed model simulations (constant basin size and mean sea level) with clear patterns of channel-shoal dynamics (Chapter 3). The discussion and conclusions are presented in Sections 4.4 and 4.5, respectively.

## 4.2 Material and methods

The numerical model Delft3D for hydrodynamics, sediment transport and bed level updates (Lesser et al., 2004; Deltares, 2014), coupled with the wave model SWAN (Booij et al., 1999; Ris et al., 1999; Holthuijsen, 2010), was used to investigate the effect of different disturbances on the cyclic behavior of ebb-tidal deltas. Using an idealized geometry and simplified forcing, we studied the disturbed morphodynamic evolution of ebb-tidal deltas for several basin size reductions and relative sea-level rise rates. The results were compared with undisturbed reference model simulations with constant basin size and mean water level with clear patterns of channel-shoal dynamics resembling those observed in tidal inlet systems. The domains and settings used here are identical to those described in Chapter 3. A brief description of the model setup, forcing and new aspects are provided below; however, for complete details the reader is referred to Chapter 3.

### 4.2.1 Model domains and settings

The Delft3D flow module solves the depth-averaged shallow water equations (conservation of mass and momentum balance) to calculate flow velocities and water levels. The rectangular model domain consists of one inlet connecting the open sea to the tidal basin. Figure 4.1 shows the basin and the area of interest (inlet and ebb-tidal delta). The domain is divided into eight two-way coupled domains (domain decomposition) with grid resolutions of 1/50 m<sup>-1</sup> for the area of interest, 1/150 m<sup>-1</sup> for the tidal basin and 1/450 m<sup>-1</sup> for the outer sea. The hydrodynamic model was coupled to the third-generation phase-averaged spectral wave model SWAN (coupling time of 60 minutes), which solves the wave action balance equation. The wave domain consists of three nested grids with decreasing grid resolutions of 1/1350 m<sup>-1</sup> (east-west extension to avoid shadowing effects), 1/450 m<sup>-1</sup> (Delft3D domain) and 1/50 m<sup>-1</sup> (area of interest). Sediment transport within the flow domains was calculated using the Van Rijn et al. (2004) transport equations with the suspended and bedload transport computed independently. Hereafter, the sum of both types is referred to as sediment

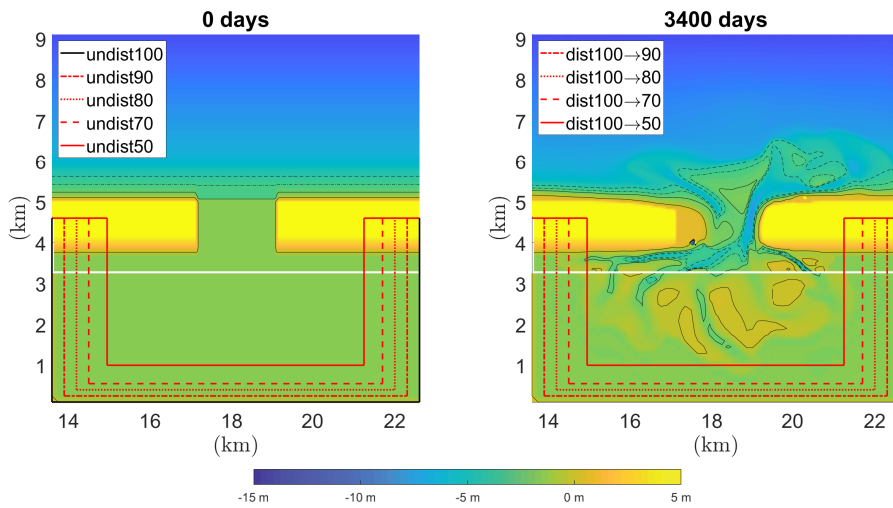


**Figure 4.1** Starting bathymetries for the undisturbed (left) and disturbed (right) runs. The white line indicates the coupling of the high-resolution domain (grid size 50 m) and the low-resolution domain (150 m). The red lines indicate the areas that were removed from the model domain for the simulations with a reduction in basin area.

transport. A single sediment fraction with a  $d_{50}$  of  $250 \mu\text{m}$  was used in all domains. Computed bed level changes were calculated from gradients in sediment transport and sediment settling/entrainment using a morphological acceleration factor  $M = 20$  to reduce computation time. The hydrodynamic boundary conditions consisted of semi-diurnal tides (amplitude 1 m and period 12 hours) and waves coming from the northwest (origin  $335^\circ$  clockwise with respect to the north). The significant wave height and peak period for all model runs were 2.0 m and 7.5 s, respectively. These settings were motivated by the obtained tidal prism and littoral drift values, which are suitable for modeling cyclic behavior (Chapter 3).

#### 4.2.2 Model simulations

The model runs presented in this chapter include both undisturbed reference model simulations and disturbed simulations with basin size reductions or relative sea-level rise. An overview of all simulations is shown in Table 4.1; the initial bathymetries are shown in Figure 4.1. The reference simulation *undis100* is the 1 m tidal amplitude and 2 m significant wave height model run as described in Chapter 3 (run 2). This model run has clear cyclic channel-shoal dynamics similar to the ebb-tidal delta breaching model of FitzGerald, 1988. The other undisturbed runs initially only differ in basin surface area, as indicated by the red lines in Figure 4.1. The reference runs *undis90*, *undis80*, *undis70* and *undis50* have 90%, 80%, 70% and 50% of the  $31.5 \text{ km}^2$  basin surface area from *undis100*, respectively. Amongst these runs, the width/length-ratio of the basin was kept constant; test runs show that only reducing the width or the length yielded similar cyclic behavior.

For the disturbed runs, the bathymetries obtained after 3000 (for relative sea-level rise) or 3400 modeled days (for basin size reduction) in *undis100* were used as a starting bathymetry. To test the effect of basin size reduction, part of the basin size area was instantaneous removed

**Table 4.1** Overview of conducted model runs. Basin area is relative to 9 km by 3.5 km in the alongshore and cross-shore direction, respectively.

Run	Basin area	sea-level rise	Initial bathymetry
<b><i>undist100</i></b>	100%	o	no ebb-tidal delta
<b><i>undist90</i></b>	90%	o	no ebb-tidal delta
<b><i>undist80</i></b>	80%	o	no ebb-tidal delta
<b><i>undist70</i></b>	70%	o	no ebb-tidal delta
<b><i>undist50</i></b>	50%	o	no ebb-tidal delta
<b><i>dist100→90</i></b>	90%	o	<i>undis100</i> after 3400 days
<b><i>dist100→80</i></b>	80%	o	<i>undis100</i> after 3400 days
<b><i>dist100→70</i></b>	70%	o	<i>undis100</i> after 3400 days
<b><i>dist100→50</i></b>	50%	o	<i>undis100</i> after 3400 days
<b><i>slr50</i></b>	100%	0.5 cm/yr	<i>undis100</i> after 3000 days
<b><i>slr100</i></b>	100%	1 cm/yr	<i>undis100</i> after 3000 days
<b><i>slr150</i></b>	100%	1.5 cm/yr	<i>undis100</i> after 3000 days
<b><i>slr200</i></b>	100%	2 cm/yr	<i>undis100</i> after 3000 days

from the model domain after 3400 days, i.e., directly after the breaching phase of the cyclic behavior. Test runs with the basin area reduction after 3000 days (during the shoal growth phase) instead of 3400 days yielded similar results with respect to changes in cyclic behavior, time scale and adaptation. The basin area reduction was either 10% (*dist100→90*), 20% (*dist100→80*), 30% (*dist100→70*) or 50% (*dist100→50*). Their outcome was compared to the undisturbed runs; for example, *dist100→70* was compared to both *undis100* and *undis70*.

To study how cyclic behavior of ebb-tidal deltas is affected by rising mean sea level, model runs were conducted with constant rates of rising sea level, ranging from 0.5 to 2 cm/year with 0.5 cm/year increments. These rates were based on Vermeersen et al. (2018), who projected rates for relative sea-level rise in 2100 for the Dutch Wadden Sea ranging from 0.22 to 1.83 cm/year. These disturbed model runs, with rising subtidal water level after 3000 days, are denoted as *slr50*, *slr100*, *slr150* and *slr200* for a rise in mean sea level per century of 50 cm, 100 m, 150 cm and 200 cm, respectively. Their outcomes were compared to the undisturbed run with equal basin area (*undis100*). Test runs showed that outcomes were not sensitive to the initial bathymetry, i.e., increasing the mean sea level after 3400 instead of 3000 days.

#### 4.2.3 Model analysis

For each model run, we analyzed and compared the:

- time scale of the cyclic behavior. For this, the period between successive breaching events ( $T_{breach}$ ) was used. The ebb-tidal delta was said to breach when a new channel splits the 3.5 m isobath into an updrift and a downdrift part;
- cross-sectional area of the inlet (CSA). For the runs with rising mean sea level, the area below the subtidal water level was computed;
- the volume of the ebb-tidal delta ( $V_{ETD}$ ), obtained by summation of the difference between the modeled and an no-inlet bathymetry multiplied by the grid cell area. Following Dean and Walton (1975), the no-inlet bathymetry was constructed based on the cross-shore profile at both sides of the inlet. Only the positive values were taken into account, i.e., channels were not considered to be negative volume. Furthermore,

the barrier islands were removed from the analysis by neglecting values above mean sea level.

- the orientation of the main channel, defined as the angle between the last and first grid point of the path of the main channel path with respect to the north (positive in clockwise direction). This path was determined in the following iterative way. Starting at the deepest grid cell in the inlet, the next point of the main channel was the deepest grid cell that was both within 100 m of the previous point and further seaward from the inlet than the previous point. The end of the channel was reached either when the deepest point was above the 3.5 m isobath or when this point was more than 2000 m from the start of the channel (as in Chapter 3);
- tidal prism ( $P$ ), i.e., the volume of water entering and leaving the basin each tidal cycle;
- mean flow and semi-diurnal flow amplitude at all locations. For this, harmonic analysis was used;
- significant wave height (tidally-averaged);
- cumulative sediment transport values through the inlet, i.e., net import/export;
- cumulative sediment transport along the updrift and downdrift coast;
- shoal growth rate ( $\Delta h_s$ ), defined as the total deposition per time unit in the area that has deposition exceeding 0.015 m/day (as in Chapter 3);
- breaching rate ( $\Delta h_b$ ), defined as the average erosion per time unit in the part of the ebb-tidal delta that (1) is shallower than 3.5 m and (2) has erosion exceeding 0.006 m/day;

As discussed in Chapter 3, the volume of the ebb-tidal delta greatly depends on the no-inlet bathymetry. In that study, the no-inlet bathymetry was reconstructed after each tidal cycle because it better represented the formation and attachment of each shoals. Here, this procedure would lead to different no-inlet bathymetries for the different runs, which complicates the comparison between the undisturbed and disturbed runs. Therefore, here we opted for a fixed no-inlet bathymetry based on the 3400 days starting bathymetry (Figure 4.1). Alternative fixed no-inlet bathymetries yielded similar results.

## 4.3 Results

### 4.3.1 Undisturbed model runs

In each undisturbed run, several cycles of channel rotation and breaching, development of a shoal and its subsequent migration and attachment to the downdrift island were modeled. Table 4.2 shows the time scales ( $T_{breach}$ ), tidal prism ( $P$ ), ebb-tidal delta volume ( $V_{ETD}$ ) and cross-sectional area (CSA) for each simulation. Note that the parameters  $P$ ,  $V_{ETD}$  and CSA were averaged over the first two cycles of the model run, because they depend on the phase of the cyclic behavior.

The modeled cyclic behavior has three characterizing phases, each with a distinct relative importance of tides and waves (see Chapter 3). During Phase 1, the channel rotates in the clockwise direction; the rotation rate scales with significant wave height and is relatively unaffected by tidal flow. Subsequently, the shoal grows in the downdrift direction during Phase 2. During this phase, wave-induced sediment concentrations are advected by a combined wave- and tide-induced mean flow. The sediment concentration is significantly reduced at the downdrift side of the ebb-tidal delta, as this part is partly sheltered from incoming wave energy by the ebb-tidal delta platform. It is this gradient that causes the shoal to

**Table 4.2** Overview of model output for undisturbed runs with periods between successive breaches ( $T_{breach}$ ) and its average value ( $\overline{T_{breach}}$ ). The values for  $P$  (tidal prism),  $V_{ETD}$  (ebb-tidal delta volume) and CSA (cross-sectional area) are averaged over the first two cycles of cyclic behavior.

Run	$T_{breach}$ (days)	$\overline{T_{breach}}$ (days)	$P$ (Mm <sup>3</sup> )	$V_{ETD}$ (Mm <sup>3</sup> )	CSA (m <sup>2</sup> )
<b>undist100</b>	760, 1160, 1700, 1500, 1350	1294	55	11	4000
<b>undist90</b>	1010, 850, 1050	970	50	10.5	3600
<b>undist80</b>	1000, 1100, 700, 500, 700	800	45	9.7	3300
<b>undist70</b>	350, 750, 350, 750, 800, 950	658	38	9	2800
<b>undist50</b>	350, 400, 650, 450	463	30	7.5	2000

grow and migrate. During Phase 3, a new channel breaches the ebb-tidal delta. The erosion rate scales with peak ebb-flow and local sediment upwelling by waves. However, for large ratios between wave height and tidal flow, the channel rotation continues and the breach is postponed.

Even though the undisturbed runs yield a type of cyclic behavior similar to each other, several differences arise. Firstly, as can be seen from the average periods ( $\overline{T_{breach}}$ ), smaller basins have shorter time scales. Secondly, Table 4.2 indicates that the volume of the ebb-tidal delta and the cross-sectional area of the inlet also depend on the basin surface area. This is because they both scale with tidal prism.

#### 4.3.2 Reduced basin area

The cyclic channel-shoal dynamics continue for the model runs with a reduction in basin area after 3400 days, albeit with noticeable differences. The first difference is in the modeled magnitudes of mean and semi-diurnal flow in the inlet (shown in Figure 4.2). These time-dependent values are the maximum value across the tidal inlet. Both values are initially but

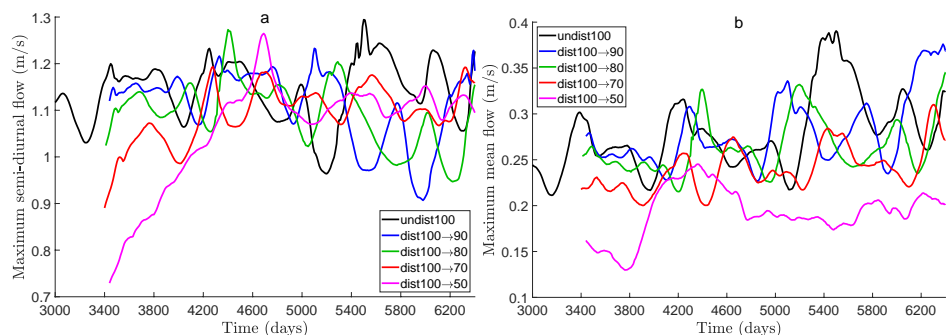


**Figure 4.2** For *undist100* and the reduced basin runs the maximum value in the inlet of the (a) semi-diurnal flow amplitude and (b) mean flow magnitude.

temporarily lowered by the reduction in basin area and tidal prism (Table 4.3), especially the semi-diurnal flow velocities. The effect of the smaller flow velocities in the inlet on the balance between sediment deposition by wave-driven littoral drift and sediment erosion by tidal currents can be seen in Figure 4.3a: in response to smaller flow velocities in the inlet, its cross-sectional area gradually becomes smaller. A new equilibrium is obtained, which brings the semi-diurnal flow velocities close to their original values (Figure 4.2a). Table 4.3 shows that the corresponding values for tidal prism are roughly equal to those in the undisturbed run with equal basin area in Table 4.2 (e.g.  $dist100 \rightarrow 70$  and  $undis70$ ).

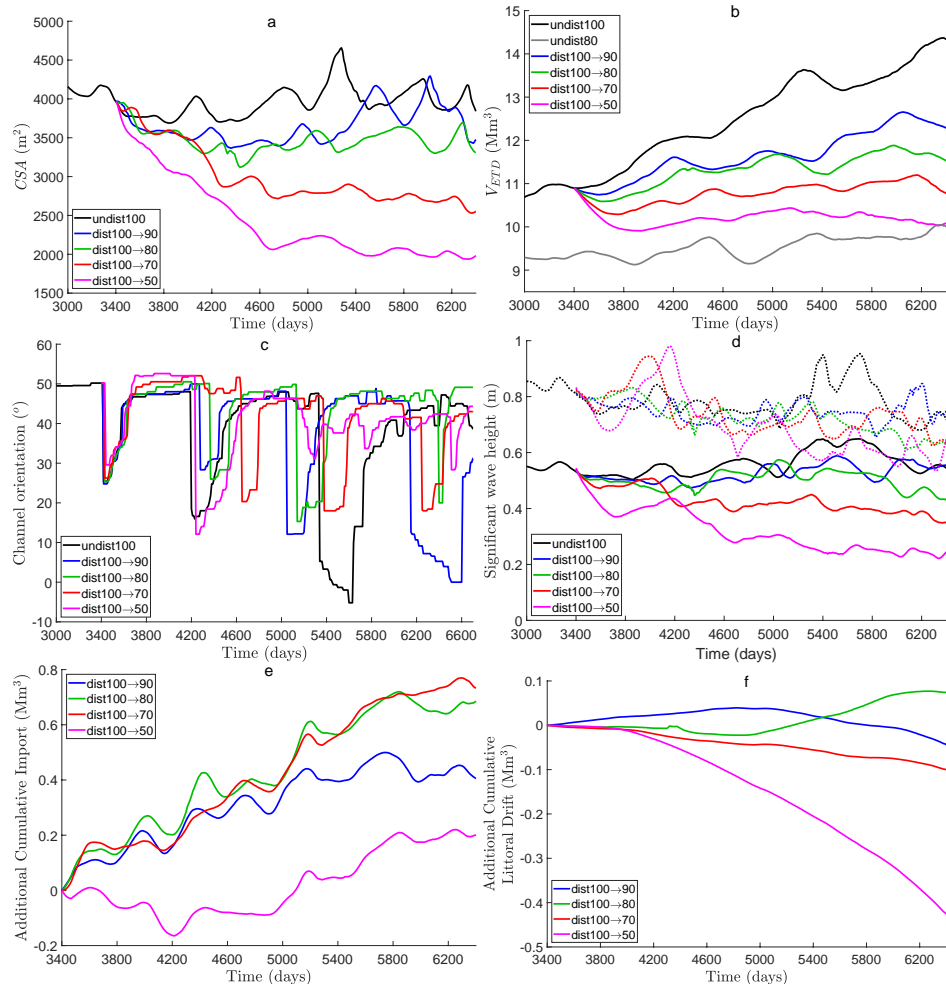


**Figure 4.3** For the reduced basin runs (a) cross-sectional area of the inlet, (b) volume of the ebb-tidal delta, (c) the orientation of the main channel, (d) the average (solid lines) and maximum (dotted) significant wave height in the inlet, (e) additional cumulative sediment import, and (f) additional cumulative littoral drift along the downdrift coast.

Figure 4.2 and Figure 4.3a show that a new equilibrium was obtained after the initial adjustment period. The adjustment time scale  $T$  was obtained from the exponential fit of the cross-sectional area of the inlet as  $CSA(t) = CSA_{new} + (CSA_{old} - CSA_{new}) \cdot exp(-t/T)$  with  $t$  the number of modeled days since the basin reduction. For a 50% basin size reduction, the adjustment time scale is 1296 days. For 10%, 20% and 30% basin area reduction,  $T$  is 185, 343 and 772 days, corresponding roughly to 14%, 26%, and 60% of the typical time scale of undisturbed cyclic behavior, respectively. This means that the period of adjustment increases with increasing basin reduction.

Table 4.3 also shows that the effect of the basin reduction on the periods between successive breaches before and after the initial adjustment period differs. Note that there is considerable variability of  $T_{breach}$  within each model run (both undisturbed and disturbed). However, relating the periods in the disturbed runs to those in the reference runs, does consistently show the following two effects. Firstly, the cyclic channel-shoal dynamics are initially slowed down by the change in basin size area and tidal prism. Within each disturbed model run, the duration of the first cycle ( $T_{first}$ ) exceeds that of *undist100*: for the disturbed runs,  $T_{first}$  is between 860 and 1260 days, whereas the matching period in *undist100* is 760 days. Secondly, the subsequent periods ( $T_{breach}$ ) are consistently shorter than in the undisturbed model run. This apparent acceleration is unsurprising as the undisturbed runs showed that period between breaches correlates with basin area and tidal prism (Table 4.2). The average values  $\overline{T_{breach}}$  suggest that the time scale remains longer than that of the undisturbed run with equal basin area, regardless of the basin area reduction. However, this could also be an effect of the variability within each model run or of the limited number of cycles.

The patterns of erosion/deposition, mean and semi-diurnal flow velocities and (tidally-averaged) sediment transport were analyzed during the three phases of cyclic behavior to explain the longer duration of the first cycle. Figure 4.4 shows these parameters after 3400 days, i.e., directly after model restart and during the phase of channel rotation. At this moment, the morphology is the same for all model runs, such that the instantaneous effect of basin reduction on tidal currents and sediment dynamics was isolated. The green contour indicates the change in tidal flow, particularly in the inlet (as in Figure 4.2a) and in the main channel. As a result, the deepening of the new channel (blue) scales with basin area. The maximum erosion along the black line across the channel is 0.033 m/day for *undist100* and 0.029, 0.025, 0.020 and 0.014 m/day for a 10%, 20%, 30% and 50% basin reduction, respectively. As

**Table 4.3** Period between successive breaches for the disturbed runs with a reduction in basin area after 3400 days with  $T_{first}$  the period of the first cycle and  $T_{breach}$  all subsequent periods. Here,  $\overline{T_{breach}}$  is the average period after first cycle and  $P$  the tidal prism averaged over the first two cycles of cyclic behavior.

Run	$T_{first}$ (days)	$T_{breach}$ (days)	$\overline{T_{breach}}$ (days)	$P$ (Mm <sup>3</sup> )
<b><i>dist100→90</i></b>	860	850, 1050, 1050	983	50
<b><i>dist100→80</i></b>	960	800, 1250	1025	46
<b><i>dist100→70</i></b>	1260	750, 900, 750	800	38
<b><i>dist100→50</i></b>	860	850, 300, 400, 400, 350, 550, 600, 500, 800	528	32

a result, the growth of the seaward end of the channel (red) decreases with basin area. However, the maximum deposition along the black line - ranging from 0.1055 to 0.1077 m/day - is surprisingly similar amongst the basin areas. This is because the wave-induced patterns of mean flow (yellow/black arrows) and sediment transport (white/magenta) over the shallow ebb-tidal delta platform are relatively unaffected. Based on the similar deposition rates, it is

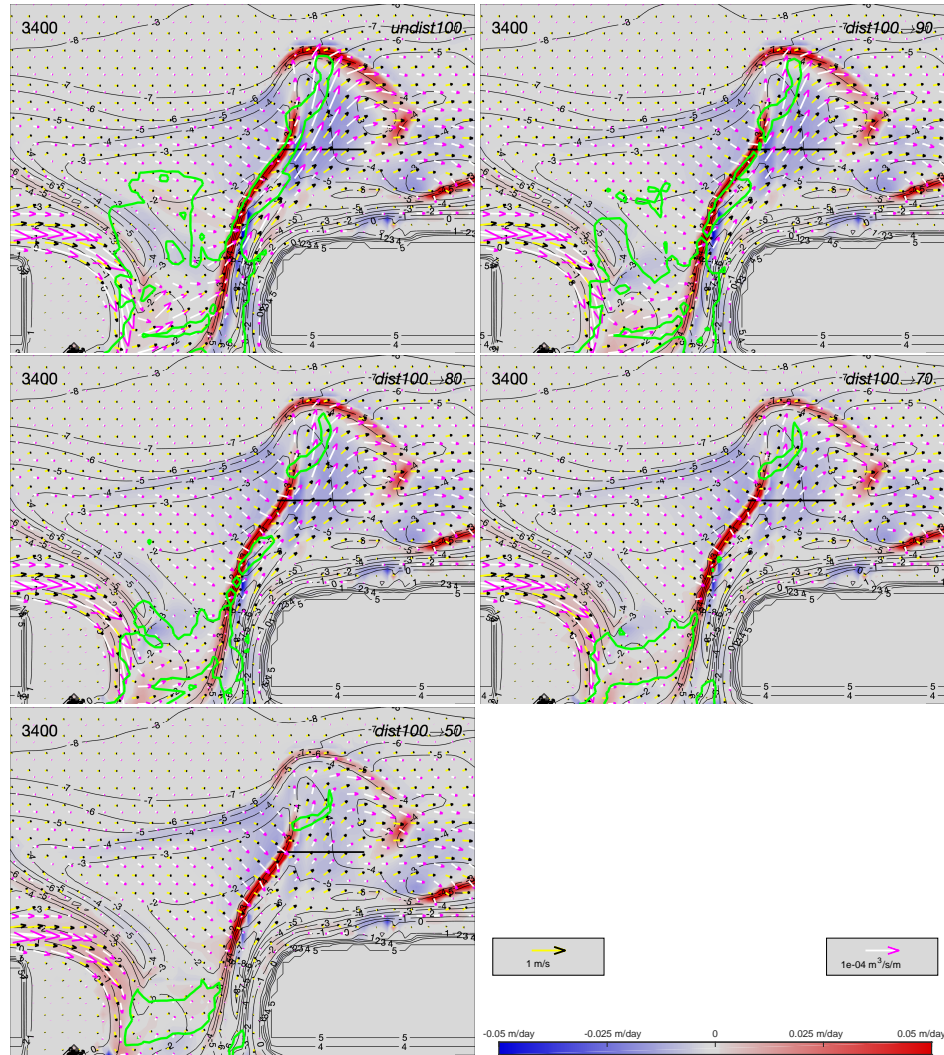


**Figure 4.4** Erosion (blue) and deposition (red) after 3400 modeled days. The vectors represent tidally-averaged total sediment transport (white/magenta) and flow velocities (yellow/black). The arrows are shown in every third grid cell in both directions. The green line encloses the area with semi-diurnal flow magnitude exceeding 0.23 m/s. The shown area is 4 km (east-west direction) by 3 km (north-south). In the upper right corner of each panel, the model run is shown.

concluded that the longer duration of the first cycle cannot be explained by changes in the channel rotation rate. This is supported by the fact that the channel orientations after 3600 days are roughly equal (see Figure 4.3c). However, due to the reduced tidal flow, both the channel dimensions and the ebb-tidal delta growth are reduced.

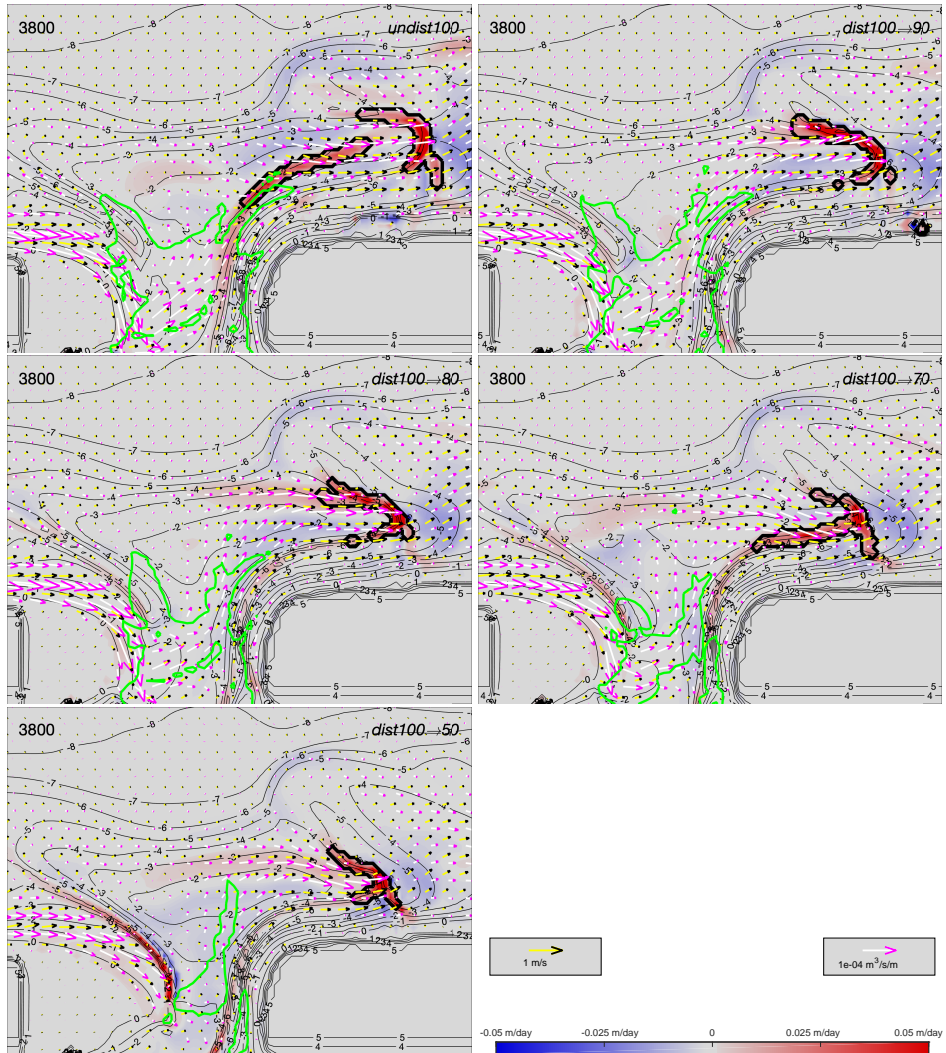


**Figure 4.5** As Figure 4.4, but after 3800 modeled days.

This smaller ebb-tidal delta is also evident from Figure 4.5, which shows the patterns of erosion/deposition, mean and semi-diurnal flow velocities and (tidally-averaged) sediment transport after 3800 days. At this moment, all model runs are characterized by shoal growth, as indicated by the areas of deposition on the downdrift side of the ebb-tidal delta. The shoal growth was quantified by the shoal growth rate, i.e., total deposition in the area in thick black contour in Figure 4.5. For *undist100*, the shoal growth rate is  $10229 \text{ m}^3/\text{day}$ , whereas for the

runs with basin reduction this is  $7837 \text{ m}^3/\text{day}$  ( $dist100 \rightarrow 90$ ),  $6338 \text{ m}^3/\text{day}$  ( $dist100 \rightarrow 80$ ),  $5909 \text{ m}^3/\text{day}$  ( $dist100 \rightarrow 70$ ) and  $4098 \text{ m}^3/\text{day}$  ( $dist100 \rightarrow 50$ ). As shown in Chapter 3, the shoal growth scales both with wave-induced sediment concentration and with mean flow magnitude (both tide- and wave-induced) over the ebb-tidal delta platform. Here, there is no significant variations in sediment concentration on the ebb-tidal delta platform amongst the simulations with different basin sizes, whereas comparison of the black/yellow arrows indeed show that the mean flows during the first cycle decrease with basin area. Therefore, we conclude that the damped shoal growth due to a drop in mean flow at least partly explains the longer duration of the first cycle.

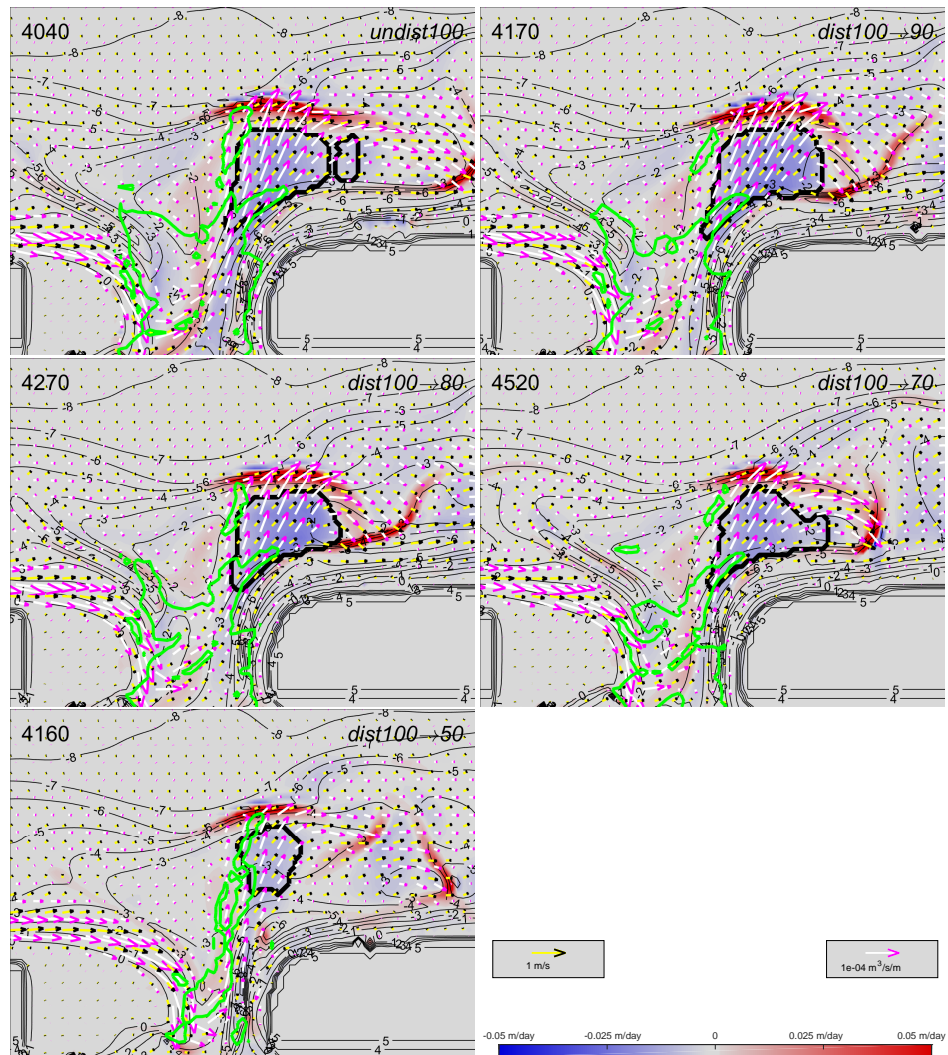


**Figure 4.6** As Figure 4.4, but when the breaching rate is maximum during the first cycle.

After the phase of shoal growth, the breaching of the ebb-tidal delta is initiated. The breaching rate was used to quantify this process, which is the average erosion in the area in thick black contour in Figure 4.6. This figure shows the patterns of erosion/deposition, mean and semi-diurnal flow velocities and (tidally-averaged) sediment transport when the breaching rate is maximum in the first cycle. For a 10% or 20% basin reduction, the breaching rates (0.0148 m/day and 0.0153 m/day, respectively) are significantly higher than that in the reference run (0.0115 m/day). This increase in erosion is due to a  $\sim 10\%$  increase in sediment concentration. For a 30% basin reduction, the breaching rate of 0.0117 m/day in the first cycle is close to that of the reference run. Only for a 50% basin reduction is a lower breaching rate obtained for the first breach (0.0086 m/day). Here, both the sediment concentration and the mean peak ebb flow velocity are roughly  $\sim 10\%$  lower than in the reference run.

The shoal growth rate and the breaching rates for all reference runs and runs with basin reduction are summarized in Table 4.4. A distinction is made between the rates before and after the adjustment. During the adjustment, the shoal growth rate decreases with decreasing basin size, whereas the opposite effect is found after the adjustment period. Following the reference runs, the shoal growth rate increases with decreasing basin size. A similar trend is found for the breaching rate: the breaching rates correlates positively and negatively with basin size before and after the adjustment period, respectively. For  $dist100 \rightarrow 90$  and  $dist100 \rightarrow 80$ , the values in Figure 4.6 are similar to those in the subsequent cycles, indicating that the adaptation was completed. This is not the case for  $dist100 \rightarrow 70$  and  $dist100 \rightarrow 50$ ; this slower adaptation corresponds with the longer adaptation period and the largest values for  $T_{first}$ .

In conclusion, the initial slowing down of the cyclic behavior can be attributed to an initial dampening of the shoal growth phase, whereas the channel rotation phase is unaffected. The subsequent acceleration is in turn due to an increase in shoal growth rate and breaching rate after the adjustment period. It remains unclear why  $T_{first}$  of  $dist100 \rightarrow 70$  exceeds that of  $dist100 \rightarrow 50$ , despite the lower shoal growth and breaching rates for the latter. Possibly, this is due to the smaller ebb-tidal delta.

**Table 4.4** The typical values for shoal growth rate ( $\Delta h_s$ ) and the breaching rate ( $\Delta h_b$ ) before and after the end of the adjustment period.

Run	$\Delta h_s$ ( $10^4$ m $^3$ /day) adjustment	$\Delta h_s$ ( $10^4$ m $^3$ /day)	$\Delta h_b$ (m/day) adjustment	$\Delta h_b$ (m/day)
<i>undist100</i>	n.a.	0.9-1.1	n.a.	0.011-0.013
<i>undist90</i>	n.a.	1.0-1.3	n.a.	0.011-0.015
<i>undist80</i>	n.a.	1.0-1.7	n.a.	0.012-0.016
<i>undist70</i>	n.a.	1.4-1.6	n.a.	0.015-0.017
<i>undist50</i>	n.a.	1.3-1.7	n.a.	0.016-0.025
<i>dist100 → 90</i>	0.8	1.2-1.5	n.a.	0.012-0.015
<i>dist100 → 80</i>	0.7	1.2-1.7	n.a.	0.013-0.016
<i>dist100 → 70</i>	0.6	1.3-1.6	0.012	0.014-0.016
<i>dist100 → 50</i>	0.4	1.4-1.7	0.009	0.018-0.026

The modeled ebb-tidal delta volumes are shown in Figure 4.3b. It reveals that a larger reduction in basin area causes a larger relative decline in volume. However, even though the inlet cross-sectional area and the tidal prism eventually converge to the value of the undisturbed runs with equal basin area, this is not the case for the volume (see difference between *undist80* and *dist100→80*). This can partly be explained by the fact there is no equilibrium volume in most model runs (see increasing trend for *undist100*). However, this increase is not found for *dist100→50* and *undist50* and we still found a difference in ebb-tidal delta volume of roughly 2.5 Mm<sup>3</sup>. Based on this, we conclude that the initial volume is partly retained and that the surplus of sediment is not entirely removed from the ebb-tidal delta within the simulated period.

Surprisingly, the smaller ebb-tidal deltas cause a decrease in both the width-averaged and the maximum significant wave height in the inlet (Figure 4.3d, solid and dashed lines, respectively). The wave height in the inlet largely depends on the size of the updrift oriented secondary channel. Because this channel is both shallower and narrower for smaller basins, more wave energy dissipates seaward of the inlet. The decrease in size of the secondary channel for decreasing basin area is visible from the black depth contours in Figures 4.5 and 4.6 and also affects the cross-sectional area (Figure 4.3a).

Figure 4.3e shows the additional cumulative sediment import caused by the basin size reduction. This is the difference in net sediment import between disturbed runs and *undist100*. Additional sedimentation of the basins for a 10-30% basin size reduction shows that the channels in the basin and the inlet are too big for the reduced basin. The additional cumulative import after 6200 days equates to an average sedimentation of the basin of 1.8 cm for *dist100→90*, 3.2 cm for *dist100→80* and 3.7 cm for *dist100→70*. After the initial adjustment period, no additional sediment import is modeled. During the adjustment period the inlet and basin find a new dynamic equilibrium, as further illustrated by the balance between tidal flow and inlet cross-sectional area (Figures 4.2 and 4.3a, respectively); it can be seen that the inlet converges to the dynamic equilibrium in the reference run with equal basin size.

Surprisingly, for a 50% basin area reduction (*dist100→50*), less infilling is modeled. In this case, only after the cross-sectional area has adjusted to the reduced tidal prism, more sediment is imported than in *undist100*. Here, the average sedimentation in the basin after 6200 days is only 1.3 cm. Possibly, the weaker mean flow magnitudes (Figure 4.2b) limit the capacity of the tidal flow to import sediment.

Figure 4.3f shows the additional cumulative sediment transport along the downdrift coast forced by the basin size reduction. The corresponding change in cumulative sediment transport along the updrift coast (roughly 0.9 Mm<sup>3</sup>/year) is negligible. Another difference between *dist100→50* and the other model runs can be seen. For a 50% basin size reduction, the sediment transported along the downdrift coast is persistently lower than for the undisturbed model runs and the model runs with a 10-30% basin size reduction. However, the difference is much smaller than the absolute littoral drift magnitude.

### 4.3.3 Relative sea-level rise

For the runs with different rates of relative sea-level rise, the bathymetries are initially very similar; but eventually, as the mean water level further rises, the cyclic behavior continues with noticeable changes. The period between successive breaches, listed in Table 4.5, shortens with rising mean sea level for the lower rates ( $\leq 1.5$  cm/yr: *slr50*, *slr100* and *slr150*). Figure 4.8c shows that the shorter periods are concurrent with an increase in the minimum

**Table 4.5** Period between successive breaches for the disturbed runs with rising subtidal water level together with *undist100* for reference. Only the first 4 periods are shown.

Run	$T_{breach}$ (days)
<b><i>undist100</i></b>	760, 1160, 1700, 1500
<b><i>slr50</i></b>	760, 1130, 1430, 1480
<b><i>slr100</i></b>	760, 1110, 1450, 1200
<b><i>slr150</i></b>	760, 1220, 1350, 1170
<b><i>slr200</i></b>	760, 1150, 1860, 1960

channel orientation. Breaches that are followed by a more downdrift oriented new channel (larger minimum channel orientation) are also followed by shorter period. This downdrift shift is due to slightly smaller semi-diurnal flow velocities (Figure 4.7a), which can be explained by an increase in inlet cross-sectional area (Figure 4.8a). For the lower rates of sea-level rises, the larger minimum channel orientation explains the shorter third and fourth period.

Only when the relative sea-level rise is 2 cm/yr (*slr200*), the cyclic behavior slows down. The larger periods are because the increase in cross-sectional area eventually is larger than that for the lower rates of sea-level rise. The increase in cross-sectional area is particularly evident after 5500 days. This increase has the effect of significantly smaller flow velocities (orange line in Figure 4.7a), which in turn causes breach postponement. In contrast to the lower rates of rising sea level, reduced tidal flow causes longer periods between successive breaching events. Again, the time scale is linked to the channel orientation after the breach (Figure 4.8c); in this case, the new channel has a more updrift orientation. Based on this transition from shorter to longer periods, we conclude that there is a critical rate of relative sea-level rise for cyclic behavior, in this system between 1.5 and 2 cm/yr. Above the critical rate, the increase in cross-sectional area cannot be compensated by additional sediment input from the littoral drift, slowing down the cyclic evolution of the ebb-tidal delta. Below the critical rate, the cross-sectional area of the inlet is relatively steady and shorter periods were modeled.

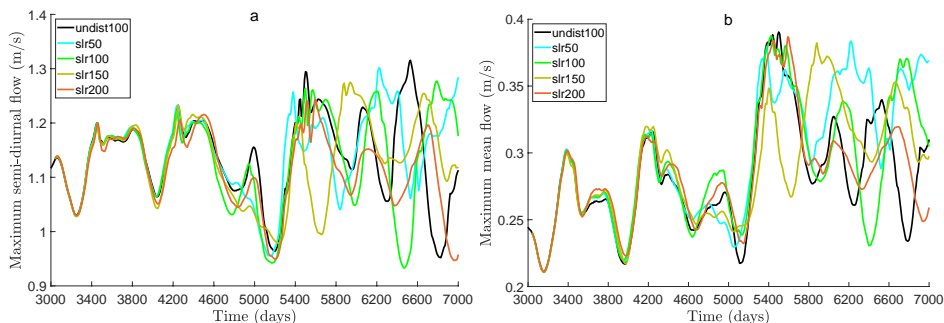


**Figure 4.7** For *undist100* and the runs with relative sea-level rise the maximum tidal flows amplitudes in the inlet with (a) semi-diurnal flow and (b) mean flow.

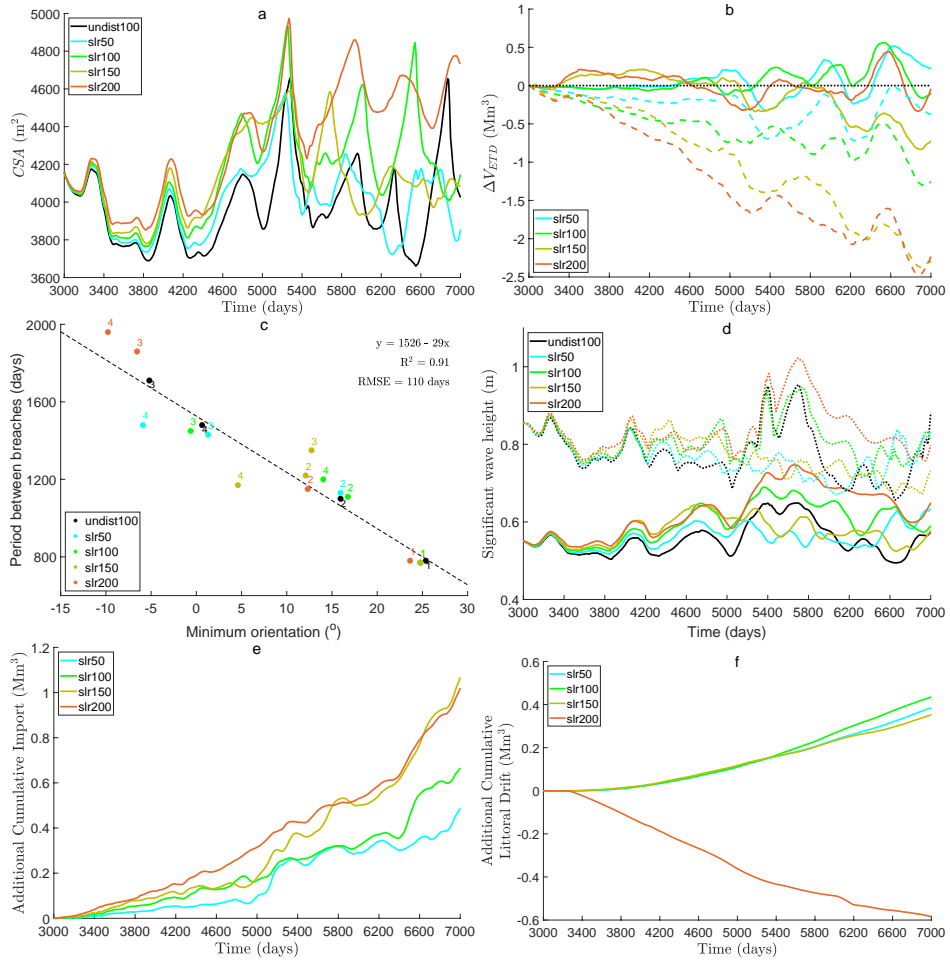


**Figure 4.8** For the runs with relative sea-level rise (a) cross-sectional area of the inlet, (b) relative volume of the ebb-tidal delta (solid lines: based on the initial mean water level; dashed lines: based on the actual mean water level), (c) the minimum orientation after the breach versus the period between the two breaches, (d) the average (solid lines) and maximum (dotted) significant wave height in the inlet, and (e) additional cumulative sediment import, and (f) additional cumulative littoral drift along the downdrift coast.

Figure 4.8b shows the relative volume of the ebb-tidal delta, i.e., the difference between the volumes in the runs with and without relative sea-level rise. The solid lines are based on the initial mean water level, whereas for the dashed lines the volume is corrected for relative sea-level rise. Surprisingly, the ebb-tidal deltas maintain most of their volume; as the dashed lines show, they are simply further submerged because the water level rises. As expected, the increased water depth reduces the offshore wave energy dissipation and thus increases the wave height in the inlet (Figure 4.8d).

Figures 4.8e and f show the additional sediment transport through cross-sections across the inlet and perpendicular to the downdrift coast, respectively. The former shows that more sediment is imported than in *undis100*. For relative sea-level rise below the critical rate, the additionally imported sediment scales with increasing water level. The additional cumulative import until 7000 days equates to an average sedimentation of the basin of roughly 0.15 cm/yr for *slr50*, 0.17 cm/yr for *slr100* and 0.32 cm/yr for *slr150*. In contrast, for *slr200*, eventually no more sediment is imported than for *slr150*. This suggests that the declining peak flow velocities due to the oversized cross-sectional area limit the capacity of tidal currents to transport sediment into the basin. The sediment transport along the downdrift coast (Figure 4.8f) reveals another difference between the model runs with rate of relative sea-level rise below and above the critical value. For rates of relative sea-level rise below the critical rate, the littoral drift at the downdrift coast increases, possibly because of the shorter periods of cyclic behavior. However, for 2 cm/yr relative sea-level rise, a decrease in littoral drift is modeled at the downdrift island. The change in cumulative sediment transport along the updrift coast due to sea-level rise is negligible (less than 0.02 Mm<sup>3</sup>).

## 4.4 Discussion

Deflecting channels and periodic breaching are natural sediment bypassing mechanisms at many ebb-tidal deltas (FitzGerald, 1988; FitzGerald et al., 2000; Ridderinkhof et al., 2016a). The feedbacks between this cyclic behavior and the underlying physical processes are relatively well understood (Cayocca, 2001; Bertin et al., 2009; Ridderinkhof et al., 2016b, and Chapters 2 and 3). Some tidal basins have been reduced in area in the last century, disrupting the natural dynamics (FitzGerald et al., 1984; Van de Kreeke, 2006; Elias et al., 2012). Many tidal inlet systems are further affected by relative sea-level rise (Van der Spek, 2018; Vermeersen et al., 2018; Wang et al., 2018). Observations indicate that these anthropogenic influences resulted in erosion of ebb-tidal deltas; slowing down of cyclic behavior of ebb-tidal deltas; and additional sediment import into the basin.

### 4.4.1 Reduced basin area

We have reproduced the observations that a reduction in basin area causes initially longer and eventually shorter cycle periods and we have shown why. Before the adjustment to the basin reduction was completed, the increased time scales of cyclic behavior were due to severely reduced tidal flow in the inlet, caused by an oversized cross-sectional area. These smaller values for semi-diurnal flow velocities and mean flow damped especially the shoal growth, whereas the channel rotation was relatively unaffected. Furthermore, the breaching rate of the ebb-tidal delta was also lower during the adjustment, albeit less pronounced. Unsurprisingly, the duration of the adjustment period correlates positively with reduced basin area. Hereafter, accelerating effects were found due to an increase in both shoal growth and breaching rate.

This study focused on relatively short basins with a partially standing tidal wave, such as the Frisian Inlet. Our results explain what has happened at this inlet, where the closure of the Lauwerszee caused additional import of sediment and slowed down the first cycle of channel-shoal dynamics (Biegel and Hoekstra, 1995; Oost, 1995; Van de Kreeke, 2006). Note that the observed formation of an exceptionally large shoal at the Frisian Inlet (Elias et al., 2012) was not reproduced in the present study. The modeled drop in ebb-tidal delta volume

was also observed at other inlets that had a reduction in basin area, such as the San Francisco Bay (Dallas and Barnard, 2011). Furthermore, our results indicate that in the future (after the adjustment) the morphological development of the Frisian Inlet and similar inlets will accelerate with shorter period of cyclic behavior because of faster shoal growth and breaching of the ebb-tidal delta. We found that the adjustment time scale increases with basin area reduction. The shorter time scale of the cyclic behavior matches the observations of Gaudiano and Kana (2001) and Ridderinkhof et al. (2016a), who found that the period of the cyclic behavior correlates positively with the tidal prism. It appears that the typical period after the adjustment remains longer than the typical period in the undisturbed runs with equal basin area. Similarly, the volume of the ebb-tidal delta after the adjustment was lower than in *undis100*, but exceeded that of the undisturbed runs with equal basin area. Because larger ebb-tidal deltas tend to have a longer period between successive breaches/shoal attachments, it is likely that the latter two results are interrelated.

Furthermore, the wave height in the inlet decreased with basin area because of the also decreasing size of the secondary (updrift oriented) channel, which is between the inlet and the predominant wave direction. This reduction is contrary to Chapter 2, where the Ameland Inlet was best protected from incoming waves when the main channel has an updrift orientation. In that case, more energy dissipated on the ebb-shield and the shallow areas flanking this channel, whereas in this chapter, the dissipation on these shallow areas was similar amongst the runs.

In some systems, reduction of the basin area has lead to an increase in tidal prism. For example, at the Texel and Vlie basins in the Dutch Wadden Sea, the construction of the Afsluitdijk caused the shift from a propagating to a standing tidal wave (Ridderinkhof et al., 2014b). Resonance effects subsequently increased the tidal prism. However, the effect of such a transition is beyond the scope of this study.

#### 4.4.2 Relative sea-level rise

The volumes of the ebb-tidal deltas subject to relative sea-level rise were relatively unaffected. They were simply submerged further because of the rising subtidal water levels. This suggests that the observed historic erosion of Dutch ebb-tidal deltas was primarily caused by the basin reduction and not by the relative sea-level rise. Nevertheless, when the average water depth above the ebb-tidal deltas increased, less offshore wave energy dissipation was modeled. Because, as a result, the wave height increased in the inlet and the basin, this will potentially cause erosion of intertidal flats in the basin. Furthermore, more energetic waves can propagate into the nearshore zone of the updrift tip of barrier islands, which further exposes the already eroding island heads.

In our model runs, the additional import of sediment was not sufficient to compensate for the accommodation space created in the basins. This is probably because of the relatively coarse sediment used in this chapter. It is known that finer sediment is transported more easily into the basin than coarse sediment (e.g. Sha, 1990; Gao and Collins, 1994; Herrling and Winter, 2014; Zhou et al., 2015). However, it was not the objective of this study to examine or replicate the morphological response of the basin area, but that of the ebb-tidal delta. Wang et al. (2018) studied the effects of relative sea-level rise on sediment dynamics and morphology at the Dutch Wadden Sea and showed that each tidal basins has an individual critical rates for ‘drowning’ of intertidal flats. In other words, if the pace of rising mean sea level exceeds this rate, the maximum volume of imported sediment is no longer suffi-

cient to maintain a portion of intertidal flats. Here, we found a similar critical rate of relative sea-level rise for cyclic behavior. Above this rate, the cross-section of the inlet was not in balance with the tidal flow, slowing down the cyclic channel-shoal dynamics. These longer periods between successive breaches were linked to an updrift shift in breach location. In contrast, if relative sea-level rise was below the critical rate, shorter period were associated with a downdrift shift in breach location.

This modeling study showed the connected adjustment of cyclic behavior, ebb-tidal delta volume, inlet cross-sectional area, tidal flow amplitudes and sediment import for both relative sea-level rise and basin area reduction. Many cyclic ebb-tidal deltas are located in an environment characterized by land reclamation, subsidence and/or sea-level rise. The outcomes of this study contribute to our understanding of the long-term evolution of tidal inlets in such an environment.

#### 4.5 Conclusions

This study has explored how natural ebb-tidal delta breaching and its time scale are affected by an instantaneous reduction in basin area and by relative sea-level rise. Basin reductions lead to longer periods of cyclic behavior during an initial adjustment period and shorter periods after the adjustment. The initial longer periods were linked to severely reduced tidal flow in the inlet, an oversized cross-sectional area, damped shoal growth and slower breaching of the ebb-tidal delta. Simultaneously a relative decrease in ebb-tidal delta volume and tidal prism was found. This decrease in tidal prism is eventually also related to the shorter periods of cyclic behavior after the adjustment period. Despite the erosion of ebb-tidal delta, the wave height in the inlet decreased.

We found shorter periods of cyclic channel-shoal dynamics for relative sea-level rise below a critical rate of 1.5 cm/yr for this particular setting. In this case, the sediment supplied to the inlet compensated for the increase in cross-sectional area due to the rising water level. The acceleration of the cycle was related to a downdrift shift in breach location due to a small decrease in peak flow magnitudes. However, above the critical rate, significantly smaller flow velocities in the inlet caused the cyclic behavior to slow down. The ebb-tidal deltas maintained their volume, but because the water depth increased, so did the wave height in the inlet.



## **Chapter 5 | The effect of mega-nourishments on long-term behavior of ebb-tidal deltas**

### **Abstract**

Sand nourishments on ebb-tidal deltas are a new approach to sustain future sediment availability in human-impacted barrier systems. They fit in a general trend to apply nature-based solutions for coastal safety. It is, however, unknown how such interventions will alter the complex mutual interaction between tides, waves and long-term morphological behavior. The focus of this research is on the effect of nourishment size, location and timing on long-term (years) morphological evolution of mixed-energy tidal inlet systems featuring cyclic channel-shoal dynamics. This behavior includes cyclic patterns of channel rotation and breaching associated with sandy shoals migrating and attaching to the down-drift coast. Using numerical simulations, we predict the effect of a wide range of nourishments on patterns of waves, tides and sediment transport and on long-term morphological evolution. If the nourishment is placed on the ebb-shield, it hardly affects the wave, flow and sediment transport patterns; also on the long-term, the effects are small. The ebb-tidal delta keeps the nourished sediment because the nourishment is placed at a location that is morphodynamic relatively inactive due to its depth. If placed on the shallower platform, the behavior depends on the timing of the nourishment with respect to the cyclic evolution. When implemented before an ebb-tidal delta breach, the new channel forming as a part of the breach attains a more downdrift orientation. This subsequently leads to a shorter period until the next breach, especially for the larger nourishments. However, a nourishment directly after the breach leads to shorter period for a different reason: it accelerates the channel rotation and also shortens the shoal growth phase. After one or two cycles, the nourishment no longer has any effect on ebb-tidal delta behavior. The nourished sediment quickly erodes, roughly within one cycle of channel rotation and breaching. A large portion of this sediment is imported into the basin. Moreover, increased wave energy dissipation over the shallow ebb-tidal delta, albeit temporary, was only found if the nourishment was implemented on the platform. An unwanted possible side-effect of an ebb-tidal delta nourishment is that it can force the channel to rotate further to the downdrift island, there causing erosional problems.

### **In preparation for submission:**

Klaas J.H. Lenstra, Linxi Fu and Maarten van der Vegt, The effect of mega-nourishments on long-term behavior of ebb-tidal deltas.

## 5.1 Introduction

Observations indicate that the ebb-tidal deltas of the Dutch Wadden Sea lost a considerable part of their sediment volume during the last century (Elias et al., 2012). This erosion has been linked to sedimentation in the Dutch Wadden Sea and human impacts such as relative sea-level rise and basin reductions (closure of the Zuiderzee and the Lauwerszee). Long-term problems for coastal safety are to be expected because eroding ebb-tidal deltas might filter less incoming wave energy and allow more energetic waves to reach the mainland coasts (Hansen et al., 2013, and Chapter 2). Moreover, in the future higher sedimentation rates in the Wadden Sea are expected because of accelerating sea-level rise (Vermeersen et al., 2018; Wang et al., 2018). Hence, ebb-tidal deltas might lose more sediment and thereby their protective function. This was already confirmed in Chapter 4, in which it was shown that rising mean sea level will result in more energetic waves in the inlet and the back-barrier basin. As a mitigation route, mega sand nourishments of ebb-tidal deltas in the order of 20 million m<sup>3</sup> (Mm<sup>3</sup>) have been proposed (DeltaProgramma, 2014; Rijkswaterstaat, 2017). Their objectives are threefold, namely to (1) increase/restore the volume of the ebb-tidal delta and thus the wave filtering, (2) enhance the sediment transport into the Wadden Sea, and (3) stimulate sediment transport to the downdrift coast. The third objective is motivated by continuing erosion of many islands due to strong tidal currents in the inlet. This nourishment approach is part of the ‘nature-based solutions’ for Dutch coastal management, where the sediment spreading after one major nourishment removes the need for periodic smaller nourishments. The first time such a solution was put into practice was the Sand Engine (Stive et al., 2013), a mega-nourishment of 20 Mm<sup>3</sup> with an expected lifespan of 20 years implemented in 2011 at the wave-dominated western coast of the Netherlands. However, knowledge is missing to predict the effects of such a nourishment on long-term morphological development in a mixed-energy setting. Ebb-tidal deltas are characterized by complex pattern of waves and tidal currents and by variations herein due to cyclic dynamics of channels and shoals (Chapter 2). It is unknown how this interaction between morphology, waves and tides is impacted by the position, size and timing of the nourishment with respect to cyclic behavior of the ebb-tidal delta. Therefore, we aim to elucidate the effect of ebb-tidal delta nourishments on the morphological behavior of undisturbed ebb-tidal deltas. This is a first step into assessing the mitigation efficiency for eroding ebb-tidal deltas subject to anthropogenic influences.

In 2018 a pilot nourishment of 5 Mm<sup>3</sup> was implemented at the ebb-tidal delta of Ameland (Figure 5.1) and its effects are extensively monitored (van Rhijn, 2019). This ebb-tidal delta of roughly 200 Mm<sup>3</sup> is the most undisturbed ebb-tidal delta in the Dutch Wadden Sea and features cyclic channel-shoal dynamics (Israel and Dunsbergen, 1999), which is typical for many ebb-tidal deltas of the Dutch and German Wadden Sea (Ridderinkhof et al., 2016a). The pilot nourishment was placed at the seaward front of the ebb-shield (Figure 5.1) and the first observations (until 2020) indicate that the nourishment is only morphologically active during storms. For the future mega-nourishment, other locations are also considered such as the shallower ebb-tidal delta platform, seaward of the updrift island (Terschelling) or in the main channel. Bak (2017) implemented different nourishment locations and grain sizes in an Ameland model in Delft3D. It was found that when composed of coarser sand ( $d_{50} > 300 \mu\text{m}$ ), the nourishment would be morphologically less active. Especially coarse sediment placed on the ebb-tidal delta platform would cause long-term shoal reinforcement, whereas finer sediment would be moved into the basin or downdrift quickly. Furthermore, Fu (2018) implemented three nourishment locations in the Ameland model of Chapter 2

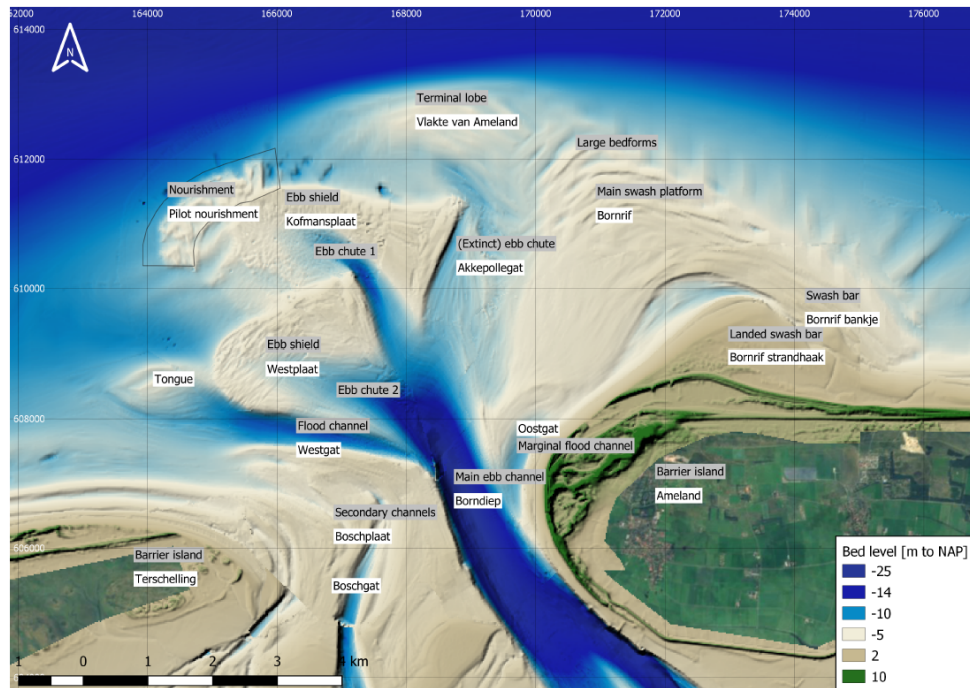


**Figure 5.1** Ameland ebb-tidal delta in 2018 after the implementation of the pilot nourishment. From van Rhijn (2019).

and showed that nourishing the shallowest part of the ebb-tidal delta platform would have the largest increase in offshore wave energy dissipation, reducing the wave energy reaching the nearshore zone of both barrier island and penetrating through the inlet. In contrast, a nourishment offshore of Terschelling would only protect against waves approaching Terschelling, which would have the side effect of weakening the littoral drift. Bak (2017) showed that this would increase the sediment volume in the nearshore zone of Terschelling and its downdrift tip; this change in updrift sediment dynamics will directly affect the ebb-tidal delta dynamics (Chapters 2 and 3). Fu (2018) further found that a nourishment placed in the deep channel would have negligible effect on the patterns of wave energy propagation, but would potentially force a transition from net export to net import.

In Chapters 3 and 4, the cyclic channel-shoal dynamics of ebb-tidal deltas was studied using an idealized model geometry and forcing. This yielded new insights in the relative role of waves and tides during the typical phases of cyclic behavior. This knowledge can be used to make hypotheses on how an ebb-tidal delta will respond to a nourishment. In Chapter 4, it was shown how a reduction in basin area results in an adjustment period of cyclic behavior. During the adjustment period, the time scale of cyclic behavior increased, while after the adjustment period the typical time scale was smaller, what is expected for a system with a smaller tidal prism (Gaudiano and Kana, 2001; Ridderinkhof et al., 2016a). The initial deceleration was attributed to severely reduced tidal flow, caused by a cross-sectional area that is too big for the reduced tidal prism. Because shoal growth depends on tides and

waves operating simultaneously, it takes longer for the shoal to grow, whereas these changes do not significantly affect the wave-induced channel rotation. The breaching of the ebb-tidal delta also takes longer because of the reduced ebb flow velocities. The subsequent shorter periods of cyclic behavior after the adjustment period originate from acceleration of both the shoal growth and the breaching phases and are in line with identified relationships between tidal prism and time scale of cyclic behavior. Like with basin area reductions, it is expected that nourishments will alter the natural cyclic behavior and associated time scales at least temporarily, especially because any nourishment instantaneously changes the ebb-tidal delta volume and causes changes in sediment import/export, wave energy dissipation, littoral drift and mean and semi-diurnal flow velocities (Bak, 2017; Fu, 2018). Because the ebb-tidal delta will have a sediment surplus, it will probably lose this extra volume on the longer term. This sediment can either be transported along the coast or into the basin, but what exactly will happen and how this depends on location of the nourishment is yet unknown. We expect that the timing of nourishment implementation is also important. When a nourishment is placed during channel rotation, the shallower platform probably causes more wave breaking and thus stronger mean flows that accelerate the channel rotation. Similarly, when placed during shoal growth, we hypothesize that the shallower platform will enhance the sediment concentrations and mean flows and thus the shoal growth. When placed during channel breaching, we expect that the surplus in sediment will prolong the channel rotation phase and cause the channel to reach larger rotation angles. It is likely that a nourishment in shallower water will have a more pronounced impact than one in deeper areas and that the impact scales with nourishment volume. It is unknown what the net effect of any ebb-tidal delta nourishment would be on the time scale of the cyclic behavior and how this depend on the size, location and timing of nourishment within the cyclic behavior. Moreover, it is to be tested if a nourishment would only enhances the short-term wave filtering by the ebb-tidal delta (as found by Fu, 2018) or if this is an sustainable long-term effect.

This study aims to assess how a mega-nourishment will affect the long-term morphological evolution of ebb-tidal deltas by studying the mutual interactions between changes in ebb-tidal delta morphology, waves, tides and sediment transport using a model approach. Because we are not yet able to simulate these processes on decadal time scales for systems like the Ameland Inlet, the idealized approach as in Chapters 3 and 4 will be used. We implemented and studied the effects and evolution for a wide range of possible nourishments and compared the outcome to non-nourished model simulations. The results will be evaluated against the three main objectives of ebb-tidal delta nourishments.

## 5.2 Material and methods

The numerical model Delft3D (Lesser et al., 2004; Deltares, 2014) was coupled with SWAN (Booij et al., 1999; Ris et al., 1999; Holthuijsen, 2010) to compute waves, hydrodynamics, sediment transport and bed level updates. Using a simplified model setup with idealized geometry and constant forcing, we implemented and studied the evolution of ebb-tidal deltas during several cycles of channel-shoal dynamics for sixteen possible ebb-tidal delta nourishments (Section 5.2.2). The results were compared with a non-nourished reference model simulation which featured several cycles of the channel-shoal dynamics. The model setup is identical to that described in Chapter 3; a brief summary is provided below.

### 5.2.1 Model domains and settings

The Delft3D flow module calculates the flow velocities and water levels by solving the depth-averaged shallow water equations and the continuity equation. The Van Rijn et al. (2004) sediment transport equations for bedload and suspended load were used with a single sediment fraction of  $d_{50} = 250 \mu\text{m}$ . Domain decomposition was implemented using eight two-way coupled domains. For the inlet and ebb-tidal delta the grid cell size was set at 50 m, for the tidal basin at 150 m and for the outer sea at 450 m.

The phase-averaged spectral wave model SWAN solves the wave action balance equation and was coupled to Delft3D with a coupling time of 60 minutes. The wave domain consists of three nested grids with decreasing grid cell sizes of 1350 m (east-west extension to avoid shadowing effects), 450 m (Delft3D domain) and 50 m (inlet and ebb-tidal delta). The offshore boundaries were forced by a semi-diurnal tidal wave propagating along the coast (amplitude 1 m and period 12 hours) and waves coming from the northwest (origin  $335^\circ$  clockwise with respect to the north, significant wave height 2.0 m and peak period 7.5 s).

### 5.2.2 Model simulations

The effect of nourishments were tested for four different initial bathymetries, two different positions and two different volumes. The initial bathymetries were taken from the non-nourished reference run described in Chapter 3 and are shown in Figure 5.2. Nourishments were placed during the phase of channel rotation and shoal migration (Phase 1, 2700 days), shoal growth (Phase 2, 3000 days), breach initiation (Transition Phase 2→3, 3200 days) or after the breach and before the channel rotation (Phase 3, 3400 days). Hereafter, if the num-

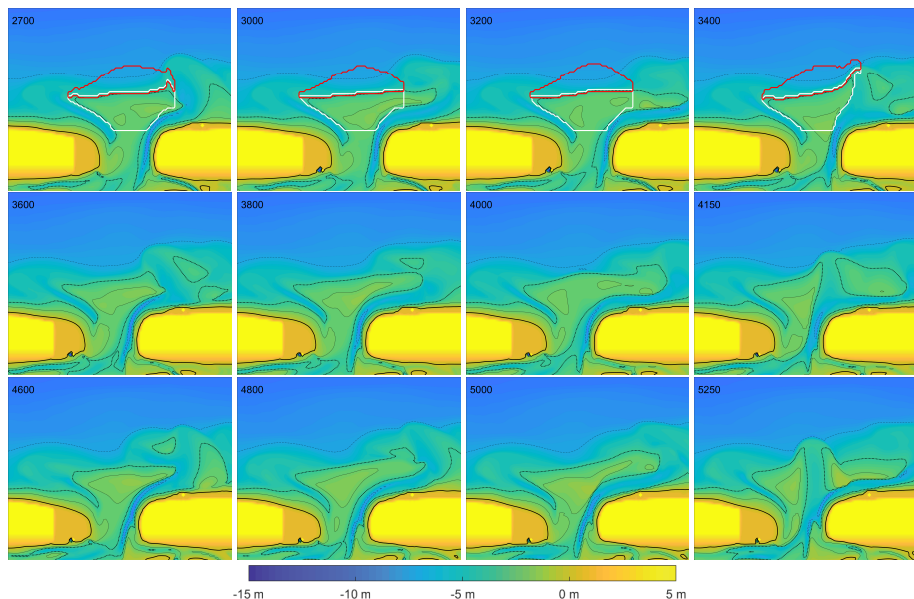


**Figure 5.2** Bathymetries obtained in the non-nourished reference model run (Run 2 from Chapter 3). The red and white contours indicate the two nourished areas. In the upper left corner of each panel, the number of modeled days is shown.

ber of modeled days is shown, this is relative to the begin of the reference model run, which starts with a flat bed in the basin and initially features no ebb-tidal delta. The two nourishment locations were the ebb-tidal delta platform (white contour in Figure 5.2) and seaward of the platform (ebb-shield, red contour). These locations were chosen because they were also tested by Bak (2017) and Fu (2018) and because they are the most probable options for the planned mega-nourishment at Ameland. Two nourished volumes were tested, namely  $0.5 \text{ Mm}^3$  and  $1 \text{ Mm}^3$ , which equate roughly to 5% and 10% of the ebb-tidal delta volume, respectively. The 10% roughly corresponds to the mega-nourishment proposed for the Ameland ebb-tidal delta. Because all combinations were tested, a total of sixteen potential nourishments were modeled.

The nourished sediment was distributed over the chosen location using the following procedure. Initially, the sediment was evenly spread after which two constraints were applied. First, after implementation the still water depth in any grid cell should exceed 1 m. This prevents the artificial creation of intertidal areas (dry during low water). Furthermore, the maximum increase in spatial gradients in bed level was 50%, such that no direct collapse of the nourishment occurred. Any surplus in sediment was evenly distributed over the rest of the nourishment location. This procedure was repeated until both constraints were met and all sediment was distributed.

Based on Chapter 3, changes in littoral drift were expected because of shoreface steepening. Any decrease in this value causes two subsequent cycles to differ substantially. Therefore, model runs were analyzed for the period that the littoral drift was steady, i.e., for most runs until roughly 8000 modeled days. For example, the reference model run taken from Chapter 3 was analyzed until 9100 days.

### 5.2.3 Model analysis

Unless stated otherwise, tidally-averaged values of significant wave height, sediment transport and sediment concentration are used hereafter. For each model run, we analyzed and compared the:

- the mean (tidally-averaged) flow magnitude and direction and the amplitude and direction of semi-diurnal flow velocities for all locations at certain moments of interest;
- sediment concentration;
- total load sediment transport, i.e., the sum of bedload and suspended load, hereafter referred to as sediment transport;
- significant wave height in the inlet. Also determined for all locations at certain moments of interest;
- cross-sectional area of the inlet. This is the area below the still water level at the inlet cross-section shown in Figure 3.2;
- the minimum still water depth of the entire ebb-tidal delta area (one value per tidal cycle);
- the orientation of the channel. This was defined as the angle with respect to the north (positive in clockwise direction) between the following two grid points in the channel. The first point was the deepest grid cell in the inlet cross-section. The second point was chosen from the local maxima in water depth along the semicircle with a radius of 1000/1050 m centered around the first point. The most upstream local maximum was ignored as this was part of the static secondary channel and the second most upstream local maximum was chosen as the second point. The main advantage is that in this way

the breaching of channels is identified earlier. In the procedure of Chapters 3 and 4 a sudden shift in main channel is only identified when the old channel has already partially been filled up;

- time of breaching of the ebb-tidal delta. In this breaching process, the new channel develops by eroding the ebb-tidal delta. During this stage, the above-defined orientation decreases as the 3.5 m isobath migrates seaward. Eventually, the new channel becomes so deep that the closed 3.5 m isobath of the ebb-tidal delta splits in an updrift and a downdrift part. As in Chapter 4, this moment is defined as the time of the breaching;
- the breach orientation. This refers to the orientation of the new channel at the moment of the breaching of the ebb-tidal delta. As mentioned above, the channel orientation can already decrease before the breach. However, the breach orientation is generally the minimum value in the cycle of channel-shoal dynamics;
- time scale of the cyclic behavior. For this, the period between successive breaching events was used;
- the volume of the ebb-tidal delta. Following Dean and Walton (1975), this volume was computed as the positive volume between the modeled and an no-inlet bathymetry below mean sea level. The fixed no-inlet bathymetry was constructed based on the cross-shore profile at both sides of the inlet after 2700 days in the reference run. Further details are given in Chapters 3 and 4.

## 5.3 Results

### 5.3.1 Nourishment on ebb-tidal delta platform

When the nourishment is implemented on the ebb-tidal delta platform (platform nourishment), various long-term effects are found. For all model runs, the cyclic behavior continues with significant changes to time scale and breach orientation. In short, a platform nourishment before the breach (Phase 1, 2, or 2→3) changes the first one or two cycles with (1) breaches taking place further downdrift, i.e., a relatively large breach orientation; and (2) shorter periods between successive breaches. When the platform nourishment is after the breach (Phase 3), the cyclic behavior speeds up during the adaptation. After these adaptation effects, the time scales, breach location, the temporal variations in tidal flow and the general cyclic morphological development become similar to those in the reference run.

Figures 5.3a and b indicate that roughly half of the additional volume supplied by the nourishment is removed from the ebb-tidal delta relatively quickly. After about a third of the duration of one cycle (~1000 days in reference run), nourishment effects have disappeared and the natural development of the volume resumes. Nevertheless, it appears that all model runs have a sustained increase in ebb-tidal delta volume, roughly equal to 50% of the nourished volume. Especially if the nourishment is placed during Phase 3 (magenta lines), the nourished volume is well maintained at the ebb-tidal delta. That a large portion of the surplus in sediment is removed from the ebb-tidal delta in the first cycle is also visible in the minimum water depth of the ebb-tidal delta. Figures 5.3c and d indicate a rapid increase in the minimum water depth until the values are within the range of the reference run within half a cycle of channel-shoal dynamics. Interestingly, the red and blue lines (Phases 2 and 2→3) in Figure 5.3d indicate relatively shallow ebb-tidal deltas, whereas the green and magenta lines (Phases 1 and 3) in Figure 5.3b indicate ebb-tidal deltas with a relatively large volume. This

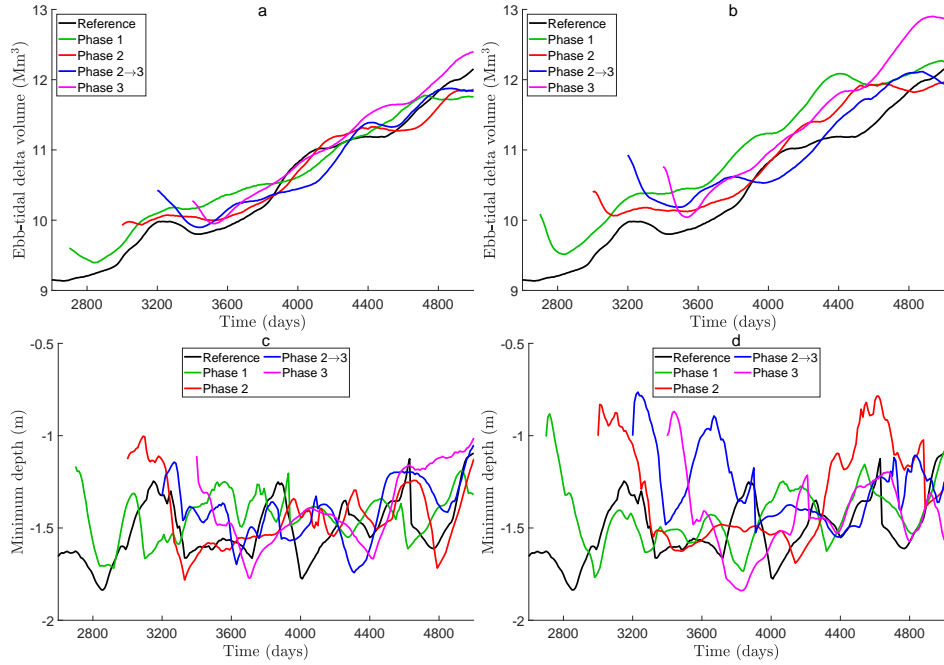


**Figure 5.3** Morphological characteristics of the ebb-tidal deltas in the runs with a nourishment placed at the ebb-tidal delta platform. (a+b) The volume of the ebb-tidal delta; and (c+d) the minimum water depth at the ebb-tidal delta for the  $0.5 \text{ Mm}^3$  (a+c) and  $1 \text{ Mm}^3$  (b+d) nourishments. Colors indicate the timing of implementation (see legend).

suggests that if the ebb-tidal delta becomes shallower for a longer period (as for nourishment in Phases 2 and  $2 \rightarrow 3$ ), the ebb-tidal delta loses its sediment more quickly.

A large portion of the nourished sediment that is removed from the ebb-tidal delta is transported into the basin. Figure 5.4a shows the additional cumulative sediment import, i.e. difference between runs with and without platform nourishments. It can be seen that during the

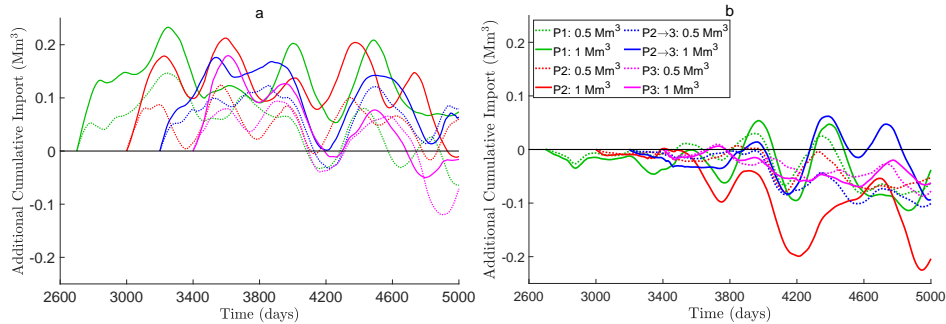


**Figure 5.4** The modeled additional cumulative sediment import for the nourishments at (a) ebb-tidal delta platform and (b) ebb-shield.

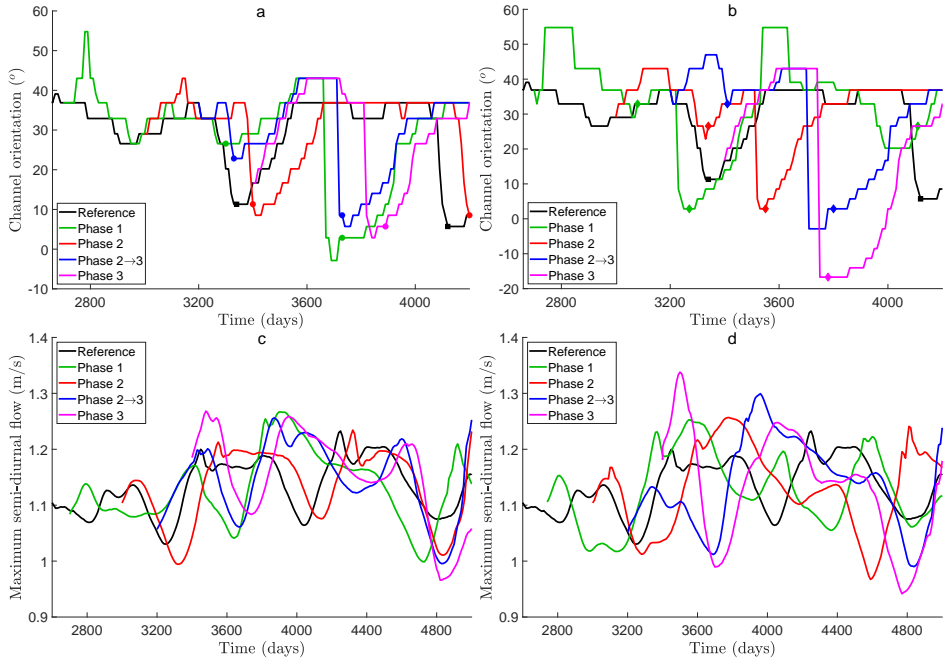


**Figure 5.5** Time series of the runs with a nourishment placed at the ebb-tidal delta platform. (a+b) the orientation of the main channel with markers indicating the breach orientation; and (c+d) maximum semi-diurnal flow amplitudes in the inlet channel for the  $0.5 \text{ Mm}^3$  (a+c) and  $1 \text{ Mm}^3$  (b+d) nourishments. Colors indicate the timing of implementation (see legend).

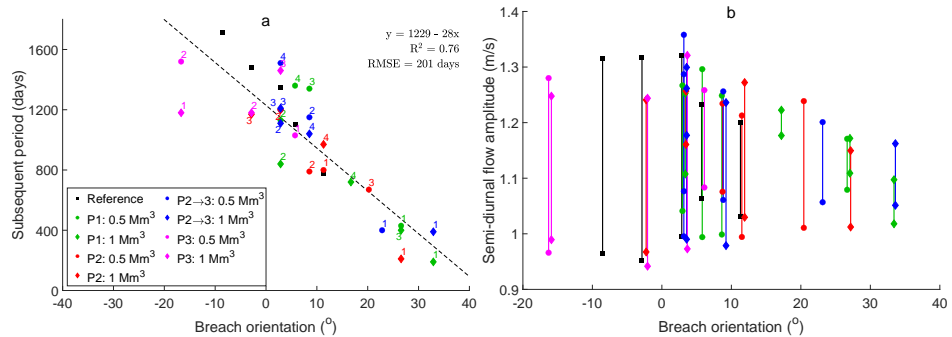
first cycle, roughly  $0.15 \text{ Mm}^3$  more sediment is imported for the  $1 \text{ Mm}^3$  nourishments (solid lines) and  $0.05\text{--}0.1 \text{ Mm}^3$  for the  $0.5 \text{ Mm}^3$  nourishments (dotted lines). This corresponds to 10 to 20% of the nourished volume and thus to 20 to 40% of the sediment that is removed from the ebb-tidal delta in the first cycle after the nourishment.

Figures 5.5a and b show that the channel orientation in the period after the nourishment is significantly affected. Firstly, the maximum channel orientation after the nourishment is generally higher than in the reference run. This is particularly evident for nourishments placed during Phase 1 ( $0.5$  and  $1 \text{ Mm}^3$ ), which forces channel orientation exceeding  $50^\circ$ , whereas the reference run has a maximum channel orientation of  $39^\circ$ . For the  $1 \text{ Mm}^3$  nourishment placed during Phase  $2\rightarrow 3$ , this is  $47^\circ$  and for all other nourishments ( $0.5$  and  $1 \text{ Mm}^3$ ), this is  $43^\circ$ . The markers in Figures 5.5a and b indicate the channel orientation at the moment of breaching, i.e., the breach orientation. They show that the duration of the cycles of channel-shoal dynamics are changed by the nourishments. In general, the first marker after the nourishment placement is relatively unaffected with a breach timing close to 3340 days, as in the reference run. However, for most model runs, the second marker indicates that the breach occurs earlier than in the reference run. For example, the second red and blue markers in Figure 5.5b are after 3550 and 3800 days, respectively, whereas this is after 4120 days for the reference run. Therefore, most runs have a period between the first

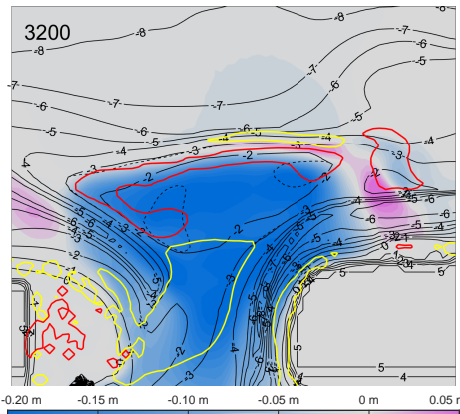
two breaches that is substantially shorter. A different effect on the time scales is modeled when the platform nourishment is placed during Phase 3, i.e., directly after the breach. The magenta lines and markers in Figures 5.5a and b show that it is the first breach rather than the second after nourishment placement that takes place roughly 250 days sooner. As a result, only the cycle in which the Phase 3 nourishment is placed is shorter. In short, all platform nourishments result in (1) an increase in maximum channel orientation and in (2) smaller time scales of cyclic behavior.

Figure 5.6a shows that these shorter periods are negatively correlated to the breach orientation. This dependency indicates that large breach orientations (newly formed channels that have a more downdrift orientation) are followed by a shorter period. Most model runs with a platform nourishment feature at least one breach orientation over  $20^\circ$  with a subsequent period less than 500 days, whereas the typical breach orientation is close to shore-normal ( $\sim 0 - 10^\circ$ ) with a subsequent period generally over 1000 days. Note that in the reference run breach orientations are always smaller than  $11^\circ$ . Interestingly, these exceptionally large breach orientations follow shortly after the nourishment implementation; there is a general tendency for the first breach to be more downdrift. The reasons for this large breach orientation will be discussed in Section 5.3.3. Figure 5.6a also shows that after the adaptation period, breach orientation and breach period are within range of the undisturbed values. Contrary to the nourishments in the other phases, the nourishment placed during Phase 3 results in a small decrease in breach orientation (magenta markers in Figure 5.6a). The identified correlation between breach orientation and period until the next breach suggests that this would cause longer time scales. However, these runs do not follow that pattern. In fact, the main effect on the time scale appears to be that the first breach occurs roughly 250 days earlier. The reasons for this discrepancy will be discussed in Section 5.3.3.

The breach orientation is linked to changes in the tidal flow characteristics after the breach. Figure 5.6b shows the range in modeled amplitudes of the semi-diurnal flow velocities in the



**Figure 5.6** For the runs with a nourishment placed at the ebb-tidal delta platform, the orientation at the moment of the breach (also indicated in Figure 5.5a+b) versus (a) the period until the next breach and (b) versus the range in semi-diurnal flow amplitudes throughout the breaching process. Colors indicate the timing of implementation (see legend). Circles and diamonds are used for  $0.5 \text{ Mm}^3$  and  $1 \text{ Mm}^3$  nourishments, respectively, and squares for the reference run. The numbers in (a) indicate the order of the breaches after the nourishment.



**Figure 5.7** Contour plot of difference in tidally-averaged significant wave height between the model runs with and without the  $0.5 \text{ Mm}^3$  nourishment placed at the ebb-tidal delta platform during transition Phase  $2 \rightarrow 3$  (at the moment of nourishment placement). Here, blue (purple) indicates lower (higher) wave height due to the nourishment. The red and yellow lines encloses the area where the corresponding difference in tidally-averaged sediment concentration exceeds  $400 \text{ gr/m}^3$  (red positive, yellow negative). The shown area is 4.5 km (east-west direction) by 3 km (north-south).

inlet (Figures 5.5c and d) during a breach cycle; this is the spatially maximum value in the inlet at any moment. The lower marker is the minimum amplitude in the cycle (i.e., the temporal minimum of the spatially maximum amplitude), which occurs between 100 and 300 days before the breach; the upper marker is the maximum amplitude in the cycle (i.e., the temporal and spatially maximum amplitude), which is modeled directly after the breach. It can be seen that the breach orientation correlates negatively with the maximum amplitude (the upper markers):  $R^2 \approx 0.47$ . This is particularly evident for breach orientations exceeding the maximum breach orientation in the reference run ( $11^\circ$ ). Furthermore, the range between minimum and maximum amplitude decreases with increasing breach orientation, especially for breach orientations greater than shore-normal ( $\sim 0^\circ$ ).

Figure 5.7 shows that at the moment of nourishment implementation, the larger ebb-tidal delta reduces the significant wave height and thereby enhances the wave sheltering of the ebb-tidal delta for especially the basin and the tip of the downdrift island. This reduction in wave energy was quantified for all nourishments by computing the maximum tidally-averaged significant wave height in the inlet. These time series are shown in Figure 5.8a and qualitatively, they are also representative of the wave sheltering of the downdrift island. It can be seen that an initial significant reduction in wave height between 0.1 and 0.4 m (given the offshore wave height of 2.0 m) is forced by the nourishments. For the  $1 \text{ Mm}^3$  nourishment, the wave height decreases even further for a short period after implementation because the minimum water depth decreases (Figure 5.3d). However, this increased wave sheltering is a short-term effect; within a period shorter than one cycle of channel-shoal dynamics, the significant wave height is within the range of the reference run.

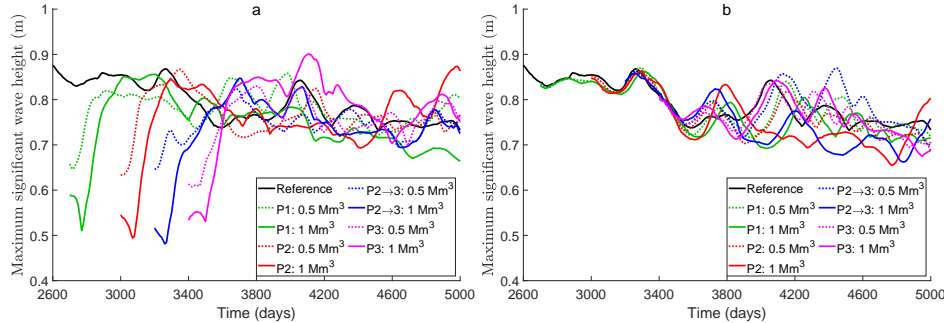


**Figure 5.8** Time series of the maximum tidally-averaged significant wave height in the inlet for the nourishments at (a) ebb-tidal delta platform and (b) ebb-shield.

### 5.3.2 Sensitivity to location

An ebb-shield nourishment has little effect on waves and morphological evolution. Figure 5.8b shows there is no initial significant reduction in wave height forced by the ebb-shield nourishment. After a few hundred days, there are changes in wave height in the inlet. However, it can be seen that this is only due to the changes in phase of the cyclic behavior and that there is no long-term increased wave energy dissipation on the nourishment.

Relative to the platform nourishment, the ebb-shield nourishment results in a more substantial long-term increase in ebb-tidal delta volume. Figures 5.9a and b show that the nourished sediment is removed from ebb-tidal delta slowly, independent of the timing. Contrary to the platform nourishment, the removed sediment is not transported into the basin; Figure 5.9b shows that, on average, no additional sediment is imported. Furthermore, Figure 5.9c shows that the initial effect of the increase in volume for the  $0.5 \text{ Mm}^3$  nourishments on the channel orientation is limited. Both the general behavior of the channel and the timing of the breaches follow the reference run in the displayed time frame. However, a  $1 \text{ Mm}^3$  nourishment (Figure 5.9d) does directly adjust both the channel orientation and the breach timing.

Figure 5.10 shows the relationship between the breach orientation and the subsequent period. It can be seen that some nourished model runs have one or more breaches with a larger breach orientation than those in the reference run. Again, these downdrift shifted breaches are followed by a period shorter than the shortest period in the reference run. Contrary to the platform nourishment, it is not necessarily the first breach that is most affected. As a result, the time scale is initially relatively unaffected for the smaller nourishments. After this, the periods deviate and the second breach is followed by a shorter period for Phase 2 and 3. For the larger nourishments, it is generally also the second breach that features a larger breach orientation and has a shorter subsequent cycle. This suggests that the effect of these nourishments is delayed. However, it remains unclear whether this is an delayed effect of the nourishment or due to nonlinear processes and inherent model variability. We checked whether the minimum water depth shows this delayed effect, but this did not show a significantly shallower platform.

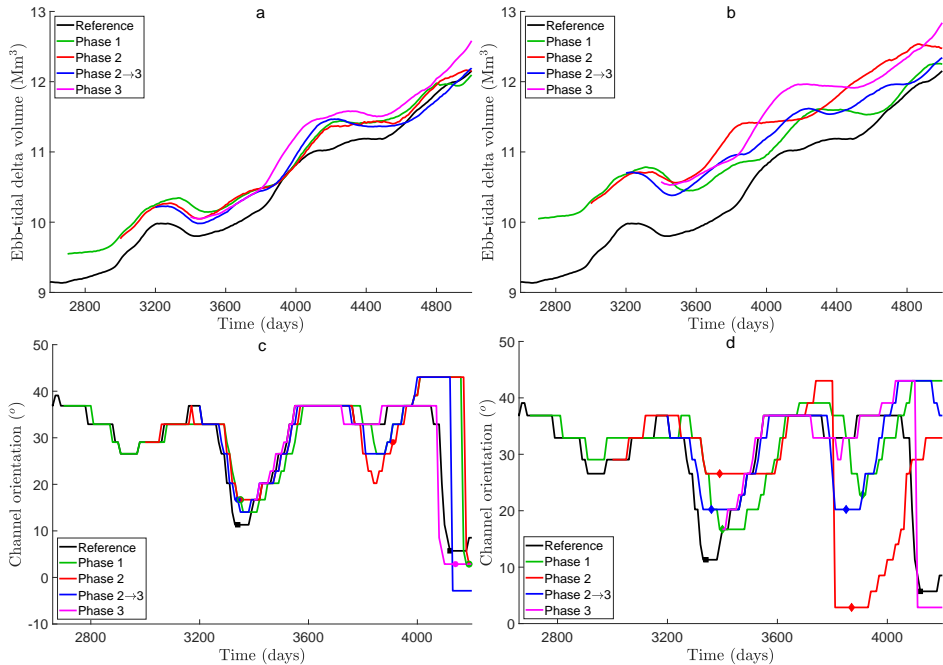


**Figure 5.9** Time series for the runs with a nourishment placed at the ebb-shield. (a+b) The volume of the ebb-tidal delta; and (c+d) the orientation of the main channel with markers indicating the breach orientation for the 0.5 Mm<sup>3</sup> (a+c) and 1 Mm<sup>3</sup> (b+d) nourishments. Colors indicate the timing of implementation (see legend).

### 5.3.3 Physical mechanisms

Figure 5.11 shows that the larger breach orientation is a direct result of the platform nourishment before the breach. This figure shows the erosion (blue) and deposition (red) at the moment of nourishment placement (Phase 2→3) for the model runs with (a) and without (b) the 0.5 Mm<sup>3</sup> nourishment. This model run is chosen because the bathymetries only differ at the nourishment location when the breach is initiated; its outcome is representative of all

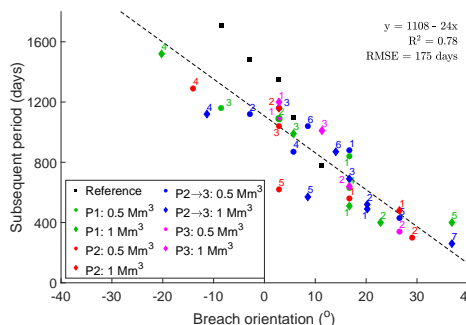


**Figure 5.10** As Figure 5.6a, but for the nourishments at the ebb-shield.

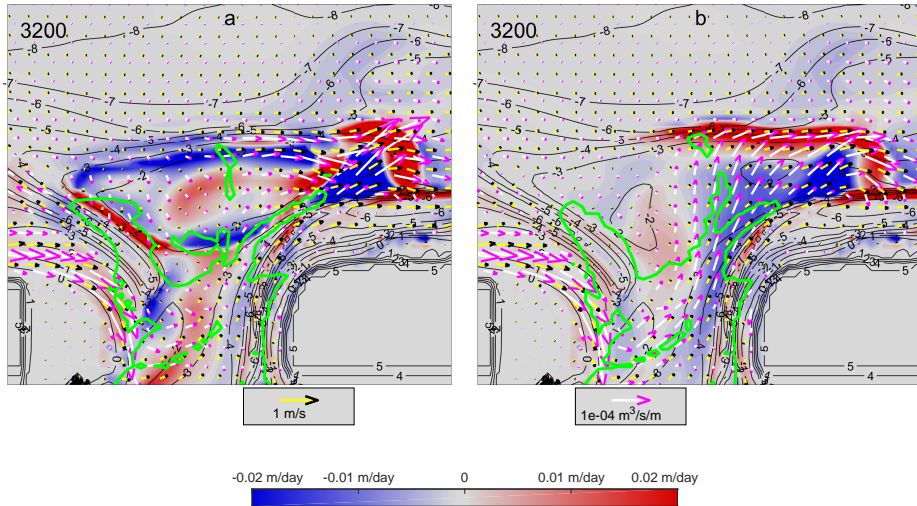


**Figure 5.11** Erosion (blue) and deposition (red) for the model runs (a) with and (b) without the  $0.5 \text{ Mm}^3$  nourishment placed at the ebb-tidal delta platform during transition Phase 2 → 3 at the moment of nourishment placement (3200 days). The vectors represent tidally-averaged total sediment transport (white/magenta) and flow velocities (yellow/black). The arrows are shown in every third grid cell in both directions. The green line encloses the area with semi-diurnal flow magnitude exceeding  $0.23 \text{ m/s}$ . The shown area is 4.5 km (east-west direction) by 3 km (north-south).

model runs with larger breach orientations. In the reference run (Figure 5.11b), a large blue area is visible on the ebb-tidal delta, indicating the breaching process. In contrast, in the run with nourishment (Figure 5.11a), deposition is found on the shallow areas of the ebb-tidal delta, whereas the erosion that represents the breach only takes place on the downdrift side of the platform. This is attributed to two effects forced by the nourishments. Firstly, because of the reduced water depth, more waves break over the shallower ebb-tidal delta and thus incoming waves force a stronger eastward mean flow in this area (see yellow/black vectors) and increase the sediment concentration at the outer lobe by means of increased bed shear stress (red contour in Figure 5.7). This is in line with the hypothesis postulated in Section 5.1. Thereby, they cause erosion of the seaward side of the ebb-tidal delta (blue area roughly between 2 m and 5 m isobaths) and deposition where the ebb-tidal delta breaches in the reference run. Secondly, as shown by the green contours in Figure 5.11, the tidal flow over the breach location is reduced because of frictional effects caused by the reduced water depths. Combined with the reduced sediment concentration landward of the ebb-tidal delta (yellow contour in Figure 5.7), this weakens the erosion by tidal flows. In Section 5.1, we expected that the final result would be that breaching would be postponed and channel rotation prolonged. However, the final result is that the breaching is shifted (i.e. larger breach orientations) rather than postponed, even though the channel does reach larger rotation angles.

In Section 5.3.1, it was shown that the nourishment placed during Phase 3 results in shorter time scales despite a small decrease in breach orientation. Therefore, the reason for the

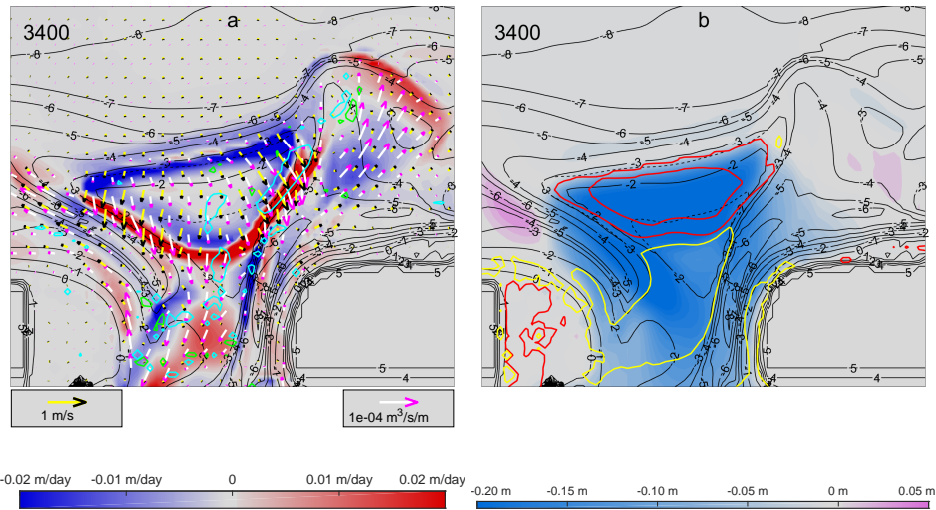


**Figure 5.12** (a) The difference in erosion and deposition between the model runs with 0.5 Mm<sup>3</sup> nourishment placed at the ebb-tidal delta platform during Phase 3 and the reference run with red and blue indicating relative deposition and erosion, respectively. The vectors represent the difference in tidally-averaged total sediment transport (white/magenta) and flow velocities (yellow/black). The arrows are shown in every third grid cell in both directions. The green and cyan lines encloses the area with difference in semi-diurnal flow magnitude exceeding 0.06 m/s with green positive (stronger flow with nourishment) and cyan negative. (b) As Figure 5.7, but for the nourishment placed during Phase 3. The shown area is 4.5 km (east-west direction) by 3 km (north-south).

shorter periods due to nourishments after the breach differs from that for the nourishments before the breach. For nourishments after the breach, shorter periods originate from the effect of the nourishment on the channel rotation and shoal growth. Figure 5.12a shows the difference in the initial erosion/deposition patterns between the model run with and without the 0.5 Mm<sup>3</sup> nourishment. The red area on the westward side of the channel shows that the channel rotation in the nourished run is more pronounced than in the reference run. This area partly overlaps with the cyan contour indicating an area with reduced tidal flow; because tides reduce channel rotation (Chapter 3), this reduction enhances channel rotation. Additionally, the yellow/black vectors in Figure 5.12a and the red contour in Figure 5.12b show an increase in wave-induced landward mean flows and sediment concentration over the nourished area, respectively. This combination causes more sediment transport to the westward side of the channel and thus faster channel rotation. As a result, there is a 5° difference in channel orientation at 3500 days (see Figure 5.5a). The acceleration in channel rotation is in line with the hypothesis for the nourishments placed during this phase (Section 5.1). This faster channel rotation only partly explains the shorter time scale for the first cycle. The second part of the explanation lies in the tidal flow velocities. In the reference run, the drop in tidal flow in the inlet which causes the breach (black lines in Figures 5.5c and d) follows after a relatively long period of shoal growth. Because of the nourishment, less shoal growth is needed to have a shoal with the same volume. Therefore, the drop in tidal flow velocities

in the inlet is earlier (magenta lines in Figures 5.5c and d) and the breach accelerated. This is contrary to what we expected; we hypothesized in Section 5.1 that shallower platform will accelerate the shoal growth, but in fact, the shoal growth phase is only shortened.

## 5.4 Discussion

### 5.4.1 Comparing model findings to nourishment objectives

Coastal authorities are considering to implement mega-nourishments on Dutch ebb-tidal deltas because of the significant loss in sediment volume in the last century (Elias et al., 2012) and because the remaining ebb-tidal deltas may not be capable of delivering the sediment needed to compensate for future relative sea-level rise (Wang et al., 2018). This innovative approach is a ‘nature-based solution’ and has analogues to the Sand Engine at the western coast of the Netherlands (Stive et al., 2013). The three objectives of ebb-tidal delta nourishments are (1) a sustainable increase in ebb-tidal delta volume, (2) more sediment transport into the Wadden Sea, and (3) acceleration of the cyclic behavior to stimulate sediment transport to the downdrift coast (‘building with nature’). In this section, our model findings are evaluated for these objectives.

Firstly, if placed at the ebb-shield, the nourished sediment is maintained on the ebb-tidal delta for several cycles of channel-shoal dynamics. However, if it is placed on the shallow ebb-tidal delta platform, roughly half of the additional sediment is removed from the ebb-tidal delta in a period much shorter than one cycle. It was expected that an increase in ebb-tidal delta volume would also enhance the offshore wave breaking. However, a nourishment at the ebb-shield has no significant effect on the short- or long-term wave energy propagation because it is in a region where depths are relatively large and extra sediment does not result in more wave breaking. A preliminary modeling study by Fu (2018) showed that a nourishment on the ebb-tidal delta platform will result in a substantial increase in offshore wave energy dissipation, reducing the wave energy reaching the nearshore zone of both barrier islands and penetrating through the inlet. In this study, we replicated these findings (Figures 5.7 and 5.8). The platform is already very shallow and additional sediment caused more intense wave breaking. Within half a cycle of channel-shoal dynamics, this sheltering effect has vanished because the minimum water depth increases as sediment is removed from the ebb-tidal delta.

The second objective is more likely to be achieved for the platform nourishment; roughly 20-40% of the sediment that is removed from the ebb-tidal delta ends up in the basin. No increase in import was modeled for the ebb-shield nourishment, independent of implementation timing and/or size of nourishment. In Section 5.4.2, the dependence of these findings on the modeling setup will be discussed.

Regarding the third objective, the model findings show that if the ebb-tidal delta platform would be nourished, one or two shorter periods of cyclic channel-shoal dynamics are expected. This is in line with the acceleration found in the modeling study of Fu (2018). These shorter periods are only for the first one or two cycles after nourishment placement and are either the result of breaches taking place further downdrift or due to faster channel rotation and a shorter period of shoal growth. If the nourishment would be placed at the ebb-shield, its effect on the time scale and morphological development of the ebb-tidal delta is less pro-

nounced than for the ebb-tidal delta platform. Also for this nourishment location, shorter periods were the result of larger breach orientations.

#### 5.4.2 Shortcomings

The patterns of sediment transport in a tidal inlet system are typically different for different types of sediment (Herrling and Winter, 2014). In the current study, a uniform grain size with a diameter of  $250 \mu\text{m}$  was used. This sediment size was chosen because it is optimal for shoal formation and migration (Herrling and Winter, 2018) and ensures that the modeled ebb-tidal delta behavior mimics real systems. However, as shown by Bak (2017), the effect of the nourishment on sediment pathways also depends on the grain size. For example, more sediment would be imported into the basin if finer sediment would be used. Figure 5.4 shows that even for the nourishment that results in the largest import, less than 20% of the nourished volume is transported into the basin, probably because of the relatively coarse sediment. In order to assess the long-term changes in sediment exchange between basin and sea more accurately, multiple sediment fractions should be used. The Wadden Sea basin mainly consists of finer sediment, and so does the imported sediment. Modeling of the different pathways of different sediment fractions was beyond the scope of this study.

Similarly, in this study, a constant wave forcing was used. Since during storms the ebb-shield is particularly active (Herrling and Winter, 2014), it could be possible that high-energetic waves interact with a nourishments placed at the ebb-shield more than we achieved by using the steady wave forcing. Furthermore, shoals can form and grow during storms (Ridderinkhof et al., 2016b); this was also not incorporated in our model forcing. Future research should address the effects of real wave climate and different sediment fractions on long-term effects of ebb-tidal delta nourishments.

#### 5.4.3 Applicability

While this study was motivated by the nourishments planned or executed for the Ameland ebb-tidal delta, our results should not be seen as actual forecast for this system. Not only is the basin in our idealized model domain much smaller than the Ameland basin, also do the time scales, the ratio between tidal prism and littoral drift and the sediment composition differ. However, the model outcomes provide a general overview of the interaction between tidal inlets and nourishments on ebb-tidal deltas.

As discussed in Section 5.4.1, different objectives can be achieved by the specific nourishment locations. It appears that nourishing the ebb-shield, which was the location of the pilot nourishment (Figure 5.1), has little effect on waves and sediment pathways. We found no additional wave shielding, nor was more sediment transport into the basin predicted. This location does, however, increase the volume of the ebb-tidal delta for several cycles. The ebb-tidal delta platform is a more efficient nourishment location for increasing the safety functions of the ebb-tidal delta. These nourishments at least temporarily enhance the offshore wave energy dissipation. Furthermore, additional sediment is available for import to the basin, even for the coarse sediment diameter. Fu (2018) suggested that it is not the nourished sediment itself that is transported along this pathway, but that the nourishment increases the import of sediment originating from more dynamic areas of the ebb-tidal delta. Therefore, even a nourishment on the platform consisting of coarse sediment can result in the import of additional sediment.

In the Netherlands, the Wadden Islands suffer from severe erosion at the side of the islands that flank the inlets. Motivated by these problems, one of the main objective of an ebb-tidal delta nourishment is to increase the sediment transport to the downdrift coast by means of faster channel-shoal dynamics. Our outcomes show that nourishments on the ebb-tidal delta will indeed have this positive effect. However, policy makers should also take into account that most nourishments will result in an increase in maximum channel orientation. Further channel rotation against the downdrift island is a negative effect because it probably increases the erosion of this island.

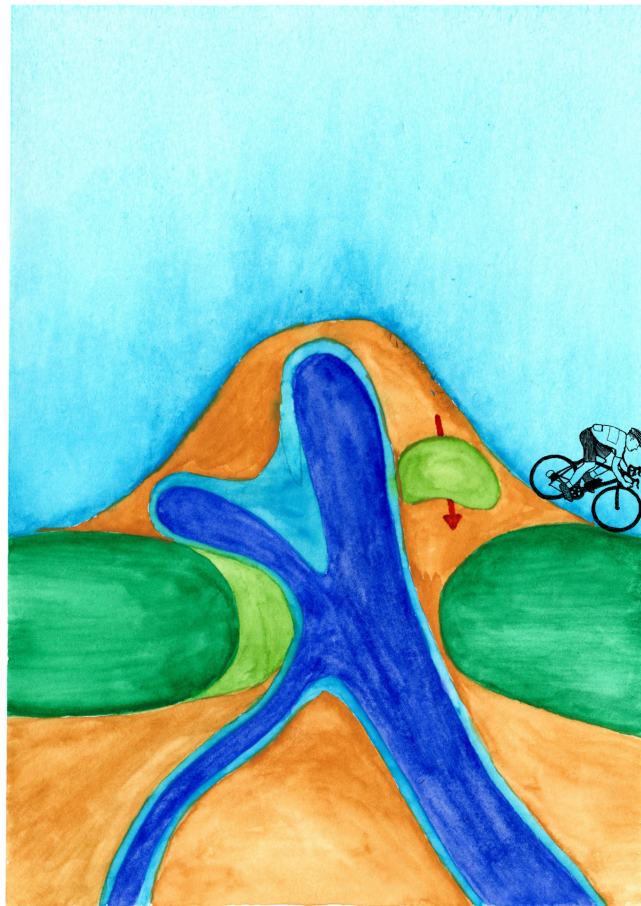
## 5.5 Conclusions

Mega-nourishments are considered on Dutch ebb-tidal deltas as a nature-based solution to combat structural erosion. This study assessed how ebb-tidal deltas will respond to large-scale nourishments. A nourishment on the ebb-tidal delta platform resulted in one or two shorter periods of cyclic channel-shoal dynamics; after this, the time scale reverted to its natural value. We found that the timing of the nourishment is important. For example, nourishments placed before the breaching of the ebb-tidal delta caused shorter time scales because of breaches taking place relatively close to the downdrift island, especially for the larger nourishment. In contrast, nourishments placed directly after the breach resulted in shorter periods because of faster channel rotation and a shorter period of shoal growth. Furthermore, roughly half of additional volume of the ebb-tidal delta was removed from the platform relatively quickly. Before this adaptation was completed, the surplus of sediment reduced the water depth and thereby increased the wave breaking over the ebb-tidal delta. Because within half a period of cyclic behavior the minimum water depth was within the range of the run without nourishment, this was found to be a relatively short-term effect.

In contrast, a nourishment at the ebb-shield had no significant effect on the wave energy dissipation because it is in a region where depths are relatively large. In other words, the extra sediment did not result in more wave breaking in the present simulations. Similarly, the nourishment effect on the morphological development of ebb-tidal deltas was limited. Because ebb-shield nourishments are relatively inactive, their volume is preserved longer on the ebb-tidal delta. Also for this nourishment location, shorter periods were the results of downdrift shifted breach locations.

Many nourishments caused the main channel to rotate further towards the downdrift island. Further channel rotation causes additional erosion of the downdrift island, which is a potential undesirable side-effect.





# Chapter 6 | Synthesis

This thesis aimed to increase the quantitative understanding of the cyclic behavior of ebb-tidal deltas in natural and human-impacted tidal inlet systems using numerical modeling simulations. Although cyclic channel-shoal dynamics has been observed at many systems, it was not well known how patterns of currents, waves and sediment dynamics change during a cycle. Furthermore, how these patterns of tides and waves in turn drive the cyclic behavior and determine the involved time scales was not well understood. These feedbacks between natural cyclic behavior, tides and waves at many ebb-tidal deltas are directly influenced by humans. From an applied perspective, it was unclear if and how cyclic channel-shoal dynamics will change during persistent sea-level rise, after basin area reduction or due to ebb-tidal delta nourishments. Below, I summarize and discuss how this thesis has advanced the knowledge on cyclic behavior of ebb-tidal deltas. In many instances I took the (Dutch) Wadden Sea as an example, but the obtained insights apply to barrier coasts and ebb-tidal deltas in general.

First, the main conclusions of this thesis are summarized, consecutively describing (1) the influence of changing ebb-tidal delta morphology on tides, waves and sediment dynamics; (2) the mechanisms causing the cyclic bed evolution; (3) the impact hereon of basin area reduction and sea-level rise; and (4) the effect of ebb-tidal delta nourishments on the morphological development of ebb-tidal deltas. Thereafter, my model findings are put in perspective and their implications are discussed. Furthermore, suggestions for future research are provided.

## 6.1 Main Conclusions

### 6.1.1 How does the cyclic behavior of the ebb-tidal delta influence the tide and wave dynamics and the sediment transport patterns?

The most common type of cyclic channel-shoal dynamics is the *ebb-tidal delta breaching* process, described by FitzGerald (1988). Herein, the cycle of shoal formation, migration and island attachment is concurrent with alternating phases of channel rotation and channel breaching. A clear example of this form of cyclic channel-shoal dynamics is present in the Dutch Ameland Inlet (Israel and Dunsbergen, 1999). Although each cycle differs greatly (Elias et al., 2019), the rough pattern of cyclic channel-shoal dynamics repeats every 50-60 years. Because the Ameland Inlet has been extensively monitored and is relatively undisturbed (Elias et al., 2012), it was used to study the effect of cyclic behavior on tides, waves and sediment transport in general. Many inlets feature cyclic behavior including the alternation between one and two channels in the inlet similar to that of Ameland Inlet (Cayocca, 2001; Kleinhans et al., 2015; Ridderinkhof et al., 2016a). Although the precise patterns and time scales differ from inlet to inlet, the outcomes of this case study are expected to be generally applicable to the inlets that feature *ebb-tidal delta breaching*.

In Chapter 2, the Delft3D/SWAN models were used to simulate these processes during four phases of the cycle at the Ameland Inlet: (1) channel rotation (one channel); (2) shoal growth; (3) channel breaching (two channels); and (4) filling up of the old channel. Historic (i.e., measured) bathymetries were implemented and forced with a representative morphological tide and 21 distinct wave classes based on 20 years of measured wave data. The wave classes cover a wide range of wave heights, periods and directions and each class was combined with the associated water level setup/setdown. This elaborate wave climate was included because the wave propagation over complex morphology strongly depends on wave height, period and direction. Furthermore, many studies on tidal inlet systems have neglected the effect of waves (Van Leeuwen et al., 2003; Van der Vegt et al., 2006; Van der Vegt et al., 2009; Dissanayake et al., 2012).

The analysis of the weighted mean patterns of waves, currents and sediment transport demonstrated a strong effect of the morphology. Firstly, the presence and position of the shoal on the ebb-tidal delta strongly influences the amount of wave energy dissipation in the nearshore zone of the downdrift island. When a shoal is present northwest (predominant wave direction) of the downdrift island, between 7% and 18% of the incoming wave energy reaches the nearshore zone. This increases to more than 40% after the shoal has attached to the island. Secondly, the wave energy in the nearshore zone of the updrift island depends on the size of the updrift oriented channel. When this channel is largest, more energy propagating in the direction of the updrift island dissipates on the ebb-shield and the shallow areas flanking this channel; only 31% reaches the nearshore zone. Due to the downdrift migration of the updrift channel and the related shallow areas, this eventually increases to 55%. Simultaneously, the wave energy entering the basin also increases during the channel rotation; it is lowest ( $< 0.45 \text{ kW m}^{-1}$ ) when the inlet features one updrift-oriented channel and highest ( $< 0.93 \text{ kW m}^{-1}$ ) when the inlet features two channels. Because waves coming from the predominant wave direction reaching the inlet cross the updrift part of the ebb-tidal delta, the inlet is better protected from incoming waves when the main channel has an updrift orientation, similar to protection of the updrift island.

The results further indicate that cyclic variations in net sediment exchange between the basin and the sea are an inherent feature of the cyclic behavior. Most sediment is exported with two channels in the inlet (Phase 3) and least when the inlet has one channel (Phase 1). This cyclic export directly results from temporal variations in tidal characteristics. In more detail, both the tidal asymmetry and the subtidal mean flow in the inlet are cyclic and follow the periodicity of the one- and two-channel inlet configurations. Because of the abundance of intertidal areas in the basin, the peak ebb flow velocities in the inlet are generally higher than the peak flood flow velocities. This tidal asymmetry is most pronounced when the secondary channel is shallow with a difference between peak ebb and flood flow velocities up to 0.52 m/s. In contrast, the tidal asymmetry is relatively weak for a one-channel configuration. In this case, a mean circulation cell up to 0.36 m/s is present, which causes import at one side of the inlet and export at the other side.

### **6.1.2 What are the physical processes and feedbacks that drive the observed cyclic channel-shoal dynamics?**

The cyclic behavior observed at Ameland Inlet and many other inlets is categorized by FitzGerald (1988) as *ebb-tidal delta breaching*. For systems where the new channel is forming at the seaward side of the ebb-tidal delta, the cyclic behavior falls within the category of

*outer delta breaching*. Both types of cyclic behavior are characterized by four phases, namely (1) channel rotation; (2) shoal growth; (3) channel breaching; and (4) filling up of the old channel and deepening of new channel. In Chapter 3 it was studied how the mutual interaction between morphology, waves, currents and sediment transport drive the cyclic evolution of ebb-tidal deltas. Using an idealized Delft3D/SWAN model and by varying the forcing such that a wide range of tidal prism/littoral drift ratios (Bruun and Gerritsen, 1960) were simulated, I was able to reproduce both types of cyclic behavior. In model runs with high ratios, no cyclic behavior was found within the simulated period. Note that the idealized tidal inlet in Chapter 3 was one order of magnitude smaller than the Ameland Inlet.

Each phase has a distinct balance in the relative role of tides and waves. During the first phase, the rotation of the channel and formation and migration of the shoal scale with significant wave height and is relatively unaffected by changes in tidal flow and tidal range. This confirms the findings of Bertin et al. (2009), who also found shoal migration due to wave-induced mean flows. The identification of shoal formation with constant wave forcing expands on the work of Ridderinkhof et al. (2016b), who showed that storms can also induce shoal formation. Analysis in Chapter 3 further shows that the subsequent shoal growth during the second phase is a mutual effect of tides and waves. The wave-induced sediment concentrations is higher at the updrift side than at the downdrift side of the ebb-tidal delta. The sediment is transported by combined wave- and tide-induced mean flow and thereby causes the shoal growth. The breaching of the ebb-tidal delta platform during the third phase was classically attributed to tides (FitzGerald, 1988; Cayocca, 2001). However, even though changes in tidal currents cause the ebb-tidal delta to breach, the analysis in Chapter 3 shows that the waves are necessary for sufficient sediment entrainment. On the other hand, when the wave height is too large, the channel rotation continues and the breach is postponed. The infilling of the old channel during the last phase is a wave effect. However, the deepening of the new channel can be explained only by waves and tides operating simultaneously.

The observations of Gaudiano and Kana (2001) and Ridderinkhof et al. (2016a) indicate a positive relationship between the tidal prism of a system and the period between successive shoal attachments. Analysis of the present simulations suggests that the typical time scale generally increases with decreasing littoral drift. For increasing ratio between tidal prism and littoral drift, the cyclic behavior dramatically slows down and, for ratios exceeding 250, no shoals are formed and the channel does not migrate. Furthermore, for increasing tidal prism the cycle period becomes larger, confirming the results of Gaudiano and Kana (2001) and Ridderinkhof et al. (2016a).

As was already shown for the Ameland Inlet, cyclic changes in sediment transport through the inlet are an inherent feature of *ebb-tidal delta breaching*. This only occurs for systems with *ebb-tidal delta breaching* because, in this type of behavior also the morphology in the inlet changes significantly. For *outer delta breaching* the main changes take place further seaward and do not affect the morphology of the inlet. The cyclic exchange for *ebb-tidal delta breaching* mainly results from variations in the mean flow in the inlet. In Chapter 2, this was also due to temporal changes in tidal asymmetry, which depended on the presence of a shallow secondary channel in the inlet. Because the model simulations presented in Chapter 3 did not include the alternation between one and two channels in the inlet, the tidal asymmetry was relatively steady throughout the cyclic behavior.

### 6.1.3 How do sea-level rise and basin area reduction affect the cyclic behavior of tidal inlet systems?

The observations used by Elias et al. (2012) have shown erosion of Dutch ebb-tidal deltas during the last century. This process has been linked to a significant reduction of the Dutch Wadden Sea basin area by the closure of the Zuiderzee and Lauwerszee. Furthermore, measurements over the last 150 years have revealed a steady relative sea-level rise of 0.2 m per century along the Dutch coast (Elias et al., 2012, and references herein). Many tidal inlet systems worldwide are threatened by these anthropogenic influences (e.g. FitzGerald et al., 1984; Sennes et al., 2007; Rizzetto et al., 2009; Beck and Kraus, 2011; Dissanayake et al., 2012; Hansen et al., 2013; Wang et al., 2014; Becherer et al., 2018; Wang et al., 2018; Benninghoff and Winter, 2019; Velasquez-Montoya et al., 2020). Erosion of ebb-tidal deltas poses problems for the coastal safety functions because these ebb-tidal deltas are less able to absorb incoming wave energy and to provide sediment to basin and islands to balance local erosion. The long-term effect of sea-level rise and basin reduction on the ebb-tidal delta dynamics was assessed in Chapter 4 using the Delft3D/SWAN model setup of Chapter 3. The outcome for a wide range of basin size reductions and rates of sea-level rise were compared with the outcomes of Chapter 3. For reasons of feasibility, only *ebb-tidal delta breaching* was considered.

The results show that basin area reduction causes the first cycle to be slower, while after the adjustment period the cycles are faster. Furthermore, during the adjustment the ebb-tidal delta volume and cross-sectional area of tidal inlet decreases. This is in line with observations of the Frisian Inlet (Oost, 1995). For a 10%, 20%, 30% and 50% basin size reduction, the identified adjustment time scale is roughly 14%, 26%, 60% and 100% of the typical time scale of undisturbed cyclic behavior, respectively. The initial longer period is due to severely reduced tidal flow in the inlet, caused by a cross-sectional area that is too big for the reduced tidal prism. As a result, it takes longer for the shoal to grow (which is caused by waves and tides), whereas the reduced tidal flows do not significantly affect the channel rotation rate (which is solely driven by waves). A small reduction in the pace of the breaching of the ebb-tidal delta was also modeled. After the adjustment period, the shorter period is in line with the reduced tidal prism. Surprisingly, for the simulations with basin reduction the waves in the inlet are less energetic despite the eroding ebb-tidal deltas.

For sea-level rise, the effect on the time scale of cyclic behavior strongly depends on the sea-level rise rate. For a rate up to 1.5 cm/yr, the cyclic behavior accelerates. For these runs, the sediment supplied to the inlet compensates for the increase in cross-sectional area due to the rising water level. A small decrease in peak flow magnitudes causes a downdrift shift in breach location, which is linked to the acceleration of the cycle. For a rate of sea-level rise above 1.5 cm/yr, the periods of cyclic behavior become longer. The cross-sectional area of the inlet gradually increases, resulting in significantly lower tidal flow magnitudes, which slows down the cyclic channel-shoal dynamics. Furthermore, for all rates of rising water level, the volume of the ebb-tidal delta is maintained. The ebb-tidal delta does not lose sediment, but is simply submerged further below the ever-increasing mean water level. However, because the wave energy dissipation over the ebb-tidal delta depends on the water depth, the waves in the inlet and therefore in the basin become more energetic. For example, a 0.2 m sea-level rise causes a 0.1 m increase in the mean significant wave height in the inlet.

#### **6.1.4 What is the effect of large-scale ebb-tidal delta nourishments on ebb-tidal delta dynamics?**

The sea-level rise at the end of the 21st century is expected to be 2 to 5 times faster than during the 20th century (Vermeersen et al., 2018), such that higher sedimentation rates in the Dutch Wadden Sea are needed to maintain system morphology (Wang et al., 2018). It is unlikely that the eroding ebb-tidal deltas are able to provide this sediment. One of the innovative mitigation routes, considered by the Dutch authorities, is to place mega-nourishments ( $\sim 20$  million Mm<sup>3</sup> or more) directly on the ebb-tidal delta. Such a ‘nature-based solution’ is inspired by the mega-nourishment at the wave-dominated western coast of the Netherlands (Sand Engine, see Stive et al., 2013). Chapter 5 explores how ebb-tidal deltas and their cyclic behavior will respond to different ebb-tidal delta nourishments. The modeling philosophy is similar to that in Chapter 4: different nourishments were placed in the undisturbed model setup of Chapter 3 and its outcomes were compared. The implemented nourishment locations are the ebb-shield and the ebb-tidal delta platform because they currently are the most probable options for the planned nourishment. Two nourished volumes were tested, equal to roughly 5% and 10% of the ebb-tidal delta volume. Nourishments were either placed during the phase of channel rotation and shoal migration, during shoal growth, during breach initiation or after the breach and before the channel rotation.

The net effect on the time scale of cyclic behavior for a nourishment placed at the shallow ebb-tidal delta platform is that it initially accelerates the cyclic behavior. In general, the periods of the first one or two cycles after nourishment placement are shorter. Most simulations with these nourishments feature one or two periods of less than 500 days, whereas the typical period for the simulation without nourishments is between 800 and 1500 days. After this initial acceleration, the nourishment no longer affects the time scales.

The maximum significant wave height in the inlet directly after the nourishment placement at the ebb-tidal delta platform decreases from roughly 0.85 m to 0.55 m for the larger and 0.65 m for the smaller nourishment. Because a large portion of the additional sediment is quickly removed from the delta, this additional capacity of the ebb-tidal delta to filter incoming wave energy diminishes when the minimum water depth increases within half a cycle of channel-shoal dynamics after nourishment implementation. No increase in offshore wave energy dissipation was found for a nourishment placed at the ebb-shield. However, this nourishment location does increase the volume of the ebb-tidal delta for a longer period. For a platform nourishment, roughly half of the nourished sediment is removed from the ebb-tidal delta in a period much shorter than one cycle. Moreover, 20-40% of the sediment that is removed from the ebb-tidal delta ends up in the basin.

Furthermore, the relative importance of tides and waves identified in Chapter 3 for the three phases are disturbed by the nourishment itself, which also adjusts the duration of the different phases. In general, larger nourishments have larger effects on the different phases than smaller ones. During the channel rotation phase, the nourishment placed at the shallow ebb-tidal delta platform decreases the local water depth and thereby increases the relative importance of waves. This in turn accelerates channel rotation. Furthermore, the shoal growth rate stays the same and, because a nourishment placed during this phase instantaneously increases the volume of the shoal, less time is needed to get a large shoal and the breach occurs earlier. When the nourishment is placed during the breaching phase, the part of the ebb-tidal delta that breaches shifts downdrift. Moreover, this nourishment causes the old channel to rotate further, incising the downdrift island. Nourishments during the other phases can also

cause further channel rotation, especially if the nourishment is placed during the phase of channel rotation. Note that the effect of the nourishments is not limited to the phase in which it is implemented. Faster channel rotation, a shorter shoal growth phase and down-drift shifted breaches also happen for nourishments implemented during the other phases, albeit less pronounced.

Both in Chapters 4 and 5, the time scale of the disturbed cyclic behavior depends on the breach location, i.e., the orientation of the new channel that is created during the breach. Shorter periods are the result of a downdrift shift in breach location, which in turn is attributable to a decrease in tidal flow and an increase in wave-induced mean flows and sediment concentration. This shift can be forced by either nourishments at the platform, sea-level rise or basin reduction. If the nourishment is placed at the ebb-shield, its effect on the time scale is much less pronounced. However, even for these model simulations, downdrift shifted breaches are followed by a shorter cycle.

## 6.2 Discussion and perspectives

### 6.2.1 Modeling system

The conclusions of this thesis were obtained using numerical models because they allow for isolated interventions and can thus be used to differentiate their impacts and study underlying mechanisms. For example, in Chapter 3, the littoral drift was varied amongst the model runs to identify the relationship between littoral drift magnitude and the time scale of cyclic behavior. Furthermore, the effect of sea-level rise, basin reduction and nourishments could be separated in Chapters 4 and 5.

Of course, models are never perfect and the results should thus be interpreted with care. Within models complex processes are often parametrized and results therefore depend on chosen model settings. The main aim of this section is to discuss how the choices that were made in the model setup might have influenced the results and conclusions.

Firstly, several model parameters strongly influenced the model results. The most important parameter was the wave-related bed load transport factor  $BedW$ , which influences the strength of the onshore transport by nonlinear waves and thereby influences the steepness of the coast. This parameter was calibrated and a value was chosen ( $BedW = 0.3$ ) for which the coastline stayed at a fixed position and for which the steepness of the nearshore zone also stayed relatively constant with time. Furthermore, the littoral drift should stay constant with time for the time scales of interest (several cycles of channel-shoal dynamics). The upper left panel in Figure 6.1 shows unrealistic coastal steepening and building out of the coast with the default value of  $BedW = 1$ . The generation of this cliff-edge coast resulted in a decline in the littoral drift over time. Because insufficient sediment was available and wave breaking was constraint to one line of grid cells, the wave-driven alongshore currents decreased. As discussed in Chapter 3, a littoral drift that decreased within a period shorter than that of the modeled cyclic behavior caused subsequent cycles to differ substantially. The model runs in Chapter 3 did not reproduce the Ameland-like alternation between a one- and a two-channel inlet configuration, however it did when  $BedW = 1$  was chosen (lower panels in Figure 6.1). Instead, the channel splitting/breaching location shifted to the ebb-tidal delta with  $BedW = 0.3$ . This clearly shows the sensitivity of model simulations to the  $BedW$  parameter. Possibly, the above-mentioned problems could be mitigated by the recent ad-

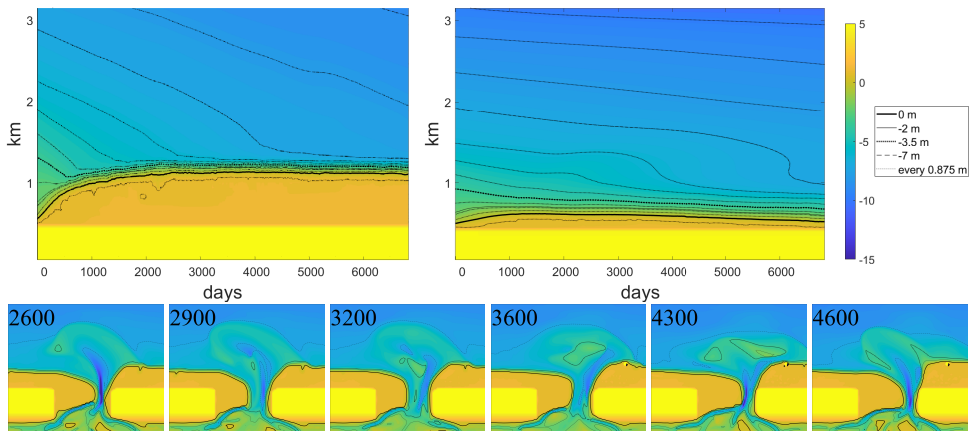


**Figure 6.1** Upper: Hovmöller diagram of the updrift cross-shore coastal profile for  $BedW = 1$  (left) and  $BedW = 0.3$  (right). Below: obtained bathymetries from a model run with  $BedW = 1$ . In the upper left corner of each panel, the number of modeled days is shown.

vancements in flexible mesh (e.g. Symonds et al., 2016) and the improved parametrization of the wave-related bed load transport due to wave asymmetry (Boechat Albernaz et al., 2019).

Secondly, the spatiotemporal dimensions of the systems in Chapter 3, 4 and 5 are relatively small. Because these chapters show morphological development that also takes place in larger systems and because I identified the relevant mechanisms for a wide range of ratios between tidal prism and littoral drift, I believe that the new insights increase our understanding of tidal inlet systems of all sizes as long as it are short basins. The model simulations in Chapters 3-5 were designed for downdrift oriented ebb-tidal deltas and relatively short basins. Furthermore, they did not feature the alternation between one and two channels in the inlet similar to that of Ameland Inlet. Because nuances in the relative roles of tides and waves might change as a function of basin size, it would complement this thesis by modeling the cyclic behavior for a system with size, time scale and channel orientation similar to Ameland. However, the modeling of the morphological development for Ameland-like systems would require improvements in both the model and the model setup, as the idealized model setup used in Chapters 3-5 was unsuitable for this task for two main reasons. Firstly, for accurate analysis, each model simulation should feature more than one cycle of the channel-shoal dynamics. In the present model setup, the littoral drift is only steady for roughly 30 years, which is close to half the time scale of Ameland. After this, a decline in littoral drift due to problems with the above-mentioned coastal stability makes the results untrustworthy. Secondly, the modeling of larger systems significantly increases the computational effort. In theory, expanding the model domain to incorporate a larger system of this size can be done without computational expense by increasing the grid size. However, a coarser grid in the current model setup amplified the existing coastal stability problems because the waves are then breaking in only one row of grid cells. Progress is needed in the cross-shore sediment balance for the long-term modeling of tidal inlet systems. Any advancements in that direction are hereby highly encouraged.

Thirdly, all model simulations in this thesis represent isolated tidal basins with no-flow boundary conditions. Similar to many modeling studies (amongst others, Van der Vegt et al., 2006; Van der Vegt et al., 2009; Dissanayake et al., 2012; Nahon et al., 2012; Ridderinkhof et al., 2014b; Ridderinkhof et al., 2016b), it was assumed that in a barrier coast, each basin can be treated as an isolated system. However, recent studies have shown that the wind-driven exchange of water and sediment between basins is much more pronounced, especially during storms (e.g. Duran-Matute et al., 2014; Herrling and Winter, 2015; Herrling and Winter, 2017; Herrling and Winter, 2018). Recent studies have shown that also for Ameland Inlet flows over the tidal divides can be large despite the relatively high divides (Li, 2018; van Weerdenburg, 2019; Xu, 2019). In Chapter 2, the isolated Ameland Inlet featured net sediment export through the inlet during fair-weather and net import during storms. The latter is in contrast with Xu (2019), who found that a passing storm surge forces net outflow of water and sediment for the Ameland Inlet. Therefore, including basin connectivity and wind-driven processes would lead to quantitative differences in the obtained patterns of waves, tides and sediment transport in Chapter 2. However, it was the aim of this chapter to isolate the effect of changing ebb-tidal delta morphology in general and not to provide accurate estimates for the chosen inlet. Ameland Inlet was used as a case study for cyclic behavior. Furthermore, the contribution of storm surges (i.e., when the exchange of water and sediment over the watersheds is relevant) to the weighted mean in Chapter 2 is limited because the presence of mean water level below 0.5 m is close to 99%. Therefore, it is likely that basin connectivity will not affect the qualitative differences among the phases of cyclic behavior considerably.

Lastly, throughout this thesis, a single grain size was used because this thesis focused on the cyclic behavior of the ebb-tidal delta and less on the development of the inlet and basin. Herrling and Winter (2018) showed that cyclic channel-shoal dynamics is the preferred pathway at a mixed-energy tidal inlet for the sediment size used in this thesis. However, it is known that finer sediment is transported more easily into the basin than coarse sediment (e.g. Sha, 1990; Gao and Collins, 1994; Herrling and Winter, 2014; Zhou et al., 2015). Thus, several sediment fractions would alter the modeling patterns of import/export through the inlet. Furthermore, Herrling and Winter (2014) showed sediment coarsening of the shoal, especially during storms, which probably impacts their growth rate and migration speed. Even the efficiency of an nourishment strongly depends on its sediment composition (Bak, 2017). For reasons of feasibility, all these complicating factors were not included in the present model simulations. Assessing the effects of nonuniform sediment distribution is a suitable future research topic.

### 6.2.2 Implications of results for coastal safety and management strategies

In the Netherlands, the current Kustgenese 2.0 program aims at generating knowledge to enable well-founded decisions on the policy and management of the Dutch coastal system as of 2020 (Rijkswaterstaat, 2017). These decisions should be in line with the coastal policy to, where possible, maintain the coastline with soft solutions rather than hard barriers. For the Wadden Sea, a nourishment of 20 million m<sup>3</sup> in the vicinity of a tidal inlet, i.e., at the ebb-tidal delta, is the proposed soft nature-based solution. The objectives of ebb-tidal delta nourishments are threefold, namely to (1) increase the ebb-tidal delta volume, (2) enhance the sediment transport into the Wadden Sea, and (3) to accelerate the cyclic behavior ('building with nature'). Such a mega-nourishment is inspired by the positive outcomes of the Sand

Engine at the west coast of the Netherlands, an unprecedented 21.5 million m<sup>3</sup> nourishment implemented in 2011 (Stive et al., 2013). To explore the possibilities for the Wadden Sea and to gain insight in the nourishment efficiency, Kustgenese 2.0 includes a pilot nourishment of roughly 5 million m<sup>3</sup> at the Ameland Inlet combined with major field campaigns. This thesis provides results that can be used to assess the effectiveness and impacts of such a nourishment.

The results of Chapter 5 indicate that the efficiency of a nourishment regarding the three objectives strongly depends on the nourishment location. Nourishments on the shallow ebb-tidal delta platform are most efficient for accelerating the cyclic behavior and enhancing the sediment transport into the basin. The ebb-shield as a nourishment location is not suitable for these objectives, but is more effective for increasing the ebb-tidal delta volume for a longer period. A potential downside of ebb-tidal delta nourishments is that it could result in an increase in maximum channel orientation, with negative effects on the downdrift island. There is ample room for future research. For example, in the simulations, the period of increased wave filtering is equal to half a cycle; for Ameland, this would correspond to 20–30 years. As a research topic, I suggest to test whether this translation is valid or whether the period of a few hundred days is not related to the duration of the cycle. This could, for example, be done by scaling the basin area and the nourishment by the same factor and examine if the period of increased wave filtering indeed also scales with the period of the cyclic behavior. Furthermore, other nourishment locations, such as the nearshore zone of the updrift island and in the inlet channel, remain to be tested. Moreover, in Chapter 5, the nourishments were implemented in a model run that represents an ebb-tidal delta unaffected by human influences. A logical next step is to combine Chapters 4 and 5 and to evaluate nourishment efficiency during periods of relative sea-level rise or combine a nourishment with a change in basin geometry.

A second unknown addressed the Kustgenese 2.0 program is the exchange of sediment between the Wadden Sea and the North Sea. This thesis did not aim to provide these estimates; these must arise from the combination of in situ measurements and realistic modeling. However, the outcomes of Chapters 2 and 3 suggest that values should be interpreted with care because they also depend on the phase of the cycle.

Currently, most Dutch Wadden Islands have severe erosional problems at their updrift heads due to strong tidal currents and incoming wave energy. The rate of erosion increases as the main channel rotates in the downdrift direction and is especially large when the channel impinges against the downdrift island (FitzGerald, 1988; Israel and Oost, 2001). In this thesis, there have been several instances where the maximum channel orientation increases, which will thus likely increase the erosion at the island heads. In Chapter 3, it was shown that an increase in wave height postpones the breach and causes further channel rotation. This suggests that a change in wave climate, for example due to climate change, will amplify these problems. Furthermore, an increase in maximum channel orientation is one of the effects of a reduction in basin size (Chapter 4) and a possible unwanted side-effect of ebb-tidal delta nourishments (Chapter 5). There exists a need to quantify the island erosion for changes in channel position. Moreover, it is unknown how an increase in maximum channel orientation affects the wave energy reaching the island head. Future research should elucidate these topics.

The erosion and sedimentation of barrier islands is linked to the position of shoal attachment (Luck et al., 1975; FitzGerald et al., 1984). In general, a net positive sediment budget

is observed at the part of the coast downdrift of the attachment location, a neutral budget directly updrift and a negative budget further updrift (near the island head). Understanding the shoal attachment position in natural and human-impacted tidal inlet systems could therefore benefit coastal safety. For example, there are two opposing hypotheses regarding the effect of a basin area reduction on the shoal attachment position. Firstly, Elias et al. (2012) expected that a basin area reduction would result in shoals attaching to the downdrift island closer to the inlet because the ebb-tidal delta contracts in the direction of the inlet. Secondly, Israel and Oost (2001) related the location of shoal attachment to the orientation of the main channel with downdrift oriented channels resulting in shoal attachment also relatively down-drift. Because a reduction in basin area results in a more downdrift oriented channel and also increases the maximum channel orientation, this mechanism suggests shoal attachment further from the inlet. It remains unknown which of these two processes dominates and how this depends on the basin reduction. Furthermore, future research can examine changes in shoal attachment position during relative sea-level rise and after ebb-tidal delta nourishment.

## Appendix A | Model description

In this thesis, we simulated the hydro- and morphodynamics using the coupled Delft3D/SWAN numerical model. Here, the governing equations and the model settings are summarized. The parameter settings are presented in Table A.1.

### A.1 Hydrodynamics

#### A.1.1 Currents

The numerical model Delft3D was used in its 2DH mode, i.e., vertical variations were ignored. The depth-averaged flow velocities in the  $x$ - and  $y$ -direction,  $u$  and  $v$  respectively, and the water level with respect to the still water level,  $\eta$ , are calculated by solving the depth-averaged shallow water equations and the continuity equation,

$$\frac{\partial u}{\partial t} + u \frac{\partial u}{\partial x} + v \frac{\partial u}{\partial y} - fv = -g \frac{\partial \eta}{\partial x} - \frac{\tau_x}{\rho h} + \frac{F_{w,x}}{\rho h} + \frac{1}{h} \left[ \frac{\partial}{\partial x} \left( \mathcal{A} \frac{\partial u}{\partial x} \right) + \frac{\partial}{\partial y} \left( \mathcal{A} \frac{\partial u}{\partial y} \right) \right], \quad (\text{A.1a})$$

$$\frac{\partial v}{\partial t} + u \frac{\partial v}{\partial x} + v \frac{\partial v}{\partial y} + fu = -g \frac{\partial \eta}{\partial y} - \frac{\tau_y}{\rho h} + \frac{F_{w,y}}{\rho h} + \frac{1}{h} \left[ \frac{\partial}{\partial x} \left( \mathcal{A} \frac{\partial v}{\partial x} \right) + \frac{\partial}{\partial y} \left( \mathcal{A} \frac{\partial v}{\partial y} \right) \right], \quad (\text{A.1b})$$

$$\frac{\partial h}{\partial t} + \frac{\partial(hu)}{\partial x} + \frac{\partial(hv)}{\partial y} = 0, \quad (\text{A.1c})$$

with  $t$  the time,  $f$  the Coriolis parameter,  $g$  the gravitational acceleration,  $h$  the local water depth,  $\rho$  the density of water and  $\mathcal{A}$  the spatially uniform horizontal eddy viscosity. Moreover,  $\tau_x$  and  $\tau_y$  are the components of the combined bed shear stress of waves and currents, which was computed using the parameterization of Soulsby et al. (1993) applied to the wave-current interaction model of Van Rijn et al. (2004) (Chapter 2) or Fredsøe (1984) (Chapter 3 to 5). The bottom roughness is determined using the Chézy formulation with a uniform Chézy coefficient of  $65 \text{ m}^{1/2}\text{s}^{-1}$ . Furthermore, the components of the wave-induced force per surface area,  $F_{w,x}$  and  $F_{w,y}$ , are computed by SWAN and are discussed below.

In Equations A.1a and b, the first three terms represent the temporal acceleration and the advective acceleration in the  $x$ - and  $y$ -direction. The last term on the left-hand side corrects for earth's rotating framework of reference (Coriolis force). The right-hand side consists of the pressure gradient term, the bed friction, the wave-force and a term that parameterizes and incorporates the aggregate effect of turbulent and sub-grid fluid motions. Moreover,

Equations A.1c assumes the water to be incompressible and simply states that the water level rises when more water enters than leaves an area.

### A.1.2 Waves

The numerical model SWAN (Simulating WAves Nearshore) is a phase-averaging spectral wave model. It computes the wave spectral action density,  $N$ , using the wave action balance equation in its stationary form

$$\frac{\partial(c_{g,x}N)}{\partial x} + \frac{\partial(c_{g,y}N)}{\partial y} + \frac{\partial(c_{g,\theta}N)}{\partial \theta} + \frac{\partial(c_{g,\sigma}N)}{\partial \sigma} = \frac{S}{\sigma}. \quad (\text{A.2})$$

Here,  $\theta$  is the spectral direction,  $\sigma$  is the relative frequency,  $c_{g,x}$  and  $c_{g,y}$  are the wave group velocity components and  $S$  represents the generation, dissipation and redistribution of wave energy. Note that  $N$  relates to the wave energy density by  $N = E/\sigma$ . The first two terms on the left-hand side of Equation A.2 describe the propagation of wave energy in  $x$ - and  $y$ -direction, the third term represents refraction due to spatial gradients in currents or water depth, and the fourth term describes any change in relative wave frequency spectrum. On the right-hand side is the sources and sinks term, which here is limited to wave breaking (formulation of Battjes and Janssen, 1978,  $\gamma = 0.73$ ), white-capping (Chapter 2: Van der Westhuyzen 2007; Chapters 3-5: Komen et al. 1984) and bottom friction (JONSWAP).

Subsequently, SWAN communicates the resulting wave-induced force to Delft3DS, which is determined by

$$F_{w,x} = -\frac{\partial T_{xx}}{\partial x} - \frac{\partial T_{xy}}{\partial y}, \quad (\text{A.3a})$$

$$F_{w,y} = -\frac{\partial T_{yx}}{\partial x} - \frac{\partial T_{yy}}{\partial y}, \quad (\text{A.3b})$$

where the elements of the radiations stress tensor (see Longuet-Higgins and Stewart, 1962),

$$T_{xx} = \int_0^{2\pi} \int_0^{\infty} E \left( n \cos^2 \theta + n - \frac{1}{2} \right) d\sigma d\theta, \quad (\text{A.4a})$$

$$T_{yy} = \int_0^{2\pi} \int_0^{\infty} E \left( n \sin^2 \theta + n - \frac{1}{2} \right) d\sigma d\theta, \quad (\text{A.4b})$$

$$T_{xy} = S_{yx} = \int_0^{2\pi} \int_0^{\infty} E n \sin \theta \cos \theta d\sigma d\theta, \quad (\text{A.4c})$$

result from the net depth-integrated fluxes of wave-induced momentum. Here,

$$n = \frac{|\vec{c}_g|}{c_w} = \left( \frac{1}{2} + \frac{\kappa h}{\sinh 2\kappa h} \right), \quad (\text{A.5})$$

with  $c_w = \sigma/\kappa$  the phase velocity of the waves and  $\kappa$  the wave number.

## A.2 Sediment transport

The used sediment transport formulations comprise of bed load and suspended load transport computed independently following the equations of Van Rijn (2007a) and Van Rijn (2007b). Sediment transport below a certain reference height is treated as bed load transport and that above the reference height is treated as suspended load. Both types are split into transport due to currents and transport due to waves.

### A.2.1 Bed load

The current-related bed load transport in the  $x$ - and  $y$ - direction,  $q_{b,c,x}$  and  $q_{b,c,y}$ , is calculated from the depth-averaged velocity as

$$q_{b,c,x} = 0.5 \frac{u}{|\vec{u}|} \frac{\tau_s^2}{\rho d_*^{0.3}} \frac{d_{50}}{\tau_{cr}} \frac{\tau_s - \tau_{cr}}{\tau_{cr}} \mathcal{H}(\tau_s - \tau_{cr}), \quad (\text{A.6a})$$

$$q_{b,c,y} = 0.5 \frac{v}{|\vec{u}|} \frac{\tau_s^2}{\rho d_*^{0.3}} \frac{d_{50}}{\tau_{cr}} \frac{\tau_s - \tau_{cr}}{\tau_{cr}} \mathcal{H}(\tau_s - \tau_{cr}), \quad (\text{A.6b})$$

where  $\tau_s$  is the shear stress experienced by the sediment due to both current and wave motion,  $\tau_{cr}$  the critical shear stress below which no bed load transport occurs, and  $\mathcal{H}$  the Heaviside step function. Furthermore,  $d_{50}$  and  $d_*$  are the median and dimensionless sediment diameter, respectively. The bed load transport components are modified to include gravitational bed-slope effects in longitudinal and in transverse directions,

$$q_{b,c,x}^* = \alpha_s q_{b,c,x} - \alpha_n q_{b,y}, \quad (\text{A.7a})$$

$$q_{b,c,y}^* = \alpha_s q_{b,c,y} + \alpha_n q_{b,x}. \quad (\text{A.7b})$$

Here,

$$\alpha_s = 1 + \alpha_{bs} \left[ \frac{\tan \psi}{\cos \beta_s (\tan \psi - \tan \beta_s)} - 1 \right], \quad (\text{A.8a})$$

$$\alpha_n = \alpha_{bn} \sqrt{\frac{\tau_{cr}}{|\tau|}} \tan \beta_n, \quad (\text{A.8b})$$

in which  $\alpha_{bs}$  and  $\alpha_{bn}$  are tuning parameters,  $\beta_s$  and  $\beta_n$  are the bed slope angles in the streamwise and transverse direction (positive down), respectively, and  $\psi$  is the internal angle of friction of bed material (assumed to be  $30^\circ$ ).

In the presence of waves, to incorporate the wave orbital velocities, the magnitude of the current-related bed load transport is divided by the factor  $\sqrt{1 + r^2 + 2|r| \cos \phi}$  with  $\phi$  the angle between currents and wave propagation direction and

$$r = \left( \frac{|u_{on}| - u_{cr}}{|\vec{u}| - u_{cr}} \right)^3. \quad (\text{A.9})$$

Here,  $u_{on}$  is the maximum of the (asymmetric) intra-wave near-bed horizontal velocity in the direction of the waves based on the significant wave height using the method of Isobe and Horikawa (1982) adjusted by Van Rijn et al. (2004), and  $u_{cr}$  is critical depth-averaged

velocity for initiation of motion based on  $\tau_{cr}$ . The components of the wave-related bed load transport  $q_{b,w,x}$  and  $q_{b,w,y}$  are given by

$$q_{b,w,x} = r|\vec{q}_{b,c}| \cos \varphi, \quad (\text{A.10a})$$

$$q_{b,w,y} = r|\vec{q}_{b,c}| \sin \varphi, \quad (\text{A.10b})$$

where  $\varphi$  is the local angle between the direction of wave propagation and the positive  $x$ -axis.

Finally, the current- and wave-related bed load transport are combined to obtain the total bed load transport:

$$q_{b,x} = q_{b,c,x} + BedW \cdot q_{b,w,x}, \quad (\text{A.11a})$$

$$q_{b,y} = q_{b,c,y} + BedW \cdot q_{b,w,y}. \quad (\text{A.11b})$$

The calibration parameter  $BedW$  is extensively discussed in Chapters 3 and 6.

### A.2.2 Suspended load

For the suspended load transport due to currents, the wave- and depth-averaged sediment concentration,  $c$ , follows from the depth-averaged advection-diffusion equation,

$$\frac{\partial(hc)}{\partial t} + \frac{\partial(huc)}{\partial x} + \frac{\partial(hvc)}{\partial y} - D_H \left[ \frac{\partial}{\partial x} \left( h \frac{\partial c}{\partial x} \right) + \frac{\partial}{\partial y} \left( h \frac{\partial c}{\partial y} \right) \right] = w_s(c_{eq} - c). \quad (\text{A.12})$$

Here,  $D_H$  is the spatially uniform horizontal eddy diffusivity and  $w_s$  the hindered sediment settling velocity. The latter incorporates hindered settling effects when the suspended sediment particles cannot settle freely, because of the presence of the surrounding particles in high concentrations. Furthermore, the equilibrium concentration,  $c_{eq}$ , depends on the skin friction due to the currents and waves. Note that the right-hand side of Equation A.12, which describes the exchange of sediment between the bed and the water column, can both be positive and negative. The terms on the left-hand side describe (from left to right) the temporal gradient in depth-integrated sediment concentration, the spatial gradient in sediment advection in both directions, and the diffusive processes due to gradients in sediment concentration in both directions.

**Table A.1** Parameter settings for the Ameland model used in Chapter 2 and the idealized model used in Chapters 3-5.

	Ameland model	idealized model
$f$	$1.16 \cdot 10^{-4} \text{ s}^{-1}$	$1.12 \cdot 10^{-4} \text{ s}^{-1}$
$\rho$	$1000 \text{ kg m}^{-3}$	$1000 \text{ kg m}^{-3}$
$\mathcal{A}$	$5 \text{ m}^2 \text{s}^{-1}$	$10 \text{ m}^2 \text{s}^{-1}$
$d_{50}$	$250 \mu\text{m}$	$250 \mu\text{m}$
$\alpha_{bs}$	1	1
$\alpha_{bn}$	1.5	1.5
$D_H$	$1 \text{ m}^2 \text{s}^{-1}$	$1 \text{ m}^2 \text{s}^{-1}$
$M$	$10^{-5}$	20
$p$	0.4	0.4
$BedW$	1	0.3

Based on the computed sediment concentrations, the current-related suspended transport rates in  $x$ - and  $y$ -directions are computed as:

$$q_{s,c,x} = huc - D_H \frac{\partial c}{\partial x}, \quad (\text{A.13a})$$

$$q_{s,c,y} = hvc - D_H \frac{\partial c}{\partial y}. \quad (\text{A.13b})$$

As the wave-related suspended load transport is rather uncertain, care must be applied to choosing the  $SusW$  calibration factor. According to Van Rijn et al. (2004) and Deltas (2014), it seems that the best results are obtained by ignoring the wave-related suspended load transports or prescribing a strongly reduced factor. Therefore, in this thesis, it is ignored by setting  $SusW = 0$ .

The change in bed level,  $z_b$ , is determined at every time step by

$$\frac{\partial z_b}{\partial t} = -\frac{M}{1-p} \left( \frac{\partial q_{b,x}}{\partial x} + \frac{\partial q_{b,y}}{\partial y} + w_s(c_{eq} - c) \right). \quad (\text{A.14})$$

Here,  $p$  and  $M$  are the porosity and the morphological acceleration factor, respectively.



## Bibliography

- Bak, J. (2017). Nourishment strategies for the Ameland Inlet. MA thesis. TU Delft, Delft University of Technology.
- Balouin, Y., H. Howa, and D. Michel (2001). Swash platform morphology in the ebb-tidal delta of the Barra Nova inlet, South Portugal. *Journal of Coastal Research* 17.4.
- Battjes, J. A. and J. P. F. M. Janssen (1978). Energy loss and set-up due to breaking of random waves. In: *Coastal Engineering 1978*, pp. 569–587.
- Becherer, J., J. Hofstede, U. Gräwe, K. Purkiani, E. Schulz, and H. Burchard (2018). The Wadden Sea in transition-consequences of sea level rise. *Ocean Dynamics* 68.1, pp. 131–151.
- Beck, T. M. and N. C. Kraus (2011). New Ebb-Tidal Delta at an Old Inlet, Shark River Inlet, New Jersey. *Journal of Coastal Research*, pp. 98–110.
- Benninghoff, M. and C. Winter (2019). Recent morphologic evolution of the German Wadden Sea. *Scientific reports* 9.1, pp. 1–9.
- Bertin, X., A. B. Fortunato, and A. Oliveira (2009). A modeling-based analysis of processes driving wave-dominated inlets. *Continental Shelf Research* 29.5, pp. 819–834.
- Biegel, E and P Hoekstra (1995). Morphological response characteristics of the Zoutkamperlaag, Frisian inlet (The Netherlands), to a sudden reduction in basin area. In: *Tidal signatures in modern and ancient sediments*. Vol. 24. Blackwell London, pp. 85–99.
- Boechat Albernaz, M., G. Ruessink, B. Jagers, and M. Kleinhans (2019). Effects of Wave Orbital Velocity Parameterization on Nearshore Sediment Transport and Decadal Morphodynamics. *Journal of Marine Science and Engineering* 7.6, p. 188.
- Booij, N., R. C. Ris, and L. H. Holthuijsen (1999). A third-generation wave model for coastal regions: 1. Model description and validation. *Journal of geophysical research: Oceans* 104.C4, pp. 7649–7666.
- Brière, C and D. Walstra (2006). Modelling of bar dynamics. *WL Delft Hydraulics report, project Z 4099*.
- Bruun, P. and F. Gerritsen (1960). Stability of coastal inlets. *Coastal Engineering Proceedings* 1.7, p. 23.
- Burningham, H. and J. French (2006). Morphodynamic behaviour of a mixed sand–gravel ebb-tidal delta: Deben estuary, Suffolk, UK. *Marine Geology* 225.1–4, pp. 23–44.
- Cayocca, F. (2001). Long-term morphological modeling of a tidal inlet: the Arcachon Basin, France. *Coastal Engineering* 42.2, pp. 115–142.
- Cheung, K. F., F. Gerritsen, and J. Cleveringa (2007). Morphodynamics and sand bypassing at Ameland Inlet, the Netherlands. *Journal of Coastal Research*, pp. 106–118.
- Dallas, K. L. and P. L. Barnard (2011). Anthropogenic influences on shoreline and nearshore evolution in the San Francisco Bay coastal system. *Estuarine, Coastal and Shelf Science* 92.1, pp. 195–204.
- Dastgheib, A. (2012). *Long-term process-based morphological modeling of large tidal basins*. IHE Delft Institute for Water Education.
- Davis, R. A. and M. O. Hayes (1984). What is a wave-dominated coast? *Marine geology* 60.1–4, pp. 313–329.
- De Swart, H. E. and J. T. F. Zimmerman (2009). Morphodynamics of tidal inlet systems. *Annual Review of Fluid Mechanics* 41, pp. 203–229.
- De Fockert, A (2008). Impact of relative sea level rise on the Amelander Inlet Morphology. MA thesis. TU Delft, Delft University of Technology.
- Dean, R. G. and T. L. Walton (1975). Sediment transport processes in the vicinity of inlets with special reference to sand trapping. *Geology and Engineering*, pp. 129–149.

- DeltaProgramma (2014). Wadden Gebied Bijlage A8. [https://www.deltacommissaris.nl/binaries/deltacommissaris/documenten/publicaties/2013/09/17/deltaprogramma-2014-bijlage-a8/DP2014+Bijlage+A8+Deltaprogramma+Waddengebied\\_tcm309-344240.pdf](https://www.deltacommissaris.nl/binaries/deltacommissaris/documenten/publicaties/2013/09/17/deltaprogramma-2014-bijlage-a8/DP2014+Bijlage+A8+Deltaprogramma+Waddengebied_tcm309-344240.pdf).
- Deltas (2009). SBW Wadden Sea, water level modelling-Calibration hydrodynamic model. Delft, *Deltas Report*, pp. 1200114–005.
- Deltas (2014). Simulation of multi-dimensional hydrodynamic flows and transport phenomena, including sediments. *User Manual Delft3D-FLOW, the Netherlands* 690.
- Dissanayake, D. M. P. K., J. A. Roelvink, and M Van der Wegen (2009). Modelled channel patterns in a schematized tidal inlet. *Coastal Engineering* 56.11, pp. 1069–1083.
- Dissanayake, D. M. P. K., R. Ranasinghe, and J. A. Roelvink (2012). The morphological response of large tidal inlet/basin systems to relative sea level rise. *Climatic change* 113.2, pp. 253–276.
- Duran-Matute, M, T Gerkema, G. J. De Boer, J. J. Nauw, and U Gräwe (2014). Residual circulation and freshwater transport in the Dutch Wadden Sea: a numerical modelling study. *Ocean Science* 10.4, pp. 611–632.
- Elias, E. P. L., A. J. F. Van der Spek, Z. B. Wang, and J De Ronde (2012). Morphodynamic development and sediment budget of the Dutch Wadden Sea over the last century. *Netherlands Journal of Geosciences* 91.03, pp. 293–310.
- Elias, E., R. Teske, A. Van der Spek, and M. Lazar (2015). MODELLING TIDAL-INLET MORPHODYNAMICS ON MEDIUM TIME SCALES. In: *The Proceedings of the Coastal Sediments 2015*. World Scientific.
- Elias, E. P. and J. E. Hansen (2013). Understanding processes controlling sediment transports at the mouth of a highly energetic inlet system (San Francisco Bay, CA). *Marine Geology* 345, pp. 207–220.
- Elias, E. P. and A. J. van der Spek (2006). Long-term morphodynamic evolution of Texel Inlet and its ebb-tidal delta (The Netherlands). *Marine Geology* 225.1-4, pp. 5–21.
- Elias, E. P., A. J. Van der Spek, S. G. Pearson, and J. Cleveringa (2019). Understanding sediment bypassing processes through analysis of high-frequency observations of Ameland Inlet, the Netherlands. *Marine Geology* 415, p. 105956.
- FitzGerald, D. M. (1982). Sediment bypassing at mixed energy tidal inlets. In: *Coastal Engineering 1982*. ASCE, pp. 1094–1118.
- FitzGerald, D. M. (1984). Interactions between the ebb-tidal delta and landward shoreline: Price Inlet, South Carolina. *Journal of Sedimentary Research* 54.4.
- FitzGerald, D. M. (1988). Shoreline erosional-depositional processes associated with tidal inlets. In: *Hydrodynamics and sediment dynamics of tidal inlets*. Springer, pp. 186–225.
- FitzGerald, D. M., S. Penland, and D. Nummedal (1984). Control of barrier island shape by inlet sediment bypassing: East Frisian Islands, West Germany. *Marine Geology* 60.1-4, pp. 355–376.
- FitzGerald, D. M., N. C. Kraus, and E. B. Hands (2000). *Natural mechanisms of sediment bypassing at tidal inlets*. Tech. rep. DTIC Document.
- Ford, M. R. and M. E. Dickson (2018). Detecting ebb-tidal delta migration using Landsat imagery. *Marine Geology* 405, pp. 38–46.
- Fredsøe, J. (1984). Turbulent boundary layer in wave-current motion. *Journal of Hydraulic Engineering* 110.8, pp. 1103–1120.
- Friedrichs, C. T. and D. G. Aubrey (1988). Non-linear tidal distortion in shallow well-mixed estuaries: a synthesis. *Estuarine, Coastal and Shelf Science* 27.5, pp. 521–545.
- Fu, L. (2018). Modeling Nourishment in the Ameland Inlet - a long-term and short-term study with Delft3D. MA thesis. Utrecht University.
- Gao, S and M. Collins (1994). Analysis of grain size trends, for defining sediment transport pathways in marine environments. *Journal of Coastal Research*, pp. 70–78.
- Garel, E., C Sousa, Ó. Ferreira, and J. Morales (2014). Decadal morphological response of an ebb-tidal delta and down-drift beach to artificial breaching and inlet stabilisation. *Geomorphology* 216, pp. 13–25.

- Gaudiano, D. J. and T. W. Kana (2001). Shoal bypassing in mixed energy inlets: geomorphic variables and empirical predictions for nine South Carolina inlets. *Journal of Coastal Research*, pp. 280–291.
- Hamerlynck, O., K. Hostens, J. Mees, R. Arellano, A. Cattrijse, P Van de Vyver, and J. Craeymeersch (1992). The ebb tidal delta of the Grevelingen: a man-made nursery for flatfish? *Netherlands journal of sea research* 30, pp. 191–200.
- Hansen, J. E., E. Elias, and P. L. Barnard (2013). Changes in surfzone morphodynamics driven by multi-decadal contraction of a large ebb-tidal delta. *Marine Geology* 345, pp. 221–234.
- Hayes, M. O. (1975). Morphology of sand accumulation in estuaries: an introduction to the symposium. *Estuarine research* 2, pp. 3–22.
- Hayes, M. O. (1979). Barrier island morphology as a function of tidal and wave regime. *Barrier islands*, pp. 1–27.
- Hayes, M. O. (1980). General morphology and sediment patterns in tidal inlets. *Sedimentary geology* 26.1, pp. 139–156.
- Herrling, G and C Winter (2014). Morphological and sedimentological response of a mixed-energy barrier island tidal inlet to storm and fair-weather conditions. *Earth Surface Dynamics* 2.1, pp. 363–382.
- Herrling, G and C. Winter (2015). Tidally-and wind-driven residual circulation at the multiple-inlet system East Frisian Wadden Sea. *Continental Shelf Research* 106, pp. 45–59.
- Herrling, G. and C. Winter (2017). Spatiotemporal variability of sedimentology and morphology in the East Frisian barrier island system. *Geo-Marine Letters* 37.2, pp. 137–149.
- Herrling, G. and C. Winter (2018). Tidal inlet sediment bypassing at mixed-energy barrier islands. *Coastal Engineering* 140, pp. 342–354.
- Holthuijsen, L. H. (2010). *Waves in oceanic and coastal waters*. Cambridge University Press.
- Isobe, M. and K. Horikawa (1982). Study on water particle velocities of shoaling and breaking waves. *Coastal Engineering in Japan* 25.1, pp. 109–123.
- Israel, C. G. and D. W. Dunsbergen (1999). Cyclic morphological development of the Ameland Inlet, the Netherlands. In: *Proceedings IAHR Symposium on river, coastal and estuarine morphodynamics, Department of Environmental Engineering, University of Genoa*, pp. 705–714.
- Israel, C. G. and A. P. Oost (2001). *Strandhaak ontwikkeling op de koppen van de Waddeneilanden*. Tech. rep. Rijkswaterstaat RIKZ werkdocument RIKZ/OS/2001.116 x, 27 pag., 24 fig. en 9 bijlagen.
- Jiao, J (2014). Morphodynamics of Ameland Inlet: Medium-term Delft3D Modelling.
- Kleinmans, M. G., R. T. Van Scheltinga, M. Van Der Vegt, and H. Markies (2015). Turning the tide: growth and dynamics of a tidal basin and inlet in experiments. *Journal of Geophysical Research: Earth Surface* 120.1, pp. 95–119.
- Komen, G. J., K Hasselmann, and K Hasselmann (1984). On the existence of a fully developed wind-sea spectrum. *Journal of physical oceanography* 14.8, pp. 1271–1285.
- Latteux, B. (1995). Techniques for long-term morphological simulation under tidal action. *Marine geology* 126.1–4, pp. 129–141.
- Lenstra, K. J. H., W. Ridderinkhof, and M. van der Vegt (2019). Model output: Unraveling the mechanisms that cause cyclic channel-shoal dynamics of ebb-tidal deltas: a numerical modeling study. DOI:10.5281/ZENODO.2613407.
- Lesser, G. R., J. v. Roelvink, J. Van Kester, and G. Stelling (2004). Development and validation of a three-dimensional morphological model. *Coastal engineering* 51.8–9, pp. 883–915.
- Li, G. and Z. Sun (2011). Morphodynamic system and the evolution of Laolonggou tidal inlet (J). *Marine Geology & Quaternary Geology* 1.31, pp. 11–19.
- Li, H (2018). The Ameland Inlet during the Sinterklaas Storm: the role of flooding of watersheds. MA thesis. Utrecht University.
- Longuet-Higgins, M. S. and R. Stewart (1962). Radiation stress and mass transport in gravity waves, with application to 'surf beats'. *Journal of Fluid Mechanics* 13.4, pp. 481–504.
- Lotze, H. K. et al. (2005). Human transformations of the Wadden Sea ecosystem through time: a synthesis. *Helgoland Marine Research* 59.1, p. 84.

- Luck, G. et al. (1975). der einfluss der schutzwerke der ostfriesischen inseln auf die morphologischen vorgaenge im bereich der seegaten und ihrer einzugsgebiete. *Mitt. Leicht weiss Inst., Braunschweig* 47, pp. 1–22.
- Nahon, A., X. Bertin, A. B. Fortunato, and A. Oliveira (2012). Process-based 2DH morphodynamic modeling of tidal inlets: a comparison with empirical classifications and theories. *Marine Geology* 291, pp. 1–11.
- Nienhuis, J. H., A. D. Ashton, W. Nardin, S. Fagherazzi, and L. Giosan (2016). Alongshore sediment bypassing as a control on river mouth morphodynamics. *Journal of Geophysical Research: Earth Surface* 121.4, pp. 664–683.
- O'Connor, M. C., J. A. G. Cooper, and D. W. Jackson (2011). Decadal behavior of tidal inlet-associated beach systems, northwest Ireland, in relation to climate forcing. *Journal of Sedimentary Research* 81.1, pp. 38–51.
- Oost, A. P. (1995). *Dynamics and sedimentary developments of the Dutch Wadden Sea with a special emphasis on the Frisian Inlet: a study of the barrier islands, ebb-tidal deltas, inlets and drainage basins*. Faculteit Aardwetenschappen.
- Ridderinkhof, H (1988). Tidal and residual flows in the Western Dutch Wadden Sea I: numerical model results. *Netherlands Journal of Sea Research* 22.1, pp. 1–21.
- Ridderinkhof, W, H. E. de Swart, M van der Vegt, and P Hoekstra (2014a). Geometry of tidal inlet systems: A key factor for the net sediment transport in tidal inlets. *Journal of Geophysical Research: Oceans* 119.10, pp. 6988–7006.
- Ridderinkhof, W, H. E. de Swart, M van der Vegt, and P Hoekstra (2014b). Influence of the back-barrier basin length on the geometry of ebb-tidal deltas. *Ocean dynamics* 64.9, pp. 1333–1348.
- Ridderinkhof, W, P Hoekstra, M van der Vegt, and H. E. de Swart (2016a). Cyclic behavior of sandy shoals on the ebb-tidal deltas of the Wadden Sea. *Continental Shelf Research* 115, pp. 14–26.
- Ridderinkhof, W, H. E. de Swart, M van der Vegt, and P Hoekstra (2016b). Modeling the growth and migration of sandy shoals on ebb-tidal deltas. *Journal of Geophysical Research: Earth Surface* 121.7, pp. 1351–1372.
- Rijkswaterstaat (2017). Kustgenese2.0. <https://waterinfo-extra.rws.nl/projecten/@217389/kustgenese-2-0/>.
- Ris, R. C., L. H. Holthuijsen, and N Booij (1999). A third-generation wave model for coastal regions: 2. Verification. *Journal of Geophysical Research: Oceans* 104.C4, pp. 7667–7681.
- Rizzetto, F., L. Tosi, M. Zecchin, G. Brancolini, L. Baradello, C. Tang, et al. (2009). Ancient geomorphological features in shallows of the Venice Lagoon (Italy). *Journal of Coastal Research* 56. Special Issue, pp. 752–756.
- Roelvink, J. and D.-J. Walstra (2004). Keeping it simple by using complex models. *Advances in hydro-science and engineering* 6, pp. 1–11.
- Sedigh, M., R. Tomlinson, A. Etemad-Shahidi, and N. Cartwright (2014). Modelling the morphological response of an ebb tidal delta to storm wave forcing. *Coastal Engineering Proceedings* 1.34, pp. 63–71.
- Sennes, G, B Castelle, X Bertin, H Mirfenderesk, and R. Tomlinson (2007). Modelling of the Gold Coast Seaway tidal inlet, Australia. *Journal of Coastal Research*, pp. 1086–1091.
- Sha, L. P. (1989). Variation in ebb-delta morphologies along the West and East Frisian Islands, The Netherlands and Germany. *Marine Geology* 89.1, pp. 11–28.
- Sha, L. P. and J. H. Van den Berg (1993). Variation in ebb-tidal delta geometry along the coast of the Netherlands and the German Bight. *Journal of Coastal Research* 9.3, pp. 730–746.
- Sha, L. (1990). Surface sediments and sequence models in the ebb-tidal delta of Texel Inlet, Wadden Sea, The Netherlands. *Sedimentary Geology* 68.1-2, pp. 125–141.
- Soulsby, R. L., A. G. Davies, J Fredsøe, D. Huntley, I. G. Jonsson, D Myrhaug, R. R. Simons, A Temperville, and T Zitman (1993). Bed shear-stresses due to combined waves and currents. Book of Abstracts, MAST-2, G8M Coastal Morphodynamics. In: *Overall Workshop, Grenoble*, pp. 2–1.

- Speer, P. E. and D. G. Aubrey (1985). A study of non-linear tidal propagation in shallow inlet/estuarine systems Part II: Theory. *Estuarine, Coastal and Shelf Science* 21.2, pp. 207–224.
- Stive, M. J. et al. (2013). A new alternative to saving our beaches from sea-level rise: The sand engine. *Journal of Coastal Research* 29.5, pp. 1001–1008.
- Stutz, M. L. and O. H. Pilkey (2005). The relative influence of humans on barrier islands: Humans versus geomorphology. *Humans as Geologic Agents* 16, p. 137.
- Stutz, M. L. and O. H. Pilkey (2011). Open-ocean barrier islands: global influence of climatic, oceanographic, and depositional settings. *Journal of Coastal Research* 27.2, pp. 207–222.
- Symonds, A. M., T. Vijverberg, S. Post, B.-J. van der Spek, J. Henrotte, and M. Sokolewicz (2016). Comparison between mikk 21 FM, delft3d and delft3d FM flow models of western port bay, Australia. *Coastal Engineering*, p. 2.
- Van Rhijn, T. (2019). Sediment transport during the execution of the pilot nourishment Ameland Inlet: Development of a tool for analysing bathymetric surveys, applied on the pilot nourishment Ameland inlet. MA thesis. TU Delft, Delft University of Technology.
- Van Weerdenburg, R. (2019). Exploring the relative importance of wind for exchange processes around a tidal inlet system: The case of Ameland Inlet. MA thesis. TU Delft, Delft University of Technology.
- Van de Kreeke, J (2006). An aggregate model for the adaptation of the morphology and sand bypassing after basin reduction of the Frisian Inlet. *Coastal Engineering* 53.2-3, pp. 255–263.
- Van der Spek, A. J. (2018). The development of the tidal basins in the Dutch Wadden Sea until 2100: the impact of accelerated sea-level rise and subsidence on their sediment budget—a synthesis. *Netherlands Journal of Geosciences* 97.3, pp. 71–78.
- Van der Vegt, M., H. M. Schuttelaars, and H. E. de Swart (2006). Modeling the equilibrium of tide-dominated ebb-tidal deltas. *Journal of Geophysical Research: Earth Surface* (2003–2012) 111.F2.
- Van der Vegt, M., H. Schuttelaars, and H. de Swart (2009). The influence of tidal currents on the asymmetry of tide-dominated ebb-tidal deltas. *Continental Shelf Research* 29.1, pp. 159–174.
- Van der Westhuysen, A. J. (2012). Spectral modeling of wave dissipation on negative current gradients. *Coastal Engineering* 68, pp. 17–30.
- Van der Westhuysen, A. J. (2007). Advances in the spectral modelling of wind waves in the nearshore.
- Van Leeuwen, S., M Van der Vegt, and H. de Swart (2003). Morphodynamics of ebb-tidal deltas: a model approach. *Estuarine, Coastal and Shelf Science* 57.5, pp. 899–907.
- Van Rijn, L., D. Walstra, and M. v. Ormondt (2004). *Description of TRANSPOR2004 and implementation in DELFT3D-ONLINE: final report*. Tech. rep. Deltares (WL).
- Van Rijn, L. C. (2007a). Unified view of sediment transport by currents and waves. I: Initiation of motion, bed roughness, and bed-load transport. *Journal of hydraulic engineering* 133.6, pp. 649–667.
- Van Rijn, L. C. (2007b). Unified view of sediment transport by currents and waves. Waves. II: Suspended Transport. *Journal of hydraulic engineering* 133.6, pp. 668–689.
- Velasquez-Montoya, L., M. F. Overton, and E. J. Sciaudone (2020). Natural and anthropogenic-induced changes in a tidal inlet: Morphological evolution of Oregon Inlet. *Geomorphology* 350, p. 106871.
- Vermeersen, B. L. et al. (2018). Sea-level change in the Dutch Wadden Sea. *Netherlands Journal of Geosciences* 97.3, pp. 79–127.
- Vincent, O. D. and L. J. Moore (2015). Barrier island bistability induced by biophysical interactions. *Nature Climate Change* 5.2, p. 158.
- Walton, T. L. and W. D. Adams (1976). Capacity of inlet outer bars to store sand. *Coastal Engineering Proceedings* 1.15.
- Wang, Y.-H., L.-Q. Tang, C.-H. Wang, C.-J. Liu, and Z.-D. Dong (2014). Combined effects of channel dredging, land reclamation and long-range jetties upon the long-term evolution of channel-shoal system in Qinzhou bay, SW China. *Ocean Engineering* 91, pp. 340–349.
- Wang, Y., Q. Yu, J. Jiao, P. K. Tonnon, Z. B. Wang, and S. Gao (2016). Coupling bedform roughness and sediment grain-size sorting in modelling of tidal inlet incision. *Marine Geology* 381, pp. 128–141.

- Wang, Z. B., E. P. Elias, A. J. van der Spek, and Q. J. Lodder (2018). Sediment budget and morphological development of the Dutch Wadden Sea: impact of accelerated sea-level rise and subsidence until 2100. *Netherlands Journal of Geosciences* 97.3, pp. 183–214.
- Xu, S. (2019). The effect of wind and waves on sediment transport patterns in the Ameland Inlet. MA thesis. Utrecht University.
- Yang, B., M. Madden, J. Kim, and T. R. Jordan (2012). Geospatial analysis of barrier island beach availability to tourists. *Tourism Management* 33.4, pp. 840–854.
- Zhou, Z., G. Coco, M. van der Wegen, Z. Gong, C. Zhang, and I. Townend (2015). Modeling sorting dynamics of cohesive and non-cohesive sediments on intertidal flats under the effect of tides and wind waves. *Continental Shelf Research* 104, pp. 76–91.

## About the author

Klaas Lenstra was born on the 2nd of August 1988 in Houten, the Netherlands. He went to the Christelijk Gymnasium in Utrecht between 2000 and 2006; the daily commute invoked his love for cycling. His interest in nature became evident from finishing both the *Nature and Science* and *Nature and Health* tracks. Because he foolishly thought physics was all about nature, Klaas started his bachelor *Physics and Astronomy* at the Utrecht University in 2006. He struggled with the elementary physics, but finally obtained his degree in 2013. Following his love for nature and natural processes, he enrolled in the master program *Meteorology, Physical Oceanography and Climate Physics* at the Institute for Marine and Atmospheric research Utrecht (IMAU). He graduated in 2015 after writing a master thesis about the effects of three-dimensional tidal currents on bed forms in the North Sea. His stay at Utrecht University continued at the Department of Physical Geography to start a PhD project on the cyclic morphodynamics of ebb-tidal deltas. Fast-forward four years (and a few months) and the results of this PhD research are presented in this thesis. In the meantime, he also supervised three students writing their master theses. In January 2020, Klaas started his new job at the Department of Rivers, Coasts and Seas at Arcadis.

## List of publications

### Journal papers

**Lenstra, KJH, SRPM Pluis, W Ridderinkhof, BG Ruessink & M van der Vegt (2019).**  
Cyclic channel-shoal dynamics at the Ameland Inlet: the impact on waves, tides, and sediment transport. *Ocean Dynamics*, 69(4):409–425,  
<https://doi.org/10.1007/s10236-019-01249-3>.

**Lenstra, KJH, W Ridderinkhof & M van der Vegt (2019).**  
Unraveling the mechanisms that cause cyclic channel-shoal dynamics of ebb-tidal deltas: a numerical modeling study. *Journal of Geophysical Research: Earth Surface*, 124(12): 2778–2797,  
<https://doi.org/10.1029/2019JF005090>.

**Lenstra, KJH & M van der Vegt (in preparation for submission).**  
The impact of sea-level rise and basin area reduction on the cyclic behavior of tidal inlet systems.

**Lenstra, KJH, L Fu & M van der Vegt (in preparation for submission).**  
The effect of mega-nourishments on long-term behavior of ebb-tidal deltas.

## **Conference abstracts**

**Lenstra, KJH, SRPM Pluis, M van der Vegt & W Ridderinkhof (2016).**  
The influence of cyclic channel-shoal dynamics on waves, currents and sediment transport on the ebb-tidal delta of Ameland Inlet.

*Physics of Estuaries and Coastal Seas Conference (PECS), 2016, Scheveningen* (poster presentation)

**Lenstra, KJH, SRPM Pluis & M van der Vegt (2017).**  
Cyclic evolution of ebb-tidal delta of Ameland results in periodically changing import and export in the inlet.  
*NCK days 2017* (oral presentation)

**Lenstra, KJH, W Ridderinkhof & M van der Vegt (2017).**  
Cyclic behavior of ebb-tidal deltas from model simulations: the role of waves and tides.  
*Symposium on River, Coastal and Estuarine Morphodynamics (RCEM), 2017, Padua, Italy* (poster presentation)

**Lenstra, KJH & M van der Vegt (2018).**  
Cyclic behavior of ebb-tidal deltas from model simulations: the role of waves and tides.  
*AGU Ocean Sciences Meeting, 2018, Portland, USA* (poster presentation)

**Lenstra, KJH, W Ridderinkhof & M van der Vegt (2018).**  
Cyclic behavior of ebb-tidal deltas from model simulations.  
*NCK days 2018* (poster presentation)

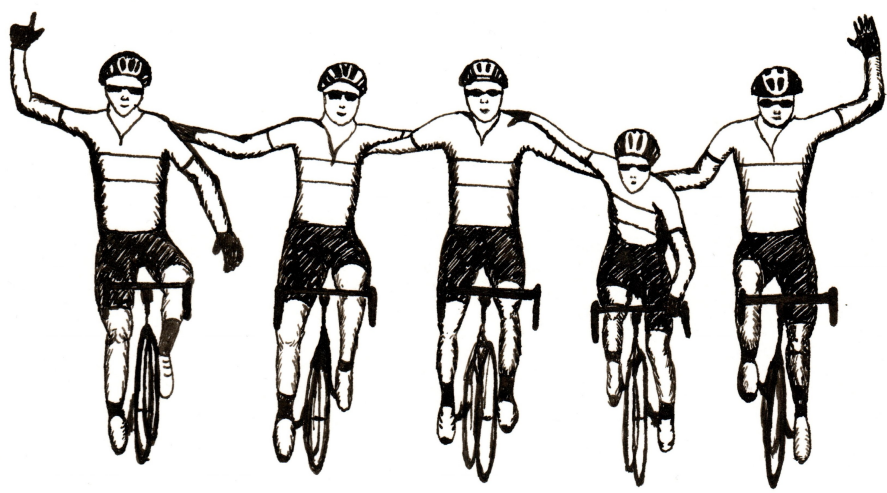
**Lenstra, KJH, L Fu & M van der Vegt (2019).**  
The effect of ebb-tidal delta nourishments on cyclic channel-shoal dynamics.  
*NCK days 2019* (oral presentation)

**Lenstra, KJH, L Fu & M van der Vegt (2019).**  
The effect of ebb-tidal delta nourishments on cyclic channel-shoal dynamics.  
*EGU General Assembly 2019, Vienna, Austria* (oral presentation)

**van der Vegt, M, SZ Xu, KJH Lenstra & N Geleynse (2019).**  
The effect of tidal basin connectivity and waves on sediment transport patterns in the Ameland Inlet.  
*EGU General Assembly 2019, Vienna, Austria* (poster presentation)

**Lenstra, KJH & M van der Vegt (2019).**  
Ebb-tidal deltas on the move: cyclic channel-shoal dynamics.  
*NCK theme day: Morphodynamics of the Wadden Sea* (oral presentation)





## Dankwoord/Acknowledgements

Promoveren is als een lange fietstocht: pieken, dalen, wind mee, wind tegen, hard werken en het is zwaarder als je het alleen doet. Gelukkig was er een heel peloton vol collega's, vrienden en familie die met me mee fietsten, me uit de wind hielden en me helpen met de te nemen route. Het is deze hulp en samenwerking die promoveren voor mij zo leuk heeft gemaakt. Samen fietsen is zoveel leuker! Ik prijs mezelf gelukkig dat ik in dit hoofdstuk zovelen mag bedanken.

De belangrijkste hulp kwam van mijn begeleiders. Maarten, je hebt me de vrijheid gegeven om eigenwijs te zijn, mijn eigen route te bepalen en daarmee fouten te maken. Het is indrukwekkend hoe jouw eerlijke commentaar en verbeterpunten me vooruitbrachten. Ook al bezorgde het me extra werk, van jouw directe feedback werd ik sterker. Ik heb genoten van onze samenwerking en van je vertrouwen. Gerben, je keek vaak van een afstandje toe bij mijn promotie. Toch stond je altijd direct klaar als ik een vraag had, sprong je zelf in als je verbeterpunten zag en hield je er een oogje op of ik wel op tijd binnen zou zijn. In de laatste periode heb je je intensief beziggehouden met de indeling en de tekst van dit proefschrift. Jouw verbeterpunten hebben enorm veel bijgedragen aan de leesbaarheid. Maarten en Gerben, bovenal wil ik jullie bedanken dat jullie er samen voor hebben gezorgd dat ik dit promotietraject ontspannen, stressvrij en met een hoop plezier heb kunnen doorlopen.

Een woord van dank voor mijn oude leermeester Huib. Het zijn jouw levendige colleges geweest die mij enthousiast hebben gemaakt voor in eerste instantie geofysische stormingsleer en later kustenfysica. Alles wat je me leerde tijdens mijn masteronderzoek heb ik nog zeer regelmatig profijt van.

Wim en Stefan, jullie hebben ervoor gezorgd dat ik met een voorsprong kon beginnen aan de tocht der promotie. Niet alleen jullie voorwerk in modelopzet, maar ook jullie feedback op resultaten en papers hebben me enorm geholpen.

Veel dank gaat naar diegenen die met mij een kantoor durfden te delen: Jasper, Daan, Pam, Timothy en Laura. Ik heb vier leuke jaren gehad met hen en de andere collega's in de kustengroep: Joost, Sepehr, Winnie, Yvonne, Anita, Anouk, Jantien, Nynke, Piet, Christian en Renske. Bedankt voor de wetenschappelijke discussies, de gezelligheid, de lunchrondjes en de broodjes op vrijdag. Jullie hebben deze rare natuurkundige in jullie midden opgenomen en getransformeerd tot een ware aardwetenschapper. Joost, Sebastiaan, Arjen, Pam, Daan en Jasper, ik heb enorm genoten van het fanatisme tijdens onze bordspelavonden.

All the people from Seawad, many thanks for involving me in your project. Your feedback, comments and suggestions were a nourishment for my work. Marcio, thank you for sharing your insights in cycling and Delft3D. Tjebbe, dank voor de gezelligheid tijdens de congressen die we samen bezochten.

It has been my privilege to supervise three students with their MSc thesis. Linxi, Li en Xu, thank you for everything I have learned from you and all the hard work you've put into helping me.

Voor de tekeningen die dit boekje kleur hebben gegeven wil ik Annelieke van harte bedanken. Harryt, bedankt voor de illustratie op de voorkant. Colette, fijn dat je een eerdere versie van dit dankwoord wilde proeflezen.

De kunst der rare routes heb ik geleerd van Harryt, Stefan en Elias. Of de bidon gevuld was met water, bier of whiskey, het was immer gezellig. Bedankt voor al het cycling behavior naast al het cyclic behavior.

Korfbal is een suf spelletje gespeeld door fantastische mensen. Ik noem geen namen om te voorkomen dat ik begin aan een opsomming zonder eind, wat op zichzelf al genoeg zegt. Eenieder die ik heb leren kennen bij Synergo en Hebbes, met wie ik samen heb gespeeld of training heb mogen geven, ik kijk met plezier terug op alle leuke trainingen, wedstrijden, toernooien, commissies, besturen en andere activiteiten.

Mijn schoonfamilie en in het bijzonder mijn schoonouders, dank voor alle hulp en interesse tijdens mijn promotie. Dat wetenschap voor jullie een vreemd wereldje is (en dat is het stiekem ook), heeft jullie er niet van weerhouden me toch alle steun te geven.

Tineke en Daan, ik ben ontzettend blij met de band die we met z'n vieren opgebouwd hebben. Ook tijdens jullie periode in Amerika bleven we close en het is heerlijk dat jullie weer terug zijn gekomen! Hoe hadden we anders zo vaak Pieter kunnen knuffelen? Sybrenne, Alex and Ruben, my family down under! I really appreciate your continuous effort to maintain a close connection, despite the many miles between us. I fondly remember your many visits over the years.

Mama en papa, jullie hebben me altijd gestimuleerd om nieuwsgierig te zijn, kritisch naar mezelf te kijken en mezelf te motiveren. De belangrijkste les die jullie me geleerd hebben is dat opgeven als het even tegenzit vrijwel altijd de slechtste keuze is. Zonder dit in m'n achterhoofd en zonder jullie liefde, vertrouwen en hulp had ik m'n bachelor en m'n promotie nooit af kunnen maken.

Lieve Nienke, het slot van dit proefschrift is voor jou. Afgelopen jaren hebben wij wel laten zien dat we samen elke berg kunnen overwinnen. Ik kan je niet genoeg bedanken voor je steun tijdens de moeilijke momenten. Bedankt voor dat je er altijd voor me was, bedankt voor alle liefde, bedankt voor al je geduld en bedankt voor al onze fietstochten samen. Ik kijk uit naar onze toekomst, met z'n drieën, naast elkaar op de stadsfiets!